Instabilities of Waves in Stratified Magnetohydrodynamics

Matthew Vine

Submitted in accordance with the requirements for the degree of
Doctor of Philosophy in Applied Mathematics

University of Leeds

September 2025

Acknowledgements

Without the help of Adrian Barker and Stephen Griffiths, I would have had no idea how to write this book. I am deeply grateful to you both. I would also like to thank Evy Kersalé and Henrik Latter for agreeing to be my examiners.

Here is a list of everyone who made my time in Leeds one that I will cherish.

Adam Aldridge
Anna Hayward
Arthur Janes
Bevelynn Whaler
Craig Cawsey
David Groothuizen Dijkema
Helen Tudor
James Crowney-Richards
Josh Montgomery
Laura Pinkney
Lawrie Wilson-Oak
Lenny Greenfield
Lucas Gosling
Luke Gostelow
Marcus Marshall
Matt Asker
Matt Dawswell
Matthew Lawrence
Megan Miller
Mikolaj Flis
Nils De Vries
Rich Wills
Rob Elliott
Rolando Rodriguez Ybarra
Ros Wartnaby
Sam Myers
Sean Robinson
Sonny Burrell

Abstract

We study instabilities of internal gravity waves (IGWs), Alfvén waves (AWs) and hybrid Alfvén-gravity waves (AGWs) propagating through a stably-stratified Boussinesq fluid with constant buoyancy frequency permeated by a uniform background magnetic field. This is achieved using the Boussinesq MHD equations, which admit plane wave solutions satisfying a quintic dispersion relation with three branches: a zero-frequency branch, an AW branch and an AGW branch.

We develop a theoretical framework with which to predict the growth rate of resonant instabilities of small-amplitude AGWs asymptotically. We also create a Floquet eigenvalue solver to describe the linear stability of finite-amplitude AGWs. Since the plane wave is an exact solution of the ideal nonlinear Boussinesq MHD equations, the eigenvalue solver allows us to study instabilities of waves with arbitrary amplitudes.

In the absence of a magnetic field, many instabilities of small-amplitude IGWs can be attributed to resonant triad interactions between three IGWs. We show that in the presence of a magnetic field, many instabilities of small-amplitude AGWs can be attributed to resonant triad interactions between AGWs and AWs in various combinations. The asymptotic framework for small-amplitude waves is used to classify instabilities observed using the eigenvalue solver in terms of such resonant interactions. Instabilities of these waves are not limited to those induced by resonant interactions. We derive a system of energetic equations to determine which physical processes are driving the instabilities energetically.

The model we use can be applied in a variety of astrophysical settings, including radiative zones in stellar interiors. Instabilities of IGWs play an important role in the mixing of matter, energy and angular momentum in astrophysical fluids, so it is crucial that we understand them mathematically. It is instructive to consider the interaction of IGWs with a magnetic field in many astrophysical fluids. We determine the influence of magnetic field strength and orientation on the growth rate of the instabilities we study.

Contents

1 Introduction **1**
- 1.1 Internal Gravity Waves . . . 1
  - 1.1.1 Fundamentals . . . 1
  - 1.1.2 Internal Gravity Waves on Earth . . . 4
- 1.2 Alfvén Waves . . . 5
- 1.3 Stellar Physics and Stellar Waves . . . 6
  - 1.3.1 Solar Structure . . . 8
  - 1.3.2 Solar Magnetic Field . . . 12
  - 1.3.3 Stellar Classification and Structure . . . 14
  - 1.3.4 Stellar Magnetic Fields . . . 17
  - 1.3.5 Asteroseismology . . . 21
- 1.4 Aims of Thesis . . . 22
- 1.5 Outline of Thesis . . . 23

2 Mathematical Model and Wave Properties **25**
- 2.1 Mathematical Model . . . 25
- 2.2 The Boussinesq Approximation . . . 27
- 2.3 Properties of Waves . . . 31
  - 2.3.1 Alfvén Waves . . . 33
  - 2.3.2 Internal Gravity Waves . . . 35
  - 2.3.3 Alfvén-Gravity Waves . . . 40
  - 2.3.4 Damped Oscillations . . . 44
- 2.4 Criterion for Overturning . . . 45

3 Triadic Resonance Interactions of IGWs **49**
- 3.1 Parametric Instabilities . . . 49
- 3.2 Resonant Triads . . . 50
- 3.3 Asymptotics . . . 55
  - 3.3.1 Growth Rate at Points of Exact Resonance . . . 55
  - 3.3.2 Short Wavelength Limit . . . 62

4 Instabilities of Finite-Amplitude IGWs **67**
- 4.1 Floquet Solver . . . 68
  - 4.1.1 The Basic State . . . 68
  - 4.1.2 The Coordinate Transformation . . . 68
  - 4.1.3 Constructing an Eigenvalue Problem . . . 71
- 4.2 Growth Rates . . . 75
  - 4.2.1 Characterising the Instability . . . 77

4.2.2 Influence of Parameters . . . 82
4.3 Eigenfunctions . . . 91
4.4 Energetics . . . 97
4.4.1 Deriving a Formula for the Total Energy Density . . . 97
4.4.2 Decomposing the Growth Rate . . . 101
4.5 Comparing Numerical and Theoretical Growth Rates . . . 107
4.5.1 Exact Resonances . . . 107
4.5.2 Short Wavelength Limit . . . 110
4.5.3 Absolute Error and Relative Error . . . 111

5 MHD Triadic Resonance Interactions **115**
5.1 MHD Resonant Triads . . . 115
5.2 Asymptotics . . . 119
5.2.1 Growth Rate at Points of Exact Resonance . . . 119
5.2.2 Explicit Solvability Conditions . . . 127

6 Instabilities of Finite-Amplitude AGWs **131**
6.1 Floquet Solver . . . 131
6.1.1 The Basic State . . . 131
6.1.2 The Coordinate Transformation . . . 133
6.1.3 Constructing an Eigenvalue Problem . . . 135
6.2 Growth Rates . . . 139
6.2.1 Characterising the Instabilities . . . 140
6.2.2 Influence of Magnetic Field Strength . . . 143
6.2.3 Influence of Magnetic Field Orientation . . . 145
6.2.4 Magnetic Field Vector Perpendicular to Primary Wavevector . . . 150
6.2.5 Magnetic Field Vector Aligned with Primary Wavevector . . . 152
6.3 Energetics . . . 153
6.3.1 Deriving a Formula for the Total Energy Density . . . 153
6.3.2 Influence of Parameters . . . 161
6.4 Comparing Numerical and Theoretical Growth Rates . . . 166
6.4.1 Growth Rates as a Function of Wavenumber . . . 167
6.4.2 Absolute Error and Relative Error . . . 174
6.4.3 Growth Rates Maximised over Wavenumber Space . . . 175
6.5 Astrophysical Significance of Field Strength Values . . . 181

7 Discussion **185**

A Derivations and Formulae **189**
A.1 The Boussinesq MHD Equations . . . 189
A.1.1 Decomposing the Lorentz force . . . 189
A.1.2 Decomposing the Magnetic Induction Term . . . 189
A.1.3 Vanishing Nonlinearities . . . 190
A.2 Eigenvalue Problem . . . 190
A.2.1 Matrix Coefficients . . . 190
A.2.2 Symmetry Arguments . . . 192
A.3 Asymptotics . . . 192
A.3.1 Deriving the HD Amplitude Equations . . . 192
A.3.2 Deriving the MHD Amplitude Equations . . . 193

A.3.3 Short Wavelength Limit 196

List of Figures

1.1 Visualisation of internal gravity waves in a tank of water created by injecting dye at several different depths and moving the bottom topography laterally to excite the observed waves (Sutherland, 2010). 3

1.2 Schematic showing how Alfvén waves form. Blue arrows: fluid velocity. Red arrows: Lorentz force. Black lines: magnetic field lines. Image credit: Finlay (2007). 6

1.3 Spherical polar coordinate system (r, θ, ϕ) describing a star. Image credit: Jorgen Christensen-Dalsgaard. 7

1.4 (Left) Fractional mass of different elements in the interior of the Sun as a function of fractional solar radius (Green et al., 2015). (Right) Internal structure of the Sun (Russell et al., 2019) 8

1.5 (Left) Angular frequency of fluid in the solar interior computed using data from helioseismology (image credit: Käpylä et al. (2023)). (Right) Angular frequency of fluid in the solar interior at different latitudes (credit: NSF National Solar Observatory). 10

1.6 (a) Solar granulation. (b) Sunspots in the photosphere. (c) Coronal loops. . . . 11

1.7 Solar quantities as a function of fractional radius. Dynamic viscosity is denoted by ν, thermal diffusivity is denoted by κ and Ohmic diffusivity is denoted by η. Squared buoyancy frequency N^2 and density ρ are taken from a solar model by Christensen-Dalsgaard et al. (1996). The point r_t marks the approximate fractional radial location occupied by the solar tachocline. 11

1.8 Schematic of a solar-type star showing convective plumes, some of which are penetrating into the radiative zone, giving rise to IGWs. Image credit: Pinçon et al. (2016). 12

1.9 The butterfly diagram, showing the total percentage sunspot coverage computed over finite-width strips of constant latitude, recorded each year since 1874. Image credit: Hathaway (2011). 13

1.10 The Hertzsprung-Russell diagram, showing the relationship between luminosity L and effective temperature T_{eff} for a selection of stars. Image credit: Chandra X-ray Observatory. 15

1.11 Typical structure of stars of mass M on the main sequence. Red arrows indicate radiative regions. Black loops indicate convective regions. $M_\odot$ denotes the mass of the Sun. Original source of image unknown. 16

1.12 Schematic describing wave motions in red giant stars. Image credit: Fuller et al. (2015). 20

2.1 Example of a valid location and orientation for the Cartesian box model within a solar-type star, together with its host (background) magnetic field $\boldsymbol{B}_0$. Shown here is a cross-section of part of the star, such that the bottom-left corner represents the centre of the star. Purple region: radiative zone. Orange region: convective zone. Green region: radiative-convective interface. The width of the radiative-convective interface is exaggerated for visual clarity. The Y-axis points directly out of the page. The size of the box is also exaggerated for visual clarity. To make a valid local Cartesian approximation, the box must be much smaller relative to the stellar radius. In this example, $\boldsymbol{B}_0$ happens to be confined to the (X, Z)-plane, though $\boldsymbol{B}_0$ may have a Y-component in general. 26

2.2 (Left) Illustration of the plane wave solution, together with its wavevector $\boldsymbol{K}$ and orientation θ with respect to the X-axis. (Right) Notation for the background magnetic field. 32

2.3 (Left) Dimensionless phase speed c_p/V_A and dimensionless group speed c_g/V_A as a function of wave propagation angle θ for pure Alfvén waves, with $\theta \in [0, 2\pi)$. (Right) Dimensionless phase velocity $\boldsymbol{c}_p(\theta)/V_A$ and dimensionless group velocity $\boldsymbol{c}_g(\theta)/V_A$ plotted as parametric curves for $\theta \in [0, 2\pi)$ for pure Alfvén waves. Magnetic field orientation: $\zeta = \pi/4$. 35

2.4 (Left) Dimensionless phase speed $(K/N)c_p$ and dimensionless group speed $(K/N)c_g$ as a function of wave propagation angle θ for pure internal gravity waves, with $\theta \in [0, 2\pi)$. (Right) Dimensionless phase velocity $(K/N)\boldsymbol{c}_p(\theta)$ and dimensionless group velocity $(K/N)\boldsymbol{c}_g(\theta)$ plotted as parametric curves for $\theta \in [0, 2\pi)$ for pure internal gravity waves. 39

2.5 Formation of the St Andrews cross from a laboratory experiment, augmented with the directions of the phase velocity $\boldsymbol{c}_p$ and the group velocity $\boldsymbol{c}_g$. Image credit: Mowbray and Rarity (1967b). 39

2.6 Dimensionless phase speed $(K/N)c_p$ and dimensionless group speed $(K/N)c_g$ as a function of θ for AGWs. Plotted for magnetic fields with orientation $\zeta = \pi/2$ and a selection of different magnetic field strengths b_0. 43

2.7 Dimensionless phase speed $(K/N)c_p$ and dimensionless group speed $(K/N)c_g$ as a function of θ for AGWs. Plotted for magnetic fields with strength $b_0 = 4$ and a selection of different magnetic field orientations ζ. 43

2.8 Dimensionless phase velocity $(K/N)\boldsymbol{c}_p(\theta)$ and dimensionless group velocity $(K/N)\boldsymbol{c}_g(\theta)$ plotted as parametric curves with parameter $\theta \in [0, 2\pi)$ for AGWs. Plotted for magnetic fields with orientation $\zeta = \pi/4$ and a selection of different magnetic field strengths b_0. 43

2.9 Dimensionless phase velocity $(K/N)\boldsymbol{c}_p(\theta)$ and dimensionless group velocity $(K/N)\boldsymbol{c}_g(\theta)$ plotted as parametric curves with parameter $\theta \in [0, 2\pi)$ for AGWs. Plotted for magnetic fields with strength $b_0 = 1$ and a selection of different magnetic field orientations ζ. 44

2.10 (Left) Schematic showing significance of amplitude parameter a and wave orientation θ. (Right) Onset of density overturning when crossing the threshold $a = a_c$, visualised by plotting dimensionless wave density (2.92) as a function of X and Z scaled by their respective wavevector components. 46

3.1 Diagram depicting a resonant triad between three waves with wavevectors $\boldsymbol{K}$, $\boldsymbol{K}_A$ and $\boldsymbol{K}_B$ respectively, corresponding to equation (3.12). 52

3.2 Pairs of k_{AX}, k_{AZ} values which produce resonant triads between IGWs when $k_{AY} = 0$. 54

3.3 Absolute value of the disturbance frequency $|\omega_A/\omega|$ as a function of horizontal wavenumber K_{AX}/K_X for resonant triads between IGWs when $K_{AY} = 0$. 54

3.4 Absolute value of the disturbance frequency $|\omega_A/\omega|$ as a function of horizontal wavenumber K_{AX}/K_X for resonant triads between IGWs when $K_{AY} = 0$. 55

4.1 Coordinate configuration showing the relative orientations of the (X, Z) and (x, z)-frames. 69

4.2 Contouring the growth rate of instabilities of an IGW in (α, β)-space. Parameter values: $a = 0.1$, $\theta = \pi/4$, $\gamma = 0$ and $\mathrm{Re} = \mathrm{Pe} = 10^6$. Resolution: $\mathcal{N} = 10$, $n_\alpha = n_\beta = 100$. 78

4.3 Relationship between the truncation point $\mathcal{N}$ of the Fourier series and the number of centres of exact resonance in (α, β)-space. Parameter values are identical to those used in Figure 4.2. 78

4.4 (Top) Growth rate contours in wavenumber space for instabilities of a pure internal gravity wave. Parameter values: $a = 0.1$, $\theta = \pi/4$, $\gamma = 0$, $\mathrm{Re} = \mathrm{Pe} = 10^6$. Resolution: $\mathcal{N} = 8$, $n_\alpha = n_\beta = 500$. (Bottom) Curves Ω representing the distance to exact triadic resonance corresponding to pure internal gravity waves for different Fourier modes. Parameter values: $\theta = \pi/4$, $\gamma = 0$. Resolution: $n_\alpha = n_\beta = 500$. Values of Ω greater than 0.01 have been omitted for ease of visibility. 81

4.5 Growth rate contours in (α, β)-space for different values of the amplitude parameter a. Parameter values: $\theta = \pi/4$, $\gamma = 0$, and $\mathrm{Re} = \mathrm{Pe} = 10^6$. Resolution: $\mathcal{N} = 15$, $n_\alpha = n_\beta = 100$. 83

4.6 Growth rate contours in (α, β)-space for higher values of the amplitude parameter a spanning the overturning threshold $a = 1$. Parameter values: $\theta = \pi/4$, $b_0 = 0$, $\gamma = 0$, and $\mathrm{Re} = \mathrm{Pe} = 10^6$. Resolution: $\mathcal{N} = 40$, $n_\alpha = n_\beta = 100$. 83

4.7 Real and imaginary parts of the complex growth rate contoured in wavenumber space for different values of the amplitude parameter a. Parameter values: $\theta = \pi/4$, $\gamma = 0$, $\mathrm{Re} = \mathrm{Pe} = 10^6$. Resolution: $\mathcal{N} = 20$, $n_\alpha = n_\beta = 100$. 85

4.8 Real and imaginary parts of the complex growth rate contoured in wavenumber space for different values of the amplitude parameter a. Real parts are scaled by $1/a$. Parameter values: $\theta = \pi/4$, $\gamma = 0$, $\mathrm{Re} = \mathrm{Pe} = 10^6$. Resolution: $\mathcal{N} = 40$, $n_\alpha = n_\beta = 100$. 85

4.9 Growth rate contours in (α, β)-space for different values of the wave propagation angle θ, scaled with the dimensionless primary wave frequency $\omega/N = \cos\theta$. Parameter values: $a = 0.1$, $\gamma = 0$, and $\mathrm{Re} = \mathrm{Pe} = 10^6$. Resolution: $\mathcal{N} = 25$, $n_\alpha = n_\beta = 100$. 86

4.10 Growth rate contours in (α, β)-space for more values of the wave propagation angle θ, scaled with the dimensionless primary wave frequency $\omega/N = \cos\theta$. Parameter values: $a = 0.1$, $b_0 = 0$, $\gamma = 0$, and $\mathrm{Re} = \mathrm{Pe} = 10^6$. Resolution: $\mathcal{N} = 25$, $n_\alpha = n_\beta = 100$. 87

4.11 Growth rate as a function of α, for a different range of γ values. Calculated at $\beta = 0$, with truncation point $\mathcal{N} = 81$, $n_\alpha = 100$, $\theta = \pi/4$ and $\mathrm{Re} = \mathrm{Pe} = 10^6$. 88

4.12 Growth rate contours in wavenumber space for different values of the Floquet modulation parameter γ. Parameter values: $a = 0.1, \theta = \pi/4, \beta = 0, \mathcal{N} = 20, \mathrm{Re} = \mathrm{Pe} = 10^6$. Resolution: $n_\alpha = 1000$. 88

4.13 Growth rate contours in wavenumber space for different values of the thermal Péclet number Pe. Parameter values: $a = 0.1, \theta = \pi/4, \gamma = 0, \mathcal{N} = 40, \mathrm{Re} = 10^6$. . . . 90
4.14 Growth rate contours in wavenumber space for different values of the thermal Péclet number Pe. Parameter values: $a = 0.1, \theta = \pi/4, \gamma = 0, \mathcal{N} = 40, \mathrm{Re} = 10^6$. . . . 90
4.15 Growth rate contours in wavenumber space for different values of the thermal Péclet number Pe. Parameter values: $a = 1, \theta = \pi/4, \gamma = 0, \mathcal{N} = 20, \mathrm{Re} = 10^6$. 91
4.16 Growth rate contours in wavenumber space for different values of the thermal Péclet number Pe. Parameter values: $a = 1, \theta = \pi/4, \gamma = 0, \mathcal{N} = 20, \mathrm{Re} = 10^6$. 91
4.17 Real parts of the perturbations U'_Y in (X, Z) space for different values of the amplitude parameter a. Parameter values: $\theta = \pi/4$, $\alpha = 2$, $\beta = 0$,$\gamma = 0$, and $\mathrm{Re} = \mathrm{Pe} = 10^6$. Resolution: $\mathcal{N} = 15$, $n_X = n_Z = 100$. . . . 93
4.18 Real parts of the perturbations U'_X in (X, Z) space for different values of the wavevector orientation θ. Parameter values: $a = 0.1$, $\alpha = 2$, $\beta = 0$, $\gamma = 0$, and $\mathrm{Re} = \mathrm{Pe} = 10^6$. Resolution: $\mathcal{N} = 25$, $n_X = n_Z = 100$. . . . 94
4.19 Eigenfunctions computed at the resonant α value corresponding to the $n = -2$ mode. Parameter values: $a = 0.1, \theta = \pi/4$, $\alpha = 0.85164528$, $\beta = 0$, $\gamma = -0.5, \mathcal{N} = 20$, $\mathrm{Re} = \mathrm{Pe} = 10^6$. Resolution: $n_X = n_Z = 100$. . . . 95
4.20 Eigenfunctions computed at the resonant α value corresponding to the $n = -2$ mode. Parameter values: $a = 0.1, \theta = \pi/4$, $\alpha = 0.60854561$, $\beta = 0$, $\gamma = 0$, $\mathcal{N} = 20$, $\mathrm{Re} = \mathrm{Pe} = 10^6$. Resolution: $n_X = n_Z = 100$. . . . 95
4.21 Eigenfunctions computed at the resonant α value corresponding to the $n = -2$ mode. Parameter values: $a = 0.1, \theta = \pi/4$, $\alpha = 0.3471065$, $\beta = 0$, $\gamma = 0.5$, $\mathcal{N} = 20$, $\mathrm{Re} = \mathrm{Pe} = 10^6$. Resolution: $n_X = n_Z = 100$. . . . 96
4.22 Schematic depicting processes of energy transfer inspired by Lombard and Riley (1996). $\tilde{E}_K$ and $\tilde{E}_P$ denote the primary wave energy densities of the kinetic and potential varieties respectively. E'_K and E'_P represent the corresponding energy densities associated with the disturbance. . . . 100
4.23 Shear production $\mathcal{E}_K$ and buoyancy production $\mathcal{E}_P$ alongside growth rate for a range of α and β values. Negative values of σ_r, $\mathcal{E}_K$ and $\mathcal{E}_P$ have been set to zero. Parameter values: $a = 0.1$, $\theta = \pi/4, \gamma = 0, \mathrm{Re} = \mathrm{Pe} = 10^6$. Resolution: $\mathcal{N} = 20$, $n_\alpha = n_\beta = 100$. . . . 102
4.24 Perturbations corresponding to an instability from Figure 4.23 driven by both shear and buoyancy. Parameter values: $a = 0.1$, $\theta = \pi/4$, $\alpha = 2.778$, $\beta = 0.650$, $\gamma = 0$, $\mathrm{Re} = \mathrm{Pe} = 10^6$. Resolution: $\mathcal{N} = 20$, $n_X = n_Z = 100$. . . . 103
4.25 Shear production $\mathcal{E}_K$ and buoyancy production $\mathcal{E}_P$ alongside growth rate for a range of α and β values. Labels I, II, and III represent divisions of wavenumber space according to regions of instability. Parameter values: $a = 1$, $\theta = \pi/4, \gamma = 0, \mathrm{Re} = \mathrm{Pe} = 10^6$. Resolution: $\mathcal{N} = 20$, $n_\alpha = n_\beta = 100$. . . . 103
4.26 Perturbations corresponding to an instability from Region I in Figure 4.25. Parameter values: $a = 1$, $\theta = \pi/4$, $\alpha = 3$, $\beta = 0$, $\gamma = 0$, $\mathrm{Re} = \mathrm{Pe} = 10^6$. Resolution: $\mathcal{N} = 40$, $n_X = n_Z = 100$. . . . 104
4.27 Perturbations corresponding to an instability from Region I in Figure 4.25. Parameter values: $a = 1$, $\theta = \pi/4$, $\alpha = 2$, $\beta = 2$, $\gamma = 0$, $\mathrm{Re} = \mathrm{Pe} = 10^6$. Resolution: $\mathcal{N} = 40$, $n_X = n_Z = 100$. . . . 105

4.28 Perturbations corresponding to an instability from Region I driven by both shear and buoyancy. Parameter values: $a = 1$, $\theta = \pi/4$, $\alpha = 0$, $\beta = 3$, $\gamma = 0$, $\mathrm{Re} = \mathrm{Pe} = 10^6$. Resolution: $\mathcal{N} = 40$, $n_X = n_Z = 100$. 105
4.29 Shear production $\mathcal{E}_K$ and buoyancy production $\mathcal{E}_P$ alongside growth rate for a range of α and β values. Parameter values: $a = 0.1$, $\gamma = 0$, $\mathrm{Re} = \mathrm{Pe} = 10^6$. Resolution: $\mathcal{N} = 25$, $n_\alpha = n_\beta = 100$. 106
4.30 Shear production $\mathcal{E}_K$ and buoyancy production $\mathcal{E}_P$ alongside growth rate for a range of α and β values. Parameter values: $a = 0.1$, $\gamma = 0$, $\mathrm{Re} = \mathrm{Pe} = 10^6$. Resolution: $\mathcal{N} = 25$, $n_\alpha = n_\beta = 100$. 107
4.31 Growth rates $\Re(\sigma)$ computed by the ideal form of the Floquet solver for a range of α values, along with growth rates $\Re(s)$ found using formula (4.88) calculated at values of α satsifying exact triadic resonance. Each resonant value of α corresponds to a Fourier mode n from the set $n \in [-9, -2]$. Parameter values: $a = 0.1$, $\theta = \pi/4$, $\beta = 0$, $\gamma = 0$. Resolution: $\mathcal{N} = 20$, $n_\alpha = 100$. 108
4.32 Growth rates $\Re(\sigma)$ calculated by the Floquet solver alongside growth rates $\Re(s)$ computed using (4.88) and adjusted by the decay rate correction Λ_κ due to thermal diffusion for different values of the thermal Péclet number Pe. Any negative growth rates obtained by either method have been set to zero. Parameter values: $a = 0.1$, $\theta = \pi/4$, $\beta = 0$, $\gamma = 0$, $\mathcal{N} = 20$. The Fourier modes used for the theoretical calculation of s are $n \in \{-2, -3, ..., -9\}$. 110
4.33 Growth rates $\Re(\sigma)$ calculated by the Floquet solver alongside growth rates $\Re(s)$ computed using (4.88) and adjusted by the decay rate correction Λ_κ due to thermal diffusion for different values of the thermal Péclet number Pe. Any negative growth rates obtained by either method have been set to zero. Parameter values: $a = 0.1$, $\theta = \pi/4$, $\beta = 0$, $\gamma = 0$, $\mathcal{N} = 20$. The Fourier modes used for the theoretical calculation of s are $n \in \{-9, -8, ..., -2\}$. 110
4.34 (Black squares) Numerical growth rate calculated via the ideal form of (4.45) maximised over (α, β) as a function of primary wave amplitude a (left panel) and as a function of primary wave orientation θ (right panel). (Red line) Theoretical prediction for the growth rate in the short wavelength limit calculated via (4.91). Parameter values: $a = 0.1$ (right panel), $\theta = \pi/4$ (left panel), $\gamma = 0$. Resolution: $\mathcal{N} = 40$. 111
4.35 Absolute error δ and relative error Δ in the growth rate as a function of amplitude a calculated at a resonant value of α corresponding to Fourier mode $n = -5$ for a selection of primary wavevector angles θ. Parameter values: $a \in (10^{-10}, 1)$, $\alpha \approx 0.20087$, $\beta = 0$, $\gamma = 0$. Resolution: $n_a = 10$, $\mathcal{N} = 50$. . . 112

5.1 Pairs of (k_{AX}, k_{AZ}) values which produce resonant triads between AGWs when $k_{AY} = 0$. Parameter values: $\theta = \pi/4$, $b_0 = 0.1$. 118
5.2 Pairs of (k_{AX}, k_{AZ}) values which produce resonant triads between AGWs when $k_{AY} = 0$. Parameter values: $\theta = \pi/4$, $\zeta = 0$. 118
5.3 Pairs of (k_{AX}, k_{AZ}) values which produce resonant triads between AGWs when $k_{AY} = 0$. Parameter values: $\theta = \pi/4$, $\zeta = 0$. 119

6.1 Spherical coordinate representation of the background magnetic field $\boldsymbol{B}_0$. . . . 133
6.2 Coordinate configuration showing the relative orientations of the (X, Z) and (x, z) frames, along with how they relate to the directions of the primary wavevector $\boldsymbol{k}$ and a cross section of the uniform background magnetic field $\boldsymbol{B}_0$. The Y-axis points directly out of the page. 133

6.3 Growth rate contours in (α, β)-space for instabilities of an IGW in the absence of a magnetic field (left) and an AGW in the presence of a magnetic field for which $\zeta = 0$, $\xi = \pi/2$ and $b_0 = 0.05$ (right). Parameter values common to both plots: $a = 0.1$, $\theta = \pi/4$, $\gamma = 0$ and $\mathrm{Re} = \mathrm{Rm} = \mathrm{Pe} = 10^6$. Resolution: $\mathcal{N} = 40$, $n_\alpha = n_\beta = 100$. 140

6.4 (Left) Contours of the growth rate in wavenumber space computed by solving (6.59). Parameter values: $a = 0.1$, $\theta = \pi/4$, $\zeta = 0$, $\xi = \pi/2$, $b_0 = 0.05$, $\gamma = 0$, $\mathcal{N} = 40$. (Right) Distance Ω from exact resonance for all three types of resonant triad, computed using (6.71). 142

6.5 Growth rate contours in (α, β)-space for different values of the background magnetic field strength. Parameter values: $a = 0.1$, $\theta = \pi/4$, $\zeta = 0$, $\xi = \pi/2$, $\gamma = 0$ and $\mathrm{Re} = \mathrm{Rm} = \mathrm{Pe} = 10^6$. Resolution: $\mathcal{N} = 40$, $n_\alpha = n_\beta = 100$. 143

6.6 Growth rate contours for different magnetic field strengths b_0. Parameter values: $a = 0.1$, $\theta = \pi/4$, $\zeta = 0$, $\xi = \pi/2$, $\gamma = 0$, $\mathrm{Re} = \mathrm{Rm} = \mathrm{Pe} = 10^6$. Resolution: $\mathcal{N} = 15$ and $n_\alpha = n_\beta = 100$. 144

6.7 Growth rate contours for different magnetic field strengths b_0. Parameter values: $a = 0.1, \theta = \pi/4, \zeta = 0, \xi = \pi/2, \gamma = 0, \mathrm{Re} = \mathrm{Rm} = \mathrm{Pe} = 10^6$. Resolution: $\mathcal{N} = 40$ and $n_\alpha = n_\beta = 100$. 144

6.8 Growth rate contours in (α, β)-space for different values of the background magnetic field strength. Parameter values: $a = 1$, $\theta = \pi/4$, $\zeta = 0$, $\xi = \pi/2$, $\gamma = 0$ and $\mathrm{Re} = \mathrm{Rm} = \mathrm{Pe} = 10^6$. Resolution: $\mathcal{N} = 40$, $n_\alpha = n_\beta = 100$. 145

6.9 Growth rate contours in wavenumber space for different values of the magnetic field angle ζ. Parameter values: $a = 0.1, \theta = \pi/4, \xi = \pi/2, b_0 = 0.02, \gamma = 0, \mathcal{N} = 12, \mathrm{Re} = \mathrm{Rm} = \mathrm{Pe} = 10^6$. 146

6.10 Growth rate contours in wavenumber space for different values of the magnetic field angle ζ. Parameter values: $a = 0.1, \theta = \pi/4, \xi = \pi/2, b_0 = 0.05, \gamma = 0, \mathcal{N} = 40, \mathrm{Re} = \mathrm{Rm} = \mathrm{Pe} = 10^6$. 147

6.11 Growth rate contours in wavenumber space, along with associated resonance curves Ω for each class of resonant triad interaction computed using (6.71). Parameter values: $a = 0.1$, $\theta = \pi/4$, $\zeta = 3\pi/4$, $\xi = \pi/2$, $b_0 = 0.05$, $\gamma = 0$, $\mathcal{N} = 40$, $\mathrm{Re} = \mathrm{Rm} = \mathrm{Pe} = 10^6$. 148

6.12 Growth rate contours in wavenumber space for different values of the magnetic field angle ζ. Parameter values: $a = 1, \theta = \pi/4, \xi = \pi/2, b_0 = 0.05, \gamma = 0, \mathcal{N} = 40, \mathrm{Re} = \mathrm{Rm} = \mathrm{Pe} = 10^6$. 149

6.13 Growth rate contours (left) in wavenumber space for instabilities of an AGW for a selection of different magnetic field orientations ξ. Parameter values: $a = 0.1$, $\theta = \pi/4$, $\zeta = 0$, $b_0 = 0.05$, $\gamma = 0$, $\mathrm{Re} = \mathrm{Rm} = \mathrm{Pe} = 10^6$. Resolution: $\mathcal{N} = 40$, $n_\alpha = n_\beta = 100$. 150

6.14 Growth rate contours in wavenumber space for instabilities of an AGW in the presence of a background magnetic field lying perpendicular to the phase velocity of the primary wave. Dashed lines: exact values of α at which AGW-AW-AW resonance occurs computed using formula (6.75). Parameter values: $a = 0.1$, $\theta = \pi/4$, $\zeta = 3\pi/4$, $\xi = \pi/2$, $\gamma = 0$, $\mathrm{Re} = \mathrm{Rm} = \mathrm{Pe} = 10^6$. Resolution: $\mathcal{N} = 40$, $n_\alpha = n_\beta = 100$. 151

6.15 Growth rate contours in wavenumber space for instabilities of an AGW in the presence of a background magnetic field lying perpendicular to the phase velocity of the primary wave. Dashed lines: exact values of β at which AGW-AW-AW resonance occurs computed using formula (6.79). Parameter values: $a = 0.1$, $\theta = \pi/4$, $\xi = 0$, $\gamma = 0$, $\mathrm{Re} = \mathrm{Rm} = \mathrm{Pe} = 10^6$. Resolution: $\mathcal{N} = 40$, $n_\alpha = n_\beta = 100$. 152

6.16 Growth rate contours in wavenumber space. The scale factor $\psi(b_0)$ is computed using formula (6.80). Parameter values: $a = 0.1$, $\theta = \pi/4$, $\zeta = \pi/4$, $\xi = \pi/2$, $b_0 = 0.3$, $\gamma = 0$, $\mathrm{Re} = \mathrm{Rm} = \mathrm{Pe} = 10^6$. Resolution: $\mathcal{N} = 20$. 153

6.17 Schematic depicting processes of energy transfer in the MHD system. $\tilde{E}_M$, $\tilde{E}_K$ and $\tilde{E}_P$ denote the primary wave energy densities of the magnetic, kinetic and potential varieties respectively. E'_M, E'_K and E'_P represent the corresponding energy densities associated with the disturbance. 159

6.18 Production values alongside growth rate σ_r for a range of α and β values. Parameter values: $a = 0.1$, $\theta = \pi/4$, $\zeta = 0$, $\xi = \pi/2$, $b_0 = 0.01$, $\gamma = 0$, $\mathrm{Re} = \mathrm{Rm} = \mathrm{Pe} = 10^6$. Resolution: $\mathcal{N} = 20$, $n_\alpha = n_\beta = 100$. 162

6.19 Production values alongside growth rate σ_r for a range of α and β values. Parameter values: $a = 0.1$, $\theta = \pi/4$, $\zeta = 0$, $\xi = \pi/2$, $b_0 = 0.05$, $\gamma = 0$, $\mathrm{Re} = \mathrm{Rm} = \mathrm{Pe} = 10^6$. Resolution: $\mathcal{N} = 40$, $n_\alpha = n_\beta = 100$. 162

6.20 Production values alongside growth rate σ_r for a range of α and β values. Parameter values: $a = 0.1$, $\theta = \pi/4$, $\zeta = 0$, $\xi = \pi/2$, $b_0 = 0.1$, $\gamma = 0$, $\mathrm{Re} = \mathrm{Rm} = \mathrm{Pe} = 10^6$. Resolution: $\mathcal{N} = 10$, $n_\alpha = n_\beta = 100$. 162

6.21 Production values alongside growth rate σ_r for a range of α and β values. Parameter values: $a = 0.1$, $\theta = \pi/4$, $\zeta = 0$, $\xi = \pi/2$, $b_0 = 0.1$, $\gamma = 0$, $\mathrm{Re} = \mathrm{Rm} = \mathrm{Pe} = 10^6$. Resolution: $\mathcal{N} = 30$, $n_\alpha = 50, n_\beta = 200$. 163

6.22 Production values alongside growth rate σ_r for a range of α and β values. Parameter values: $a = 0.1$, $\theta = \pi/4$, $\zeta = 0$, $\xi = \pi/2$, $b_0 = 1$, $\gamma = 0$, $\mathrm{Re} = \mathrm{Rm} = \mathrm{Pe} = 10^6$. Resolution: $\mathcal{N} = 20$, $n_\alpha = n_\beta = 500$. 163

6.23 Production values alongside growth rate σ_r for a range of α and β values. Parameter values: $a = 0.1$, $\theta = \pi/4$, $\zeta = 0$, $\xi = \pi/2$, $b_0 = 1$, $\gamma = 0$, $\mathrm{Re} = \mathrm{Rm} = \mathrm{Pe} = 10^6$. Resolution: $\mathcal{N} = 20$, $n_\alpha = n_\beta = 100$. 163

6.24 Production values alongside growth rate σ_r for a range of α and β values. Parameter values: $a = 0.1$, $\theta = \pi/4$, $\zeta = 0$, $\xi = \pi/2$, $b_0 = 10$, $\gamma = 0$, $\mathrm{Re} = \mathrm{Rm} = \mathrm{Pe} = 10^6$. Resolution: $\mathcal{N} = 10$, $n_\alpha = 100, n_\beta = 100$. 164

6.25 Production values alongside growth rate σ_r as a function of disturbance wavenumbers α and β for a range of magnetic field strengths b_0. Parameter values: $a = 0.1$, $\theta = \pi/4$, $\zeta = 0$, $\xi = \pi/2$, $\gamma = 0$, $\mathrm{Re} = \mathrm{Rm} = \mathrm{Pe} = 10^6$. Resolution: $\mathcal{N} = 40$, $n_\alpha = n_\beta = 100$. 164

6.26 Production values alongside growth rate σ_r for a range of α and β values. Parameter values: $a = 0.1$, $\theta = \pi/4$, $\xi = \pi/2$, $b_0 = 0.05$, $\gamma = 0$, $\mathrm{Re} = \mathrm{Rm} = \mathrm{Pe} = 10^6$. Resolution: $\mathcal{N} = 40$, $n_\alpha = n_\beta = 100$. 165

6.27 Production values alongside growth rate σ_r for a range of α and β values. Parameter values: $a = 0.1$, $\theta = \pi/4$, $\xi = \pi/2$, $b_0 = 0.05$, $\gamma = 0$, $\mathrm{Re} = \mathrm{Rm} = \mathrm{Pe} = 10^6$. Resolution: $\mathcal{N} = 40$, $n_\alpha = n_\beta = 100$. 166

6.28 Ideal Floquet growth rates $\Re(\sigma)$ alongside theoretical predictions $\Re(s)$ as a function of α for different values of the magnetic field strength b_0. Each value of $\Re(s)$ represents the AGW-AGW-AGW TRI corresponding to one Fourier mode n, computed using (6.110). Parameter values: $a = 0.1$, $\theta = \pi/4$, $\zeta = 0$, $\xi = \pi/2$, $\beta = 0$, $\gamma = 0$. Resolution: $\mathcal{N} = 20$. 168
6.29 Ideal Floquet growth rates $\Re(\sigma)$ alongside theoretical predictions $\Re(s)$ as a function of α for different values of the magnetic field strength b_0. Each value of $\Re(s)$ represents the AGW-AGW-AGW TRI corresponding to one Fourier mode n. Parameter values: $a = 0.1$, $\theta = \pi/4$, $\zeta = 0$, $\xi = \pi/2$, $\beta = 0$, $\gamma = 0$. Resolution: $\mathcal{N} = 20$. 169
6.30 Ideal Floquet growth rates $\Re(\sigma)$ alongside theoretical predictions $\Re(s)$ as a function of α for different values of the magnetic field strength b_0. Each value of $\Re(s)$ represents the AGW-AGW-AGW TRI corresponding to one Fourier mode n, computed using (6.110). Parameter values: $a = 0.1$, $\theta = \pi/4$, $\zeta = 0$, $\xi = \pi/2$, $\beta = 0$, $\gamma = 0$. Resolution: $\mathcal{N} = 20$. 169
6.31 Ideal Floquet growth rates $\Re(\sigma)$ as a function of α alongside theoretical prediction $\Re(s)$ for the AGW-AGW-AGW TRI corresponding to Fourier mode $n = -2$, computed using (6.110). Parameter values: $a = 10^{-4}$, $\theta = \pi/4$, $\zeta = 0$, $\xi = \pi/2$, $\beta = 0$, $\gamma = 0$, $\mathcal{N} = 20$. 169
6.32 Ideal Floquet growth rates $\Re(\sigma)$ alongside theoretical predictions $\Re(s)$ as a function of α for different values of the magnetic field strength b_0. Each value of $\Re(s)$ represents the AGW-AGW-AGW TRI corresponding to one Fourier mode n, computed using (6.110). Parameter values: $a = 0.1$, $\theta = \pi/4$, $\zeta = \pi/4$, $\xi = \pi/2$, $\beta = 0$, $\gamma = 0$. Resolution: $\mathcal{N} = 40$. 170
6.33 Ideal Floquet growth rates $\Re(\sigma)$ as a function of α alongside theoretical prediction $\Re(s)$ for AGW-AW-AW TRIs, computed using (6.111). Parameter values: $a = 0.01$, $\theta = \pi/4$, $\zeta = 0$, $\xi = \pi/2$, $\beta = 10$, $\gamma = 0$, $\mathcal{N} = 20$. 171
6.34 Ideal Floquet growth rates $\Re(\sigma)$ as a function of α alongside theoretical prediction $\Re(s)$ corresponding to an AGW-AW-AW TRI, computed using (6.111). Parameter values: $a = 0.01$, $\theta = \pi/4$, $\zeta = 0$, $\xi = \pi/2$, $\beta = 10$, $\gamma = 0$, $\mathcal{N} = 20$. 172
6.35 Ideal Floquet growth rates $\Re(\sigma)$ as a function of α alongside theoretical prediction $\Re(s)$ corresponding to an AGW-AW-AW TRI computed using (6.111) for different ζ values. Parameter values: $a = 0.1$, $\theta = \pi/4$, $\xi = \pi/2$, $b_0 = 0.05$, $\beta = 10$, $\gamma = 0$, $\mathcal{N} = 20$. 172
6.36 Ideal Floquet growth rates $\Re(\sigma)$ as a function of α alongside theoretical prediction $\Re(s)$ corresponding to an AGW-AW-AW TRI, computed using (6.111). Parameter values: $a = 0.02$, $\theta = \pi/4$, $\zeta = 7\pi/8$, $\xi = \pi/2$, $b_0 = 0.05$, $\beta = 10$, $\gamma = 0$, $\mathcal{N} = 20$. 173
6.37 Ideal Floquet growth rates $\Re(\sigma)$ as a function of α alongside theoretical prediction $\Re(s)$ corresponding to an AGW-AW-AW TRI, computed using (6.111). Parameter values: $a = 0.02$, $\theta = \pi/4$, $\zeta = 7\pi/8$, $\xi = \pi/2$, $b_0 = 0.05$, $\beta = 10$, $\gamma = 0$, $\mathcal{N} = 50$. 173
6.38 Absolute error δ and relative error Δ in the growth rate as a function of amplitude a calculated at a resonant value of α corresponding to Fourier mode $n = -5$ for an AGW-AGW-AGW TRI. Parameter values: $a \in (10^{-10}, 1)$, $\theta = \pi/4$, $\zeta = 0$, $\xi = \pi/2$, $\alpha = 0.20087$, $\beta = 0$, $\gamma = 0$. Resolution: $n_a = 10$, $\mathcal{N} = 50$. 174

6.39 Absolute error δ and relative error Δ in the growth rate as a function of amplitude a calculated at a resonant value of α corresponding to Fourier mode $n = -5$ for an AGW-AW-AW TRI. Parameter values: $a \in (10^{-10}, 1)$, $\theta = \pi/4$, $\zeta = 0$, $\xi = \pi/2$, $\alpha = 0.20087$, $\beta = 10$, $\gamma = 0$. Resolution: $n_a = 10$, $\mathcal{N} = 50$. . 175

6.40 Dependence of growth rate maximised over our chosen range of α and β on primary wave amplitude for different magnetic field strengths. Points: Growth rates computed using the Floquet solver. Parameter values for points: $\theta = \pi/4$, $\zeta = 0$, $\xi = \pi/2$, $\alpha \in [0, 4]$, $\beta \in [0, 4]$, $\gamma = 0$, $\mathrm{Re} = \mathrm{Rm} = \mathrm{Pe} = 10^6$. Resolution: $\mathcal{N} = 40$, $n_\alpha = n_\beta = 10$. Lines: Theoretical predictions for growth rate calculated using formula (5.82) from Chapter 5. Parameter values for lines: $\theta = \pi/4$, $\zeta = 0$, $\xi = \pi/2$, $\alpha \in [0, 4]$, $\beta = 0$, $\gamma = 0$. 176

6.41 Dependence of growth rate maximised over our chosen range of α and β on primary wave amplitude for different magnetic field strengths. Points: Growth rates computed using the Floquet solver. Parameter values for points: $\theta = \pi/4$, $\zeta = 0$, $\xi = \pi/2$, $\alpha \in [0, 4]$, $\beta \in [0, 4]$, $\gamma = 0$, $\mathrm{Re} = \mathrm{Rm} = \mathrm{Pe} = 10^6$. Resolution: $\mathcal{N} = 40$, $n_\alpha = n_\beta = 10$. Lines: Theoretical predictions for growth rate calculated using formula (5.82) from Chapter 5. Parameter values for lines: $\theta = \pi/4$, $\zeta = 0$, $\xi = \pi/2$, $\alpha \in [0, 4]$, $\beta = 0$, $\gamma = 0$. 176

6.42 Dependence of growth rate maximised over our chosen range of α on primary wave amplitude for different magnetic field strengths. Points: Growth rates computed using the ideal form of the Floquet solver. Lines: Theoretical predictions for growth rate calculated using formula (5.82) from Chapter 5. Parameter values: $\theta = \pi/4$, $\zeta = 0$, $\xi = \pi/2$, $\alpha \in [0, 10]$, $\beta = 0$, $\gamma = 0$. Resolution: $\mathcal{N} = 40$, $n_\alpha = 100$. 177

6.43 Dependence of growth rate maximised over our chosen range of α on primary wave amplitude for different magnetic field strengths. Points: Growth rates computed using the ideal form of the Floquet solver. Lines: Theoretical predictions for growth rate calculated using formula 5.82 from Chapter 5. Parameter values: $\theta = \pi/4$, $\zeta = 0$, $\xi = \pi/2$ $\alpha \in [0, 10]$, $\beta = 0$, $\gamma = 0$. Resolution: $\mathcal{N} = 40$, $n_\alpha = 100$. 178

6.44 Dependence of ideal growth rate maximised over our chosen range of α on background magnetic field strength. Points: Growth rates computed by Floquet solver. Curve: theoretical maximum growth rate for an AGW-AGW-AGW TRI plotted using formula (5.82) from Chapter 5. Parameter values: $a = 0.1$, $\theta = \pi/4$, $\zeta = 0$, $\xi = \pi/2$, $\alpha \in [0, 10]$, $\beta = 0$, $\gamma = 0$. Resolution: $\mathcal{N} = 20$, $n_{b0} = 100$, $n_\alpha = 50$. 178

6.45 Dependence of ideal growth rate maximised over our chosen range of α on background magnetic field strength. Points: Growth rates computed by Floquet solver. Curve: theoretical maximum growth rate for an AGW-AGW-AGW TRI plotted using formula (5.82). Parameter values: $a = 0.1$, $\theta = \pi/4$, $\xi = \pi/2$, $\alpha \in [0, 10]$, $\beta = 0$, $\gamma = 0$. Resolution: $\mathcal{N} = 20$, $n_{b0} = 100$, $n_\alpha = 100$. 179

6.46 Dependence of ideal growth rate maximised over our chosen range of α on background magnetic field strength. Points: Growth rates computed by Floquet solver. Curve: theoretical maximum growth rate for an AGW-AGW-AGW TRI plotted using formula (5.82) from Chapter 5. Parameter values: $a = 0.01$, $\theta = \pi/4$, $\xi = \pi/2$, $\alpha \in [0, 10]$, $\beta = 0$, $\gamma = 0$. Resolution: $\mathcal{N} = 20$, $n_{b0} = 10$, $n_\alpha = 100$. 180

6.47 Solar quantities as a function of fractional radius. Squared buoyancy frequency N^2 and density ρ are taken from a solar model by Christensen-Dalsgaard et al. (1996). r_t marks the approximate fractional radial location occupied by the solar tachocline. 181
6.48 Base-10 logarithms of solar quantities as a function of fractional radius. Squared buoyancy frequency N^2 and density ρ are taken from a solar model by Christensen-Dalsgaard et al. (1996). r_t marks the approximate fractional radial location occupied by the solar tachocline. 181
6.49 Dimensional background magnetic field strengths as a function of fractional solar radius for different dimensionless field strengths b_0, computed using data from Christensen-Dalsgaard et al. (1996) with spherical harmonic degree $l = 2$. The period $\mathcal{P}$ is in units of days. Black dashed lines: approximate bounds for the field strength of a poloidal magnetic field in the solar tachocline according to Mestel and Weiss (1987). 182

List of Tables

2.1 Dimensional variables appearing in the equations of compressible MHD. 27

2.2 Regimes for internal gravity waves. 38

4.1 Pairs of Fourier modes n and $n+1$ which resonantly interact with the primary wave to produce a TRI at the stated α values, along with frequencies ω_A/N pertaining to each mode of disturbance n computed using formula (4.62). For each pair, we state the imaginary part of the complex growth rate $\Im(\sigma_A)$ found using the ideal form of the Floquet solver. Parameter values: $a = 10^{-4}$, $\theta = \pi/4$, $\beta = 0$, $\gamma = 0$. Resolution for Floquet solver: $\mathcal{N} = 40$. 82

4.2 Growth rates at $(\alpha, \beta) = (2, 0)$ corresponding to Figure 4.5. 93

4.3 Growth rates and frequencies at $(\alpha, \beta) = (2, 0)$ corresponding to Figure 4.9 and Figure 4.18. 94

4.4 Values of α at which a TRI of IGWs occurs corresponding to the $n = -2$ Fourier mode for a selection of values of γ. Parameter values: $\theta = \pi/4$, $\beta = 0$. 95

4.5 Values of energetic quantities calculated at values of α satisfying exact triadic resonance. Parameter values: $a = 0.1, \theta = \pi/4, \beta = 0, \gamma = 0, \mathrm{Re} = \mathrm{Pe} = 10^6$. Resolution: $\mathcal{N} = 20$, $n_\alpha = n_\beta = 100$. 101

4.6 Errors alongside corresponding amplitudes and growth rates calculated at a resonant value of α corresponding to Fourier mode $n = -5$. Parameter values: $a \in (10^{-10}, 1)$, $\theta = \pi/4$, $\alpha = 0.20087$, $\beta = 0$, $\gamma = 0$. Resolution: $n_a = 10$. . . 113

5.1 Possible resonant interactions in the MHD system between two daughter waves and a primary wave of hybrid Alfvén-gravity character. 116

6.1 Possible resonant interactions in the MHD system. 142

6.2 Sign choices required for triadic resonance with different combinations of daughter waves A and B. 142

6.3 Physical significance of different magnetic field angles ζ for a primary wave with $\theta = \pi/4$. 147

6.4 Energy transfer routes associated with each production term. 158

6.5 Values of energetic quantities calculated at values of α satisfying exact triadic resonance. σ_r values are computed via (6.99). $\Re(\sigma)$ values are computed via the numerical Floquet solver (6.59). Parameter values: $a = 0.1$, $\theta = \pi/4$, $\zeta = 0$, $\xi = \pi/2$, $b_0 = 0.01$, $\beta = 0$, $\gamma = 0$, $\mathrm{Re} = \mathrm{Rm} = \mathrm{Pe} = 10^6$. Resolution: $\mathcal{N} = 20$, $n_\alpha = n_\beta = 100$. 160

6.6 Values of energetic quantities calculated at values of α satisfying exact triadic resonance. σ_r values are computed via (6.99). $\Re(\sigma)$ values are computed via the numerical Floquet solver (6.59). Parameter values: $a = 0.1$, $\theta = \pi/4$, $\zeta = 0$, $\xi = \pi/2$, $b_0 = 1$, $\beta = 0$, $\gamma = 0$, $\mathrm{Re} = \mathrm{Rm} = \mathrm{Pe} = 10^6$. Resolution: $\mathcal{N} = 20$, $n_\alpha = n_\beta = 100$. 161
6.7 Possible resonant interactions in the MHD system between two daughter waves and a primary wave of hybrid Alfvén-gravity character. 167

Chapter 1

Introduction

The universe is home to many fluids which are density-stratified. From the thermocline nestled within the interior of the ocean to the aptly-named stratosphere sitting several kilometres above the ground we stand on, a vast quantity of stably-stratified fluid is confined to the Earth alone. Opportunities to study stratified fluids become even more numerous when we consider stellar and planetary interiors too.

When a fluid is organised vertically according to its density, with fluid of a lower density sitting directly on top of fluid with a higher density, vertical motions are inhibited. The stable stratification is an equilibrium state in hydrostatic balance; buoyancy forces do their best to prevent fluid from travelling along the density gradient. Naturally, any means by which this strict prohibition of vertical motion can be overcome is of interest to us. In fact, it is vital that this ordering is disrupted for many of the atmospheric processes we depend on. The permanent redistribution of matter in such stratified fluids is known as *mixing*. Irreversible mixing is primarily achieved through turbulence. The instability and breakdown of waves makes a significant contribution to turbulence and mixing processes in stratified fluids. It is therefore incredibly important for us to have a solid understanding of the instabilities of waves in stratified fluids.

Fluids permeated by magnetic fields are also widespread in the universe. Stars certainly contain magnetic fields, with our own Sun being a notable example. We can also find them in planetary interiors and accretion disks. Both buoyancy and Lorentz forces are able to support waves generally. It is these waves that serve as the subject of this thesis.

1.1 Internal Gravity Waves

1.1.1 Fundamentals

All waves require some kind of restoring force. *Gravity waves* are waves for which buoyancy is the restoring force. The essential ingredient for the existence of these waves is stable stratification. We separate gravity waves into two distinct forms: *surface gravity waves* and *internal gravity waves*.

Surface gravity waves are the waves we observe propagating along an air-water interface. They are excited on the surface of terrestrial bodies of water, typically by wind or by the movements of solid floating bodies.

Internal gravity waves propagate through the interior of a stably-stratified fluid medium. We shall hereafter refer to them as IGWs. As a general rule, stratification is said to be stable when its density increases vertically in the direction in which gravity is acting. This description of stable stratification is an oversimplification, however; we will discuss the exact criterion for stratification to be stable later in this chapter. Density stratification is usually a consequence of temperature gradients or some kind of concentration gradient. This could be a salinity gradient in the case of the ocean (e.g. Staquet and Sommeria, 2002). In freshwater, temperature gradients are the *only* cause of stratification (e.g. Sutherland, 2010).

Interfacial IGWs are IGWs which propagate along the interface between two discrete layers of fluid. This could be a layer of fresh water sitting directly on top of a layer of saline water, as one might find in the Norwegian fjords (Lighthill, 2001).

IGWs can also propagate through the interior of a continuously-stratified fluid medium. When the stable stratification is continuous, propagation is no longer confined to the horizontal direction alone since the waves are no longer confined to a discrete interface (Sutherland, 2010). It is this exact form of IGW that this thesis concerns. Figure 1.1 demonstrates what IGWs might look like in a continuously-stratified fluid.

Mechanism of Excitation

How do IGWs get excited within stably-stratified fluids? Here we provide a fluid parcel argument detailing each step of the process (e.g. Grayson, 2021).

1. The fluid parcel is perturbed upwards away from its equilibrium position in the stably-stratified fluid.
2. The parcel is more dense and heavier than the surrounding fluid.
3. Gravity acts as a restoring force, so the parcel sinks downward.
4. The parcel moves further downward than its original equilibrium due to inertia. This happens because at its original position, there is no buoyancy force acting upward. If this buoyancy force were present, it would inhibit further downward motion.
5. The parcel is now less dense and lighter than the surrounding fluid.
6. Buoyancy acts as a restoring force, so the parcel is shifted upward.
7. This process repeats until the oscillation is sufficiently damped by viscosity or thermal diffusion for propagation to cease.

The Buoyancy Frequency

Crucial to the study of internal gravity waves is a quantity known as the *buoyancy frequency*. We denote it by N. It represents the maximum theoretical frequency at which IGWs can propagate and acts as a measure of the degree of stratification within the fluid.

The buoyancy frequency for a compressible gas is given by

$$N^2 = \frac{g}{\gamma \bar{\mathcal{P}}} \frac{\mathrm{d}\bar{\mathcal{P}}}{\mathrm{d}Z} - \frac{g}{\bar{\rho}} \frac{\mathrm{d}\bar{\rho}}{\mathrm{d}Z}. \tag{1.1}$$

The spatial coordinate Z represents the direction of gravity, treated as vertical. $\bar{\mathcal{P}}(Z)$ and $\bar{\rho}(Z)$ denote static vertical variations in pressure and density respectively. The constant g denotes gravitational acceleration and γ is the heat capacity ratio, also known as the adiabatic index.

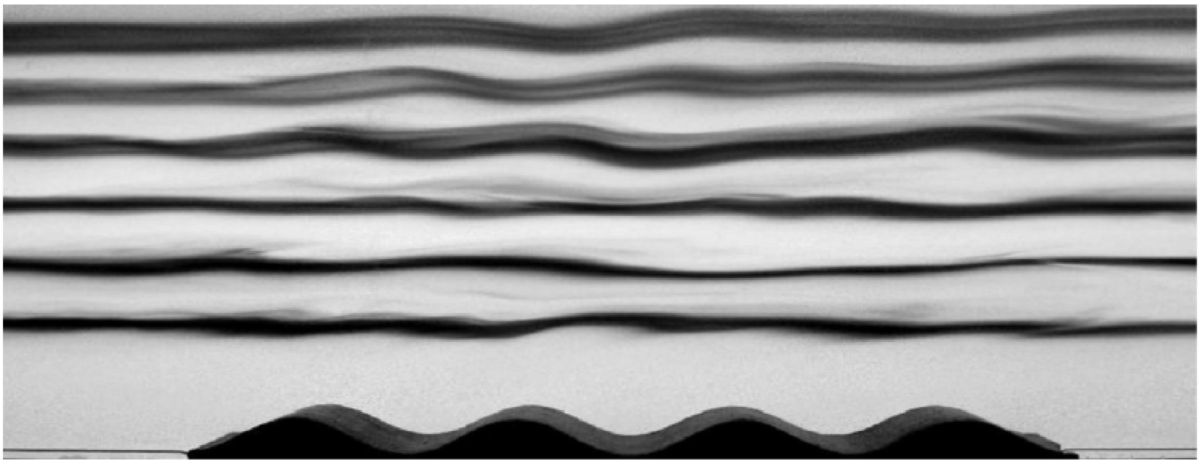

Figure 1.1: Visualisation of internal gravity waves in a tank of water created by injecting dye at several different depths and moving the bottom topography laterally to excite the observed waves (Sutherland, 2010).

The value (or range of values) of N is specific to whichever fluid medium we consider. N can be treated as uniform in some media and varying in others. At any location within the fluid, IGWs with frequencies greater than the local value of N are said to be *evanescent* — these waves exhibit spatial decay and do not propagate.

The angular frequency ω_{IGW} of internal gravity waves satisfies a dispersion relation:

$$\omega_{\text{IGW}}^2 = \frac{N^2 K_\perp^2}{K^2}. \tag{1.2}$$

K is the norm of the wavevector and $K_\perp$ is the norm of the wavevector component in the direction perpendicular to gravity. The significance of buoyancy frequency extends beyond the study of IGWs. The sign of the buoyancy frequency determines whether a given fluid medium is in stable equilibrium. In particular, this is specified by the *Schwarzschild criterion*.

The Schwarzschild criterion for convective stability is as follows:

- If $N^2 > 0$, fluid is stable to convection.
- If $N^2 \leq 0$, fluid is unstable to convection.

This criterion will become important later in this chapter when discussing the solar interior. The condition $N^2 > 0$ must be satisfied in order for the parcel argument above to be valid. Propagating IGWs can only exist in fluid media for which $N^2 > 0$.

The Schwarzchild criterion can be described equivalently in terms of entropy gradients. We define the specific entropy $\mathcal{S}$ as

$$\mathcal{S} := c_v \log\left(\frac{\bar{\mathcal{P}}}{\bar{\rho}^\gamma}\right), \tag{1.3}$$

where c_v is the specific heat capacity at constant volume. If the entropy gradient is increasing in the direction antiparallel to gravity then the Schwarzschild criterion is satisfied everywhere and the fluid is stable to convection. If the entropy gradient is locally increasing in the direction parallel to gravity somewhere in the fluid, then the Schwarzschild criterion is violated somewhere and the fluid is unstable to convection. It is useful to relate this to the pressure gradient (see equation 1.1). The fluid is stable to convection if and only if the entropy gradient is anti-parallel to the pressure gradient everywhere in the fluid. The Schwarzchild criterion can be explained physically using a fluid parcel argument (e.g. Pringle and King, 2007).

1.1.2 Internal Gravity Waves on Earth

Our planet is home to two global stratified fluids: the ocean and the atmosphere. IGWs are of interest to both atmospheric scientists and oceanographers. Here, we discuss each of these two settings, in terms of which regions are stably-stratified and in terms of the role IGWs play in their respective dynamics.

Internal Gravity Waves in the Ocean

The *thermocline* is the name given to a stably-stratified part of the ocean. It sits below a well-mixed surface layer and sits above the far-reaching abyss, which is only weakly stratified. What creates stable stratification in the ocean? Density is a function of pressure, temperature and salinity in the ocean. Profiles of temperature and salinity with depth are produced using temperature-salinity-depth recorders, which are devices lowered from ships. These gradients in temperature and salinity are directly responsible for stratification in the thermocline. Naturally, in freshwater, temperature gradients are the *only* cause of stratification (e.g. Sutherland, 2010).

In the ocean, IGWs are an important contributor to mixing processes (permanent changes in the composition of the fluid), which have impacts on biological activity. Garwood et al. (2020) discuss how IGWs can vertically displace plankton by several metres. Plankton displaced downwards have reduced exposure to solar irradiance. This reduces the amount of light energy they can absorb, which is game-changing for plankton because they cannot propel themselves. Booth et al. (2012) discuss the advection of hypoxic water into marine habitats on the Californian coast by IGWs. This is a seasonal event in which IGWs prevent areas near the shore from being sufficiently well-mixed to support marine life with essential oxygen.

Additionally, there are a number of larger-scale impacts of oceanic IGWs. IGWs contribute to the dissipation and mixing of internal tides in the ocean (Munk and Wunsch, 1998). Garrett and Munk (1972) famously created an oceanic internal wave spectrum. This was a formula for oceanic internal wave energy as a function of the wavenumber and frequency. Garrett and Munk (1972) also discuss how breaking IGWs induce oceanic mixing. IGWs have a considerable effect on *ocean circulation*, which is the name given to the bulk transport of nutrients and freshwater through the large-scale shifting of water around the globe (Müller and Willebrand, 1986). Such an effect is possible because IGWs contribute to the mixing of mass and thermal energy.

Internal Gravity Waves in the Atmosphere

The *stratosphere* is the name given to one of the stably-stratified regions of the atmosphere. It sits on top of the troposphere, the well-mixed layer adjacent to the Earth's surface which is host to our weather. It is common for IGWs to be excited in this layer. IGWs excited in the stratosphere predominantly transport momentum. This has an impact on wind speeds and the thermal structure of the atmosphere. Wind speeds and atmospheric temperature would not be predicted correctly without taking into account IGWs (e.g. Sutherland, 2010).

How do IGWs get excited in the atmosphere? Plougonven and Zhang (2014) explain how jets are sources of IGWs in the atmosphere. IGWs can also be excited in the troposphere by the flow of air across topography, such as the surfaces of mountains (Vosper, 1996).

Why are people interested in atmospheric IGWs? IGWs cause mixing and turbulence in the upper troposphere. They affect atmospheric circulation, particularly in the stratosphere, because they transfer momentum as they dissipate. The meridional thermal gradient in the mesosphere undergoes periodic reversals, for which IGWs are thought to be responsible. See Fritts and Alexander (2003) for a review of the effects of IGWs on the stratosphere and the mesosphere. The transfer of momentum by IGWs is also partly responsible for driving Quasi-Biennial Oscillations (QBOs) (Lindzen and Holton, 1968). This is a periodic phemomenon in which zonal stratospheric winds alternate between the Eastward and Westward directions (Baldwin et al., 2001).

1.2 Alfvén Waves

So far, everything we have discussed has been done so without reference to magnetic fields, which are important in many of the plasma-based applications we discuss later in this thesis. It is the introduction of MHD which makes this work novel. In doing so, a new type of wave must be considered in addition to IGWs.

Alfvén waves (AWs) are waves for which magnetic tension is the restoring force. They propagate along magnetic field lines in an electrically-conducting plasma. Naturally, the presence of a magnetic field is *essential* for the existence of Alfvén waves. The velocity with which Alfvén waves propagate is called the Alfvén velocity $\boldsymbol{V}_A$.

The Alfvén velocity $\boldsymbol{V}_A$ is given by

$$\boldsymbol{V}_A \coloneqq \pm \frac{\boldsymbol{B}_0}{\sqrt{\mu_0 \rho_0}}. \tag{1.4}$$

$\boldsymbol{B}_0$ is a background magnetic field, μ_0 is the permeability of free space and ρ_0 is the constant background density of the fluid. In Chapter 2 we show that the Alfvén velocity is the group velocity of Alfvén waves. Let $\boldsymbol{K}$ denote the wavevector. The Alfvén velocity relates the frequency of Alfvén waves to their wavevector via a dispersion relation.

The angular frequency ω_{AW} of Alfvén waves satisfies a dispersion relation:

$$\omega_{\text{AW}} = \boldsymbol{K} \cdot \boldsymbol{V}_A. \tag{1.5}$$

Alfvén waves impact the transport of energy and momentum in many astrophysical flows. Notable examples include stellar atmospheres, stellar interiors and accretion disks. Alfvén waves have also been detected in Earth's core, where they help us to measure the internal magnetic field strength and are thought to be able to explain interannual fluctuations in the Earth's magnetic field (Gillet et al., 2022).

Mechanism of Excitation

In a fluid which is in magnetohydrostatic balance, magnetic field lines are in a position of equilibrium when they are straight. If field lines are bent, the curvature induces a Lorentz force

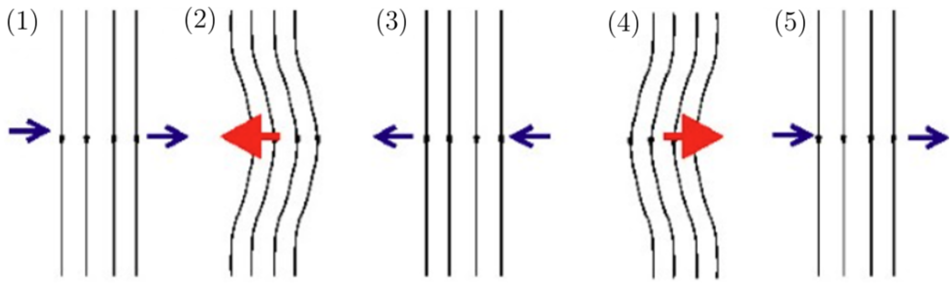

Figure 1.2: Schematic showing how Alfvén waves form. Blue arrows: fluid velocity. Red arrows: Lorentz force. Black lines: magnetic field lines. Image credit: Finlay (2007).

acting in the direction perpendicular to the field lines. In the bent state, the field lines are in a state of tension. This can be likened to the tension created when a guitar string is pulled.

The magnetic Reynolds number Rm of a flow is the ratio of magnetic induction to magnetic diffusivity. When Rm is large, the fluid is highly electrically conducting and we can regard magnetic field lines as being 'frozen into the fluid', i.e. field lines are carried by the flow. This allows for the formation of Alfvén waves via the following physical mechanism (e.g. Davidson, 2017), which is depicted in Figure 1.2.

1. Fluid passes over magnetic field lines in their straight equilibrium state as a result of a disturbance. Fluid moves in the direction perpendicular to the field lines.

2. Because the field lines are frozen into the flow, the field lines get pulled into a bent position. Magnetic tension arises as a result, accompanied by a Lorentz force acting in the direction perpendicular to the field lines.

3. The perturbed magnetic field lines are not in equilibrium so the system tries to restore its equilibrium, pushing the displaced fluid and the field lines back to their straight position.

4. The fluid and field lines overshoot the equilibrium position due to inertia. Field lines are now bent the other way, with a Lorentz force acting in the opposite direction.

5. The oscillation repeats until all energy has been dissipated away to the surroundings by Ohmic diffusion or viscosity.

1.3 Stellar Physics and Stellar Waves

We devote this section to introducing the main physical setting to which our model can be applied: magnetised stellar interiors. We outline the structure of these interiors, describe some of the physical processes which take place within and discuss the role which internal gravity waves (IGWs) and Alfvén waves (AWs) play in their dynamics. We start with our own Sun and then expand our attention to other stars. Prior to that, we outline some key notation.

Notation for Stellar Oscillations

Throughout this section, we refer to both small-scale propagating waves which might exist in a small portion of a stellar interior and large-scale global standing oscillations which occupy the entire expanse of a stellar interior. We refer to the latter as *modes*, of which we shall consider two different forms: p-modes and g-modes. The p-modes are acoustic modes (for which pressure

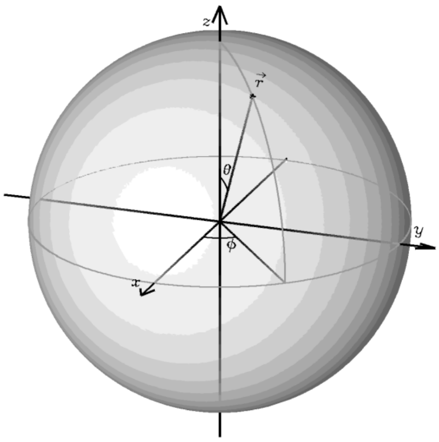

Figure 1.3: Spherical polar coordinate system (r, θ, ϕ) describing a star. Image credit: Jorgen Christensen-Dalsgaard.

is the restoring force) and the g-modes are gravity modes (for which buoyancy is the restoring force).

When describing modes, it is useful to adopt global spherical polar coordinates (r, θ, ϕ). This formulation is appropriate in a star which can be approximated as spherically symmetric. Here, r is the radial coordinate, θ represents colatitude and ϕ represents longitude. Oscillations contain fixed points known as nodes.

How do we define the oscillation nodes in each spatial direction within a star?

- r nodes are concentric spherical shells.
- θ nodes are cones of constant θ.
- ϕ nodes are planes of constant ϕ.

Spherical Harmonics

Stellar oscillations are described by spherical harmonics. These are functions which take arguments on the stellar surface. The spherical harmonics are given by

$$Y_l^m(\theta, \phi) := (-1)^m \sqrt{\frac{(2l+1)(l-m)!}{4\pi(l+m)!}} P_l^m(\cos\theta) \exp(im\phi), \tag{1.6}$$

where P_l^m is a Legendre polynomial. Modes of oscillation are defined by a set of parameters called *quantum numbers* (l, m, n), two of which appear in equation (1.6). Each distinct mode has a distinct combination of (l, m, n) values.

Each quantum number is interpreted as follows:

- l is the *degree*. This is related to the number of wavelengths occupying the stellar circumference.
- m is the *azimuthal order*, where $|m|$ is the number of nodes occupying the equator of the star.
- n is the *overtone*, which depends on the number of radial nodes.

1.3.1 Solar Structure

The Sun is an approximately spherical body of matter comprised predominantly of hydrogen and helium. It contains a smattering of other elements which form a much smaller proportion (e.g. carbon, nitrogen and oxygen). These are often dubbed *heavy elements* in a solar context, owing to their high atomic mass relative to hydrogen and helium. The relative abundance of hydrogen and helium varies markedly with fractional solar radius $r/R_\odot$, where $R_\odot$ denotes the radius of the Sun (Figure 1.4). The changes in these relative abundances as time elapses determine how the Sun evolves.

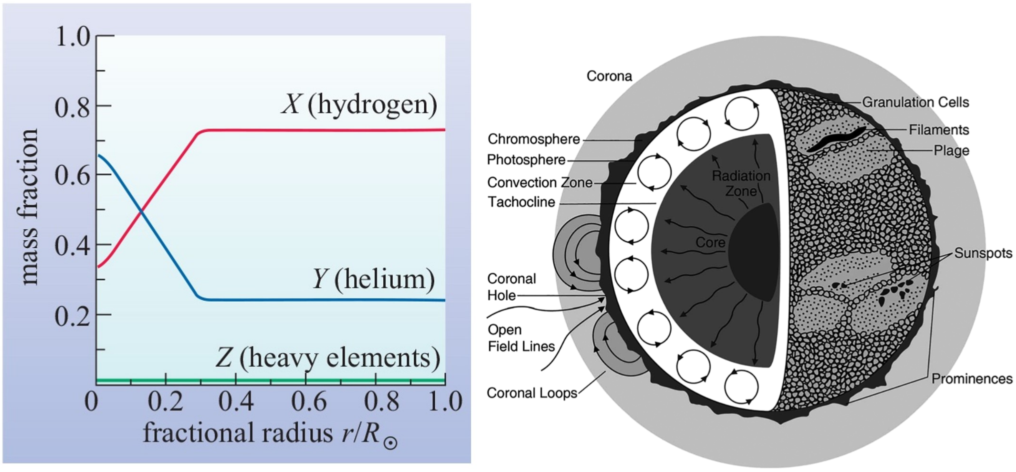

Figure 1.4: (Left) Fractional mass of different elements in the interior of the Sun as a function of fractional solar radius (Green et al., 2015). (Right) Internal structure of the Sun (Russell et al., 2019)

.

The matter in the Sun does not exist in the form of neutral atoms, but rather in the form of charged positive ions situated amongst a sea of free electrons. In this sense, the fluid is said to be *plasma* rather than strictly a gas. The high temperature is what causes the particles to be ionised. It is this abundance of free electrons which allows the plasma to be electrically conducting, facilitating the presence of a magnetic field. The internal structure of the Sun is shown in Figure 1.4.

The Core

The dependence of the mass fractions of hydrogen and helium on solar radius is explained by the primary activity which the Sun engages in. This is the conversion of hydrogen into helium via nuclear fusion. These fusion reactions take place at the centre of the Sun, which we call the *core*. The core extends only to about $0.3R_\odot$, yet it contains about half of the entire solar mass (the Sun's mass is $M_\odot \approx 2 \times 10^{30}$ kg). It burns about 5×10^6 tonnes of hydrogen per second. Such rapid reactions are made possible by the extreme temperatures in the core, which reach up to 15×10^6 K (e.g. Priest, 2014).

The Radiative Zone

Encasing the core is a region we call the *radiative zone*. It is characterised by its stable stratification. In the radiative zone, $N^2 > 0$, so by the Schwarzschild criterion the region is stable to convection. The fact that entropy increases radially outwards in the radiative zone allows it to be stably-stratified despite the fact that temperature decreases radially outwards in the solar interior. It is this stable stratification property which allows the radiative zone to be host to IGWs. The plasma within the radiative zone is often taken to be effectively quiescent. The density gradient generally inhibits vertical motion within the plasma. The radiative zone also exhibits approximately *solid-body rotation*, i.e. adjacent layers of fluid move at approximately the same angular velocity as each other (e.g. Davidson, 2017). The existence of solid-body rotation requires efficient transport of angular momentum within a stellar interior. In fact, it is the transport of angular momentum by IGWs in the radiative zone which is thought to be one of the processes responsible for this solid-body rotation (Schatzman, 1993; Kumar and Quataert, 1997; Zahn et al., 1996).

As the name suggests, energy is transferred across the radiative zone by radiation of photons. Instead of a direct radial passage, the motion takes the form of a random walk. Dense plasma means photons are considerably obstructed along the way. The indirect nature of this photon movement means that radiation is glacially slow here. It is estimated that energy from fusion taking place in the core right now will take about 2×10^5 years to be transferred to the solar surface (e.g. Green et al., 2015). The rate of thermal diffusion is denoted by κ. The variation of κ with fractional solar radius $r/R_\odot$ is shown in Figure 1.7.

The Solar Tachocline

Situated at about $0.7R_\odot$ is a thin interface separating the radiative zone and the convective zone, typically referred to as the *solar tachocline*. It is partly in this spherical shell that the Sun's magnetic field is thought to be continuously generated by dynamo action (e.g. Hughes et al., 2007).

This is a region of very strong shear, which is a necessary consequence of the stark difference between the way the radiative and convective zones rotate. In the radiative zone, angular velocity has no dependence on latitude, but in the convective zone, angular velocity is a function of latitude (e.g. Davidson, 2017). We call this *differential rotation*. Figure 1.5 illustrates this concept.

The Convective Zone

The convective zone comprises the rest of the solar interior. Here, $N^2 < 0$, so the Schwarzschild criterion is violated. Entropy $\mathcal{S}$ decreases radially outwards in the convective zone. This region is therefore not stably-stratified, but instead is subject to *static convective instability*. The transfer of energy therefore takes a very different form compared to that of the radiative zone. The transfer takes place via fluid motions rather than radiation. Here, plasma is organised into convective 'cells', in which plumes of relatively hot fluid repeatedly rise from the lower extremities of the convective zone towards the surface, radiate their thermal energy outwards, and descend

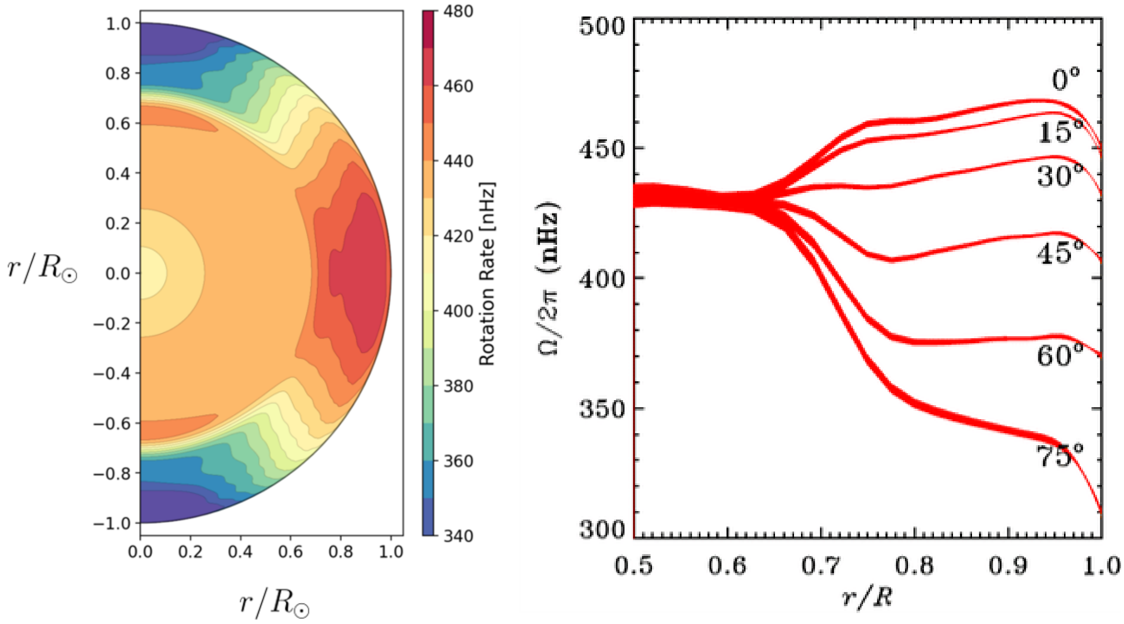

Figure 1.5: (Left) Angular frequency of fluid in the solar interior computed using data from helioseismology (image credit: Käpylä et al. (2023)). (Right) Angular frequency of fluid in the solar interior at different latitudes (credit: NSF National Solar Observatory).

as they cool down. The timescale for the largest-scale convective motions at the base of the convective zone is on the order of weeks (e.g. Davidson, 2017). Each of these cells can measure up to 3×10^4 km across at the bottom of the convective zone and about 1000km across at the top of the convective zone (e.g. Green et al., 2015).

The Photosphere

So far, we have referred to 'the surface of the Sun' ambiguously. This phrase refers to the photosphere, which is the layer of the Sun visible to us on Earth. It is the radial coordinate of the outer boundary of this layer which we define as the value of $R_\odot$, which is taken to be 7×10^5km. The photosphere is said to be *granulated* (Figure 1.6a). This texture is a direct consequence of the convection currents occurring beneath. The bright regions correspond with rising convective plumes, whereas the darker interstitial regions correspond with cooler, sinking fluid (e.g. Priest, 2014). Global wave motions can be detected on the photosphere, from which we can make a number of inferences regarding the solar interior. This concept is known as *helioseismology*. We describe it in more detail in Section 1.3.5.

The Solar Atmosphere

Beyond the photosphere lies a wispy expanse of sparse plasma, separated into the chromosphere (directly above the photosphere) and the corona (directly above the chromosphere). The corona has no obvious radial boundary (e.g. Davidson, 2017). It is also the site of a number of magnetohydrodynamic waves (e.g. Cally and Bogdan, 2024). The solar atmosphere is stably-stratified, allowing for the presence of IGWs (Vigeesh et al., 2017). The plasma in the corona is partly contained in structures called *coronal loops* suspended above the surface (Figure 1.6c). These are held in place by the magnetic field (e.g. Priest, 2014). In Section 1.3.2 we discuss exactly how this magnetic field is interspersed throughout the Sun.

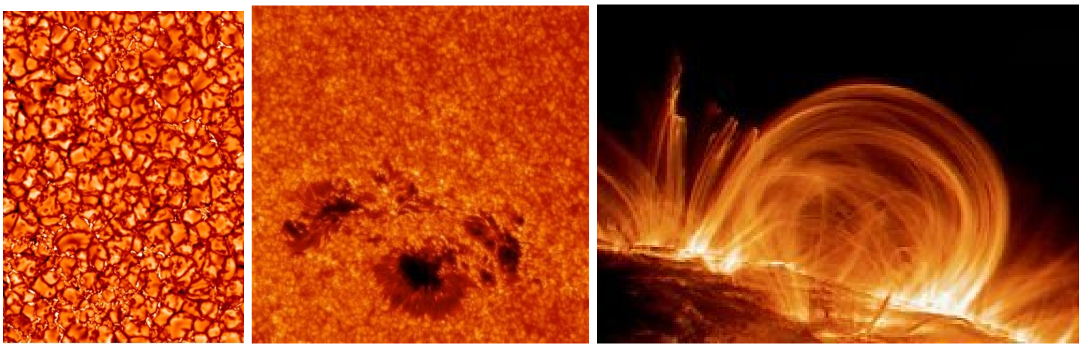

Figure 1.6: (a) Solar granulation. (b) Sunspots in the photosphere. (c) Coronal loops.

Solar Internal Gravity Waves

The buoyancy frequency governs where IGWs can exist in the Sun. Figure 1.7 shows the variation of N^2 with fractional solar radius, as predicted by a solar model (Christensen-Dalsgaard et al., 1996). In the Sun, N^2 only takes a positive value in the core, the radiative zone and the tachocline. Propagating IGWs are hence permitted. In the convective zone, $N^2 < 0$, so only evanescent IGWs are permitted. In the solar interior, IGWs are excited at the solar tachocline.

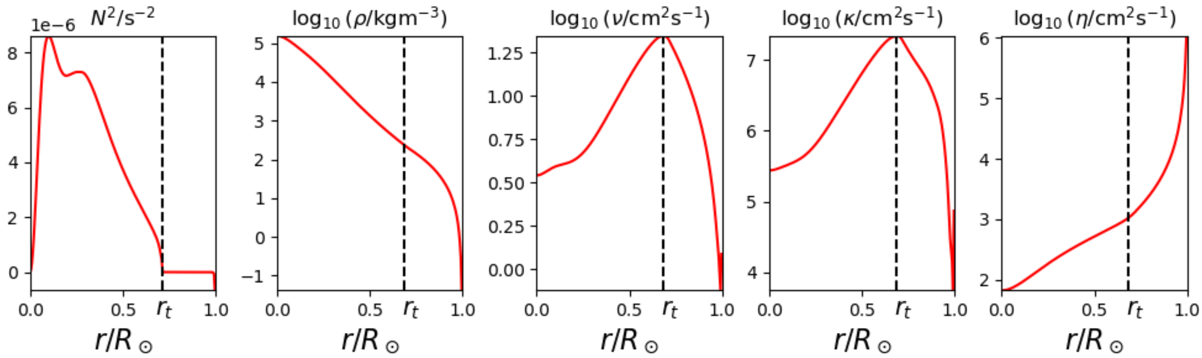

Figure 1.7: Solar quantities as a function of fractional radius. Dynamic viscosity is denoted by ν, thermal diffusivity is denoted by κ and Ohmic diffusivity is denoted by η. Squared buoyancy frequency N^2 and density ρ are taken from a solar model by Christensen-Dalsgaard et al. (1996). The point r_t marks the approximate fractional radial location occupied by the solar tachocline.

This typically takes place through *convective penetration* (also known as *convective overshoot*). The convective zone is turbulent and unstable. Fluid within exhibits rolling convective motions. Convective plumes in the lower convective zone can occasionally escape the convective zone and pass across the thin solar tachocline. Such motion provides enough of a disturbance to excite IGWs in the radiative zone. How does this occur? Plumes are slowed down by buoyancy braking when crossing the tachocline. In other words, the radial motion of the plume is impeded by the stable stratification. This deceleration causes some of their kinetic energy to be released in the form of IGWs (e.g. Pinçon et al., 2016). Convective penetration is illustrated in Figure 1.8. Solar IGWs can also be excited by Reynolds stresses associated with turbulent convection (e.g. Lecoanet and Quataert, 2013).

These waves propagate through the radiative interior until they are sufficiently damped by thermal diffusion. They transfer angular momentum to their surroundings when they are damped. In particular, they extract angular momentum from the convective zone when they are generated and transfer it to the radiative zone when they are damped (Fuller et al., 2014). Given that we expect a magnetic field in the tachocline and in the radiative zone, it is not unreasonable to expect these IGWs to have some AW character, too.

There are two likely fates of IGWs propagating through the radiative zone:

1. The IGW reaches the solar centre, where it will likely be reflected, possibly establishing a global standing g-mode if it arrives back at the tachocline.

2. The IGW is fully-damped by thermal diffusion or by fluid instabilities either before or after it reaches the solar centre, preventing the establishment of a global standing g-mode.

The study of solar IGWs is important because they have been linked with angular momentum transport in the solar interior. In the past, it has been proposed that angular momentum transport due to IGWs is how solid-body rotation is maintained in the solar radiative zone (Schatzman, 1993; Kumar and Quataert, 1997; Zahn et al., 1996). This idea has since been debated. IGWs usually have a tendency to accentuate angular velocity gradients (i.e. have a tendency to accentuate shear). This is said to be an antidiffusive effect. This is why the idea that IGWs are responsible for maintaining the solid-body rotation in the radiative zone was met with such controversy (Gough and McIntyre, 1998).

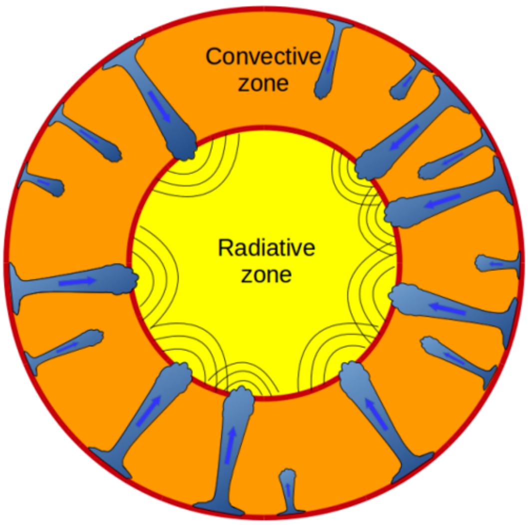

Figure 1.8: Schematic of a solar-type star showing convective plumes, some of which are penetrating into the radiative zone, giving rise to IGWs. Image credit: Pinçon et al. (2016).

1.3.2 Solar Magnetic Field

The notion that the Sun possesses a magnetic field was first proposed by Hale (1908). Many believe that the present-day solar magnetic field is a remnant of an ancient, weak, poloidal magnetic field which was present amongst the accumulating matter during the formation of the Sun. The current solar magnetic field fluctuates too much for this ancient magnetic field to be the sole contributor, however (e.g. Davidson, 2017). There must be an additional source. This is where the solar dynamo becomes important.

It is widely thought that part of the solar dynamo is seated in the tachocline. Here, a strong toroidal magnetic field is generated from the weak poloidal magnetic field by the Ω-effect (e.g. Mestel, 2012). In particular, the Ω-effect creates magnetic flux tubes. These flux tubes rise due to the magnetic buoyancy instability (Hughes and Proctor, 1988). Through this process, the magnetic field produced in the tachocline is distributed radially upwards towards the photosphere. This buoyant movement gives rise to what are known as *sunspots* — pockets of strong magnetic field visible on the solar surface as dark blemishes (Figure 1.6b). Once a flux tube reaches the solar surface, it becomes a coronal loop which protrudes into the solar corona. Sunspots are the two points at which each coronal loop is attached to the solar surface. Field strengths of sunspots are $\sim 10^3$G. Such field strengths inhibit fluid motion within the sunspot. The high field strength is also responsible for the fact that most sunspots are about 2000K cooler than their surroundings. This is because of the thermal insulation provided by the magnetic field (e.g. Priest, 2014).

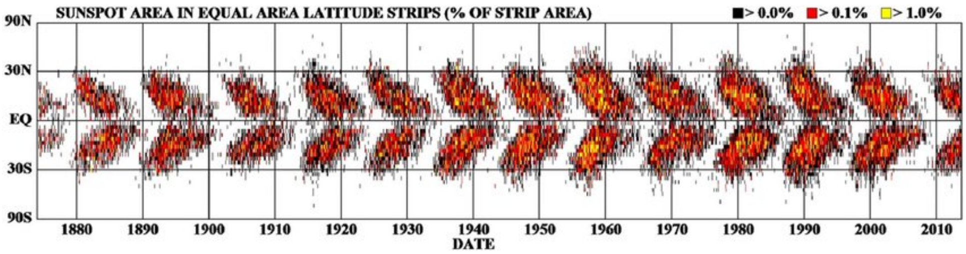

Figure 1.9: The butterfly diagram, showing the total percentage sunspot coverage computed over finite-width strips of constant latitude, recorded each year since 1874. Image credit: Hathaway (2011).

Sunspots have supposedly been observed since 350BC (e.g. Mestel, 2012). The first indication that the Sun is a rotating body came from recording the positions of sunspots. Figure 1.9 depicts a modern example of the *butterfly diagram*, which is an extended version of the original by Maunder (1913). It takes thin rectangles placed over curves of constant latitude and records the percentage of the area of each rectangle covered by sunspots at a fixed time each year. The diagram demonstrates an 11-year periodic behaviour pattern known as the *solar cycle*. Babcock (1959) discovered that the polarity reversal of the Sun's magnetic field is synchronised with the 11-year solar cycle.

What kind of magnetic field strengths can we expect throughout the Sun? Mestel and Weiss (1987) estimated bounds on the field strength of a poloidal field that could survive in the radiative interior of the Sun. They estimated the field strength to be between 5×10^{-1}G and 5×10^3G. Lin et al. (2000) recorded magnetic field strengths in the range 10-33G in the solar corona.

Influence of Solar Magnetic Field on Internal Gravity Waves

Some work has gone into understanding the influence of the magnetic field in the solar tachocline on IGWs (Schatzman, 1993; Burgess et al., 2004; Mathis and De Brye, 2011, 2012), with a central aim of determining whether it is feasible that waves are responsible for angular momentum transport between the solar convection zone and the solar core (Donati and Landstreet, 2009).

Rogers and MacGregor (2010) sought to determine the effect of a purely toroidal magnetic field situated in the solar tachocline on angular momentum transport induced by IGWs. This was performed under the anelastic approximation for artificially-forced prograde and retrograde IGWs. They found that IGWs are efficiently reflected when $\omega_{\rm AW} \sim \omega_{\rm IGW}$. The freqencies $\omega_{\rm IGW}$ and $\omega_{\rm AW}$ are given by formulae (1.2) and (1.5) respectively. This reflection results in the divergence of the Reynolds stress, which in turn causes an increase in angular momentum transport. The relative values of ω_{AW} and ω_{IGW} are predominantly what controls the interaction between IGWs and magnetic fields.

Rogers and MacGregor (2011) continued this avenue of investigation by studying angular momentum transport by IGWs excited in simulations by convective penetration. This is a more realistic forcing mechanism than the artificial forcing used by Rogers and MacGregor (2010). Rogers and MacGregor (2011) used a simulated convective zone sitting above the radiative domain of the simulations. In this scenario the magnetic field is able to evolve. Rogers and MacGregor (2011) found that the interaction between IGWs and the field induces fluctuations in the magnetic field. In particular, the magnetic field in the solar tachocline can be entrained into the convective zone by these interactions. Rogers and MacGregor (2011) also observed wave reflection as a result of collision of internal gravity waves with magnetic flux surfaces. They found that wave reflection can increase the velocity of the mean flow in the solar tachocline.

Solar Alfvén Waves

Given the undeniable presence of magnetic fields, we have reason to believe that Alfvén waves exist in the tachocline and the radiative zone. However, the fact that these oscillations are buried deep within the solar interior makes it very difficult for us to observe them as such.

This is not the case for the solar atmosphere. Thanks to satellite missions, Alfvén waves have conclusively been detected in the solar atmosphere (Aschwanden et al., 1999; Nakariakov et al., 2000; Ofman and Wang, 2008; McIntosh et al., 2011). The Coronal Multi-channel Polarimeter (CoMP) has been used to observe Alfvén waves (e.g. Mathioudakis et al., 2013). Oscillations in the solar atmosphere are predominantly generated by convective overshoot. Solar flares can also contribute to wave excitation here, though (Cally and Bogdan, 2024).

Alfvén waves have been linked with the *coronal heating problem*. This is a long-standing problem in solar MHD (Kuperus et al., 1981; Zirker, 1993; Ofman et al., 2005; Ofman, 2007; Klimchuk, 2006; Taroyan and Erdélyi, 2009; Mathioudakis et al., 2013). It seeks an understanding as to how it is possible for the solar corona to be so much hotter than the solar photosphere. Much heat is lost by the corona. Withbroe and Noyes (1977) attributed these losses to radiation, conduction and the solar wind, with a total estimated heat loss of 1.11 erg $\mathrm{cm}^{-2}\ \mathrm{s}^{-1}$. However, with temperatures of $\sim 10^6$ K, the corona is about three orders of magnitude hotter than the photosphere ($\sim 10^3$ K). We require some kind of heating mechanism to maintain such a temperature disparity despite coronal heat losses. MHD waves such as Alfvén waves have been put forward as drivers of coronal heating (Alfvén and Lindblad, 1947; Osterbrock, 1961; Ionson, 1978; Hollweg, 1991; Mathioudakis et al., 2013). When these waves are dissipated, we can expect thermal energy to be released. Alfvén waves can drive MHD turbulence, which could contribute to coronal heating (e.g. Matthaeus et al., 1999).

1.3.3 Stellar Classification and Structure

We have seen how the Sun is arranged internally, but how does this change in other stars? We first discuss how stars are categorised. This is done using the *Hertzsprung–Russell diagram* (Figure 1.10). The two most fundamental properties of stars we can infer from observations are luminosity L and effective temperature T_{eff}. The effective temperature of a star is the temperature a black body would have if it were to emit the same total energy as the star in the form of electromagnetic radiation. The Hertzsprung–Russell depicts the extent to which luminosity and effective temperature are correlated. The diagram also refers to *absolute magnitude*, which is a measure of illumination. Each point on the Hertzsprung-Russell diagram generally corresponds to a particular star, though multiple stars can have the same place on the diagram in theory. It is important to note that the position of a star on the Hertzsprung-Russell diagram is not fixed. The evolution of a star is represented by its trajectory across the (L, T_{eff})-plane. We can think of this trajectory as a parametric curve for which the parameter representing progress along the curve is the time elapsed since the birth of the star. The Hertzsprung-Russell diagram we see represents a snapshot in time.

What determines how a star moves across the Hertzsprung-Russell diagram in time? For a recently-formed star, we expect the mass fraction of hydrogen to be $X \approx 0.7$ and the mass fraction of helium to be $Y \approx 0.3$. We expect the mass fraction of heavy elements to be minuscule in comparison. It is generally agreed that the chemical composition of stars at the beginning of their lifespan is similar in all stars. The initial mass, however, varies dramatically amongst different stars. This initial mass is the primary factor governing the Hertzsprung-Russell path of a star. We can deduce the radius R of any star on the Hertzsprung-Russell diagram through the relation $L = 4\pi\sigma R^2 T_{\text{eff}}^4$, where σ is the Stefan–Boltzmann constant (e.g. Prialnik, 2009).

Figure 1.10 shows the positions of several stellar categories, each occupying a *branch* of the Hertzsprung-Russell diagram. At any moment in time, the vast majority of stars occupy the *main sequence*, the largest branch visible on the diagram. Whether a star occupies the main sequence is largely determined by its age. Exactly which part of the main sequence a star occupies is largely determined by its initial mass. In fact, luminosity has a power-law dependence on initial mass along the main sequence. Stars spend the bulk of their lifetime sitting somewhere on the main sequence. The next most significant branches are known as the *red giant* and *white dwarf* branches (e.g. Prialnik, 2009). Most main sequence stars move on to the Red Giant Branch (RGB) once their time on the main sequence is done. The exhaustion of their supply of hydrogen to burn is what signals the end of the main sequence (e.g. Kippenhahn et al., 2012).

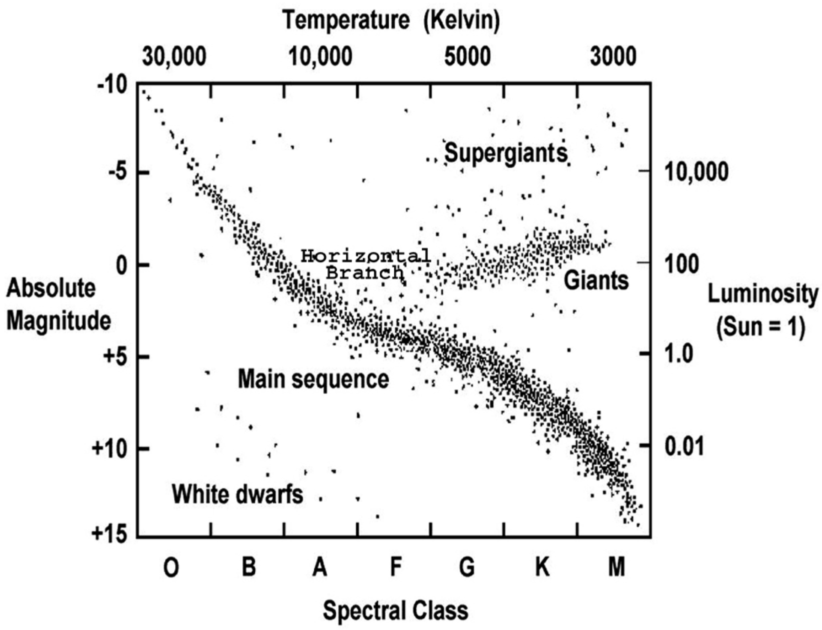

Figure 1.10: The Hertzsprung-Russell diagram, showing the relationship between luminosity L and effective temperature T_{eff} for a selection of stars. Image credit: Chandra X-ray Observatory.

Figure 1.11 illustrates different stellar internal configurations. By this, we refer to the arrangement of internal regions of the star labelled according to the primary physical process occuring in each region (convection versus radiation). In Figure 1.11 we see that the smallest main sequence stars tend to have fully convective interiors. Main sequence stars with similar masses to the Sun tend to have radiative cores surrounded by convective envelopes. In main sequence stars significantly more massive than the Sun, the interior is also mostly radiative and a convective envelope is also present (though this is omitted from the diagram). A convective core additionally develops.

Stars are grouped into discrete *spectral classes* with other stars whose spectra are deemed to be similar. A stellar spectrum is a plot of the intensity of stellar radiation as a function of wavelength recorded for a particular star. It consists of absorption and emission lines, with each line roughly corresponding to a different chemical species. Fundamentally, the different spectral classes are defined by different relative abundances of the many chemical species which produce the emission lines (e.g. Jaschek and Jaschek, 1987). The internal structure of a star during its time spent on the main sequence can roughly be determined by which spectral class it falls into.

The theory of stellar structure began with Eddington (1926). It relates the internal structural configuration of a star to T_{eff}, L and the Schwarzschild criterion. The internal configuration is predominantly dependent on the type of nuclear fusion taking place. A rule-of-thumb is that lower central temperatures are associated with ppI chain fusion, and that higher central temperatures are associated with CN-cycle fusion (e.g. Mestel, 2012).

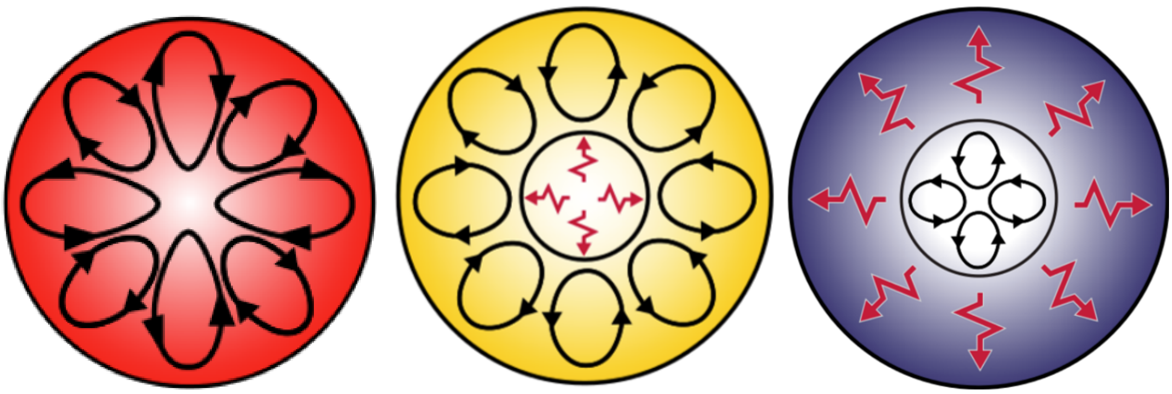

(a) $M < 0.4M_{\odot}$ **(b)** $0.4M_{\odot} < M < 1.1M_{\odot}$ **(c)** $1.1M_{\odot} < M < 1.6M_{\odot}$

Figure 1.11: Typical structure of stars of mass M on the main sequence. Red arrows indicate radiative regions. Black loops indicate convective regions. $M_{\odot}$ denotes the mass of the Sun. Original source of image unknown.

Stellar Internal Gravity Waves

In stellar interiors, IGWs are typically excited at the radiative-convective interface. This usually occurs via one of two processes. These processes are *convective penetration* and *tidal forcing*.

Earlier, we discussed convective penetration as the mechanism of excitation of solar IGWs. This form of IGW excitation is not limited to the Sun. It has the potential to occur in any star or planet possessing a radiative region adjacent to a convective region.

How does excitation by tidal forcing differ? IGWs can be excited this way in stars with close-orbiting exoplanets. These could be solar-type stars or hot binary stars, to name a few examples. Tidal excitation is possible when the buoyancy frequency N is comparable with or larger than the tidal forcing frequency (Barker and Ogilvie, 2010). In solar-type stars, we expect tidal excitation to be particularly efficient in places where N is comparable with $1/P$, where P is the orbital period of the associated exoplanet (Barker, 2011).

IGW instabilities have been linked with orbital decay in exoplanets such as hot Jupiters (Weinberg et al., 2024). Hot Jupiters are exoplanets with masses comparable to Jupiter which have very short orbital periods (usually 10 Earth days or fewer). Astronomers are interested in orbital decay in these close-orbiting planets because of the prospect of them being consumed by their host star. WASP-12b is a hot Jupiter which orbits the star WASP-12. So far, it is the only exoplanet for which orbital decay has been directly detected (Weinberg et al., 2017; Bailey and Goodman, 2019; Yee et al., 2020).

What role do IGWs play in the orbital decay of hot Jupiters? IGWs excited by tidal forcing at the radiative-convective interface propagate towards the stellar centre. If the exoplanet is massive enough, and the excited waves have sufficiently large amplitudes, the waves can break when they reach the centre (Barker and Ogilvie, 2010). This can cause tidal dissipation, which may be strong enough to pull the orbiting exoplanet closer to its host star as a consequence of conservation of angular momentum (Guo et al., 2023). Tidal dissipation has also been investigated in binary systems (Zahn, 1977; Goodman and Dickson, 1998).

IGWs are of interest in stars generally because they contribute to the mixing of chemical species and angular momentum transport within stellar interiors. It is important to understand angular momentum transport because it is essential for maintaining solid-body rotation in the radiative zones of stars (Fuller et al., 2014). As for the mixing of chemical species, IGWs are thought to play a role in the lithium depletion problem. F stars contain smaller quantities of lithium than theoretically predicted. Garcia Lopez and Spruit (1991) proposed that this could be caused by diffusion of lithium induced by mixing due to IGWs.

1.3.4 Stellar Magnetic Fields

Though we knew as early as 1908 that the Sun possesses a magnetic field, magnetic fields in other solar-type stars were not confirmed until 1980 (Robinson, 1980; Robinson et al., 1980). As a general rule, magnetic fields are more likely to be detectable in low-mass stars. Magnetic fields have an impact on stars at all stages of their evolutionary cycle. During their time on the main sequence, the presence of magnetic fields tends to slow down the rotation of many stars (Donati and Landstreet, 2009).

The appearance of stellar spectra is directly influenced by the structure of atomic and molecular energy levels within a star. Such energy levels can be modified by magnetic fields. The Zeeman effect is one way this can happen. It essentially describes the splitting of spectral lines induced by a magnetic field. Hale (1908) used the Zeeman effect to detect magnetic fields of about 3×10^3G within sunspots. Using Zeeman-splitting, we can estimate the percentage of the visible hemisphere of a star which is permeated by magnetic fields. We can also use stellar spectra to estimate the field strength averaged across the stellar surface (Saar, 1988). The limitation of using Zeeman-splitting to ascertain information about stellar magnetic fields is that it cannot tell us anything about the orientation of the field. It cannot tell us whether a field is poloidal, toroidal, or a combination of the two (Donati and Landstreet, 2009).

If we want to know this information, we should instead measure the polarisation properties of spectral lines using a *polarimeter* (Degl'Innocenti and Landolfi, 2004). The interpretation of a spectrograph with a polarimeter fitted is known as *spectropolarimetry*. In general, we use magnetic imaging techniques such as Zeeman–Doppler Imaging (Semel, 1989) to deduce the orientations of stellar magnetic fields.

Magnetic Fields in Low-Mass Main Sequence Stars

We refer to a star as 'low-mass' if its mass is lower than $1.6M_{\odot}$. What is the relationship between stellar magnetic fields and rotation period? As a general rule, magnetic fields induce a braking torque which slows down the rotation of their host stars. This is related to the idea that magnetic fields are generated through dynamo action, which involves interaction between convective motions and the rotation of the star. If the Coriolis force has a strong impact on convective motions, then stars tend to exhibit strong magnetic activity (Donati and Landstreet, 2009).

How about the relationship between stellar magnetic fields and stellar mass? As stellar mass decreases, the proportion of the interior of a main sequence star which is convectively unstable increases. This appears to increase the efficiency with which dynamo action can produce axisymmetric poloidal magnetic fields via the α effect in the convection zone (Donati and Landstreet, 2009). In some cases, the entirety of the interior of a main sequence star can be convectively unstable. Understanding the generation of a large-scale toroidal magnetic field is more difficult in the case of fully convective stars because they do not possess a radiative-convective interface (which is typically the location at which a large-scale toroidal field is generated by the Ω effect).

We know that dynamo action in the Sun is a periodic process (i.e. the Sun has an 11-year solar cycle for its magnetic activity). The solar magnetic field undergoes a global polarity reversal every time this 11-year cycle completes. For the most part, magnetic imaging studies have not had much success in capturing any such polarity reversal in other stars. This suggests if they do in fact have periodic dynamo action, the periods are much longer than that of the Sun. There are some exceptions, however. Donati et al. (2008) document a star known as τ Boo for which there exists evidence of polarity switching.

There are two proposed ideas as to the source of a stellar magnetic field generally:

1. It is generated through dynamo action.
2. It is a remnant of an ancient fossil magnetic field which already existed in the very early stages of the star's evolution.

Only the first of these two options is backed up by solid evidence. Let Ro denote the Rossby number, which is the ratio of inertial forces to the Coriolis force in a fluid. Spectroscopy shows that magnetic flux increases with increasing $1/\mathrm{Ro}$ generally, which is consistent with dynamo theory. Some argue that dynamo processes take place through a range of depths in the convective zone, not just at the radiative-convective interface (Donati and Cameron, 1997; Donati et al., 1999, 2003). For instance, Brandenburg (2005) investigated the idea of dynamo processes near to the solar photosphere.

In the case of cool stars, fossil fields are predicted to be dissipated away by convection within a thousand years of their conception. Fields generally fluctuate too much for them to be possibly based on the remnants of an ancient evolutionary process. However, in the case of hotter stars, the fossil field hypothesis cannot be dismissed in the same way. The plasma in hotter stars is almost fully ionised. More ionised plasma means higher conductivity and therefore reduced Ohmic dissipation. For this reason, hotter stars are more likely to retain their fossil fields (Donati and Landstreet, 2009).

Magnetic fields are responsible for generating the atmospheres of low-mass stars (chromospheres and coronae). Magnetised winds (e.g. the solar wind) and prominences are the most common ways in which early main sequence stars transfer their angular momentum to their surroundings. The resulting decrease in angular velocity is called *spinning down*.

Magnetic Fields in High-Mass Main Sequence Stars

Here, we refer to a star as 'high-mass' if its mass is greater than $1.6M_\odot$. Along the main-sequence, this generally consists of spectral types O, A and B. Compared to lower-mass stars, very few stars with magnetic fields have been detected amongst these three spectral types. Those stars which are magnetic tend to be of type Ap or Bp. The minimum surface field strength for type Ap and Bp stars is 300G (Donati and Landstreet, 2009). These magnetic fields were originally encountered by Babcock (1947), through the Zeeman effect. Ap-type and Bp-type stars have different magnetic field orientations depending on their rotation period (Landstreet and Mathys, 2000). If the period is less than one month, the field tends to be perpendicular to the rotation axis. If the period is greater than one month, the field tends to be parallel to the rotation axis.

In such stars, magnetic fields remain relatively constant over timescales of many years. They are much less fluctuating than those of low-mass stars. We do not observe the same trend with rotation that we do in low-mass stars (i.e. that magnetic activity scales with $1/\mathrm{Ro}$ in low-mass stars). In hotter high-mass stars, it is generally agreed that magnetic fields are the remnants of fossil fields, as explained earlier. Ap and Bp stars are not the only high-mass stars in which magnetic fields have been detected. Magnetic fields are also present in stars occupying the red giant branch, where dynamo processes are also expected to occur (Aurière et al., 2008). Red giant stars have surface magnetic fields with strengths of 1-10G (Konstantinova-Antova et al., 2013).

Naturally, stellar magnetic fields are much easier to detect on the surface than they are deep in the stellar interior. There are some exceptions, though. Lecoanet et al. (2022) show how asteroseismology can be used to measure the magnetic field strength near the core of a main sequence star of spectral type B.

Magnetic Fields in Red Giant Stars

Red giants are former main-sequence stars. They are the subject of the *dipole dichotomy problem*. A dipole mode is an oscillation for which the degree is $l = 1$ (see Section 1.3). The spacecraft Kepler has identified several red giants for which the amplitudes of observed dipole modes are smaller than expected (Mosser et al., 2015, 2017). We refer to these as *depressed dipole modes*. The dipole dichotomy problem seeks to understand why these dipole modes are depressed. Fuller et al. (2015) show that the cause of these dipole modes being depressed could be strong internal magnetic fields in RGB stars. Work on the dipole dichotomy problem was continued by Lecoanet et al. (e.g. 2017); Loi and Papaloizou (e.g. 2018) and Loi (2020).

Figure 1.12 shows how waves can get trapped in the cores of RGB stars by the magnetic field. While trapped inside the core, they get dissipated. This is called the magnetic greenhouse effect (Fuller et al., 2015). This notion of trapped waves is linked with the suppression of dipole modes.

Influence of Stellar Magnetic Fields on Internal Gravity Waves

IGWs begin to interact with magnetic fields when the Alfvén frequency ω_A becomes comparable to the buoyancy frequency N. Loi and Papaloizou (2018) found that the transition between a weak field and a strong field corresponds with a significant change in the spatial structure of g-mode amplitudes. Through ray tracing, we find that a transition between weak and strong field causes a shift from regular dynamics to chaotic dynamics. Internal gravity wave rays propagating towards magnetic regions can align with critical surfaces of magnetic flux. In this way, they

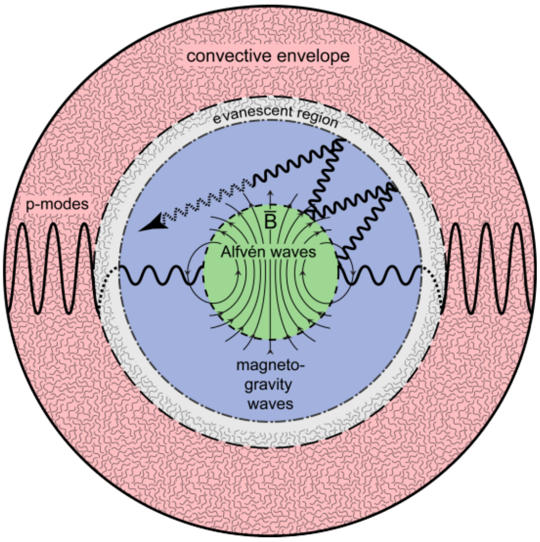

Figure 1.12: Schematic describing wave motions in red giant stars. Image credit: Fuller et al. (2015).

get converted to Alfvén waves (Loi and Papaloizou, 2018). Such waves are said to be 'trapped'. These converted modes are similar to the torsional Alfvén modes studied by Loi and Papaloizou (2017).

Loi and Papaloizou (2018) explain how torsional Alfvén waves can be resonantly excited from spheroidal g-modes. In the presence of a magnetic field, modes with frequencies similar to the forcing frequency are more likely to be excited than modes with different frequencies. It is these modes which can resonantly interact with the magnetic field to produce torsional Alfvén waves.

When the frequencies of IGWs and AWs are comparable, propagation of IGWs is significantly affected. For a propagating IGW, a surface along which its frequency is equal to the Alfvén frequency is called a *critical surface*. Upon such surfaces, propagating IGWs can be reflected or trapped. Whether they are reflected or trapped is dependent on the orientation of the background magnetic field with respect to the direction of stratification. It is also dependent on the value of the wave's frequency relative to the buoyancy frequency N. Reflection of IGWs can lead to the formation of global Alfvén-gravity modes through constructive interference (Loi and Papaloizou, 2018).

Stellar Alfvén Waves

Like internal gravity waves, Alfvén waves contribute to the transport of energy and momentum within stellar interiors. It is also important to study Alfvén waves in stars generally because they play a role in MHD turbulence (Sridhar and Goldreich, 1994; Goldreich and Sridhar, 1995; Ng and Bhattacharjee, 1996; Takahashi and Langer, 2025). Alfvén waves can explain variations in rotational period in magnetic stars (Krtička et al., 2017). Takahashi and Langer (2025) used Alfvén waves to derive constraints on the internal magnetic field structure for a selection of ten different stars. They also used Alfvén waves to predict the variation in rotational period of stars and to quantify angular momentum transport in stellar interiors.

1.3.5 Asteroseismology

How do we know that these waves exist in stars? More importantly, how do we know what the interiors of these stars look like in the first place? Techniques such as spectroscopy, photometry, astrometry and interferometry alone can only give us a very limited insight into stellar interiors (e.g. Aerts et al., 2010). To get a better insight, we require something else. This is where asteroseismology is crucial. This is the use of observed oscillations at stellar surfaces to make deductions regarding the structure and properties of stellar interiors.

Asteroseismology is possible because the internal properties of stars have effects on the observable frequencies of global stellar oscillations. In particular, the observable frequencies are affected by the rate of rotation and the strength and orientation of stellar magnetic fields (e.g. Aerts et al., 2010).

Description of Method

The process of asteroseismology can be summarised in three steps (e.g. Aerts et al., 2010):

1. Photometry and spectroscopy are used to measure frequencies and amplitudes of p-modes at the surface of the star.

2. Based on these frequencies and amplitudes, mathematical models can be used to deduce the variation of the sound speed, density and pressure throughout the radial extent of the interior.

3. With knowledge of these three variables, an equation of state can be used to derive the internal temperature profile.

The p-modes can be reflected from the stellar surface because acoustic energy cannot escape the stellar fluid medium. p-modes with higher values of spherical harmonic degree l have more points of reflection. The higher the degree l of a mode, the shallower the radial depth of penetration. The frequency of a mode observed at the surface depends on the travel time of sound traced along the ray path. However, the speed of sound varies with radius, i.e. it varies along the ray path. The speed of sound must therefore be integrated over depth to obtain said travel time. *Inversion* is the name given to this technique, which is used to create a map of the sound speed throughout the interior of the star based on these frequency observations at the surface. From the sound speed map we can use an equation of state to form a temperature profile of the interior (e.g. Aerts et al., 2010).

How can asteroseismology be used to make deductions about stellar rotation rate? *Rotational splitting* is the rotation-induced modification of the observed frequencies of global oscillations. We can identify the particular l and m values corresponding to observed rotational splitting and use the splitting to measure the rotation rate of the astrophysical body. Our measurements of solar differential rotation (see Figure 1.5) are thanks to rotational splitting (e.g. Aerts et al., 2010).

Helioseismology

Helioseismology is the name given to asteroseismology when performed on the Sun. We owe our measurements of solar differential rotation to helioseismology. In helioseismology, g-modes in the radiative zone become evanescent once they reach the convective zone. Their amplitude is progressively reduced across the radial extent of the convective zone, to the point where their amplitude is so small once it reaches the photosphere that they become difficult to detect using helioseismology. This is why there have been no conclusive observations of IGWs in the Sun.

Detection of g-modes via helioseismology has been incredibly sought-after for a long time (Brookes et al., 1976; Severny et al., 1976; Kotov et al., 1978; Lecoanet and Quataert, 2013). Though detections of p-modes have been plentiful, g-modes are thought to be potentially much more useful than p-modes for deducing stellar structure, especially in the core (Turck-Chièze et al., 2004; Lecoanet and Quataert, 2013).

Limitations

Lecoanet et al. (2022) used asteroseismology to measure the field strength at the surface of the core of a type B star. Other authors have also inferred the possible existence of internal stellar fields in this way (Fuller et al., 2015; Stello et al., 2016; Li et al., 2022, 2023). At the moment, asteroseismology of stellar interiors is only able to detect fields locally in this specific region: the surface of the stellar core. Asteroseismic inference of fields at other locations within the stellar interior has yet to be achieved (Takahashi and Langer, 2025).

1.4 Aims of Thesis

This thesis is about instabilities. Many of the research motives we have discussed in this chapter are related to consequences of IGWs and AWs becoming unstable. If a wave becomes unstable, it is more likely to be efficiently dissipated, so is more likely to have an impact on the transport of energy and momentum. In this thesis, there is a large focus on *parametric instabilities* - instabilities associated with resonance. An example of parametric instability which will form a large component of this thesis is the *triadic resonance instability* (TRI). This is a parametric instability which occurs as a result of a resonant interaction between three waves. We will discuss this type of instability in more detail in Chapter 3. These resonant instabilities are the dominant flavour of instability occurring at small wave amplitudes. For these instabilities, we can develop theory to predict their occurence analytically.

The instabilities we study are not limited to small-amplitude waves. The waves we consider constitute exact solutions to the ideal equations of motion for any wave amplitude, allowing us to study the instabilities numerically for a range of different amplitudes.

Instabilities of IGWs in the absence of a magnetic field have been well-studied. In the case where a plane wave is used as basic state, much of the linear stability analysis has been done via a *Floquet* method. We will discuss this method in more detail in Chapter 4. Mied (1976), Drazin (1977) and Klostermeyer (1982) were the first to use a Floquet method to study the stability of a plane IGW in a Boussinesq fluid. All three authors found that in small-amplitude waves, instability tends to be caused by resonant interactions alone (e.g. triadic resonance instability). Klostermeyer (1991) showed that new types of instability (e.g. static convective instability) appear as the amplitude is increased. Varma et al. (2022) provide a comprehensive review of this topic.

The issue here is that stability analysis of planar IGWs in a Boussinesq fluid via Floquet analysis has only been attempted in a purely hydrodynamic context. Many of the fluids which our model is applicable to are magnetic (e.g magnetic stars), so we wish to establish the impact of introducing a magnetic field on the stability of these waves. We thereby study a hybrid of IGWs and AWs, referred to as *Alfvén-gravity waves* (AGWs). These are alternatively called *internal magnetogravity waves* or simply *magnetogravity waves* in some literature (e.g. McLellan and Winterberg, 1968). In fact, resonant instabilities involving AGWs have been studied in the presence of an oscillatory linear shear flow by Salhi and Nasraoui (2013). It should be emphasised that the model in this thesis is fundamentally different to that of Salhi and Nasraoui (2013) in that we study instabilities of plane AGWs propagating through a fluid at rest. In contrast, Salhi and Nasraoui (2013) studied instabilities of the background shear flow which result from resonance between the shear flow and its AGW disturbances. Some key questions we would like to answer include:

1. How does the strength and orientation of a magnetic field influence the growth rate of instabilities of plane IGWs?

2. Does it suppress, enhance, or have no impact on the instabilities observed in the hydrodynamic setting?

3. Does it introduce new types of instability not observed in the hydrodynamic setting?

4. Does wave amplitude play the same role in determining which types of instability can occur in the magnetic setting as it does in the non-magnetic setting?

5. Can we attribute small-amplitude instabilities of plane AGWs to resonant triad interactions in the same way that we can for pure IGWs?

6. What physical processes are driving the instabilities of plane AGWs energetically in stably-stratified fluids (e.g. shear, buoyancy, Maxwell stress, electric current)?

Earlier in this chapter we discussed the importance of studying instabilities of IGWs and AWs in the radiative zones of the Sun, solar-type stars, red giants and in the solar atmosphere. Each of the six points above are important to consider when studying AGWs in these astrophysical applications, giving us a greater understanding of the instabilities which contribute to mixing and transport of energy and momentum in these astrophysical settings. We use solar models to relate the dimensionless field strengths used in these calculations to the dimensional field strength values we can expect in the solar interior.

1.5 Outline of Thesis

In Chapter 2 we introduce the mathematical concepts and assumptions which are fundamental to this work. We reveal the equations which govern the problem and use simple solutions of the equations to describe pure Alfvén waves, pure internal gravity waves and hybrid Alfvén-gravity waves. For each type of wave, we derive a dispersion relation and expressions for the phase and group velocities. We plot the dependence of the phase and group velocities on the angle of the wavevector. In the case of Alfvén-gravity waves, such plots are novel. We also explain how the amplitude of the wave relates to overturning.

In Chapter 3 we present a theoretical framework with which to study resonant instabilities of small-amplitude pure internal gravity waves. We derive a formula to predict the growth rate of such instabilities using multiple-scale analysis. This is a reformulation of work originally performed by Davis and Acrivos (1967) and later by Drazin (1977).

In Chapter 4 we perform a linear stability analysis of finite-amplitude internal gravity waves using a numerical Floquet approach, building upon the work of Lombard and Riley (1996). We show how the growth rate of instabilities of IGWs depends on amplitude, wavevector orientation and thermal diffusion before determining what physical processes are driving the instabilities energetically. Though the Floquet method used in this chapter is not original, we use it to derive some original results not attempted by Lombard and Riley (1996). In particular, we perform a much more comprehensive exploration of parameter space than in previous literature and plot the disturbance as a function of spatial coordinates. We also demonstrate agreement between the asymptotic approach of Chapter 3 and the numerical Floquet approach in terms of the computed growth rates.

In Chapter 5 we extend the theoretical framework to represent instabilities of internal gravity waves modified by a magnetic field for the first time (i.e. instabilities of Alfvén-gravity waves). Like the Chapter 3 framework, it is applicable to small-amplitude waves only. In the MHD problem, more classes of resonance are possible because the system permits two types of wave. This results in a much more diverse range of dynamics than the equivalent hydrodynamic problem.

In Chapter 6 we apply the same numerical method used in Chapter 4 to study the stability of Alfvén-gravity waves for any wave amplitude. We show how the growth rate of instabilities of AGWs additionally depends on the strength and orientation of the magnetic field, as well as on amplitude and wavevector orientation. The physical processes driving the instabilities are discussed, which are much more diverse than in Chapter 4 now that a magnetic field has been included. We also demonstrate agreement between the asymptotic approach of Chapter 5 and the numerical Floquet approach, again in terms of the computed growth rates.

Chapter 2

Mathematical Model and Wave Properties

This chapter establishes the fundamental mathematical characteristics underpinning the waves we study in this thesis. We begin by introducing the mathematical model we use to represent stratified, magnetised fluids. We explain why and how we use the Boussinesq approximation in the model. In this thesis we are interested in three tyes of wave: pure Alfvén waves (AWs), pure internal gravity waves (IGWs) and hybrid Alfvén-gravity waves (AGWs). We demonstrate how each of these three types of wave can be described mathematically, in terms of their wavenumbers, frequencies, phase velocities and group velocities.

2.1 Mathematical Model

We consider a stably-stratified fluid in magnetohydrostatic equilibrium permeated by a uniform background magnetic field $\boldsymbol{B}_0$. Our model is valid for any such fluid. We use local Cartesian (X, Y, Z)-coordinates, such that the negative Z-direction is aligned with gravity. We choose to neglect the effects of rotation in this thesis for simplicity. This eliminates the dynamics of inertial waves and allows us to more easily compare our results with those of previous studies of IGW instabilities, many of which do not consider the dynamics of inertial waves (e.g. Mied, 1976; Drazin, 1977; Klostermeyer, 1982). The orientation of X and Y is therefore arbitrary.

This model could be applied in a number of astrophysical contexts. We have discussed the stellar context in detail in Chapter 1. How about a planetary context? It has been suggested that there could be a stably-stratified layer just below the core-mantle boundary in Earth's interior (e.g. Higgins and Kennedy, 1971), though its existence has been contested (e.g. Verhoogen, 1973). If stable stratification were to exist here, where the Earth's magnetic field is generated by the geodynamo, then we could certainly expect the propagation of AWs, IGWs and hybrids of the two. Magnetised stably-stratifed layers are also thought to exist in Jupiter (e.g. Moore et al., 2022), Saturn and similar planets, with potential to foster such waves.

The context we shall focus on is the radiative zones of stellar interiors. Figure 2.1 shows an example of how we might position a Cartesian box in a solar-type star. We must be able to assume that the star's magnetic field and buoyancy frequency profile can be locally approximated as uniform. Within these constraints, the box can be placed at any arbitrary radial depth within the radiative zone.

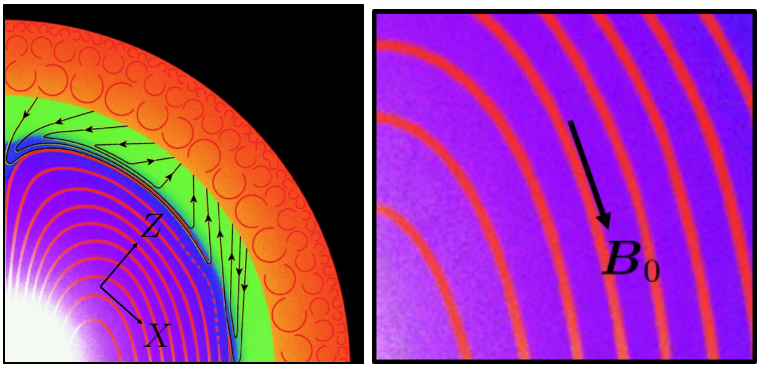

Figure 2.1: Example of a valid location and orientation for the Cartesian box model within a solar-type star, together with its host (background) magnetic field $\boldsymbol{B}_0$. Shown here is a cross-section of part of the star, such that the bottom-left corner represents the centre of the star. Purple region: radiative zone. Orange region: convective zone. Green region: radiative-convective interface. The width of the radiative-convective interface is exaggerated for visual clarity. The Y-axis points directly out of the page. The size of the box is also exaggerated for visual clarity. To make a valid local Cartesian approximation, the box must be much smaller relative to the stellar radius. In this example, $\boldsymbol{B}_0$ happens to be confined to the (X, Z)-plane, though $\boldsymbol{B}_0$ may have a Y-component in general.

Equations of Compressible MHD

In their most general form, the governing equations that describe the fluids we study are the equations of compressible MHD. These consist of the *mass continuity equation*:

$$\frac{\partial \breve{\rho}}{\partial T} + \nabla \cdot (\breve{\rho} \boldsymbol{U}) = 0, \tag{2.1}$$

the *momentum equation*:

$$\breve{\rho}\frac{\mathrm{D}\boldsymbol{U}}{\mathrm{D}T} = -\nabla \breve{\mathcal{P}} + \breve{\rho}\boldsymbol{g} + \breve{\rho}\nu \left[\nabla^2 \boldsymbol{U} + \frac{1}{3}\nabla(\nabla\cdot\boldsymbol{U})\right] + \frac{1}{\mu_0}(\nabla\times\boldsymbol{B})\times\boldsymbol{B}, \tag{2.2}$$

the *induction equation*:

$$\frac{\partial \boldsymbol{B}}{\partial T} = \nabla\times(\boldsymbol{U}\times\boldsymbol{B}) + \eta\nabla^2\boldsymbol{B}, \tag{2.3}$$

and the *solenoidal constraint*:

$$\nabla\cdot\boldsymbol{B} = 0. \tag{2.4}$$

The symbols used in these equations have the interpretations listed in Table 2.1, where $\breve{\rho}\nu$ and η are assumed constant. The mass continuity equation represents the idea that the rate of change of mass in a fluid volume is equal to the net mass flux into or out of the fluid volume. The momentum equation is derived from Newton's second law for a fluid parcel. It contains the Lorentz force $(\nabla\times\boldsymbol{B})\times\boldsymbol{B}/\mu_0$, which represents the force exerted on the fluid flow by the magnetic field. Supplemented with the Lorentz force, the momentum equation accounts for the influence of the magnetic field on the temporal evolution of the fluid flow. The induction equation accounts for the influence of the fluid flow and the diffusion of the magnetic field on the temporal evolution of the magnetic field. The solenoidal constraint represents the idea that magnetic flux is conserved. In the next section, we use the Boussinesq approximation to simplify equations (2.1)-(2.2).

Table 2.1: Dimensional variables appearing in the equations of compressible MHD.

Independent variables	X	Cartesian spatial direction
	Y	Cartesian spatial direction
	Z	Cartesian spatial direction increasing anti-parallel to gravity
	T	Time
Dependent variables	$\boldsymbol{U}$	Fluid velocity
	$\boldsymbol{B}$	Magnetic field
	$\breve{\mathcal{T}}$	Fluid temperature
	$\breve{\mathcal{P}}$	Fluid pressure
	$\breve{\rho}$	Fluid density
Parameters	ν	Kinematic fluid viscosity
	η	Ohmic diffusivity
	κ	Thermal diffusivity
	$\mathcal{K}$	Thermal conductivity
Physical constants	μ_0	Permeability of free space
	$\boldsymbol{g}$	Acceleration due to gravity

Thermodynamic Equations

We also use two equations arising from thermodynamics. The first of these comes from the first law of thermodynamics and is known as the *internal energy equation* (Priest, 2014):

$$\breve{\rho} c_p \frac{\mathrm{D}\breve{\mathcal{T}}}{\mathrm{D}T} - \frac{\mathrm{D}\breve{\mathcal{P}}}{\mathrm{D}T} = \mathcal{K}\nabla^2\breve{\mathcal{T}} + \frac{\eta}{\mu_0}(\nabla \times \boldsymbol{B})^2 + \breve{\rho}\nu\left(\partial_i U_j + \partial_j U_i - \frac{2}{3}\delta_{ij}\partial_k U_k\right)\partial_i U_j, \qquad (2.5)$$

where $\breve{\mathcal{T}}$ denotes fluid temperature and $\mathcal{K}$ denotes the thermal conductivity of the fluid, the latter of which is taken to be constant. Here c_p denotes the specific heat capacity at constant pressure. The second of these thermodynamic equations is an equation of state, known as the *ideal gas law*:

$$\breve{\rho} = \frac{\breve{P}}{\mathcal{R}\breve{\mathcal{T}}}, \qquad (2.6)$$

where $\mathcal{R}$ is the ideal gas constant.

2.2 The Boussinesq Approximation

The Boussinesq approximation is used to isolate the important effects of density variation in continuously-stratified fluids. Based on assumptions introduced by Boussinesq (1903), it was first formalised as an approximation for compressible gases by Spiegel and Veronis (1960). It is now widely considered to be an appropriate approximation for a vast array of continuously-stratified fluids, with frequent uses in oceanography and astrophysical fluids.

The basic premise can be captured by two notions. One notion is that the vertical length scale of fluid motion is much smaller than any member of a group of quantities known as scale heights associated with the flow. There is a scale height associated with each of the thermodynamic variables $\breve{T}$, $\breve{P}$ and $\breve{\rho}$. For each of $\breve{T}$, $\breve{P}$ and $\breve{\rho}$, the scale height is defined as the vertical distance over which the respective variable changes by a factor of Euler's number e.

In general, in a coordinate system for which Z represents vertical height, the scale height H_F for a quantity F is given by

$$H_F := \left[\frac{1}{F}\left|\frac{\mathrm{d}F}{\mathrm{d}Z}\right|\right]^{-1}. \tag{2.7}$$

In other words, the Boussinesq approximation assumes that

$$H \ll H_{\breve{\rho}}, \quad H \ll H_{\breve{\mathcal{P}}}, \quad H \ll H_{\breve{\mathcal{T}}}. \tag{2.8}$$

where H is a characteristic height associated with the fluid motion.

It follows from (2.8) that fluctuations in the fluid density are small compared to some constant background value of the density. We phrase this mathematically in inequality (2.13) shortly.

The second notion is that the flow velocity must be much smaller than the sound speed. Mathematically, this is expressed as

$$\mathrm{Ma} \ll 1, \tag{2.9}$$

where $\mathrm{Ma} := U/c$ is the *Mach number*. Here, U is the norm of the flow velocity vector $\boldsymbol{U}$ and c is the speed of sound.

It is vital that we must be able to assume (2.9) when neglecting the dynamics of acoustic waves. The Boussinesq approximation is only valid under assumptions (2.8) and (2.9).

Purpose of the Boussinesq Approximation

In the absence of rotation, the equations of compressible MHD describe internal gravity waves, Alfvén waves and acoustic waves, as well as various hybrids of these wave types. The Boussinesq approximation eliminates the dynamics of acoustic waves. This is a useful way of isolating the dynamics of internal gravity waves and Alfvén waves (on the condition that the Alfvén speed is much less than the sound speed), enabling us to study them in detail. It then becomes easier to reformulate the governing equations in a manner which makes them analytically or numerically tractable. Another benefit is that simulations can be run at lower resolutions with shorter computation times (since the dynamics of acoustic waves occur on very small temporal scales).

It is sensible to make the Boussinesq approximation in the ocean because the depth of the ocean is much less than the density scale height. In the ocean, density only varies by about 3% from the surface to the ocean floor (e.g. Gladkikh and Tenzer, 2012), implying a scale height much larger than the ocean depth. Density varies much more across the radial extent of the radiative zones of stars (Figure 1.7), so here it is only sensible to use the Boussinesq approximation when we use a local Cartesian box model. This means that the Boussinesq approximation is valid for waves with short wavelengths relative to the stellar radius, but not for waves with wavelengths comparable to the width of the radiative zone. Several of the equations of motion simplify under the Boussinesq approximation.

The Boussinesq MHD Equations

We use the Boussinesq approximation to simplify equations (2.1)-(2.2). To do so, we decompose the overall fluid pressure $\breve{\mathcal{P}}$, density $\breve{\rho}$ and temperature $\breve{\mathcal{T}}$ as follows.

$$\breve{\rho}(\boldsymbol{X}, T) = \rho_0 + \bar{\rho}(Z) + \rho(\boldsymbol{X}, T), \tag{2.10}$$
$$\breve{\mathcal{P}}(\boldsymbol{X}, T) = \mathcal{P}_0 + \bar{\mathcal{P}}(Z) + \mathcal{P}(\boldsymbol{X}, T), \tag{2.11}$$
$$\breve{\mathcal{T}}(\boldsymbol{X}, T) = \mathcal{T}_0 + \bar{\mathcal{T}}(Z) + \mathcal{T}(\boldsymbol{X}, T). \tag{2.12}$$

Here, ρ_0, $\mathcal{P}_0$ and $\mathcal{T}_0$ are constant background reference values for density, pressure and temperature respectively. $\bar{\rho}(Z)$, $\bar{\mathcal{P}}(Z)$ and $\bar{\mathcal{T}}(Z)$ are static vertical variations in density, pressure and temperature respectively, representing the degree of stratification in the fluid. ρ is the deviation from the hydrostatic density $\rho_0 + \bar{\rho}(Z)$. Similarly, $\mathcal{P}$ is the pressure deviation from the hydrostatic pressure $\mathcal{P}_0 + \bar{\mathcal{P}}(Z)$. Together, F_0 and $\bar{F}(Z)$ quantities represent the equilibrium state.

Let ε be defined as $\varepsilon := H/H_{\breve{\rho}}$. Then an assumption which is fundamental to the Boussinesq approximation is that

$$\frac{\rho}{\rho_0} \sim \frac{\mathrm{Ma}^2}{\varepsilon}, \quad \frac{\mathcal{P}}{\mathcal{P}_0} \sim \mathrm{Ma}^2. \tag{2.13}$$

Assumption (2.13) is a consequence of combining assumption (2.8) with assumption (2.9).

The result of applying the Boussinesq approximation is equations (2.14)-(2.17). We can refer to these as the *Boussinesq MHD equations* for a stably-stratified fluid permeated by a background magnetic field. These consist of the momentum equation:

$$\frac{\partial \boldsymbol{U}}{\partial T} + \boldsymbol{U} \cdot \nabla \boldsymbol{U} = -\frac{1}{\rho_0}\nabla \mathcal{P} + \frac{\rho \boldsymbol{g}}{\rho_0} + \nu \nabla^2 \boldsymbol{U} + \frac{1}{\mu_0 \rho_0}(\nabla \times \boldsymbol{B}) \times \boldsymbol{B}, \tag{2.14}$$

the induction equation:

$$\frac{\partial \boldsymbol{B}}{\partial T} = \nabla \times (\boldsymbol{U} \times \boldsymbol{B}) + \eta \nabla^2 \boldsymbol{B}, \tag{2.15}$$

the internal energy equation:

$$\frac{\partial \rho}{\partial T} + \boldsymbol{U} \cdot \nabla \rho + U_Z \frac{\mathrm{d}\bar{\rho}}{\mathrm{d}Z} = \kappa \nabla^2 \rho, \tag{2.16}$$

as well as two divergence-free constraints:

$$\nabla \cdot \boldsymbol{U} = 0, \quad \nabla \cdot \boldsymbol{B} = 0. \tag{2.17}$$

The equation $\nabla \cdot \boldsymbol{U} = 0$ from (2.17) is the reduced form of the mass continuity equation under the Boussinesq approximation. In equation (2.16) κ denotes the thermal diffusivity of the fluid. It is related to the thermal conductivity K by $\kappa := K/(\rho_0 c_p)$.

The Boussinesq Momentum Equation

After substituting decompositions (2.10) and (2.11) and (2.12) into the compressible momentum equation (2.2), we use (2.13) to neglect a number of terms involving ρ. The result is the Boussinesq momentum equation (2.14). Note that though all other terms in ρ are neglected, we cannot neglect $\rho\boldsymbol{g}$ from the momentum equation. In a system with stratification, $\rho\boldsymbol{g}$ is certainly important in determining the dynamics.

The Boussinesq Internal Energy Equation

Equation (2.16) is derived by combining (2.5) and (2.6). We summarise how (2.16) is obtained in this way. The Taylor series for $\breve{\rho}(\breve{P}, \breve{\mathcal{T}})$ centred at $(\mathcal{T}_0 + \bar{\mathcal{T}}, \mathcal{P}_0 + \bar{\mathcal{P}})$ to linear order is

$$\breve{\rho} = \rho_0 + \bar{\rho} + (\breve{\mathcal{T}} - \mathcal{T}_0 - \bar{\mathcal{T}}) \frac{\partial \breve{\rho}}{\partial \breve{\mathcal{T}}}\bigg|_{(\mathcal{P}_0+\bar{\mathcal{P}}, \mathcal{T}_0+\bar{\mathcal{T}})} + (\breve{\mathcal{P}} - \mathcal{P}_0 - \bar{\mathcal{P}}) \frac{\partial \breve{\rho}}{\partial \breve{\mathcal{P}}}\bigg|_{(\mathcal{P}_0+\bar{\mathcal{P}}, \mathcal{T}_0+\bar{\mathcal{T}})} + \ldots \tag{2.18}$$

Spiegel and Veronis (1960) show that the ideal gas law (2.6) can be combined with Taylor series (2.18) to yield the following expansion.

$$\breve{\rho} = (\rho_0 + \bar{\rho}) \left(1 - \frac{\breve{\mathcal{T}} - \mathcal{T}_0 - \bar{\mathcal{T}}}{\mathcal{T}_0 + \bar{\mathcal{T}}} + \frac{\breve{\mathcal{P}} - \mathcal{P}_0 - \bar{\mathcal{P}}}{\mathcal{P}_0 + \bar{\mathcal{P}}} \right) + \ldots \tag{2.19}$$

where we have omitted any terms which are nonlinear in $\breve{\mathcal{T}}$ or $\breve{\mathcal{P}}$. Using (2.10), (2.11) and (2.12), equation (2.19) becomes

$$\frac{\rho}{\rho_0 + \bar{\rho}} = \frac{\mathcal{P}}{\mathcal{P}_0 + \bar{\mathcal{P}}} - \frac{\mathcal{T}}{\mathcal{T}_0 + \bar{\mathcal{T}}} + \ldots \tag{2.20}$$

Kimbley (2024) explains how we can use (2.20) to derive (2.16) from (2.5) by neglecting Ohmic heating and applying (2.10)-(2.13), as well as the mass continuity equation from (2.17).

Reformulated Governing Equations

Going forward, $\boldsymbol{U}, \boldsymbol{B}, P$ and ρ are the four principal dependent variables which concern us. The components of $\boldsymbol{U}$ are labelled (U_X, U_Y, U_Z) and those of $\boldsymbol{B}$ are labelled (B_X, B_Y, B_Z). We reformulate the momentum equation by decomposing the Lorentz force into a *magnetic pressure* and a *magnetic tension*. We also rephrase the $\nabla \times (\boldsymbol{U} \times \boldsymbol{B})$ term in a way which is more convenient for constructing the eigenvalue problem. Both of these modifications are made explicit in Appendix A.1. Below, P encapsulates both the fluid pressure $\mathcal{P}$ and the magnetic pressure $B^2/(2\mu_0)$, where $B := \|\boldsymbol{B}\|$. Specifically, we define the total pressure P as

$$P = \mathcal{P} + \frac{B^2}{2\mu_0}. \tag{2.21}$$

In summary, the governing equations we use going forward are

$$\nabla \cdot \boldsymbol{U} = 0, \tag{2.22}$$
$$\nabla \cdot \boldsymbol{B} = 0, \tag{2.23}$$
$$\frac{\mathrm{D}\boldsymbol{U}}{\mathrm{D}T} = \nu \nabla^2 \boldsymbol{U} + \frac{\boldsymbol{B} \cdot \nabla \boldsymbol{B}}{\mu_0 \rho_0} - \frac{\nabla P}{\rho_0} + \frac{\rho \boldsymbol{g}}{\rho_0}, \tag{2.24}$$
$$\frac{\mathrm{D}\boldsymbol{B}}{\mathrm{D}T} = \eta \nabla^2 \boldsymbol{B} + \boldsymbol{B} \cdot \nabla \boldsymbol{U}, \tag{2.25}$$
$$\frac{\mathrm{D}\rho}{\mathrm{D}T} = \kappa \nabla^2 \rho - U_Z \frac{\mathrm{d}\bar{\rho}}{\mathrm{d}Z}, \tag{2.26}$$

where the Lagrangian derivative operator $\mathrm{D}/\mathrm{D}T$ is defined as

$$\frac{\mathrm{D}}{\mathrm{D}T} \coloneqq \frac{\partial}{\partial T} + \boldsymbol{U} \cdot \nabla. \tag{2.27}$$

2.3 Properties of Waves

The Ideal Boussinesq MHD Equations

We want to study the dynamics of waves propagating through an unbounded stably-stratifed Boussinesq fluid permeated by a magnetic field. For this section, we hence consider *plane wave solutions* to the *ideal* form of governing equations (2.22)-(2.26). The 'ideal form' refers to the governing equations as they appear in the absence of viscosity, thermal diffusion or Ohmic diffusion. We denote such solutions by $\tilde{\boldsymbol{U}}$, $\tilde{\boldsymbol{B}}$, $\tilde{P}$ and $\tilde{\rho}$.

We demand that the plane wave solution exhibits no Y-dependence and confine it to the (X, Z)-plane, which we are free to do without loss of generality. The background magnetic field is denoted by $\boldsymbol{B}_0$. In this thesis we consider uniform $\boldsymbol{B}_0$ only, i.e. constant in space and time. Its strength is denoted by B_0 and the angle it makes with the X-axis is denoted by ζ. The background magnetic fields we consider are 3D in general; the angle that $\boldsymbol{B}_0$ makes with the Y-axis is denoted by ξ.

The plane wave solution has a wavevector $\boldsymbol{K}$ of length K. Since we consider waves in an unbounded medium, the components of $\boldsymbol{K}$ can take any real value. The plane wave also has a real amplitude a and an orientation θ with respect to the X-axis. The significance of a is discussed later in this chapter. Each combination (a, θ, ζ, B_0) specifies a unique plane wave solution. The angle ξ is not necessary for specifying the plane wave solution because the frequency of the plane wave is independent of ξ. This is explained by dispersion relation (2.78) later in this chapter. A plane wave solution with $\theta = \pi/4$ is illustrated in Figure 2.2.

Based on Figure 2.2, we can express the components of the wavevector $\boldsymbol{K}$ and the background magnetic field $\boldsymbol{B}_0$ trigonometrically in the (X, Z)-plane:

$$\boldsymbol{K}(\theta) = K(\hat{\boldsymbol{X}} \cos\theta + \hat{\boldsymbol{Z}} \sin\theta), \tag{2.28}$$
$$\boldsymbol{B}_0(\zeta) = B_0(\hat{\boldsymbol{X}} \cos\zeta + \hat{\boldsymbol{Z}} \sin\zeta). \tag{2.29}$$

Since this section discusses the ideal form of the Boussinesq MHD equations, this is a sensible point to define three dimensionless numbers quantifying the influence of diffusion on the dy-

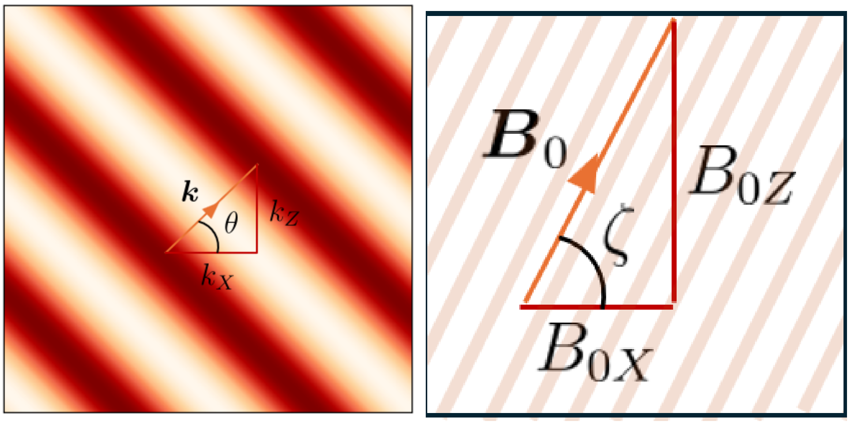

Figure 2.2: (Left) Illustration of the plane wave solution, together with its wavevector $\boldsymbol{K}$ and orientation θ with respect to the X-axis. (Right) Notation for the background magnetic field.

namics. These are the fluid Reynolds number Re, the magnetic Reynolds number Rm and the thermal Péclet number Pe.

The dimensionless numbers Re, Rm and Pe are given by

$$\mathrm{Re} := \frac{N}{\nu K^2}, \quad \mathrm{Rm} := \frac{N}{\eta K^2}, \quad \mathrm{Pe} := \frac{N}{\kappa K^2}. \tag{2.30}$$

The expression for N in the Boussinesq limit is provided in Section 2.3.2. We make the following assumption regarding the plane wave solutions $\tilde{\boldsymbol{U}}$, $\tilde{\boldsymbol{B}}$, $\tilde{P}$ and $\tilde{\rho}$:

$$\mathrm{Re} \to \infty, \quad \mathrm{Rm} \to \infty, \quad \mathrm{Pe} \to \infty. \tag{2.31}$$

It should be stressed that we only make assumption (2.31) regarding the plane wave solutions $\tilde{\boldsymbol{U}}$, $\tilde{\boldsymbol{B}}$, $\tilde{P}$ and $\tilde{\rho}$. We do not make assumption (2.31) for $\boldsymbol{U}$, $\boldsymbol{B}$, P and ρ in general. We can make this assumption provided that the growth timescale is much larger than the diffusion timescale for the primary wave. Assumption (2.31) allows us to neglect ν, η and κ from the Boussinesq MHD equations (2.22)-(2.26).

This yields the ideal Boussinesq MHD equations:

$$\nabla \cdot \boldsymbol{U} = 0, \tag{2.32}$$

$$\nabla \cdot \boldsymbol{B} = 0, \tag{2.33}$$

$$\frac{\mathrm{D}\boldsymbol{U}}{\mathrm{D}T} = -\frac{1}{\rho_0}\nabla P + \frac{\rho \boldsymbol{g}}{\rho_0} + \frac{1}{\mu_0 \rho_0}\boldsymbol{B} \cdot \nabla \boldsymbol{B}, \tag{2.34}$$

$$\frac{\mathrm{D}\boldsymbol{B}}{\mathrm{D}T} = \boldsymbol{B} \cdot \nabla \boldsymbol{U}, \tag{2.35}$$

$$\frac{\mathrm{D}\rho}{\mathrm{D}T} = -U_Z \frac{\mathrm{d}\bar{\rho}}{\mathrm{d}Z}. \tag{2.36}$$

We suppose that the waves we consider are disturbances relative to a state of rest (about $\boldsymbol{U} = 0$) permeated by a constant background magnetic field $\boldsymbol{B}_0$. The rest state is in hydrostatic equilibrium, which is accounted for by $\mathcal{P}_0, \rho_0, \bar{\mathcal{P}}$ and $\bar{\rho}$ in equations (2.10) and (2.11). To find a dispersion relation for these plane waves, we set

$$\boldsymbol{U}(\boldsymbol{X},T) = \tilde{\boldsymbol{U}}(X,Z,T), \tag{2.37}$$
$$\boldsymbol{B}(\boldsymbol{X},T) = \tilde{\boldsymbol{B}}(X,Z,T) + \boldsymbol{B}_0, \tag{2.38}$$
$$P(\boldsymbol{X},T) = \tilde{P}(X,Z,T), \tag{2.39}$$
$$\rho(\boldsymbol{X},T) = \tilde{\rho}(X,Z,T). \tag{2.40}$$

We substitute (2.37)-(2.40) into (2.32)-(2.36) and linearise the results.

$$\nabla \cdot \tilde{\boldsymbol{U}} = 0, \tag{2.41}$$
$$\nabla \cdot \tilde{\boldsymbol{B}} = 0, \tag{2.42}$$
$$\frac{\partial \tilde{\boldsymbol{U}}}{\partial T} = -\frac{1}{\rho_0}\nabla \tilde{P} + \frac{\tilde{\rho}\boldsymbol{g}}{\rho_0} + \frac{\boldsymbol{B}_0 \cdot \nabla \tilde{\boldsymbol{B}}}{\mu_0 \rho_0}, \tag{2.43}$$
$$\frac{\partial \tilde{\rho}}{\partial T} = -\tilde{U}_Z \frac{\mathrm{d}\bar{\rho}}{\mathrm{d}Z}, \tag{2.44}$$
$$\frac{\partial \tilde{\boldsymbol{B}}}{\partial T} = \boldsymbol{B}_0 \cdot \nabla \tilde{\boldsymbol{U}}. \tag{2.45}$$

These are the equations satisfied by our plane wave solution.

So far, we have left the character of the plane wave solution unspecified. We now consider two simplifying cases for equations (2.41)-(2.45), each describing a particular type of wave. For each type of wave, we derive a dispersion relation as well as the phase and group velocity.

2.3.1 Alfvén Waves

In this section we look at the type of wave solution which arises when we remove any consideration of the effects of buoyancy and stratification from (2.41)-(2.45). This allows us to derive a dispersion relation, along with phase and group velocities pertinent to Alfvén waves. Our plane wave equations become

$$\nabla \cdot \tilde{\boldsymbol{U}} = 0, \tag{2.46}$$
$$\nabla \cdot \tilde{\boldsymbol{B}} = 0, \tag{2.47}$$
$$\frac{\partial \tilde{\boldsymbol{U}}}{\partial T} = -\frac{1}{\rho_0}\nabla \tilde{P} + \frac{\boldsymbol{B}_0 \cdot \nabla \tilde{\boldsymbol{B}}}{\mu_0 \rho_0}, \tag{2.48}$$
$$\frac{\partial \tilde{\boldsymbol{B}}}{\partial T} = \boldsymbol{B}_0 \cdot \nabla \tilde{\boldsymbol{U}}. \tag{2.49}$$

Dispersion Relation

Assuming modal solutions of the form

$$\tilde{F}(X,Z,T) = F_W \exp(i\boldsymbol{K}\cdot\boldsymbol{X} - i\omega T) \quad \text{for} \quad F \in \{\boldsymbol{U}, \boldsymbol{B}, P\},$$

where $\boldsymbol{K} := (K_X, 0, K_Z)$ is the *wavevector* and ω is the *angular frequency* of the wave, we get the following from equations (2.46)-(2.49).

$$\begin{aligned}
\boldsymbol{K} \cdot \tilde{\boldsymbol{U}} &= 0, \\
\boldsymbol{K} \cdot \tilde{\boldsymbol{B}} &= 0, \\
\omega \tilde{\boldsymbol{U}} &= \frac{\tilde{P}\boldsymbol{K}}{\rho_0} - \frac{(\boldsymbol{K} \cdot \boldsymbol{B}_0)\tilde{\boldsymbol{B}}}{\mu_0 \rho_0}, \\
\omega \tilde{\boldsymbol{B}} &= -(\boldsymbol{K} \cdot \boldsymbol{B}_0)\tilde{\boldsymbol{U}}.
\end{aligned}$$

These can be combined to give the dispersion relation for Alfvén waves.

$$\omega(\boldsymbol{K}) = \pm \frac{\boldsymbol{K} \cdot \boldsymbol{B}_0}{\sqrt{\mu_0 \rho_0}}. \tag{2.50}$$

Phase and Group Velocities

The phase velocity of a wave $\boldsymbol{c}_p$ represents the velocity at which individual wave crests propagate. The group velocity $\boldsymbol{c}_g$ represents the velocity at which a wave packet propagates. We calculate $\boldsymbol{c}_p$ and $\boldsymbol{c}_g$ for pure Alfvén waves using dispersion relation (2.50):

$$\boldsymbol{c}_p = \pm \frac{(\boldsymbol{K} \cdot \boldsymbol{B}_0)\boldsymbol{K}}{K^2 \sqrt{\mu_0 \rho_0}}, \quad \boldsymbol{c}_g = \pm \frac{\boldsymbol{B}_0}{\sqrt{\mu_0 \rho_0}}, \tag{2.51}$$

where $K := \sqrt{K_X^2 + K_Z^2}$ is the norm of the plane wavevector. In the study of Alfvén waves, the *Alfvén velocity* $\boldsymbol{V_A}$ is the name given to the positive root for the group velocity:

$$\boldsymbol{V_A} := \frac{\boldsymbol{B}_0}{\sqrt{\mu_0 \rho_0}}. \tag{2.52}$$

The norm V_A of the Alfvén velocity $\boldsymbol{V}_A$ is called the *Alfvén speed*. These results have several important physical implications.

1. The speed at which wave crests propagate is at its maximum when the wavevector $\boldsymbol{K}$ is aligned with the background magnetic field $\boldsymbol{B}_0$.
2. The equations $\boldsymbol{K} \cdot \tilde{\boldsymbol{U}} = 0$ and $\boldsymbol{K} \cdot \tilde{\boldsymbol{B}} = 0$ imply that fluid motions and magnetic field perturbations are perpendicular to the wavevector. The waves are therefore transverse.
3. The direction of energy propagation by Alfvén waves follows the trajectory of the magnetic field lines.
4. The group velocity is constant for Alfvén waves (rather than being a function of $\boldsymbol{K}$).

To plot (2.51) numerically, we can express the dimensionless phase and group velocities for Alfvén waves in terms of θ and ζ alone:

$$\boldsymbol{c}_p / V_A = (\cos\theta \cos\zeta + \sin\theta \sin\zeta)(\hat{\boldsymbol{X}} \cos\theta + \hat{\boldsymbol{Z}} \sin\theta), \tag{2.53}$$

$$\boldsymbol{c}_g / V_A = \hat{\boldsymbol{X}} \cos\zeta + \hat{\boldsymbol{Z}} \sin\zeta. \tag{2.54}$$

Results (1), (3) and (4) can be visualised in Figure 2.3, where we plot the phase speed and group speed as a function of the orientation of the plane wavevector and also plot the phase and group velocity parametrically in (X, Z)-space using (2.54). The group speed c_g is a circle in Figure 2.3 because the group velocity has the same magnitude for all wavevector orientations. However, the group velocity $\boldsymbol{c}_g$ is just a point because the direction of the group velocity is independent of the wave orientation. Figure 2.3 is inspired by similar plots produced by Priest (2014).

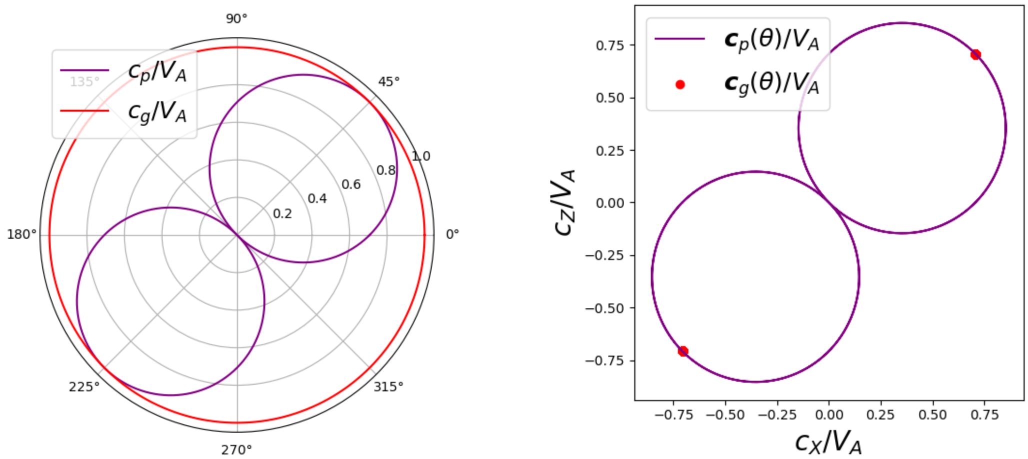

Figure 2.3: (Left) Dimensionless phase speed c_p/V_A and dimensionless group speed c_g/V_A as a function of wave propagation angle θ for pure Alfvén waves, with $\theta \in [0, 2\pi)$. (Right) Dimensionless phase velocity $\boldsymbol{c}_p(\theta)/V_A$ and dimensionless group velocity $\boldsymbol{c}_g(\theta)/V_A$ plotted as parametric curves for $\theta \in [0, 2\pi)$ for pure Alfvén waves. Magnetic field orientation: $\zeta = \pi/4$.

2.3.2 Internal Gravity Waves

We now discuss the mathematical properties of internal gravity waves, covering their dispersion relation, phase velocity and group velocity. To do so, we first derive an important physical quantity related to the frequency of internal gravity waves.

Derivation of the Buoyancy Frequency for a Boussinesq Fluid

In Chapter 1 we introduced the buoyancy frequency N as the theoretical maximum frequency at which internal gravity waves can propagate. We now derive its formula using a fluid parcel argument. It should be stressed that this derivation only applies in an incompressible fluid, or under the Boussinesq approximation. Consider a stably-stratified fluid at rest. We denote the static vertical variation in density by $\bar{\rho}(Z)$. Within this fluid, we consider a fluid parcel with a fixed volume which is initially at height Z_0. We suppose that this parcel is displaced to a height of Z_1. We define the density of the parcel at its initial position as $\rho_0 := \bar{\rho}(Z_0)$ and the density of the surrounding fluid at its new position as $\rho_1 := \bar{\rho}(Z_1)$. We define the size of the displacement as

$$\delta := Z_1 - Z_0.$$

We demand that $\delta \ll H_{\bar{\rho}}$. According to Newton's second law, the buoyancy force per unit volume F experienced by the parcel is equal to its initial density multiplied by its acceleration. Newton's second law can be expressed as

$$F = \rho_0 \frac{\mathrm{d}^2\delta}{\mathrm{d}T^2}. \tag{2.55}$$

According to Archimedes' principle, the buoyancy force per unit volume experienced by the parcel is given by

$$F := g(\rho_1 - \rho_0). \tag{2.56}$$

Equating expressions (2.55) and (2.56) for F gives

$$\rho_0 \frac{\mathrm{d}^2\delta}{\mathrm{d}T^2} = g(\rho_1 - \rho_0). \tag{2.57}$$

We expand $\bar{\rho}(Z)$ as a Taylor series centred at $Z = Z_0$:

$$\bar{\rho}(Z) = \bar{\rho}(Z_0) + (Z - Z_0)\bar{\rho}'(Z_0) + O[(Z - Z_0)^2]. \tag{2.58}$$

If we evaluate Taylor series (2.58) at $Z = Z_1$ then we get

$$\rho_1 = \rho_0 + \bar{\rho}'(Z_0)\delta + O(\delta^2). \tag{2.59}$$

Substituting (2.59) into (2.55) yields

$$\rho_0 \frac{\mathrm{d}^2\delta}{\mathrm{d}T^2} = g\bar{\rho}'(Z_0)\delta + O(\delta^2). \tag{2.60}$$

We define the following important quantity:

$$N_0^2 := -g\bar{\rho}'(Z_0)/\rho_0.$$

To leading order in δ, equation (2.60) then reads

$$\frac{\mathrm{d}^2\delta}{\mathrm{d}T^2} + N_0^2\delta = 0. \tag{2.61}$$

The fluids we consider are stably-stratified, so $\bar{\rho}'(Z_0) < 0$ and hence $N_0^2 > 0$. This means that ODE (2.61) represents simple harmonic motion with angular frequency N_0. The frequency N_0 applies at the particular height $Z = Z_0$. We can generalise this to obtain a formula for the buoyancy frequency at any height Z under the Boussinesq approximation:

$$N(Z) := \sqrt{-\frac{g}{\bar{\rho}}\frac{\mathrm{d}\bar{\rho}}{\mathrm{d}Z}}. \tag{2.62}$$

This is the theoretical maximum frequency at which propagating internal gravity waves can oscillate in a Boussinesq fluid. In this thesis, $\bar{\rho}'(Z)$ is constant and it is sufficient to use a constant reference density ρ_0 in place of $\bar{\rho}$, since vertical variations in density are treated as small.

We instead use a constant buoyancy frequency

$$N := \sqrt{-\frac{g}{\rho_0}\frac{\mathrm{d}\bar{\rho}}{\mathrm{d}Z}}. \tag{2.63}$$

In addition to the significance already discussed, the buoyancy frequency can be interpreted as a measure of the mean stratification in the fluid in cases where $N^2 > 0$ and the Schwarzschild criterion for convective stability is satisfied. More precisely, it is the square root of the vertical gradient of the mean potential buoyancy of the fluid when $N^2 > 0$ (Sutherland, 2010). This interpretation of the buoyancy frequency does not apply in the case $N^2 < 0$.

Dispersion Relation

We now derive a dispersion relation for pure internal gravity waves. Since pure internal gravity waves are restored by buoyancy only (with no contribution from magnetic tension), we remove the magnetic contributions from equations (2.41)-(2.45). This yields

$$\begin{aligned}\nabla \cdot \tilde{\boldsymbol{U}} &= 0,\\ \frac{\partial \tilde{\boldsymbol{U}}}{\partial T} &= -\frac{1}{\rho_0}\nabla \tilde{P} + \frac{\tilde{\rho}\boldsymbol{g}}{\rho_0},\\ \frac{\partial \tilde{\rho}}{\partial T} &= -\tilde{U}_Z \frac{\mathrm{d}\bar{\rho}}{\mathrm{d}Z}.\end{aligned}$$

Again assuming modal solutions of the form $\tilde{F}(X,Z,T) = F_W \exp(i\boldsymbol{K}\cdot\boldsymbol{X} - i\omega T)$, these become

$$\begin{aligned}\boldsymbol{K}\cdot\tilde{\boldsymbol{U}} &= 0,\\ \omega\tilde{\boldsymbol{U}} &= \frac{\tilde{P}\boldsymbol{K}}{\rho_0} + \frac{i\tilde{\rho}\boldsymbol{g}}{\rho_0},\\ \omega\tilde{\rho} &= -i\tilde{U}_Z\frac{\mathrm{d}\bar{\rho}}{\mathrm{d}Z}.\end{aligned}$$

These can be combined to give

$$\left[\omega^2(K_X^2 + K_Z^2) + \frac{gK_X^2}{\rho_0}\frac{\mathrm{d}\bar{\rho}}{\mathrm{d}Z}\right]\tilde{U}_Z = 0. \tag{2.64}$$

This motivates the inclusion of the buoyancy frequency N, given by (2.63).

Equipped with the buoyancy frequency, we can extract the dispersion relation for internal gravity waves from equation (2.64):

$$\omega(\boldsymbol{K}) = \pm\frac{NK_X}{K}, \tag{2.65}$$

where $K := \sqrt{K_X^2 + K_Z^2}$ is the norm of the plane wavevector.

The buoyancy frequency is physically significant because it serves as an upper bound for the angular frequency ω at which propagation of internal gravity waves is permissible. Mathematically, dispersion relation (2.65) demands that $|\omega| \leq |N|$ for propagating internal gravity waves.

Evanescent Waves

What if $|\omega| > |N|$? Consider the following rearranged form of dispersion relation (2.65).

$$K_Z^2 = K_X^2\left(\frac{N^2}{\omega^2} - 1\right). \tag{2.66}$$

If we suppose that $K_X \in \mathbb{R}$, then if $|\omega| > |N|$, (2.66) implies that K_Z is purely imaginary. We can thus rewrite our modal solution form as

$$F(X,Z,T) = F_W \exp(-\lambda Z)\exp(iK_X - i\omega T), \tag{2.67}$$

where $\lambda := iK_Z$ (so $\lambda \in \mathbb{R}$). To ensure that the solution (2.67) makes sense physically, we must have $\lambda Z > 0$. The resulting modal solution form (2.67) exhibits exponential decay in space. Such disturbances are known as *evanescent*. If instead we had assumed that $K_Z \in \mathbb{R}$ together with $|\omega| > |N|$, then we would have obtained an exponentially decaying solution in X (Sutherland, 2010). Table 2.2 summarises the two regimes for internal gravity waves with frequency ω:

Frequency Range	Regime	Behaviour
$\lvert\omega\rvert \leq \lvert N\rvert$	Propagating	Purely oscillatory
$\lvert\omega\rvert > \lvert N\rvert$	Evanescent	Oscillatory with spatial exponential decay

Table 2.2: Regimes for internal gravity waves.

An example of a situation in which evanescent IGWs can arise is the interior of a solar-type star. IGWs propagate through the radiative zone, where $|\omega| \leq |N|$ is likely to be locally satisfied. These IGWs can pass into the convective zone, where the local value of $|N^2|$ is much smaller than anywhere in the radiative zone. $|\omega| \leq |N|$ is unlikely to be satisfied for IGWs in the convective zone, so we expect IGWs to be evanescent.

Dispersion Relation in Terms of Wavevector Orientation

We define θ to be the angle the wavevector $\boldsymbol{K}$ makes with the positive X axis in the (X, Z)-plane. Using basic trigonometric arguments, it is easy to deduce that

$$\omega^2 = N^2 \cos^2 \theta. \tag{2.68}$$

This means that for internal gravity waves, the angular frequency is dependent only on the direction of $\boldsymbol{K}$ (and not on its magnitude). Equation (2.68) was first found by Rayleigh (1883). We can see that for each pair (ω, N), there are four distinct solutions for θ in the interval $[0, 2\pi)$ admitted by (2.68).

Phase and Group Velocities

Let us now take a look at the phase velocity $\boldsymbol{c}_p$ and the group velocity $\boldsymbol{c}_g$ associated with internal gravity waves. From dispersion relation (2.65) we obtain

$$\boldsymbol{c}_p = \pm \frac{NK_X}{K^3}\boldsymbol{K}, \quad \boldsymbol{c}_g = \pm \frac{NK_Z}{K^3}\boldsymbol{K}_P, \tag{2.69}$$

where $\boldsymbol{K}_P := K_Z\hat{\boldsymbol{X}} - K_X\hat{\boldsymbol{Z}}$ is the vector confined to the (X, Z)-plane which is perpendicular to the wavevector $\boldsymbol{K} := K_X\hat{\boldsymbol{X}} + K_Z\hat{\boldsymbol{Z}}$. From (2.69) we observe an important property of internal gravity waves: $\boldsymbol{c}_p \cdot \boldsymbol{c}_g = 0$. The physical significance of this is that in the case of pure internal gravity waves, the direction in which wave crests propagate is always exactly perpendicular to the direction in which energy propagates.

Since $K_X/K = \cos\theta$ and $K_Z/K = \sin\theta$, we can alternatively express the phase and group velocity in terms of θ alone. The parametric representation of the dimensionless phase and group velocity is given by

$$(K/N)\boldsymbol{c}_p(\theta) = \cos^2\theta\hat{\boldsymbol{X}} + \sin\theta\cos\theta\hat{\boldsymbol{Z}}, \quad (K/N)\boldsymbol{c}_g(\theta) = \sin^2\theta\hat{\boldsymbol{X}} - \sin\theta\cos\theta\hat{\boldsymbol{Z}}. \tag{2.70}$$

In Figure 2.4 we plot the dimensionless forms of c_p, c_g, $\boldsymbol{c}_p$ and $\boldsymbol{c}_g$ as a function of θ according to (2.70). Figure 2.4 is consistent with the property $\boldsymbol{c}_p \cdot \boldsymbol{c}_g = 0$ in the sense that the points at which the phase and group speeds reach their respective maxima are separated by an angle of $\pi/2$.

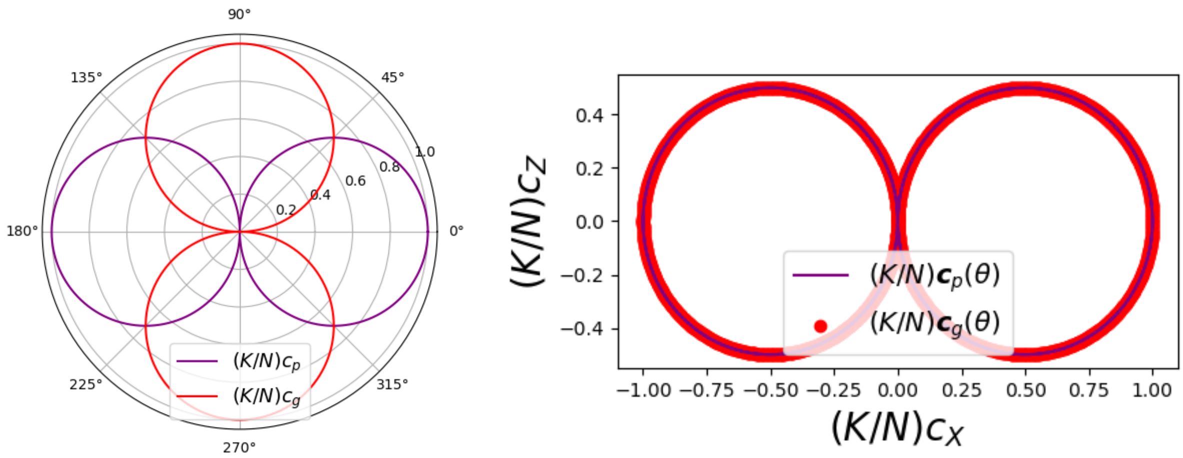

Figure 2.4: (Left) Dimensionless phase speed $(K/N)c_p$ and dimensionless group speed $(K/N)c_g$ as a function of wave propagation angle θ for pure internal gravity waves, with $\theta \in [0, 2\pi)$. (Right) Dimensionless phase velocity $(K/N)\boldsymbol{c}_p(\theta)$ and dimensionless group velocity $(K/N)\boldsymbol{c}_g(\theta)$ plotted as parametric curves for $\theta \in [0, 2\pi)$ for pure internal gravity waves.

The St Andrews Cross

If a cylinder oscillates in the direction of gravity at a fixed frequency ω in a stably-stratified fluid with constant buoyancy frequency N, we observe the *St Andrews cross*. This is a phenomenon in which four internal wave beams are generated, with each wave beam corresponding to one of the four solutions for θ in the range $[0, 2\pi)$ satisfying dispersion relation (2.68). Each beam only spans a finite width extending outwards from the position of the oscillating cylinder. The length of the finite width depends on the radius of the cylinder. The St Andrews cross was first created experimentally by Mowbray and Rarity (1967a,b). An experimental realisation of the St Andrews cross is shown in Figure 2.5.

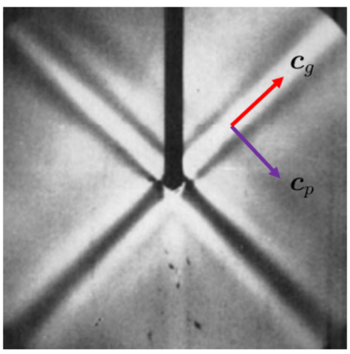

Figure 2.5: Formation of the St Andrews cross from a laboratory experiment, augmented with the directions of the phase velocity $\boldsymbol{c}_p$ and the group velocity $\boldsymbol{c}_g$. Image credit: Mowbray and Rarity (1967b).

2.3.3 Alfvén-Gravity Waves

We have looked at both pure internal gravity waves and pure Alfvén waves each in isolation. We are also interested in what happens when we combine the two, i.e. when we consider what are known as *Alfvén-gravity waves* (AGWs). As mentioned in Chapter 1, these waves have been studied in previous work, sometimes under the name *magnetogravity waves*. Studying AGWs is interesting from a purely theoretical perspective, but also in terms of our applications of interest. The combination of stable stratification and magnetism appears in various parts of stellar and planetary interiors.

Dispersion Relation

A dispersion relation can be generated pertinent to Alfvén-gravity waves using the linearised algebraic equations (2.41)-(2.45), this time maintaining both the buoyancy term and the magnetic terms. The modal solution form $\tilde{F} = F_W \exp(i\boldsymbol{K}\cdot\boldsymbol{X} - i\omega T)$ converts (2.41)-(2.45) to

$$\boldsymbol{K}\cdot\tilde{\boldsymbol{U}} = 0, \tag{2.71}$$

$$\boldsymbol{K}\cdot\tilde{\boldsymbol{B}} = 0, \tag{2.72}$$

$$\omega\tilde{\boldsymbol{U}} = \frac{\tilde{P}\boldsymbol{K}}{\rho_0} + \frac{i\tilde{\rho}\boldsymbol{g}}{\rho_0} - \frac{(\boldsymbol{K}\cdot\boldsymbol{B}_0)\tilde{\boldsymbol{B}}}{\mu_0\rho_0}, \tag{2.73}$$

$$\omega\tilde{\rho} = -i\tilde{U}_Z\frac{\mathrm{d}\bar{\rho}}{\mathrm{d}Z}, \tag{2.74}$$

$$\omega\tilde{\boldsymbol{B}} = -(\boldsymbol{K}\cdot\boldsymbol{B}_0)\tilde{\boldsymbol{U}}. \tag{2.75}$$

The fact that $\boldsymbol{B}_0$ only appears in the equations as part of the $\boldsymbol{K}\cdot\boldsymbol{B}_0$ scalar product explains why we can describe all plane wave solutions in this system without needing to specify a value for ξ. It is only the component of $\boldsymbol{B}_0$ which is proportional to $\boldsymbol{K}$ which matters in these equations. Since $\boldsymbol{K}$ is confined to the (X, Z)-plane, we not need to consider the Y-component of $\boldsymbol{B}_0$ in the equations describing plane waves.

We can assemble a 5×5 eigenvalue problem in terms of eigenvalue ω from equations (2.71)-(2.75). To do so, we must eliminate two of the seven equations. We do this by taking $\boldsymbol{K}\cdot$(2.73), which makes use of (2.71) and (2.72) to yield

$$\tilde{P} = ig\frac{K_Z}{K^2}\tilde{\rho}. \tag{2.76}$$

Both divergence-free constraints (2.71) and (2.72) are thus encapsulated by (2.76). We use (2.76) to replace $\tilde{P}$ with $\tilde{\rho}$ in (2.73). In matrix form, equations (2.73)-(2.75) then appear as the following closed system:

$$\begin{pmatrix} \omega & 0 & \frac{\boldsymbol{K}\cdot\boldsymbol{B}_0}{\mu_0\rho_0} & 0 & -\frac{igK_XK_Z}{\rho_0K^2} \\ 0 & \omega & 0 & \frac{\boldsymbol{K}\cdot\boldsymbol{B}_0}{\mu_0\rho_0} & \frac{igK_X^2}{\rho_0K^2} \\ \boldsymbol{K}\cdot\boldsymbol{B}_0 & 0 & \omega & 0 & 0 \\ 0 & \boldsymbol{K}\cdot\boldsymbol{B}_0 & 0 & \omega & 0 \\ 0 & i\frac{\mathrm{d}\bar{\rho}}{\mathrm{d}Z} & 0 & 0 & \omega \end{pmatrix} \begin{pmatrix} \tilde{U}_X \\ \tilde{U}_Z \\ \tilde{B}_X \\ \tilde{B}_Z \\ \tilde{\rho} \end{pmatrix} = 0. \tag{2.77}$$

In the 3D analogue of matrix problem (2.77), $\tilde{U}_Y$ and $\tilde{B}_Y$ are decoupled from the other variables.

We could equally have solved a 6×6 system with $\tilde{P}$ as an additional component of the vector. We choose to eliminate $\tilde{P}$ for the sake of cleanliness. For non-trivial solutions, we require the determinant of the matrix in (2.77) to vanish.

This amounts to a quintic dispersion relation governing our full system:

$$\omega\left[\omega^2-\frac{(\boldsymbol{K}\cdot\boldsymbol{B}_0)^2}{\mu_0\rho_0}\right]\left[\omega^2-\frac{N^2K_X^2}{K^2}-\frac{(\boldsymbol{K}\cdot\boldsymbol{B}_0)^2}{\mu_0\rho_0}\right]=0. \tag{2.78}$$

The full dispersion relation for this problem is thus split into a zero-frequency branch, a lower-frequency branch (corresponding to two pure Alfvén waves) and a higher frequency branch (corresponding to two mixed Alfvén-gravity waves). In the case where $N \ll KV_A$, the non-zero frequency branches have comparable frequencies.

This is a significant result in that by introducing a magnetic field into the problem, we move from a system with just two distinct wave solutions (two pure internal gravity waves) to one with four distinct wave solutions (two pure Alfvén waves and two hybrid Alfvén-gravity waves) and one zero-frequency solution. We can expect this to diversify the range of resonant interactions possible when analysing wave instabilities.

The higher frequency branch corresponds to the dispersion relation for hybrid Alfvén-gravity waves:

$$\omega(\boldsymbol{K})=\pm\sqrt{\frac{N^2K_X^2}{K^2}+\frac{(\boldsymbol{K}\cdot\boldsymbol{B}_0)^2}{\mu_0\rho_0}}. \tag{2.79}$$

Observe that if the magnetic field $\boldsymbol{B}$ is set to zero, (2.79) becomes the dispersion relation for internal gravity waves. Conversely, if the magnetic field is non-zero but the buoyancy frequency N is set to zero instead, we recover the dispersion relation for Alfvén waves.

In the work to come, we shall refer to the positive roots (chosen arbitrarily) for the internal gravity wave dispersion relation and the Alfvén wave dispersion relation as

$$\omega_G(\boldsymbol{K}):=\frac{NK_X}{K} \quad \text{and} \quad \omega_A(\boldsymbol{K}):=\frac{\boldsymbol{K}\cdot\boldsymbol{B}_0}{\sqrt{\mu_0\rho_0}}. \tag{2.80}$$

We can introduce a dimensionless form of the magnetic field strength b_0:

$$b_0:=\frac{KB_0}{N\sqrt{\mu_0\rho_0}}. \tag{2.81}$$

We then can write the dimensionless form of ω for the higher frequency branch parametrically in terms of b_0, θ and ζ alone using equations (2.28),(2.29) and (2.81):

$$\frac{\omega(\theta,\zeta)}{N}=\pm\sqrt{\cos^2\theta+b_0^2(\cos\theta\cos\zeta+\sin\theta\sin\zeta)^2}. \tag{2.82}$$

Pure Alfvén Waves

The lower frequency branch corresponds to the dispersion relation for pure Alfvén waves. Does it make sense physically for pure Alfvén waves to exist in a system with density stratification? It can be shown that pure Alfvén waves can only exist in a system with density stratification in the Z direction if their velocity and magnetic field vectors are confined to the (X, Y)-plane, i.e. if they are perpendicular to the direction of gravity, and if their pressure and density do not oscillate. To demonstrate this, we substitute (2.75) into (2.73) to get

$$\left[\omega^2 - \frac{(\boldsymbol{K}\cdot\boldsymbol{B}_0)^2}{\mu_0\rho_0}\right]\tilde{\boldsymbol{U}} = \frac{\tilde{P}\boldsymbol{K}}{\rho_0} + \frac{i\tilde{\rho}\boldsymbol{g}}{\rho_0}. \tag{2.83}$$

If we substitute the pure Alfvén wave dispersion relation (2.50) into (2.83), the components of (2.83) become

$$K_X\tilde{P} = 0, \quad K_Z\tilde{P} = ig\tilde{\rho}. \tag{2.84}$$

Equations (2.84) must be true for *any* primary Alfvén wave we consider, i.e. for any wavevector $\boldsymbol{K}$. Hence we must have $\tilde{P} = 0$ for pure Alfvén waves. From equation (2.76) it is then clear that $\tilde{\rho} = 0$. It then follows from (2.74) that $\tilde{U}_Z = 0$ and then from (2.75) that $\tilde{B}_Z = 0$. So the velocities and magnetic fields of any pure Alfvén waves in the system must be horizontally oscillating (i.e. oscillations must be confined to the (X, Y)-plane). Their pressure and density must also not oscillate.

An important question here was whether it was plausible to have waves which disregard buoyancy entirely (like Alfvén waves) existing in a system with density stratification. The existence of such waves is indeed physically plausible if their oscillations are perpendicular to the direction of gravity. However, it is important to recognise that these are not dynamically equivalent to the pure Alfvén waves we would observe in a system devoid of density stratification. In such a system, the velocity and magnetic field oscillations may have a non-zero Z-component.

Phase and Group Velocities

To understand some of the fundamental properties of Alfvén-gravity waves, we use dispersion relation (2.79) to find expressions for the phase velocity $\boldsymbol{c}_p$ and the group velocity $\boldsymbol{c}_g$.

$$\boldsymbol{c}_p = \frac{\boldsymbol{K}\omega(\boldsymbol{K})}{K^2}, \quad \boldsymbol{c}_g = \frac{1}{\omega(\boldsymbol{K})}\left[\frac{N^2K_XK_Z}{K^4}\boldsymbol{K}_P + \frac{(\boldsymbol{K}\cdot\boldsymbol{B}_0)}{\mu_0\rho_0}\boldsymbol{B}_0\right], \tag{2.85}$$

where $\omega(\boldsymbol{K})$ is given by formula (2.79). In the absence of a background magnetic field $\boldsymbol{B}_0$, (2.85) reduce to the familiar phase and group velocities for internal gravity waves. In the absence of stratification, (2.85) reduce to the familiar phase and group velocities for Alfvén waves.

In the previous section we discussed the important property $\boldsymbol{c}_p \cdot \boldsymbol{c}_g = 0$ of internal gravity waves i.e. that the phase and group velocities are perpendicular. Note that this property is not preserved upon the inclusion of a magnetic field. In other words, for Alfvén-gravity waves, the phase velocity is not necessarily perpendicular to the group velocity.

To plot these quantities, we use the dimensionless forms expressed parametrically in terms of θ and ζ:

$$\frac{K}{N}\boldsymbol{c}_p(\theta,\zeta) = \frac{\omega(\theta,\zeta)}{N}(\hat{\boldsymbol{X}}\cos\theta + \hat{\boldsymbol{Z}}\sin\theta),$$
$$\frac{K}{N}\boldsymbol{c}_g(\theta,\zeta) = \frac{N}{\omega(\theta,\zeta)}\left[\cos\theta\sin\theta(\hat{\boldsymbol{X}}\sin\theta - \hat{\boldsymbol{Z}}\cos\theta) + b_0^2(\cos\theta\cos\zeta + \sin\theta\sin\zeta)\right],$$

where $\omega(\theta, \zeta)$ is given by formula (2.82). In Figures 2.6 and 2.7 we plot the dimensionless magnitudes of the phase velocity and group velocity as a function of θ for Alfvén-gravity waves. In Figures 2.8 and 2.9 we plot the dimensionless phase velocity and group velocity as parametric curves for $\theta \in [0, 2\pi)$. We demonstrate this for a range of different magnetic field strengths b_0 and orientations ζ. We find that an increase in field strength b_0 is met with a similar increase in the values of both c_p and c_g maximised over θ. We also find that the orientations of c_p and c_g rotate as we change the orientation ζ of the background magnetic field. Figures 2.6, 2.7, 2.8 and 2.9 are novel.

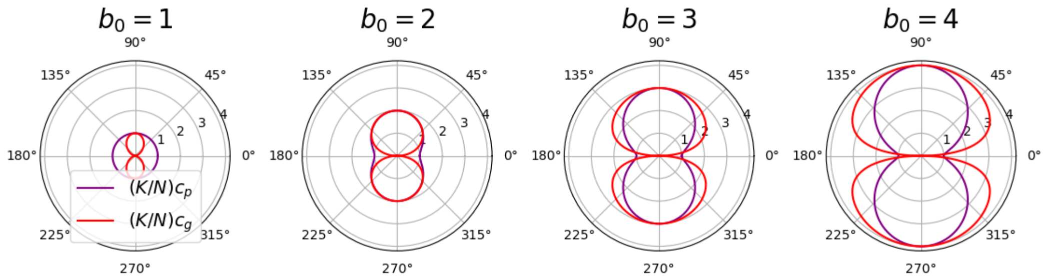

Figure 2.6: Dimensionless phase speed $(K/N)c_p$ and dimensionless group speed $(K/N)c_g$ as a function of θ for AGWs. Plotted for magnetic fields with orientation $\zeta = \pi/2$ and a selection of different magnetic field strengths b_0.

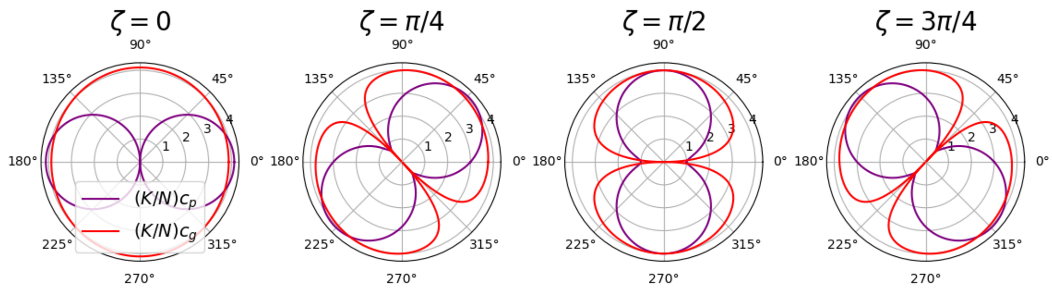

Figure 2.7: Dimensionless phase speed $(K/N)c_p$ and dimensionless group speed $(K/N)c_g$ as a function of θ for AGWs. Plotted for magnetic fields with strength $b_0 = 4$ and a selection of different magnetic field orientations ζ.

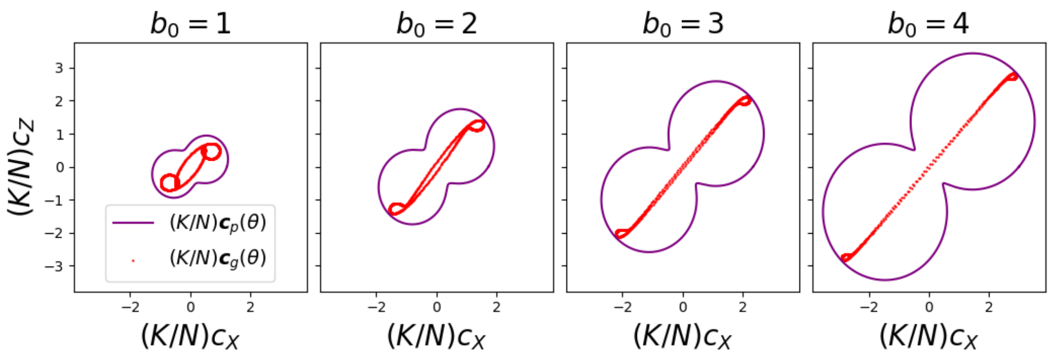

Figure 2.8: Dimensionless phase velocity $(K/N)\boldsymbol{c}_p(\theta)$ and dimensionless group velocity $(K/N)\boldsymbol{c}_g(\theta)$ plotted as parametric curves with parameter $\theta \in [0, 2\pi)$ for AGWs. Plotted for magnetic fields with orientation $\zeta = \pi/4$ and a selection of different magnetic field strengths b_0.

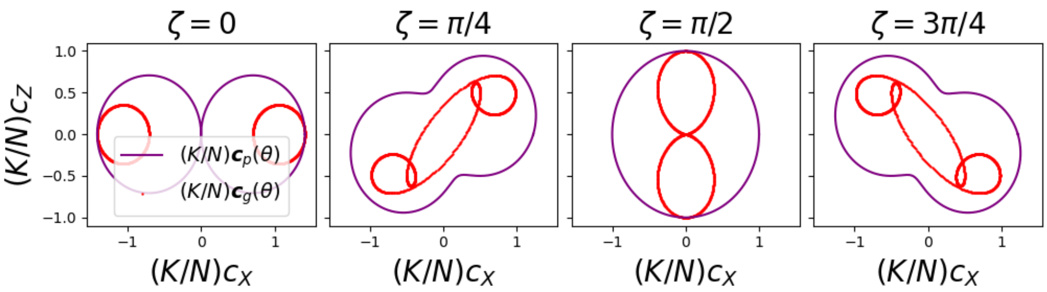

Figure 2.9: Dimensionless phase velocity $(K/N)\boldsymbol{c}_p(\theta)$ and dimensionless group velocity $(K/N)\boldsymbol{c}_g(\theta)$ plotted as parametric curves with parameter $\theta \in [0, 2\pi)$ for AGWs. Plotted for magnetic fields with strength $b_0 = 1$ and a selection of different magnetic field orientations ζ.

2.3.4 Damped Oscillations

Diffusive Dispersion Relation

Despite the fact that Re is typically large in astrophysical settings, it is interesting to determine how viscosity and thermal diffusion influence the dispersion relation for internal gravity waves. How are the complex frequencies of the solutions modified by viscosity and thermal diffusion? We want to determine decay rates for perturbations under the influence of diffusion. We will compute this decay rate numerically for pure internal gravity waves in Chapter 4, so our results here will provide a means of verifying our implementation later.

Internal Gravity Waves

We start from the linearised Boussinesq equations in the absence of a magnetic field, this time incorporating the effects of diffusion. The system is

$$\begin{aligned}
\nabla \cdot \tilde{\boldsymbol{U}} &= 0, \\
\frac{\partial \tilde{\boldsymbol{U}}}{\partial T} &= \nu \nabla^2 \tilde{\boldsymbol{U}} - \frac{1}{\rho_0} \nabla \tilde{P} + \frac{\tilde{\rho} \boldsymbol{g}}{\rho_0}, \\
\frac{\partial \tilde{\rho}}{\partial T} &= \kappa \nabla^2 \tilde{\rho} - \tilde{U}_Z \frac{\mathrm{d}\bar{\rho}}{\mathrm{d}Z}.
\end{aligned}$$

If we write

$$\tilde{F}(\boldsymbol{X}, T) = F_W \exp(i\boldsymbol{K} \cdot \boldsymbol{X} - i\omega T),$$

these equations become

$$\boldsymbol{K} \cdot \boldsymbol{U}_W = 0, \tag{2.86}$$

$$\omega \boldsymbol{U}_W = -i\nu K^2 \boldsymbol{U}_w + \frac{P_w \boldsymbol{K}}{\rho_0} + \frac{i\rho_W \boldsymbol{g}}{\rho_0}, \tag{2.87}$$

$$\omega \rho_W = -i\kappa K^2 \rho_W - iU_{WZ} \frac{\mathrm{d}\bar{\rho}}{\mathrm{d}Z}. \tag{2.88}$$

Taking $\boldsymbol{K} \cdot$ (2.87) eliminates pressure via

$$P_W = \frac{igK_Z \rho_w}{K^2}.$$

The equations are thus

$$(\omega + i\nu K^2)\boldsymbol{U}_W = \frac{ig\rho_w}{\rho_0}\left(\frac{K_Z}{K^2}\boldsymbol{K} - \hat{\boldsymbol{Z}}\right),$$
$$(\omega + i\kappa K^2)\rho_W = -iU_{WZ}\frac{\mathrm{d}\bar{\rho}}{\mathrm{d}Z}.$$

In matrix form these appear as

$$\begin{pmatrix} \omega + i\nu K^2 & 0 & -igK_X K_Z/(\rho_0 K^2) \\ 0 & \omega + i\nu K^2 & igK_X^2/(\rho_0 K^2) \\ 0 & i\partial_Z \bar{\rho} & \omega + i\kappa K^2 \end{pmatrix} \begin{pmatrix} U_{WX} \\ U_{WZ} \\ \rho_W \end{pmatrix} = 0.$$

This determinant must vanish. The resulting dispersion relation is

$$(\omega + i\nu K^2)\left[(\omega + i\nu K^2)(\omega + i\kappa K^2) - N^2 K_X^2/K^2\right] = 0. \tag{2.89}$$

Dispersion Relation with Thermal Diffusion Only

We define the Prandtl number Pr as the ratio of viscosity to thermal diffusion, i.e. $\mathrm{Pr} := \nu/\kappa$. In the case where viscosity is negligible in comparison to thermal diffusion, which is relevant in stellar interiors where $\mathrm{Pr} \ll 1$, the dispersion relation (2.89) becomes

$$\omega\left[\omega^2 + i\omega\kappa K^2 - N^2 K_X^2/K^2\right] = 0.$$

This admits three solutions:

$$\omega = 0, \quad \omega = -i\kappa K^2/2 \pm 1/2\sqrt{-\kappa^2 K^4 + 4N^2 K_X^2/K^2}.$$

If we assume $\mathrm{Pe} \gg 1$ and maintain only the $O(\kappa)$ terms, then the non-zero solution reduces to

$$\omega = -i\kappa K^2/2 \pm NK_X/K. \tag{2.90}$$

The first term represents the linear decay rate due to thermal diffusion. It represents the deviation from the ideal frequency induced by thermal diffusion:

$$\omega = \omega_{\text{ideal}} - i\kappa K^2/2. \tag{2.91}$$

If we included a small non-zero viscosity ν also, the decay rate of the wave would be the arithmetic mean of the viscous and thermal decay rates. Equation (2.91) describes mathematically how IGWs damp due to diffusion as they propagate.

2.4 Criterion for Overturning

We now return to the full nonlinear system of governing equations (2.32)-(2.36). We seek a plane wave which solves the nonlinear system exactly, as opposed to just its linearised form. This allows us to study the linear stability of waves with any amplitude.

It is also useful to introduce some kind of parameter in the system which governs whether overturning takes place, i.e. whether at some location in the fluid the uniform stratification is disrupted in a way that reverses the negative vertical density gradient. The idea that overturning gets 'switched on' when internal gravity waves surpass a certain amplitude is well-established.

This threshold has an impact on wave instabilities; whether the amplitude reaches this threshold determines whether the wave breaks. By incorporating this threshold into the nonlinear solution we seek, we can specify whether the wave overturns.

It should be stressed that the amplitude reaching this threshold is not a requirement for instability, however. In Chapter 4, we show that ideal internal gravity waves are unstable for any wave amplitude.

We introduce this parameter in the form of the wave amplitude a. We want there to be some threshold value $a = a_c$ which separates waves that cannot produce overturning ($a < a_c$) from waves that can produce overturning ($a > a_c$).

To illustrate overturning, we define the dimensionless wave density $\tilde{\varrho}$ as

$$\tilde{\varrho} := -\frac{K_Z \tilde{\rho}}{\mathrm{d}\bar{\rho}/\mathrm{d}Z}. \tag{2.92}$$

A formula for ρ is derived later in this section. Figure 2.10 illustrates the onset of overturning as we transition from $a < a_c$ to $a > a_c$. Here, we take a grid of points (X, Z) in dimensionless spatial coordinates and plot the dimensionless wave density $\tilde{\varrho}$ using formula (2.92) for two values of a. One value of a satisfies $a < a_c$ and the other value satisfies $a > a_c$. For $a > a_c$, we observe localised overturning, i.e. points in space at which denser fluid sits directly on top of less dense fluid. We do not observe this when $a < a_c$.

We can choose a solution for which the nonlinear terms of the governing equations vanish identically. In §2.3.3 we supposed that plane wave solutions took the form $\tilde{F} = F_W \exp(i\boldsymbol{K} \cdot \boldsymbol{X} - i\omega T)$. Any plane wave solution for which the nonlinear terms vanish identically is also a solution of the linearised system (2.77). We are therefore free to choose one of the amplitudes F_W to be whatever we wish, and deduce the remaining amplitudes F_W from the chosen one using the linearised system (2.77). The formulae for F_W are sensible places to incorporate the parameter a in the problem. We choose our threshold to be $a_c = 1$ and choose the amplitude ρ_w in a way that allows $a > 1$ to correspond with the possibility of satisfying $\partial_z\breve{\rho} > 0$. This choice is maintained throughout the remainder of this thesis.

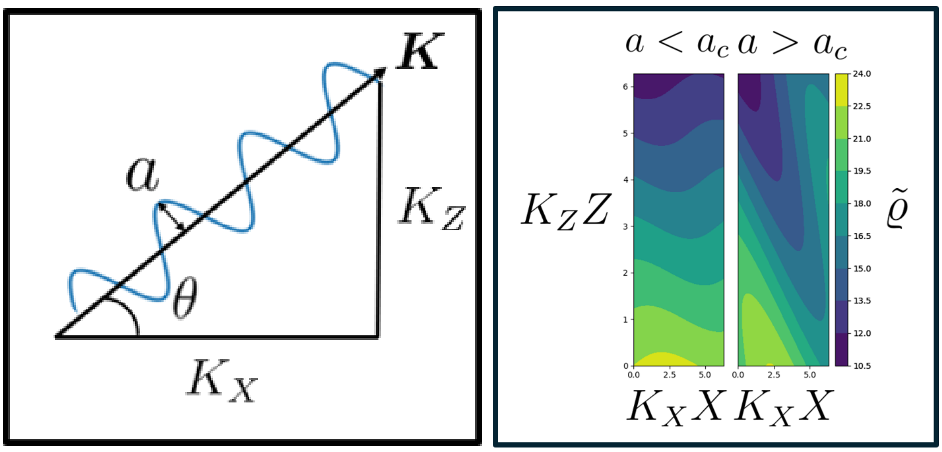

Figure 2.10: (Left) Schematic showing significance of amplitude parameter a and wave orientation θ. (Right) Onset of density overturning when crossing the threshold $a = a_c$, visualised by plotting dimensionless wave density (2.92) as a function of X and Z scaled by their respective wavevector components.

Choosing Eigenvector Amplitudes

We use a plane wave solution of the form

$$\tilde{F}(X, Z, T) = 2aF_W \exp(i\boldsymbol{K} \cdot \boldsymbol{X} - i\omega T) \quad \text{for} \quad F \in \{\boldsymbol{U}, \boldsymbol{B}, P, \rho\}. \tag{2.93}$$

The factor of 2 is introduced solely for algebraic convenience in later chapters. The matrix problem (2.77) gives us relations between the eigenvectors F_W, but how do we choose the magnitude of these eigenvectors? We choose them such that $a = 1$ represents the onset of static convective instability $\partial_Z \breve{\rho} = 0$. We will choose a value for ρ_W which allows us to satisfy the overturning criterion only when $a > 1$ and determine values for $\boldsymbol{U}_W$ and $\boldsymbol{B}_W$ from ρ_W using the relationships between the eigenvector components given by (2.77).

Real Solutions

For our solutions to make sense physically, we are interested in the real part of the plane wave solution. If we choose ρ_W to be purely imaginary, then the real part of $\tilde{\rho}$ must be

$$\Re[\tilde{\rho}] = 2ia\rho_W \sin(\boldsymbol{K} \cdot \boldsymbol{X} - \omega T). \tag{2.94}$$

Incorporating the Overturning Criterion

The criterion for overturning is

$$\frac{\partial \breve{\rho}}{\partial Z} = \frac{\mathrm{d}\bar{\rho}}{\mathrm{d}Z} + \frac{\partial \rho}{\partial Z} > 0. \tag{2.95}$$

If we consider the real plane wave solution (2.94) for ρ then (2.95) becomes

$$\frac{\mathrm{d}\bar{\rho}}{\mathrm{d}Z} + 2iaK_Z\rho_W \cos(\boldsymbol{K} \cdot \boldsymbol{X} - \omega T) > 0. \tag{2.96}$$

We want $a > 1$ to be a necessary condition for (2.96) to be satisfied. Since $\mathrm{d}_Z\bar{\rho} < 0$, (2.96) can only be satisfied if

$$2iaK_Z\rho_W > -\frac{\mathrm{d}\bar{\rho}}{\mathrm{d}Z}.$$

Thus, if we choose

$$\rho_W = \frac{i}{2K_Z}\frac{\mathrm{d}\bar{\rho}}{\mathrm{d}Z}, \tag{2.97}$$

then $a > 1$ is a necessary condition for (2.96) to be satisfied. We hence use (2.97) as our choice of plane wave eigenvector amplitude in this thesis. Using matrix problem (2.77), we can thus deduce the following expressions for the other eigenvectors. The resulting real plane wave solution we find is

$$\Re[\tilde{\boldsymbol{U}}(X, Z, T)] = 2a\boldsymbol{U}_W \cos(\boldsymbol{K} \cdot \boldsymbol{X} - \omega T), \tag{2.98}$$
$$\Re[\tilde{\boldsymbol{B}}(X, Z, T)] = 2a\boldsymbol{B}_W \cos(\boldsymbol{K} \cdot \boldsymbol{X} - \omega T), \tag{2.99}$$
$$\Re[\tilde{\rho}(X, Z, T)] = 2ia\rho_W \sin(\boldsymbol{K} \cdot \boldsymbol{X} - \omega T), \tag{2.100}$$

where the coefficients $\boldsymbol{U}_W, \boldsymbol{B}_W$ and ρ_W are given by

$$\boldsymbol{U}_W := \frac{\omega}{2}\left(\frac{\hat{\boldsymbol{X}}}{K_X} - \frac{\hat{\boldsymbol{Z}}}{K_Z}\right), \quad \boldsymbol{B}_W := \frac{\boldsymbol{K}\cdot\boldsymbol{B}_0}{2}\left(\frac{\hat{\boldsymbol{Z}}}{K_Z} - \frac{\hat{\boldsymbol{X}}}{K_X}\right), \quad \rho_W := \frac{i}{2K_Z}\frac{\mathrm{d}\bar{\rho}}{\mathrm{d}Z}. \quad (2.101)$$

We obtained (2.98)-(2.100) as solutions of the ideal linearised Boussinesq MHD equations (2.41)-(2.45). If we substitute (2.98)-(2.100) into the ideal nonlinear Boussinesq MHD equations (2.32)-(2.36), it can be shown that the nonlinear terms vanish identically. We show this in Appendix A.1.3. Equations (2.98)-(2.100) are therefore not just solutions of the linearised Boussinesq MHD equations, but in fact solutions of the nonlinear Boussinesq MHD equations too. This is a powerful result because it allows us to study the linear stability of waves with any amplitude by using (2.98)-(2.100) as a basic state.

The above argument is only valid for a monochromatic wave. In general, a superposition of two waves is not an exact solution of the ideal nonlinear Boussinesq MHD equations.

Summary

In this chapter we introduced the mathematical model and stated some physical contexts to which it can be applied. We introduced the fully compressible MHD equations and applied the Boussinesq approximation to eliminate the dynamics of acoustic waves. We acquired the Boussinesq MHD equations, which permit the existence of three kinds of wave: pure internal gravity waves, pure Alfvén waves and hybrid Alfvén-gravity waves. We then discussed some of the mathematical properties of each type of wave and included graphical representations of the phase speed, group speed, phase velocity and group velocity. These took the form of polar plots and parametric Cartesian curves. In the case of Alfvén-gravity waves, these plots constitute original work.

We will now study the stability of a single monochromatic wave, referred to as the *primary wave*. This is an exact solution to the ideal nonlinear Boussinesq MHD equations, to which we will subject small-amplitude disturbances. In Chapter 3, we assume that the amplitude of the primary wave is small and perform an asymptotic analysis of the triadic resonanance instability. In Chapter 4, we allow arbitrarily large primary wave amplitudes and perform linear stability analysis by constructing an algebraic eigenvalue problem from the Boussinesq MHD equations.

In Chapters 3 and 4, we remove the presence of a magnetic field entirely. Under these conditions, the governing equations permit only one type of wave: pure internal gravity waves. The primary wave is prescribed by only two parameters in this scenario: the dimensionless amplitude parameter a and the wavevector angle θ with respect to the positive X-axis. We reintroduce the background magnetic field in Chapters 5 and 6. In these chapters, the primary wave is additionally prescribed by the background magnetic field strength B_0 and the background magnetic field orientation ζ.

Chapter 3

Triadic Resonance Interactions of IGWs

In Chapters 3 and 4, we consider a stably-stratified Boussinesq fluid in the absence of a magnetic field. Under these conditions, the governing equations permit only one type of wave: pure IGWs. The purpose of this chapter is to derive an analytical formula for the growth rate of a particular class of parametric instability of IGWs using asymptotics. In Chapter 2, we discussed a plane wave solution to the ideal Boussinesq equations with wave amplitude a. Throughout this thesis, we refer to the plane wave solution as the primary wave. To study instabilities of the primary wave, we consider disturbances with respect to the primary wave. The method presented in this chapter is valid only for small values of a.

In the absence of a magnetic field, the plane wave solution is an IGW and is prescribed by only two parameters: the dimensionless amplitude parameter a and the wavevector angle θ with respect to the positive X-axis. In Chapters 3 and 4 we focus on the influence of these two parameters on IGW instabilities. Following these chapters, we focus on the influence of the parameters ζ, ξ and B_0 introduced by the magnetic field in Chapters 5 and 6.

3.1 Parametric Instabilities

The class of instability we study in this chapter is a type of parametric instability, so we begin by stating what parametric instabilities are and discuss previous studies of parametric instabilities of IGWs in the literature. Generally speaking, parametric instability is a consequence of nonlinear resonance in an oscillatory system. By resonance, we mean the phenomenon in which an oscillator is forced at the same frequency as that which it naturally oscillates at. In fluids, parametric instability can arise as a consequence of resonant interactions between waves. In this chapter, these waves are IGWs, but in Chapter 5 we introduce a magnetic field and consider resonant interactions between AGWs and AWs.

Parametric Instabilities of Internal Gravity Waves

In this section, literature concerns 2D IGWs (i.e. plane waves). Their wavevectors are confined to a plane, so are completely described by two Cartesian components. This is the primary wave. We frequently refer to both 2D disturbances and 3D disturbances with respect to the primary wave. By 2D disturbances, we mean disturbances which are coplanar with the plane to which the primary wave is confined. By 3D disturbances, we mean disturbances which are not confined to the same plane as the primary wave.

Parametric instabilities of IGWs in the absence of a magnetic field are well-studied. Davis and Acrivos (1967) studied parametric instabilities of 2D IGWs propagating through a Boussinesq fluid. They considered two different regimes: one in an infinite fluid medium in which $N(Z) = \mathrm{sech}^2(Z)$ and another in a bounded fluid in which N is uniform. In both regimes, they derived asymptotic formulae for predicting the growth rates of parametric instabilities. McEwan and Robinson (1975) studied parametric instabilities of IGWs via a Mathieu equation. They took disturbance wavelengths to be much smaller than the primary wavelength and considered 2D disturbances.

Much of the later work in this problem was performed using techniques based on Floquet theory. Mied (1976) performed the first example of Floquet linear stability analysis of 2D IGWs propagating through an ideal Boussinesq fluid. He introduced a useful coordinate transformation in which one of the coordinate axes aligns with the phase velocity of the primary wave. He showed that for a primary wave orientation of $\theta = \pi/6$ with respect to the horizontal axis, waves of any amplitude could become parametrically unstable. He only considered 2D disturbances to the plane IGW. Klostermeyer (1982) also studied parametric instabilities of 2D IGWs propagating through an ideal Boussinesq fluid using a Floquet method. His aim was to generalise the work of Mied (1976). He used a similar approach to Mied to show that waves of any amplitude a and any primary wavevector orientation θ could become parametrically unstable in an ideal Boussinesq fluid. Klostermeyer (1983) extended his work to incorporate the effects of viscosity. In ideal Boussinesq fluids, the fastest-growing modes of disturbance have wavelengths much smaller than that of the primary wave. Klostermeyer (1983) showed that with non-zero viscosity at high Re, the fastest-growing modes of disturbance have wavelengths which are comparable or potentially larger than that of the primary wave.

All work mentioned thus far was restricted to the case of 2D disturbances. A result common to all of the aforementioned literature is that at low amplitudes, instabilities of IGWs can be attributed to resonant interactions between three IGWs. Klostermeyer (1991) extended the problem further by considering 3D disturbances and showed that waves of any amplitude could become parametrically unstable to 3D disturbances too. He also showed that at overturning amplitudes (i.e. values $a > 1$ such that IGWs are statically unstable), higher order resonant interactions become important, which could involve couplings between more than three IGWs. At lower amplitudes, the fastest growing modes of disturbance are 2D, but at higher amplitudes, the fastest growing modes of disturbance are 3D. Drazin (1977) independently arrived at similar conclusions to these authors by deriving an analytical instability criterion for resonant interactions of IGWs propagating through a Boussinesq fluid.

Instabilities of IGWs are not limited to those which are parametric. More recent work on IGW instabilities has widened the scope to include other classes of instability too (Lombard and Riley, 1996; Sonmor and Klaassen, 1997). We extend this work in Chapter 4.

3.2 Resonant Triads

It turns out that we can attribute many such instabilities to a particular type of parametric instability known as the triadic resonance instability (TRI). In Section 3.3 we present an approach to quantifying TRI growth rates analytically for IGWs using a small-amplitude approximation. This chapter provides a means of classifying instabilities observed in Chapter 4.

> In this chapter, we temporarily redefine the symbols ρ and P as follows to simplify the algebra:
>
> $$\rho g/\rho_0 \to \rho, \quad P/\rho_0 \to P. \tag{3.1}$$

The variables P and ρ do not have dimensions of pressure and density respectively in this chapter as a result. At the end of this chapter, the interpretations of P and ρ are reset according to how they appeared in Chapter 2.

Here, we develop theory pertaining to ideal IGWs, which means we take the following limits regarding the dimensionless numbers:

$$\mathrm{Re} \to \infty, \quad \mathrm{Pe} \to \infty. \tag{3.2}$$

We treat viscosity ν and thermal diffusion κ as negligible in this chapter as a result.

To observe how resonant triads arise between pure internal gravity waves, we start from the ideal Boussinesq equations for a stably-stratified fluid with constant buoyancy frequency N:

$$\frac{\partial \boldsymbol{U}}{\partial T} + \boldsymbol{U} \cdot \nabla \boldsymbol{U} = -\nabla P - \rho \hat{\boldsymbol{Z}}, \tag{3.3}$$

$$\frac{\partial \rho}{\partial T} + \boldsymbol{U} \cdot \nabla \rho = N^2 U_Z, \tag{3.4}$$

$$\nabla \cdot \boldsymbol{U} = 0. \tag{3.5}$$

Equations (3.3)-(3.5) are taken from equations (2.32)-(2.36), modified by (3.1) and with the presence of the magnetic field removed. We would like to obtain a scalar equation from these which separates the terms which are linear in the dependent variables from those which are nonlinear in the dependent variables. A sensible way of doing so is to take $\nabla \times \nabla \times \partial_T$ (3.3):

$$\frac{\partial^2}{\partial T^2}(\nabla \times \nabla \times \boldsymbol{U}) + \frac{\partial}{\partial T}[\nabla \times \nabla \times (\boldsymbol{U} \cdot \nabla)\boldsymbol{U}] = -\nabla \times \nabla \times \left(\frac{\partial \rho}{\partial T}\hat{\boldsymbol{Z}}\right).$$

Using the identity $\nabla \times \nabla \times \boldsymbol{v} \equiv \nabla(\nabla \cdot \boldsymbol{v}) - \nabla^2 \boldsymbol{v}$ together with (3.5) yields

$$\frac{\partial^2}{\partial T^2}(\nabla^2 \boldsymbol{U}) - \left(\frac{\partial}{\partial Z}\nabla - \hat{\boldsymbol{Z}}\nabla^2\right)\frac{\partial \rho}{\partial T} = \frac{\partial}{\partial T}[\nabla \times \nabla \times (\boldsymbol{U} \cdot \nabla)\boldsymbol{U}].$$

Using (3.4) to replace $\partial_T \rho$ gives

$$\frac{\partial^2}{\partial T^2}(\nabla^2 \boldsymbol{U}) - \left(\frac{\partial}{\partial Z}\nabla - \hat{\boldsymbol{Z}}\nabla^2\right) N^2 U_Z = \boldsymbol{F}, \tag{3.6}$$

where $\boldsymbol{F}$ is a nonlinear forcing term given by

$$\boldsymbol{F} := \frac{\partial}{\partial T}[\nabla \times \nabla \times (\boldsymbol{U} \cdot \nabla)\boldsymbol{U}] - \left(\frac{\partial}{\partial Z}\nabla - \hat{\boldsymbol{Z}}\nabla^2\right)(\boldsymbol{U} \cdot \nabla \rho).$$

The Z-component of (3.6) is

$$(\partial_T^2 \nabla^2 + N^2 \nabla_\perp^2) U_Z = F_Z, \tag{3.7}$$

where $\nabla_\perp^2 := \partial_X^2 + \partial_Y^2$ and $F_Z := \boldsymbol{F} \cdot \hat{\boldsymbol{Z}}$.

We shall use the $\perp$ notation throughout this chapter and future chapters to denote a vector quantity with no Z-component, i.e. with no component in the direction of gravity.

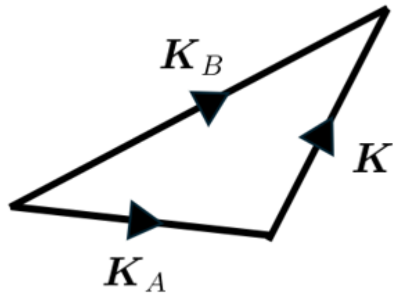

Figure 3.1: Diagram depicting a resonant triad between three waves with wavevectors $\boldsymbol{K}, \boldsymbol{K}_A$ and $\boldsymbol{K}_B$ respectively, corresponding to equation (3.12).

The homogeneous form of PDE (3.7) is

$$(\partial_T^2 \nabla^2 + N^2 \nabla_\perp^2) U_Z = 0, \tag{3.8}$$

the solutions of which describe IGWs. Consider a plane wave solution for U_Z given by

$$U_Z(\boldsymbol{X}, T) = \Re \left[U_{WZ} \exp(i\boldsymbol{K} \cdot \boldsymbol{X} - i\omega T) \right].$$

Placing this into the homogeneous PDE (3.8) yields the IGW dispersion relation

$$\frac{\omega^2}{N^2} = \frac{K_\perp^2}{K^2}, \tag{3.9}$$

where $\boldsymbol{K}_\perp := (K_X, K_Y)$. Consider instead a linear combination of two waves

$$\begin{aligned} U_Z &= \Re \left[U_A e^{i\phi_A} + U_B e^{i\phi_B} \right] \\ &= \Re \left[U_A \exp(i\boldsymbol{K}_A \cdot \boldsymbol{X} - i\omega_A T) + U_B \exp(i\boldsymbol{K}_B \cdot \boldsymbol{X} - i\omega_B T) \right]. \end{aligned}$$

When we put this into the inhomogeneous PDE (3.7), the nonlinear forcing term F_Z will contain subterms proportional to $\exp[\pm i(\phi_A + \phi_B)]$. If the combination $\phi_A + \phi_B$ happens to satisfy the dispersion relation associated with the unforced equation (3.8), i.e. if

$$\pm \boldsymbol{K}_A \pm \boldsymbol{K}_B = \boldsymbol{K}, \tag{3.10}$$

$$\pm \omega_A \pm \omega_B = \omega, \tag{3.11}$$

then the forced frequency will be the same as the natural frequency of the oscillator represented by equations (3.7) and (3.8). In other words, resonance occurs. In particular, these two waves A and B can extract energy from the primary wave. Here, we consider the case where two such waves A and B are ‘daughter waves’ excited as disturbances relative to the ‘parent wave’ (the primary wave). This scenario is depicted in Figure 3.1 and is the subject of the remainder of this chapter.

Naturally, a triad of waves is just one of many possible resonant combinations. We could equally observe resonant couplings between four or more waves. This setting does naturally lend itself towards triads, however, since the nonlinearities in the equations of motion are quadratic and no higher in order.

Key Formulae

Here we establish some key formulae for the wavenumbers and frequencies involved in resonant triads between IGWs in this thesis.

There are multiple ways of formulating the equations (3.10) and (3.11) depending on the sign choices we make. In this thesis, without loss of generality, we make the choice

$$\boldsymbol{K} + \boldsymbol{K}_A - \boldsymbol{K}_B = 0, \tag{3.12}$$

$$\omega + \omega_A - \omega_B = 0. \tag{3.13}$$

The frequencies ω_A and ω_B are given by

$$\frac{\omega_A}{N} := -\frac{K_{A\perp}}{K_A}, \quad \frac{\omega_B}{N} := \frac{K_{B\perp}}{K_B}, \tag{3.14}$$

where the horizontal wavevectors $\boldsymbol{K}_{A\perp}$ and $\boldsymbol{K}_{B\perp}$ are given by

$$\boldsymbol{K}_{A\perp} := (K_{AX}, K_{AY}), \quad \boldsymbol{K}_{B\perp} := (K_{BX}, K_{BY}).$$

This particular choice of signs in ω_A and ω_B is required later to satisfy the frequency resonance condition (3.13) for positive $\boldsymbol{K}_A$ and $\boldsymbol{K}_B$.

Resonance Curves for 2D Resonant Triads

Here, we find combinations of daughter waves which resonantly interact with the primary wave by finding wavenumbers which satisfy the resonance conditions (3.12) and (3.13) simultaneously. If we restrict ourselves to the (X, Z)-plane, the resonance condition (3.13) becomes

$$\frac{|K_X|}{\sqrt{K_X^2 + K_Z^2}} - \frac{|K_{AX}|}{\sqrt{K_{AX}^2 + K_{AZ}^2}} - \frac{|K_{BX}|}{\sqrt{K_{BX}^2 + K_{BZ}^2}} = 0,$$

Using the wavenumber resonance condition to replace $\boldsymbol{K}_B$ gives

$$\frac{|K_X|}{\sqrt{K_X^2 + K_Z^2}} - \frac{|K_{AX}|}{\sqrt{K_{AX}^2 + K_{AZ}^2}} - \frac{|K_X + K_{AX}|}{\sqrt{(K_X + K_{AX})^2 + (K_Z + K_{AZ})^2}} = 0. \tag{3.15}$$

We now define dimensionless wavenumbers

$$k_{AX} := K_{AX}/K_X, \quad k_{AZ} := K_{AZ}/K_Z.$$

Recall that

$$K_X = K\cos\theta, \quad K_Z = K\sin\theta,$$

which means

$$K_Z/K_X = \tan\theta.$$

We can rearrange (3.15) to get

$$|\cos\theta| = \frac{|k_{AX}|}{\sqrt{k_{AX}^2 + (\tan^2\theta)k_{AZ}^2}} + \frac{|1 + k_{AX}|}{\sqrt{(1 + k_{AX})^2 + (\tan^2\theta)(1 + k_{AZ})^2}}. \tag{3.16}$$

We plot the functional relationship between k_{AX} and k_{AZ} described by equation (3.16) for three values of θ in Figure 3.2. This reveals which pairs of (k_{AX}, k_{AZ}) values are resonant when $k_{AY} = 0$. The relationship is not a one-to-one mapping. For each value of k_{AX} we consider, we observe two resonant values of k_{AZ}, giving two 'branches' for each panel. Figure 3.2 is inspired by similar figures produced by Sonmor and Klaassen (1997) and Varma et al. (2022). We can see that in the limit as $|k_{AX}| \to \infty$ and $|k_{AZ}| \to \infty$, the relationship between k_{AX} and k_{AZ} becomes linear. We also find that there is a threshold for $|k_{AZ}|$ below which resonance does not occur.

We plot the absolute values of the corresponding resonant daughter wave frequencies for each k_{AX} in Figures 3.3. In each panel, there are two frequency branches, one for each branch of the wavenumber resonance curves in Figure 3.2. We find that as we increase the wavevector angle θ, the separation between the two frequency branches becomes increasingly large.

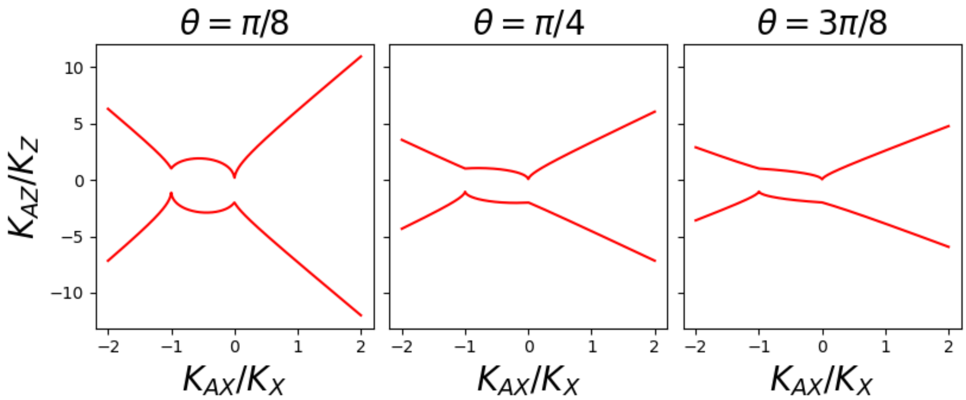

Figure 3.2: Pairs of k_{AX}, k_{AZ} values which produce resonant triads between IGWs when $k_{AY} = 0$.

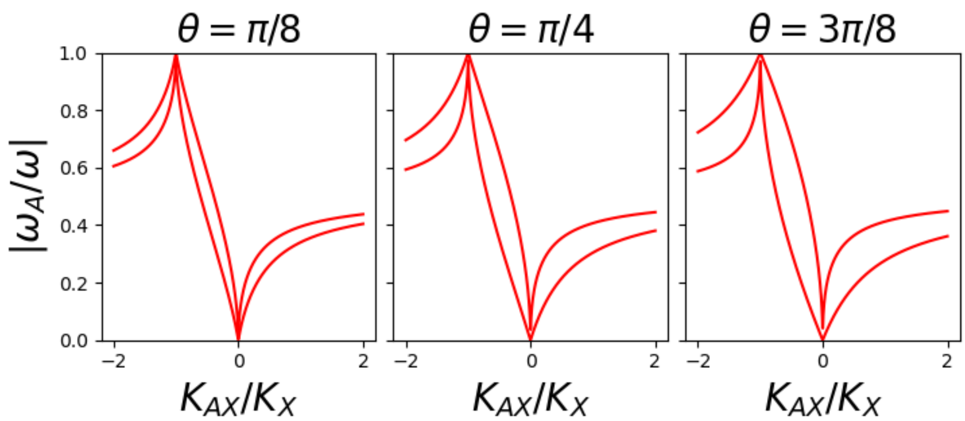

Figure 3.3: Absolute value of the disturbance frequency $|\omega_A/\omega|$ as a function of horizontal wavenumber K_{AX}/K_X for resonant triads between IGWs when $K_{AY} = 0$.

Parametric Subharmonic Instability

Here we consider what happens to the frequencies in the limit in which the daughter waves have much shorter wavelengths than the primary wave, i.e. when

$$K_A \gg K, \quad K_B \gg K. \tag{3.17}$$

Since the wavevector resonance condition for a TRI is (3.12), taking the limit (3.17) amounts to

$$\boldsymbol{K}_A \approx \boldsymbol{K}_B. \tag{3.18}$$

As a consequence, we have the following relation between daughter wave frequencies:

$$\omega_A \approx -\omega_B. \tag{3.19}$$

Together with the frequency resonance condition (3.13), the relation $\omega_A \approx -\omega_B$ leads to the following result, which characterises what is known as the *parametric subharmonic instability*.

$$\omega_A \approx -\omega/2, \quad \omega_B \approx \omega/2. \tag{3.20}$$

The parametric subharmonic instability (PSI) is a subclass of the triadic resonance instability (TRI). The PSI is thought to represent the fastest-growing instability associated with any particular primary wave prescribed by a and θ (e.g. Varma et al., 2022). This notion is discussed later on in Chapter 4 and we provide evidence of such a conclusion.

In Figure 3.2 the linear extents of the resonance curves at the largest wavenumber magnitudes approach the PSI limit. To illustrate (3.20), we plot absolute values of resonant frequencies $|\omega_A/\omega|$ as a function of K_{AX}/K_X in Figure 3.4. We can see the PSI limit $|\omega_A/\omega| \to 1/2$ being approached as $|K_{AX}/K_X|$ gets increasingly large. It is important to emphasise that this limit represents the behaviour in the limit of no diffusion. If we incorporate the effects of diffusion, the frequency relationship deviates from $|\omega_A| \sim |\omega_B| \sim |\omega/2|$.

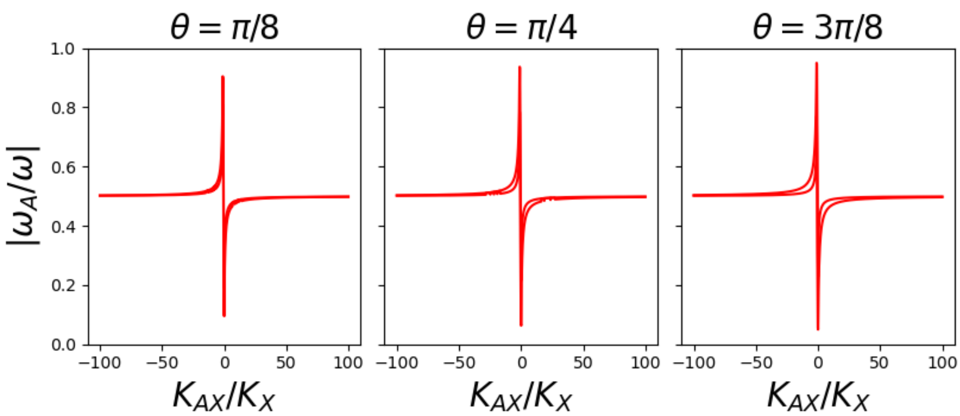

Figure 3.4: Absolute value of the disturbance frequency $|\omega_A/\omega|$ as a function of horizontal wavenumber K_{AX}/K_X for resonant triads between IGWs when $K_{AY} = 0$.

3.3 Asymptotics

3.3.1 Growth Rate at Points of Exact Resonance

In this section we present an asymptotic derivation of a formula for the growth rate of IGW instabilities under the conditions where triadic resonance is exactly satisfied. The method used is inspired by Cui and Latter (2022), who used the same approach to generate growth rates for TRIs of inertial waves excited by the vertical shear instability (VSI) in protoplanetary disks. The formula we derive allows us to arrive at conclusions which are similar to those found by Davis and Acrivos (1967), Mied (1976) and Drazin (1977).

Davis and Acrivos (1967) performed a multiple scale analysis to describe TRIs of IGWs in a Boussinesq fluid. The objectives were to determine which disturbances produce instability and to determine the growth rate of unstable disturbances analytically. They performed this in two different contexts: a fluid with buoyancy frequency $N^2 = \mathrm{sech}^2(Z)$ (in our notation) and a uniformly-stratified fluid with constant buoyancy frequency bounded by two walls. In the former case, the $N^2 = \mathrm{sech}^2(Z)$ profile creates a fluid with two layers of uniform density separated by an interstitial region over which density varies continuously (peaking at $Z = 0$). Davis and Acrivos created an approximate experimental realisation of such a fluid using a combination of saline water and fresh water. The latter case is equivalent to the work we present here, with the only differences being that Davis and Acrivos (1967) use a bounded domain (our domain has no boundaries) and that they consider 2D disturbances. In both cases, Davis and Acrivos found that the number of unstable disturbances was infinite for any given wave. They also derived a minimum amplitude at which IGWs can become unstable to TRIs.

Mied (1976) studied parametric instabilities of 2D IGWs in a Boussinesq fluid. He used expansions of disturbance wavenumber K in powers of the amplitude parameter a (our notation) to compute curves of neutral stability and constant growth rate for disturbances with respect to IGWs. In this way, Mied produced results similar to those obtained by Davis and Acrivos (1967). He did not perform any multiple scale analysis to get those results, however. Drazin (1977) similarly derived an analytical instability criterion for TRIs of IGWs in a Boussinesq fluid.

Introducing Multiple Time Scales

In this chapter, where we consider a Boussinesq fluid in the absence of a magnetic field, the daughter waves A and B are pure internal gravity waves in the limit in which $a \ll 1$. For larger amplitudes, the daughter waves are not necessarily restored by buoyancy alone, as they may be influenced by the shear of the primary wave.

In the following derivation, we use the wave amplitude a as an asymptotic ordering parameter. To begin the multiple-scale analysis, we consider a 'slow' timescale τ related to the original 'fast' timescale T by $\tau = aT$. We are interested in instabilities which grow slowly relative to the oscillation timescale. We hence use the fast timescale T as the timescale on which the waves oscillate, and the slow timescale τ as the timescale on which the amplitudes of the disturbances grow.

We seek a set of equations which are linearised with respect to disturbances to the primary wave. We again start from the ideal governing equations (3.3)-(3.5). To incorporate both timescales into the problem, we write

$$\frac{\partial}{\partial T} \to \frac{\partial}{\partial T} + a\frac{\partial}{\partial \tau}. \tag{3.21}$$

We also decompose dependent variables into primary wave quantities and disturbance quantities:

$$\boldsymbol{U}(\boldsymbol{X}, T, \tau) = \tilde{\boldsymbol{U}}(X, Z, T) + \boldsymbol{U}'(\boldsymbol{X}, T, \tau), \tag{3.22}$$

$$P(\boldsymbol{X}, T, \tau) = \tilde{P}(X, Z, T) + P'(\boldsymbol{X}, T, \tau), \tag{3.23}$$

$$\rho(\boldsymbol{X}, T, \tau) = \tilde{\rho}(X, Z, T) + \rho'(\boldsymbol{X}, T, \tau). \tag{3.24}$$

Tilde notation denotes primary wave quantities. The explicit formulae for $\tilde{\boldsymbol{U}}$, $\tilde{\boldsymbol{B}}$ and $\tilde{\rho}$ were provided in Section 2.4. Prime notation denotes disturbances with respect to the primary wave. To make a small-amplitude approximation, we consider asymptotic expansions of the form

$$F' = F'_0 + aF'_1 + a^2F'_2 + O(a^3) \quad \text{for} \quad F \in \{\boldsymbol{U}, P, \rho\}. \tag{3.25}$$

To make the dependence of $\tilde{\boldsymbol{U}}$ and $\tilde{\rho}$ on the ordering parameter a explicit, we define $\check{\boldsymbol{U}}$ and $\check{\rho}$ via

$$\tilde{\boldsymbol{U}} = a\check{\boldsymbol{U}}, \quad \tilde{\rho} = a\check{\rho}. \tag{3.26}$$

We substitute (3.21)-(3.24) and (3.26) into equations (3.3)-(3.5).

The linearised form of equations (3.3)-(3.5) with respect to perturbations is then

$$\frac{\partial \boldsymbol{U'}}{\partial T} + a\left(\frac{\partial \boldsymbol{U}'}{\partial \tau} + \check{\boldsymbol{U}} \cdot \nabla \boldsymbol{U'} + \boldsymbol{U'} \cdot \nabla \check{\boldsymbol{U}}\right) = -\nabla P' - \rho' \hat{\boldsymbol{Z}}, \tag{3.27}$$

$$\frac{\partial \rho'}{\partial T} + a\left(\frac{\partial \rho'}{\partial \tau} + \check{\boldsymbol{U}} \cdot \nabla \rho' + \boldsymbol{U'} \cdot \nabla \check{\rho}\right) = N^2 U'_Z, \tag{3.28}$$

$$\nabla \cdot \boldsymbol{U'} = 0, \tag{3.29}$$

given that the nonlinear equations satisfied by the primary wave are

$$\begin{aligned} \frac{\mathrm{D}\tilde{\boldsymbol{U}}}{\mathrm{D}T} &= -\nabla \tilde{P} - \tilde{\rho}\hat{\boldsymbol{Z}}, \\ \frac{\mathrm{D}\tilde{\rho}}{\mathrm{D}T} &= N^2 \tilde{U}_Z, \\ \nabla \cdot \tilde{\boldsymbol{U}} &= 0. \end{aligned}$$

We now substitute asymptotic expansion (3.25) into (3.27)-(3.29) and collect terms at each successive order in a.

Equations at $O(a^0)$

Using the fact that any terms containing appearances of $\tilde{F}$ are at most $O(a^1)$, from (3.27)-(3.29) we retain only the following at $O(a^0)$:

$$\frac{\partial \boldsymbol{U}'_0}{\partial T} = -\nabla P'_0 - \rho'_0 \hat{\boldsymbol{Z}}, \tag{3.30}$$

$$\frac{\partial \rho'_0}{\partial T} = N^2 U'_{0Z}, \tag{3.31}$$

$$\nabla \cdot \boldsymbol{U}'_0 = 0. \tag{3.32}$$

Taking $\nabla \times \nabla \times$(3.30) yields

$$\frac{\partial}{\partial T}(\nabla \times \nabla \times \boldsymbol{U}'_0) = -\nabla \times \nabla \times \left(\rho'_0 \hat{\boldsymbol{Z}}\right).$$

Applying the vector identity $\nabla \times \nabla \times \boldsymbol{v} \equiv \nabla(\nabla \cdot \boldsymbol{v}) - \nabla^2 \boldsymbol{v}$ and incorporating (3.32) gives

$$\frac{\partial}{\partial T}(\nabla^2 \boldsymbol{U}_0') = \nabla \left(\frac{\partial \rho_0'}{\partial Z} \right) - (\nabla^2 \rho_0') \hat{\boldsymbol{Z}}.$$

We then differentiate and use (3.31) to replace $\partial_T \rho_0'$.

$$\frac{\partial^2}{\partial T^2}(\nabla^2 \boldsymbol{U}_0') = -N^2 \left[(\nabla^2 U_{0Z}') \hat{\boldsymbol{Z}} - \nabla \left(\frac{\partial U_{0Z}'}{\partial Z} \right) \right].$$

We now have a second order PDE entirely in terms of $\boldsymbol{U}_0'$:

$$\frac{\partial^2}{\partial T^2}(\nabla^2 \boldsymbol{U}_0') + N^2 \left[(\nabla^2 U_{0Z}') \hat{\boldsymbol{Z}} - \nabla \left(\frac{\partial U_{0Z}'}{\partial Z} \right) \right] = 0. \tag{3.33}$$

This is the end point of deriving a leading order equation describing daughter waves. Its Z-component, shown below, gives us the IGW dispersion relation (3.14) we expect when we insert a plane wave solution.

$$\frac{\partial^2}{\partial T^2} \left(\nabla^2 U_{0Z}' \right) + N^2 \nabla_\perp^2 U_{0Z}' = 0. \tag{3.34}$$

General Solution

Typically, since $\boldsymbol{U}_0'$ must be purely real, we would write the solution at this stage as the superposition of two complex conjugates, namely

$$\boldsymbol{U}_0' = A(\tau) \boldsymbol{U}_A E_A + A^*(\tau) \boldsymbol{U}_A^* E_{-A},$$

where $E_{\pm C}$ for any wave C is defined via

$$E_{\pm C} := \exp[i(\pm \boldsymbol{K}_C \cdot \boldsymbol{X} \mp \omega_C T)].$$

Since we are concerned with resonant triads involving two daughter waves A and B, the general solution we need to consider is

$$\begin{aligned} \boldsymbol{U}_0' = A(\tau) \boldsymbol{U}_A E_A + A^*(\tau) \boldsymbol{U}_A^* E_{-A} + \\ B(\tau) \boldsymbol{U}_B E_B + B^*(\tau) \boldsymbol{U}_B^* E_{-B}. \end{aligned}$$

We consider a similar general solution for the other dependent variables P_0' and ρ_0'. For each daughter wave we must consider the superposition of two complex conjugate exponential solutions, since $\boldsymbol{U}_0'$ must be purely real. The vectors $\boldsymbol{U}_A$ and $\boldsymbol{U}_B$ are eigenvectors of equation (3.33), with magnitudes which are free to be chosen at our convenience. A and B are the amplitudes of each daughter wave. The amplitudes of the disturbance vary on the slow timescale τ, so it makes sense physically for these quantities to have τ-dependence.

Eigenvector Components

To determine a convenient choice for the eigenvector magnitudes pertaining to daughter wave A, we seek solutions of the form $F = F_A E_A$ for all dependent variables and substitute them in equations (3.30)-(3.32). This produces

$$\omega_A U_{AX} = K_{AX} P_A, \tag{3.35}$$
$$\omega_A U_{AY} = K_{AY} P_A, \tag{3.36}$$
$$\omega_A U_{AZ} = K_{AZ} P_A - i\rho_A, \tag{3.37}$$
$$\omega_A \rho_A = iN^2 U_{AZ}, \tag{3.38}$$
$$0 = K_{AX} U_{AX} + K_{AY} U_{AY} + K_{AZ} U_{AZ}. \tag{3.39}$$

Taking K_{AX}(3.35) + K_{AY}(3.36) and incorporating (3.39) gives

$$-\omega_A K_{AZ} U_{AZ} = (K_{AX}^2 + K_{AY}^2) P_A.$$

If we choose $U_{AZ} = K_{AX}^2 + K_{AY}^2$, then $P_A = -\omega_A K_{AZ}$ and from (3.35) - (3.37) we get

$$\begin{aligned} U_{AX} &= -K_{AX} K_{AZ} \\ U_{AY} &= -K_{AY} K_{AZ} \\ \rho_A &= i\omega_A K_A^2. \end{aligned}$$

In summary, our eigenvector components for daughter wave A are

$$\begin{aligned} \boldsymbol{U}_A &= -K_{AX} K_{AZ} \hat{\boldsymbol{X}} - K_{AY} K_{AZ} \hat{\boldsymbol{Y}} + K_{A\perp}^2 \hat{\boldsymbol{Z}}, \\ P_A &= -\omega_A K_{AZ}, \\ \rho_A &= i\omega_A K_A^2. \end{aligned}$$

The eigenvector components for daughter wave B are analogous. This completes the work at $O(a^0)$. The objective now is to obtain a second order PDE with $\boldsymbol{U}_1'$ as the dependent variable at $O(a^1)$, from which we can produce solvability conditions which allow us to obtain a formula for the growth rate.

Equations at $O(a^1)$

At $O(a^1)$, from equations (3.27)-(3.29) we retain

$$\frac{\partial \boldsymbol{U}_1'}{\partial T} + \nabla P_1' + \rho_1' \hat{\boldsymbol{Z}} = -\boldsymbol{F}_U, \tag{3.40}$$
$$\frac{\partial \rho_1'}{\partial T} - N^2 U_{1Z}' = -F_\rho, \tag{3.41}$$
$$\nabla \cdot \boldsymbol{U}_1' = 0, \tag{3.42}$$

with forcing terms $\boldsymbol{F}_U$ and F_ρ defined as:

$$\boldsymbol{F}_U := \frac{\partial \boldsymbol{U}_0'}{\partial \tau} + \check{\boldsymbol{U}} \cdot \nabla \boldsymbol{U}_0' + \boldsymbol{U}_0' \cdot \nabla \check{\boldsymbol{U}}, \tag{3.43}$$
$$F_\rho := \frac{\partial \rho_0'}{\partial \tau} + \check{\boldsymbol{U}} \cdot \nabla \rho_0' + \boldsymbol{U}_0' \cdot \nabla \check{\rho}. \tag{3.44}$$

Taking $\nabla \times \nabla \times \partial_T$ (3.40), replacing $\partial_T \rho_1'$ using (3.41) and incorporating (3.42) yields

$$\frac{\partial^2}{\partial T^2}(\nabla^2 \boldsymbol{U}_1') + N^2 \left[(\nabla^2 U_{1Z}') \hat{\boldsymbol{Z}} - \nabla \left(\frac{\partial U_{1Z}'}{\partial Z} \right) \right] = \boldsymbol{G}, \tag{3.45}$$

where the vector $\boldsymbol{G}$ is defined as

$$\boldsymbol{G} := \nabla \times \nabla \times \left(\frac{\partial \boldsymbol{F}_U}{\partial T} \right) + (\nabla^2 F_\rho) \hat{\boldsymbol{Z}} - \nabla \left(\frac{\partial F_\rho}{\partial Z} \right). \tag{3.46}$$

Again we have used the identity $\nabla \times \nabla \times \boldsymbol{v} \equiv \nabla(\nabla \cdot \boldsymbol{v}) - \nabla^2 \boldsymbol{v}$.

Deriving Solvability Conditions in Matrix Form

To derive solvability conditions, we use all three components of the PDE (3.45) to construct a matrix equation. We start from the corresponding homogeneous PDE (3.33):

$$\frac{\partial^2}{\partial T^2}(\nabla^2 \boldsymbol{U}_0') + N^2 \left(\hat{\boldsymbol{Z}} \nabla^2 - \nabla \frac{\partial}{\partial Z} \right) U_{0Z}' = 0.$$

In matrix form, this reads

$$\mathcal{L} \boldsymbol{U}_0' = 0, \tag{3.47}$$

where the linear operator $\mathcal{L}$ is defined as

$$\mathcal{L} = \begin{pmatrix} \partial_T^2 \nabla^2 & 0 & -N^2 \partial_Z \partial_X \\ 0 & \partial_T^2 \nabla^2 & -N^2 \partial_Z \partial_Y \\ 0 & 0 & \partial_T^2 \nabla^2 + N^2 \nabla_\perp^2 \end{pmatrix}.$$

At $O(a)$ the analogous PDE (3.45) can be expressed as

$$\mathcal{L} \boldsymbol{U}_1' = \boldsymbol{G}. \tag{3.48}$$

We write $\boldsymbol{G}$ as

$$\boldsymbol{G} = \boldsymbol{G}_A E_A + \boldsymbol{G}_B E_B + \ldots$$

where the ellipsis contains terms which are proportional to exponential factors other than E_A and E_B, as well as the relevant complex conjugates. When considering solutions of the form

$$\boldsymbol{U}_0'(\boldsymbol{X}, T) = \boldsymbol{U}_A \exp(i \boldsymbol{K}_A \cdot \boldsymbol{X} - i \omega_A T),$$

the $O(1)$ PDE (3.47) becomes

$$(M_A - \omega_A^2 I) \boldsymbol{U}_A = 0, \tag{3.49}$$

where I is the 3×3 identity matrix and the matrix M_A is given by

$$M_A := \begin{pmatrix} 0 & 0 & -N^2 K_{AZ} K_{AX} / K_A^2 \\ 0 & 0 & -N^2 K_{AZ} K_{AY} / K_A^2 \\ 0 & 0 & N^2 K_{A\perp}^2 / K_A^2 \end{pmatrix}.$$

This matrix is non-symmetric, which means the left eigenvectors are not necessarily the same as the right eigenvectors. If we were to use the governing equations to construct a vorticity equation and rephrase everything in terms of a 3D streamfunction, we could produce a symmetric matrix. In this situation, the left and right eigenvectors would be identical. We can still derive solvability conditions regardless of whether the left and right eigenvectors are identical. At $O(a)$, the component of the PDE (3.48) proportional to E_A is

$$(M_A - \omega_A^2 I)\boldsymbol{U}_{1A} = \boldsymbol{G}_A. \tag{3.50}$$

We can think of $\boldsymbol{U}_A$ as a right eigenvector for the matrix M_A. Consider the corresponding left eigenvector $\hat{\boldsymbol{U}}_A$, which must satisfy

$$\hat{\boldsymbol{U}}_A^\top (M_A - \omega_A^2 I) = 0, \tag{3.51}$$

where $\boldsymbol{U}_A^\top$ denotes the transpose of $\boldsymbol{U}_A$. We multiply (3.50) by the left eigenvector $\boldsymbol{U}_A^\top$ on the left to get

$$\hat{\boldsymbol{U}}_A^\top \boldsymbol{G}_A = 0. \tag{3.52}$$

This is the desired solvability condition for daughter wave A. Similarly, we find that the solvability condition for daughter wave B is

$$\hat{\boldsymbol{U}}_B^\top \boldsymbol{G}_B = 0. \tag{3.53}$$

The matrix M_A has two eigenvalues: $\omega_A^2 = 0$ (with multiplicity two) and a third eigenvalue with multiplicity one which satisfies the dispersion relation for IGWs:

$$\omega_A^2 = N^2 K_{A\perp}^2 / K_A^2. \tag{3.54}$$

The right eigenvector associated with the non-zero eigenvalue is

$$\boldsymbol{U}_A = -K_{AZ}K_{AX}\hat{\boldsymbol{X}} - K_{AZ}K_{AY}\hat{\boldsymbol{Y}} + K_{A\perp}^2\hat{\boldsymbol{Z}},$$

which is consistent with the eigenvector components we found earlier in this chapter. The left eigenvector associated with the non-zero eigenvalue is

$$\hat{\boldsymbol{U}}_A = \hat{\boldsymbol{Z}}.$$

The eigenvalues and eigenvectors for M_B are analogous. Solvability conditions (3.52) and (3.53) thus reduce to

$$G_{AZ} = 0, \quad G_{BZ} = 0,$$

where G_{AZ} and G_{BZ} are the Z-components of $\boldsymbol{G}_A$ and $\boldsymbol{G}_B$ respectively.

Amplitude Equations

The coefficients G_{AZ} and G_{BZ} can be expressed as

$$G_{AZ} := c_1 \frac{\mathrm{d}A}{\mathrm{d}\tau} + c_2 B,$$
$$G_{BZ} := c_3 \frac{\mathrm{d}B}{\mathrm{d}\tau} + c_4 A.$$

Let $\boldsymbol{K}_W := \boldsymbol{K}$. The coefficients c_i, derived in Appendix A.3.1, are given by

$$\begin{aligned} c_1 =& -2i\omega_A K_A^2 K_{A\perp}^2, && (3.55)\\ c_2 =& -\omega_A(\boldsymbol{K}_W\cdot\boldsymbol{U}_B)(\boldsymbol{U}_A\cdot\boldsymbol{U}_W)\\ &+\omega_A(\boldsymbol{K}_B\cdot\boldsymbol{U}_W)(\boldsymbol{U}_A\cdot\boldsymbol{U}_B)\\ &-\rho_B(\boldsymbol{K}_B\cdot\boldsymbol{U}_W)iK_{A\perp}^2\\ &-\rho_W(\boldsymbol{K}_W\cdot\boldsymbol{U}_B)iK_{A\perp}^2, && (3.56)\end{aligned}$$

along with

$$\begin{aligned} c_3 =& -2i\omega_B K_B^2 K_{B\perp}^2, && (3.57)\\ c_4 =& +\omega_B(\boldsymbol{K}_W\cdot\boldsymbol{U}_A)(\boldsymbol{U}_B\cdot\boldsymbol{U}_W)\\ &+\omega_B(\boldsymbol{K}_A\cdot\boldsymbol{U}_W)(\boldsymbol{U}_B\cdot\boldsymbol{U}_A)\\ &-\rho_A(\boldsymbol{K}_A\cdot\boldsymbol{U}_W)iK_{B\perp}^2\\ &-\rho_W(\boldsymbol{K}_W\cdot\boldsymbol{U}_A)iK_{B\perp}^2. && (3.58)\end{aligned}$$

Provided $c_1 \neq 0 \neq c_3$, the solvability conditions $G_{AZ} = G_{BZ} = 0$ thus constitute a coupled system of first order ODEs, which we refer to as the *amplitude equations*:

$$\frac{\mathrm{d}A}{\mathrm{d}\tau} = -\frac{c_2}{c_1}B, \quad \frac{\mathrm{d}B}{\mathrm{d}\tau} = -\frac{c_4}{c_3}A. \tag{3.59}$$

From this coupled system we can form a second order ODE in terms of A, which reads

$$\frac{\mathrm{d}^2A}{\mathrm{d}\tau^2} = \left(\frac{c_2c_4}{c_1c_3}\right)A.$$

Suppose we write solutions of this ODE as $A \propto \exp(s_\tau\tau)$. The complex growth rate s on the slow timescale is thus calculated via

$$s_\tau = \pm\sqrt{\frac{c_2c_4}{c_1c_3}}. \tag{3.60}$$

Since $\tau = aT$, the corresponding growth rate on the fast timescale is $s := as_\tau$, so

$$s = \pm a\sqrt{\frac{c_2c_4}{c_1c_3}}. \tag{3.61}$$

Equation (3.61) can be implemented numerically to predict instability growth rates at points in parameter space which exactly satisfy the resonance conditions (3.12) and (3.13). This achieves the first aim of this chapter. There is nothing to stop us from making further analytical progress by taking the following limit.

3.3.2 Short Wavelength Limit

Here we consider what happens to the leading order growth rate formula (3.61) in the limit in which the daughter waves have much shorter wavelengths than the primary wave, i.e. when

$$K_A \gg K, \quad K_B \gg K. \tag{3.62}$$

We saw earlier that this leads to the parametric subharmonic instability, which is represented by

$$\omega_B \approx -\omega_A \approx \omega/2. \tag{3.63}$$

We also have the following relations between daughter wave eigenvectors in this limit:

$$\boldsymbol{U}_A \approx \boldsymbol{U}_B, \quad \rho_A \approx -\rho_B. \tag{3.64}$$

Our aim is to use these assumptions to derive a formula for s which depends entirely on the parameters which prescribe the primary wave: a and θ. For each combination (a, θ), this serves as an estimate for the maximum growth rate across the space of disturbance wavenumber vectors in the absence of diffusion and in the limit $a \ll 1$. In other words, for $a \ll 1$ it represents the fastest-growing instability for each unique primary wave prescribed by (a, θ).

Simplifying the Growth Rate Formula

We start from the general expression for the theoretical growth rate on the fast timescale (3.61). We eliminate any appearances of daughter wave B from the coefficients c_i using relations (3.18)-(3.19), and neglect several terms by making order of magnitude estimates. Details of this process are included in Appendix A.3.3.

The resulting growth rate formula in the short wavelength limit is given by

$$s \approx \pm \frac{a(\boldsymbol{K}_W \cdot \boldsymbol{U}_A)}{2\omega_A K_A^2 K_{A\perp}^2} \left[\omega_A (\boldsymbol{U}_A \cdot \boldsymbol{U}_W) + i\rho_W K_{A\perp}^2 \right]. \tag{3.65}$$

2D Disturbances

In formula 3.65 for s, we can immediately express $\boldsymbol{K}_W$, $\boldsymbol{U}_W$ and ρ_W in terms of a and θ using (2.28) and (2.101):

$$s = \pm \frac{a}{4} \left(\frac{K_{AX} K_{AZ}}{K_{A\perp}^2} - \frac{\sin\theta}{\cos\theta} \right) \left[\cos\theta \left(\frac{K_{AX} K_{AZ}}{K_A^2} \right) + \frac{K_{A\perp}^2}{K_A^2} \left(\frac{\cos^2\theta + 2}{\sin\theta} \right) \right]. \tag{3.66}$$

To express the remaining quantities in terms of a and θ, we need to make one final assumption. We take disturbances to be two-dimensional by fixing $K_{AY} = 0$. This is justified later in Chapter 4 by the idea that the fastest-growing instabilities are observed on the axis along which $K_{AY} = 0$ in wavenumber space. Crucially, this means that $K_{A\perp}$ and K_A simplify to

$$K_{A\perp} = K_{AX}, \quad K_A = \sqrt{K_{AX}^2 + K_{AZ}^2}. \tag{3.67}$$

From (3.20) we know that

$$\frac{K_{AX}^2}{K_{AX}^2 + K_{AZ}^2} = \frac{\omega^2}{4N^2},$$

which can be rearranged to yield

$$\frac{K_{AZ}^2}{K_{AX}^2} = \frac{4N^2 - \omega^2}{\omega^2}. \tag{3.68}$$

Given that for pure internal gravity waves the dispersion relation is $\omega/N = \pm\cos\theta$, equations (3.67) and (3.68) can be used to deduce that

$$\frac{K_{AX}K_{AZ}}{K_{A\perp}^2} = \pm\frac{\sqrt{4-\cos^2\theta}}{\cos\theta}, \quad \frac{K_{AX}K_{AZ}}{K_A^2} = \pm\frac{\cos\theta}{4}\sqrt{4-\cos^2\theta}, \quad \frac{K_{A\perp}^2}{K_A^2} = \frac{\cos^2\theta}{4}.$$

This gives us everything we need to rewrite (3.66) in terms of a and θ only.

We arrive at the following growth rate formula which computes the fastest-growing 2D instability for any pair of a and θ values:

$$s(a,\theta) = \frac{a}{16}\frac{\cos\theta}{\sin\theta}\left[\pm 2\sin^3\theta + (1+2\cos^2\theta)\sqrt{4-\cos^2\theta}\right]. \tag{3.69}$$

This is identical to a formula obtained by Sonmor and Klaassen (1997), hereafter referred to as SK97, who took the same short disturbance wavelength limit:

$$s = \frac{A}{8}\cos\theta[\pm 2\sin^3\theta + (1+2\cos^2\theta)\sqrt{4-\cos^2\theta}]. \tag{3.70}$$

Equation (3.70) is presented as equation (9a) by SK97, who use a slightly different amplitude parameter to us which they call A. The conversion between the two amplitude parameters is

$$A = \frac{a}{2\sin\theta}.$$

This conversion formula is deduced from the fact that SK97's overturning threshold is

$$A > \frac{1}{2\sin\theta}.$$

Summary

We performed a multiple-scale analysis of TRIs of IGWs in stably-stratified Boussinesq fluids. We considered a fast timescale T on which the waves oscillate and a slow timescale τ on which the amplitude of the disturbance grows. This creates a theoretical framework with which to study TRIs of IGWs. We took the method of Cui and Latter (2022), originally devised for inertial waves, and applied it to IGWs.

There are two keystones to this chapter. The first of which is formula (3.61), which predicts the growth rate for parameter values at which exact triadic resonance is satisfied. The second of which is formula (3.69), which also predicts the growth rate for parameter values at which exact triadic resonance is satisfied, but with the additional requirement that the disturbance wavelength is much smaller than the primary wavelength. This represents the limit of PSI. It is the limit in which we observe the fastest-growing 2D instability associated with any particular primary wave prescribed by a and θ for $a \ll 1$.

An analytical formula for the growth rate of a TRI between IGWs was originally derived by Davis and Acrivos (1967). We presented a reformulation of this result. A formula in the short wavelength limit was originally derived by Sonmor and Klaassen (1997). Though the results derived in this chapter are not original, the way in which they are derived is original and provides a more transparent alternative to previous literature. It is useful to present the derivation and resulting formulae here because in Chapter 5 we will extend the framework to describe TRIs between small-amplitude AGWs in the presence of a magnetic field.

Chapter 3 presented a way of analysing instabilities of IGWs under a strict set of conditions, namely those specified by triadic resonance. IGW parametric instabilities are not limited to three-wave interactions, however. Any number of waves could interact to produce instabilities. In Chapter 4 we will analyse the instabilities of IGWs more broadly through the construction of a numerical eigenvalue problem. Such a task does not require the same strict adherence to triadic resonance conditions. At the end of Chapter 4 we will use formula (3.61) and formula (3.69) to vouch for some of the numerical results acquired.

Chapter 4

Instabilities of Finite-Amplitude IGWs

Chapter 3 used a small-amplitude approximation to theoretically predict the growth rate of TRIs between a plane IGW and two daughter IGWs. In this chapter we widen the scope of the stability analysis and remove this restriction on the size of the amplitude parameter a. Here, we use linear stability analysis to explore instabilities of finite-amplitude IGWs propagating through Boussinesq fluids with constant buoyancy frequency N.

Mied (1976) used a Floquet method to study 2D instabilities of IGWs in Boussinesq fluids. The method for linear stability analysis used in the present thesis is based on the method used by Lombard and Riley (1996), hereafter referred to as LR96, who were originally inspired by the method of Mied (1976). Like LR96, we use the method to assemble an eigenvalue problem from the equations of motion and use its numerical solution to understand instabilities of finite-amplitude IGWs. This adds to an existing body of work on the subject by Mied (1976), Drazin (1977), Klostermeyer (1982, 1983, 1991), LR96, SK97 and others. In particular, we build on their results by searching for instabilities in a wider range of parameter space and by exploring the eigenfunctions corresponding to the disturbance, which have not been presented in previous literature. We also provide a detailed comparison of our numerical results with the theoretical framework for TRIs of IGWs presented in Chapter 3, which is also lacking in previous literature. The method can be summarised as follows.

We first apply a coordinate transformation so that we can derive a one-dimensional eigenvalue problem to solve numerically instead of a multi-dimensional eigenvalue problem. We split variables into a fluctuating basic state and a disturbance. The transformed governing equations are then linearised with respect to this disturbance, to which we subject an eigenmode decomposition. Applying an aspect of Floquet theory and expressing all variables in terms of a Fourier series allows us to reduce the system of differential equations to a 1D algebraic eigenvalue problem. The resulting eigenvalues allow us to gauge the conditions (i.e. ranges of parameter values) under which instability arises. We wish to answer the following key questions, some of which have already been partially explored by the authors above:

1. How does the amplitude a of the primary wave influence the growth rate of the disturbance?

2. How does the primary wave orientation θ influence the growth rate of the disturbance?

3. How does the periodicity of the disturbance relative to the primary wave influence its growth rate?

4. What role do viscosity and thermal diffusion play?

5. Can we characterise the instabilities observed in terms of some kind of resonant interaction?

6. Can we reinforce the numerical results acquired using the theoretical results of Chapter 3?

4.1 Floquet Solver

4.1.1 The Basic State

Before diving into the process of linear stability analysis, let us clarify exactly what state we are perturbing.

We shall suppose that all dependent variables $F(\boldsymbol{X}, T)$ comprise two parts:

$$F(\boldsymbol{X}, T) = \tilde{F}(X, Z, T) + F'(X, Y, Z, T) \quad \text{for} \quad F \in \{\boldsymbol{U}, P, \rho\}, \tag{4.1}$$

where $\tilde{F}(X, Z, T)$ represents a plane wave solution to the Boussinesq equations in the absence of thermal diffusion and viscosity, which we refer to as the primary wave.

The plane wave solution has the following explicit form:

$$\tilde{\boldsymbol{U}}(X, Z, T) = 2a\boldsymbol{U}_W \cos(\boldsymbol{K} \cdot \boldsymbol{X} - \omega T), \tag{4.2}$$

$$\tilde{\rho}(X, Z, T) = 2ia\rho_W \sin(\boldsymbol{K} \cdot \boldsymbol{X} - \omega T), \tag{4.3}$$

where $\boldsymbol{K} := K_X\hat{\boldsymbol{X}} + K_Z\hat{\boldsymbol{Z}} = K\hat{\boldsymbol{K}}$ is its wavevector and ω is its angular frequency.

The coefficients $\boldsymbol{U}_W$ and ρ_W are given by

$$\boldsymbol{U}_W := \frac{\omega}{2}\left(\frac{\hat{\boldsymbol{X}}}{K_X} - \frac{\hat{\boldsymbol{Z}}}{K_Z}\right), \quad \rho_W := \frac{i}{2K_Z}\frac{\mathrm{d}\bar{\rho}}{\mathrm{d}Z}. \tag{4.4}$$

In Section 2.4 we showed that (4.4) are a sensible choice of coefficients for the plane wave solution, configured such that $a = 1$ serves as the threshold amplitude beyond which overturning occurs. The plane wave $\tilde{F}$ forms the basic state for our stability analysis, with F' representing perturbations to that basic state. The perturbations we consider are three-dimensional and their associated diffusion is treated as non-zero.

This plane wave constitutes an exact solution to the nonlinear equations of motion in the absence of diffusion. In this chapter, the wave can be classified as a propagating IGW. The fact that it is an exact nonlinear solution is crucial because it allows us to perform a linear stability analysis at *any* value of the amplitude parameter a. This is the most important difference between this chapter's method of stability analysis and the asymptotic calculation presented in Chapter 3. The method from Chapter 3 is strictly valid on the assumption that a is small.

4.1.2 The Coordinate Transformation

We undergo a coordinate transformation from (X, Y, Z)-coordinates to (x, y, z)-coordinates. We establish a new (x, z)-frame by rotating the axes about Y such that the vertical axis coincides

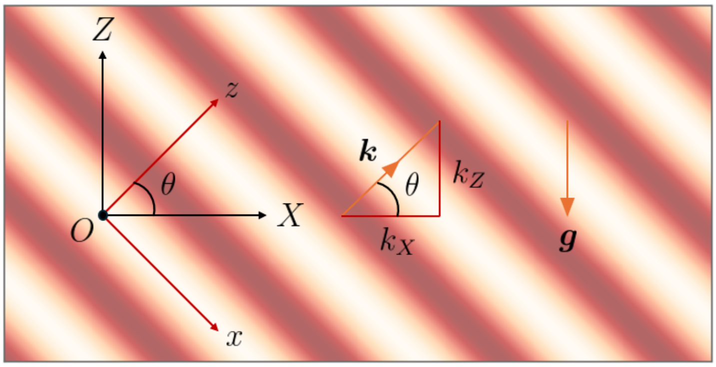

Figure 4.1: Coordinate configuration showing the relative orientations of the (X, Z) and (x, z)-frames.

with the primary wavevector $\boldsymbol{K}$. This is illustrated in Figure 4.1. The Y-coordinate is unaffected by the rotation of the axes, i.e. the Y-axis (and the y-axis) both point directly 'into the page' in Figure 4.1. Additionally, the (x, z)-frame moves at phase speed $c_p = \omega/K$ with respect to the (X, Z)-frame, in the direction of the wavevector $\boldsymbol{K}$ pertaining to the primary wave. This means that the z-coordinate in the new frame represents the wave phase. Therefore, to an observer in the (X, Z)-plane, the wave appears to be propagating, but to an observer in the (x, z)-plane, the wave appears to be stationary.

This transformation is heavily inspired by that which was first applied by Mied (1976). Its purpose is to reduce the number of axes along which the wave is periodic. In other words, in the original (X, Y, Z)-coordinates, the wave is periodic in two directions (X and Z) as well as time T, but in the new (x, y, z)-coordinates, the wave is periodic in one variable only (z).

In Figure 4.1, we need only consider two dimensions for each coordinate frame since the base wave is planar. Based on the configuration depicted in Figure 4.1, we must have $x = \boldsymbol{K}_P \cdot \boldsymbol{X}$, where $\boldsymbol{K}_P$ is defined as

$$\boldsymbol{K}_P := K_Z \hat{\boldsymbol{X}} - K_X \hat{\boldsymbol{Z}},$$

the vector perpendicular to the wavevector $\boldsymbol{K}$ within the (X, Z)-plane. This is because the new coordinate x represents the component of the original position vector $\boldsymbol{X} := (X, Y, Z)$ in the direction of $\boldsymbol{K}_P$. Similarly, the wave phase z must satisfy

$$z := \boldsymbol{K} \cdot \boldsymbol{X} - \omega T,$$

since z must instead represent the component of $\boldsymbol{X}$ in the direction of the wavevector itself, $\boldsymbol{K}$. Here, we also need to account for the fact that the new frame is moving with respect to the old frame. Clearly, we must subtract the displacement quantity ωT to account for the amount by which a fixed point in the (X, Z)-frame has moved in the (x, z)-frame after time T has elapsed.

The Y coordinate is unchanged by the transformation, so we simply nondimensionalise it with the wavevector magnitude $K := \|\boldsymbol{K}\|$, giving $y = KY$. The spatial coordinate transformation is hence given by

$$\begin{pmatrix} x \\ y \\ z \end{pmatrix} = \begin{pmatrix} K_Z & 0 & -K_X \\ 0 & K & 0 \\ K_X & 0 & K_Z \end{pmatrix} \begin{pmatrix} X \\ Y \\ Z \end{pmatrix} - \begin{pmatrix} 0 \\ 0 \\ \omega T \end{pmatrix}. \tag{4.5}$$

Each of (x, y, z) are dimensionless. To derive the formulae for the velocity component transformation, we note that by definition we have

$$\boldsymbol{U} := \frac{\mathrm{D}\boldsymbol{X}}{\mathrm{D}T}, \quad \text{so} \quad \boldsymbol{u} := \frac{1}{N}\frac{\mathrm{D}\boldsymbol{x}}{\mathrm{D}T}, \tag{4.6}$$

where $\boldsymbol{x} := (x, y, z)$ is the position vector in the rotated coordinate system. The factor of $1/N$ is introduced as our unit of time because we would like all of our transformed variables to be dimensionless. In this system, $\mathrm{D}_T := \partial_T + \boldsymbol{U} \cdot \nabla$. The velocity component transformation is therefore

$$\begin{pmatrix} u_x \\ u_y \\ u_z \end{pmatrix} = \frac{1}{N} \begin{pmatrix} K_Z & 0 & -K_X \\ 0 & K & 0 \\ K_X & 0 & K_X \end{pmatrix} \begin{pmatrix} U_X \\ U_Y \\ U_Z \end{pmatrix} - \begin{pmatrix} 0 \\ 0 \\ \omega/N \end{pmatrix}. \tag{4.7}$$

The remaining variables to be transformed are

$$\varrho = -\frac{K_Z \rho}{\mathrm{d}\bar{\rho}/\mathrm{d}Z}, \quad p = \frac{K^2 P}{\rho_0 N^2} \quad \text{and} \quad t = NT. \tag{4.8}$$

To obtain each of these three variables, we have merely nondimensionalised the corresponding variable in the original set of variables. None of these variables are affected by rotating the axes, so no transformation associated with rotation has been applied.

The dimensionless plane wavevector components are

$$k_X = K_X/K = \cos\theta, \quad k_Z = K_Z/K = \sin\theta. \tag{4.9}$$

We also acquire a dimensionless, transformed dispersion relation:

$$\frac{\omega}{N} = \pm\cos\theta. \tag{4.10}$$

The equations to be transformed are the dimensional Boussinesq equations for a stably-stratified fluid with constant buoyancy frequency N in the absence of a magnetic field. This system is the hydrodynamic equivalent of the system which first appeared in Chapter 2 as (2.22)-(2.26):

$$\nabla \cdot \boldsymbol{U} = 0, \tag{4.11}$$

$$\frac{\mathrm{D}\boldsymbol{U}}{\mathrm{D}T} = -\frac{1}{\rho_0}\nabla P + \frac{\rho \boldsymbol{g}}{\rho_0} + \nu\nabla^2\boldsymbol{U}, \tag{4.12}$$

$$\frac{\mathrm{D}\rho}{\mathrm{D}T} = -U_Z\frac{\mathrm{d}\bar{\rho}}{\mathrm{d}Z} + \kappa\nabla^2\rho. \tag{4.13}$$

We now state the governing equations for this chapter.

The complete set of governing equations we acquire as a result of applying the coordinate transformation to the original governing equations (4.11)-(4.13) is

$$\frac{\mathrm{D}\boldsymbol{u}}{\mathrm{D}t} = \frac{\nabla^2\boldsymbol{u}}{\mathrm{Re}} - \nabla p + \left(\frac{k_x}{k_z}\hat{\boldsymbol{x}} - \hat{\boldsymbol{z}}\right)\varrho, \tag{4.14}$$

$$\frac{\mathrm{D}\varrho}{\mathrm{D}t} = \frac{\nabla^2\varrho}{\mathrm{Pe}} + k_z\left(k_z u_z - k_x u_x + \frac{k_z\omega}{N}\right), \tag{4.15}$$

along with the divergence-free constraint $\nabla \cdot \boldsymbol{u} = 0$.

The equations (4.14)-(4.15) are derived by inverting the coordinate transformation (4.7) (i.e. obtaining expressions for U_X, U_Y and U_Z in terms of u_x, u_y and u_z) and expressing all differential operators in $\boldsymbol{X}$ and T in terms of $\boldsymbol{x}$ and t. Here Re is the *fluid Reynolds number* and Pe

is the *thermal Péclet number*. According to our temporal scaling $1/N$ and spatial scaling $1/K$, these have the following formulae in our system:

$$\mathrm{Re} := \frac{N}{\nu K^2}, \quad \mathrm{Pe} := \frac{N}{\kappa K^2}. \tag{4.16}$$

The Lagrangian derivative in rotated coordinates is given by

$$\frac{\mathrm{D}}{\mathrm{D}t} := \frac{\partial}{\partial t} + \boldsymbol{u} \cdot \nabla,$$

and ∇ is now interpreted as

$$\nabla := \hat{\boldsymbol{x}}\partial_x + \hat{\boldsymbol{y}}\partial_y + \hat{\boldsymbol{z}}\partial_z,$$

in the rotated coordinate system.

The transformed plane wave solution is

$$\tilde{u}_x(z) = 2u_w \cos z, \quad \tilde{u}_z = -\omega/N, \quad \tilde{\varrho}(z) = 2\varrho_w \sin z, \tag{4.17}$$

with amplitudes u_w and ϱ_w given by

$$u_w := \frac{a}{2k_z}, \quad \varrho_w = \frac{a}{2}.$$

4.1.3 Constructing an Eigenvalue Problem

Constructing a System of ODEs

The construction of the eigenvalue problem begins with linearisation. We decompose dependent variables into the static background state, the primary wave and a disturbance.

We adopt a decomposition of the form

$$\boldsymbol{u}(x,y,z,t) = \tilde{\boldsymbol{u}}(z) + \boldsymbol{u'}(x,y,z,t), \tag{4.18}$$
$$p(x,y,z,t) = \tilde{p}(z) + p'(x,y,z,t), \tag{4.19}$$
$$\varrho(x,y,z,t) = \tilde{\varrho}(z) + \varrho'(x,y,z,t), \tag{4.20}$$

where $\tilde{f}$ and f' for $f \in \{\boldsymbol{u}, \boldsymbol{p}, \varrho\}$ are the transformed, dimensionless forms of the variables defined in §4.1.1. Applying this decomposition, accounting for the fact that the plane wave $\tilde{f}$ is an exact nonlinear solution and linearising yields

$$\frac{\partial \boldsymbol{u'}}{\partial t} + \tilde{\boldsymbol{u}} \cdot \nabla \boldsymbol{u'} + \boldsymbol{u'} \cdot \nabla \tilde{\boldsymbol{u}} = \frac{\nabla^2 \boldsymbol{u'}}{\mathrm{Re}} - \nabla p' + \left(\frac{k_x}{k_z}\hat{\boldsymbol{x}} - \hat{\boldsymbol{z}}\right)\varrho', \tag{4.21}$$
$$\frac{\partial \varrho'}{\partial t} + \tilde{\boldsymbol{u}} \cdot \nabla \varrho' + \boldsymbol{u'} \cdot \nabla \tilde{\varrho} = \frac{\nabla^2 \varrho'}{\mathrm{Pe}} + k_z(k_z u_z' - k_x u_x'), \tag{4.22}$$
$$\nabla \cdot \boldsymbol{u'} = 0. \tag{4.23}$$

It is now apparent why there was no incentive to derive an explicit trigonometric expression for the basic pressure fluctuation $\tilde{p}$ in (4.17). The linearised equations contain appearances of each of $\tilde{u}_x, \tilde{u}_z$ and $\tilde{\varrho}$, but no appearances of $\tilde{p}$.

As is typical in linear stability analysis, we now assume a separable form of the perturbations. Since z represents the phase of the primary wave, it is useful to separate the z-dependence of perturbations from the dependence on the other independent variables x, y and t.

Namely, we introduce the eigenmode decomposition

$$f'(x,y,z,t) = f^\dagger(z)\exp(i\alpha x + i\beta y + \sigma t), \quad \text{for} \quad f \in \{\boldsymbol{u}, p, \varrho\}. \tag{4.24}$$

Above, $\alpha, \beta \in \mathbb{R}$ are the x and y components of the 'disturbance wavevector' in the (x, y, z) coordinate system. This disturbance wavevector (α, β) is the wavevector in the transformed coordinate system associated with disturbances to the primary wave. The quantity $\sigma \in \mathbb{C}$ is the complex growth rate of the disturbance. There is no appearance of z in the exponent from (4.24) because the linearised governing equations have explicit z-dependence. x, y and t on the other hand are not variables for which the linearised equations exhibit explicit dependence, so we are free to include each of them in the exponential part of the solution (4.24). This explains why the z-dependence of the solution (4.24) must instead be incorporated into the amplitude $f^\dagger$ of these perturbations. We define the convective derivative operator c and the Laplacian operator l as

$$c := \sigma + i\alpha\tilde{u}_x + \tilde{u}_z\frac{\mathrm{d}}{\mathrm{d}z}, \quad l := -\alpha^2 - \beta^2 + \frac{\mathrm{d}^2}{\mathrm{d}z^2}. \tag{4.25}$$

The linearised PDEs (4.21)-(4.23) become a system of ODEs:

$$c\boldsymbol{u}^\dagger + u_z^\dagger\frac{\mathrm{d}\tilde{\boldsymbol{u}}}{\mathrm{d}z} = \frac{l\boldsymbol{u}^\dagger}{\mathrm{Re}} - \left(i\alpha\hat{\boldsymbol{x}} + i\beta\hat{\boldsymbol{y}} + \hat{\boldsymbol{z}}\frac{\mathrm{d}}{\mathrm{d}z}\right)p^\dagger + \frac{k_x\varrho^\dagger}{k_z} - \varrho^\dagger\hat{\boldsymbol{z}}, \tag{4.26}$$

$$c\varrho^\dagger + u_z^\dagger\frac{\mathrm{d}\tilde{\varrho}}{\mathrm{d}z} = \frac{l\varrho^\dagger}{\mathrm{Pe}} + k_z(k_z u_z^\dagger - k_x u_x^\dagger), \tag{4.27}$$

$$i\alpha u_x^\dagger + i\beta u_y^\dagger + \frac{\mathrm{d}u_z^\dagger}{\mathrm{d}z} = 0. \tag{4.28}$$

Incorporating Floquet Theory

As described by Bender and Orszag (1999), *Floquet theory* is the common name given to the theory of linear differential equations with periodic coefficients. An elementary aspect of Floquet theory concerns second order linear ordinary differential equations for dependent variable $f(z)$ with independent variable z of the form

$$c_1(z)\frac{\mathrm{d}^2 f}{\mathrm{d}z^2} + c_2(z)\frac{\mathrm{d}f}{\mathrm{d}z} + c_3(z)f + c_4(z) = 0, \tag{4.29}$$

for which each coefficient c_1, c_2, c_3 and c_4 is a 2π-periodic function of z. Bender and Orszag (1999) explain in detail why the solution $f(z)$ of any equation satisfying the above criteria can be written as

$$f(z) = \exp(\mu z)\hat{f}(z),$$

where μ is complex in general and $\hat{f}$ is a 2π-periodic function of z. Clearly, (4.29) can be generalised to vector-valued dependent variables (with the coefficients c_1, c_2, c_3 and c_4 becoming matrices). One can thus notice that equations (4.26)-(4.28) can be cast as a second-order linear ordinary differential equation of type (4.29) if we choose z to be the independent variable and choose the vector $(u_x^\dagger, u_y^\dagger, u_z^\dagger, p^\dagger, \varrho^\dagger)$ to be the dependent variable, since each matrix-valued coefficient function is either 2π-periodic in z or constant in this case.

As a consequence, we may write $f^\dagger(z) = \exp(\mu z)\hat{f}(z)$, for some quantity μ. This chapter deals with finite-amplitude internal gravity waves, so in compliance with this restriction, we demand that μ is purely imaginary on a physical basis.

Equivalently, we may cast μ as $\mu := i\gamma$ for some $\gamma \in \mathbb{R}$, yielding the decomposition

$$f^\dagger(z) = \exp(i\gamma z)\hat{f}(z) \quad \text{for} \quad f \in \{\boldsymbol{u}, p, \varrho\}. \tag{4.30}$$

The object γ is called the *Floquet modulation parameter* in this context. It determines the periodicity of the perturbations. A detailed account of its physical significance is provided by Sonmor and Klaassen (1997). Before going any further, we define two new operators to simplify the algebra. These are the convective derivative operator C and the Laplacian operator L:

$$C := \sigma + i\alpha\tilde{u}_x + \tilde{u}_z\left(i\gamma + \frac{\mathrm{d}}{\mathrm{d}z}\right), \quad L := -\alpha^2 - \beta^2 + \left(i\gamma + \frac{\mathrm{d}}{\mathrm{d}z}\right)^2. \tag{4.31}$$

We get the following system of equations when applying (4.30) to (4.26)-(4.28).

$$C\hat{\boldsymbol{u}} + \hat{u}_z\frac{\mathrm{d}\tilde{\boldsymbol{u}}}{\mathrm{d}z} = \frac{L\hat{\boldsymbol{u}}}{\mathrm{Re}} - \left[i\alpha\hat{\boldsymbol{x}} + i\beta\hat{\boldsymbol{y}} + \hat{\boldsymbol{z}}\left(i\gamma + \frac{\mathrm{d}}{\mathrm{d}z}\right)\right]\hat{p} + \frac{k_x\hat{\varrho}}{k_z}\hat{\boldsymbol{x}} - \hat{\varrho}\hat{\boldsymbol{z}}, \tag{4.32}$$

$$C\hat{\varrho} + \hat{u}_z\frac{\mathrm{d}\tilde{\varrho}}{\mathrm{d}z} = \frac{L\hat{\varrho}}{\mathrm{Pe}} + \frac{k_z}{k^2}(k_z\hat{u}_z - k_x\hat{u}_x), \tag{4.33}$$

along with

$$i\alpha\hat{u}_x + i\beta\hat{u}_y + \left(i\gamma + \frac{\mathrm{d}}{\mathrm{d}z}\right)\hat{u}_z = 0. \tag{4.34}$$

Constructing a Matrix Equation

We now express each variable using a Fourier series representation.

This involves letting

$$\hat{f}(z) = \textstyle\sum_{n=-\infty}^{\infty} f_n \exp(inz) \quad \text{for} \quad f \in \{\boldsymbol{u}, p, \varrho\}. \tag{4.35}$$

Overall, by combining decomposition (4.35) with decompositions (4.30) and (4.24), we arrive at the following expression for perturbation quantities f':

$$f'(x, y, z, t) = \textstyle\sum_{n=-\infty}^{\infty} f_n \exp\left[i\alpha x + i\beta y + i(n+\gamma)z + \sigma t\right]. \tag{4.36}$$

The objects α, β and γ are purely real, so the quantity $i\alpha x + i\beta y + i(n+\gamma)z$ must be purely imaginary. As a result, σt is the only term in the exponent of (4.36) which can contribute to the exponential growth of a disturbance, since it is the only term that can have a non-zero real part. The growth rate of the observed instability (when it occurs) is therefore $\Re(\sigma)$. Instability occurs when $\Re(\sigma) > 0$. For this reason, we proceed by constructing an eigenvalue problem for which σ is the eigenvalue from equations (4.32)-(4.33). It is advantageous to exclude the divergence-free constraint (4.34) from the eigenvalue problem because it contains no appearances of the eigenvalue σ. We then need only take the real part of the eigenvalues σ found to obtain the growth rates we seek. Note also that the imaginary part of the eigenvalues σ represents the oscillatory frequency of the perturbations in the moving coordinate frame (x, y, z).

Though it is advantageous to remove the divergence-free constraint (4.34), it is not strictly necessary to do so in order to solve the system for stability. We could retain the divergence-free constraint and piece together a generalised eigenvalue problem in place of the standard eigenvalue problem which follows. Selecting this option would be more computationally expensive, though, so we opt for the standard eigenvalue problem.

Upon substitution of (4.35), we find that the complete set of Fourier space equations of motion (4.38)-(4.42) contains all equations needed to produce the eigenvalue problem (plus a few more). Below, the algebraic Laplacian operator L_n is defined as

$$L_n := -\alpha^2 - \beta^2 - (\gamma + n)^2. \tag{4.37}$$

To simplify the algebra, we define

$$\Gamma_n^\nu = L_n/\mathrm{Re} - i\tilde{u}_z(\gamma + n),$$
$$\Gamma_n^\kappa = L_n/\mathrm{Pe} - i\tilde{u}_z(\gamma + n).$$

We also define the disturbance wavevector as

$$\boldsymbol{k}' := \alpha\hat{\boldsymbol{x}} + \beta\hat{\boldsymbol{y}} + (\gamma + n)\hat{\boldsymbol{z}}.$$

The Fourier space momentum equation components are

$$(\sigma - \Gamma_n^\nu)u_n^x = -\,i\alpha p_n + (k_x/k_z)\varrho_n - i\alpha u_w(u_{n-1}^x + u_{n+1}^x) + iu_w(u_{n+1}^z - u_{n-1}^z), \tag{4.38}$$
$$(\sigma - \Gamma_n^\nu)u_n^y = -\,i\beta p_n - i\alpha u_w(u_{n-1}^y + u_{n+1}^y), \tag{4.39}$$
$$(\sigma - \Gamma_n^\nu)u_n^z = -\,i(\gamma + n)p_n - \varrho_n - i\alpha u_w(u_{n-1}^z + u_{n+1}^z). \tag{4.40}$$

The Fourier space thermodynamic equation is

$$(\sigma - \Gamma_n^\kappa)\varrho_n = k_z(k_z u_n^z - k_x u_n^x) - i\alpha u_w(\varrho_{n-1} + \varrho_{n+1}) - i\varrho_w(u_{n-1}^z + u_{n+1}^z). \tag{4.41}$$

The Fourier space solenoidal constraint is

$$i\alpha u_n^x + i\beta u_n^y + i(\gamma + n)u_n^z = 0. \tag{4.42}$$

Echoing Klostermeyer (1991), we can form an equation with p_n as the subject in order to eliminate p_n from the momentum equation, thereby reducing the size of the system and improving efficiency. On top of this, it serves as a 'replacement' for the divergence-free constraint (4.42), since, as already stated, this must be excluded in order to form a standard eigenvalue problem (rather than a generalised eigenvalue problem). We form such an equation by taking $i\alpha\hat{\boldsymbol{x}} \cdot (4.32) + i\beta\hat{\boldsymbol{y}} \cdot (4.32) + (i\gamma + \mathrm{d}_z)\hat{\boldsymbol{z}}(4.32)$, which, in terms of Fourier modes, leaves

$$L_n p_n = i[\alpha k_x/k_z - (\gamma + n)]\varrho_n + 2\alpha u_w(u_{n-1}^z - u_{n+1}^z). \tag{4.43}$$

Equations (4.38)-(4.43) are identical to equations (16b)-(16f) from LR96. Equation (4.43) corrects a typographical error from LR96, namely the sign of the u_{n+1}^z term in (16f).

As stated previously, the mass continuity equation does not feature in the eigenvalue problem. We need not make use of equations (4.39) or (4.43) in the eigenvalue problem either. To explain why, we note that the mass continuity equation from (4.42) can be used to eliminate any one of u_n^x, u_n^y or u_n^z from the remaining equations. Observe also that each of u_n^x, u_n^z and ϱ_n are completely decoupled from u_n^y in the momentum and thermodynamic equations. It therefore makes sense to choose to express u_n^y in terms of u_n^x and u_n^z using (4.42). It is achievable to eliminate p_n from (4.38) and (4.40) through (4.43) and then construct an eigenvalue problem in terms of u_n^x, u_n^z and ϱ_n alone. From there, p_n can be calculated via (4.43). The variable u_n^y can then be calculated via (4.42). In other words, $u_n^x, u_n^y, u_n^z, \varrho_n$ and p_n can all be found even if u_n^y and p_n are excluded from the eigenvalue problem.

Hence, we can arrive at a system of 3 equations for each value of n that we consider. To implement this system numerically we must truncate the infinite series into a finite series, still centred at $n = 0$. We use $2\mathcal{N} + 1$ modes in the calculation, such that

$$\hat{f}(z) = \textstyle\sum_{n=-\mathcal{N}}^{\mathcal{N}} f_n \exp(inz) \quad \text{for} \quad f \in \{\boldsymbol{u}, p, \varrho\}. \tag{4.44}$$

Substitution of (4.43) into (4.38)-(4.40) and (4.41) reveals that the eigenvalue problem is

$$M\boldsymbol{v} = \sigma \boldsymbol{v}, \tag{4.45}$$

where $\boldsymbol{v}$ is the vector defined as

$$\boldsymbol{v} = (u_{-\mathcal{N}}^x, u_{-\mathcal{N}}^z, \varrho_{-\mathcal{N}}, \dots, u_0^x, u_0^z, \varrho_0, \dots, u_{\mathcal{N}}^x, u_{\mathcal{N}}^z, \varrho_{\mathcal{N}}).$$

We define the matrix M as

$$M = \begin{pmatrix} M_{-\mathcal{N}}^2 & M_{-\mathcal{N}}^3 & & & & & & & & \mathbb{O} \\ M_{1-\mathcal{N}}^1 & M_{1-\mathcal{N}}^2 & M_{1-\mathcal{N}}^3 & & & & & & & \\ & M_{2-\mathcal{N}}^1 & M_{2-\mathcal{N}}^2 & M_{2-\mathcal{N}}^3 & & & & & & \\ & & \ddots & \ddots & \ddots & & & & & \\ & & & M_0^1 & M_0^2 & M_0^3 & & & & \\ & & & & \ddots & \ddots & \ddots & & & \\ & & & & & M_{\mathcal{N}-2}^1 & M_{\mathcal{N}-2}^2 & M_{\mathcal{N}-2}^3 & & \\ & & & & & & M_{\mathcal{N}-1}^1 & M_{\mathcal{N}-1}^2 & M_{\mathcal{N}-1}^3 \\ \mathbb{O} & & & & & & & M_{\mathcal{N}}^1 & M_{\mathcal{N}}^2 \end{pmatrix},$$

where M_n^1, M_n^2 and M_n^3 are 3×3 matrix-valued functions of n (i.e. 3×3 blocks) extracted from the coefficients in (4.38)-(4.43), and $\mathbb{O}$ represents an appropriately-sized block of zeroes. The individual entries within matrices M_n^1, M_n^2 and M_n^3 are listed in Appendix A.2.1. This is a sparse tri-diagonal system of 3×3 blocks, which is efficiently solved numerically via the Numpy routine `linalg.eig`. The system would still have been efficiently solved had we not replaced the mass continuity equation with (4.43) and left the system as a generalised eigenvalue problem, just not quite as quickly. In Section 4.2 we present the results of solving (4.45) numerically for eigenvalue σ.

4.2 Growth Rates

The truncated Fourier series representation for disturbances is

$$f'(x, y, z, t) = \textstyle\sum_{n=-\mathcal{N}}^{\mathcal{N}} f_n \exp\left[i\alpha x + i\beta y + i(n + \gamma)z + \sigma t\right]. \tag{4.46}$$

In this section we are interested in two quantities:

1. $\Re(\sigma)$, which represents the *exponential growth rate* of the disturbance,
2. $\Im(\sigma)$, which represents the *oscillatory frequency* of the disturbance.

We call σ itself the *complex growth rate* of the disturbance.

Values of σ with positive real parts represent *direct instability* if $\Im(\sigma) = 0$, but if $\Im(\sigma) \neq 0$ then the mode is said to be *overstable*. We can determine which of these two categories the instabilities fall into by plotting these quantities as a function of various parameters.

Upon solving this numerical eigenvalue problem, the first task is to contour the growth rate in (α, β)-space, revealing which modes of disturbance are subject to instability. We take an $n_\alpha \times n_\beta$ grid of α and β values and solve the eigenvalue problem individually for each of these pairs. We obtain a set of $6\mathcal{N} + 3$ eigenvalues for each pair. For each set of $6\mathcal{N} + 3$ values for σ, the recorded growth rate is the largest positive value of $\Re(\sigma)$. In other words we record only the fastest-growing mode for each pair of (α, β) values. Any negative values of $\Re(\sigma)$ are set to zero in the growth rate contours that follow.

For most of these results, the Floquet modulation parameter is fixed at $\gamma = 0$. We dedicate a section to observing the impact of varying γ, however. We specify the frequency of the primary wave through specifying the primary wave orientation θ. For a given angle θ, the dimensionless frequency of the primary wave is $\omega/N = \cos\theta$.

Disturbance Frequencies in Different Reference Frames

The quantity $\Im(\sigma)$ represents the frequency of the disturbance in the transformed frame, which is in motion with respect to the original reference frame. How do we relate $\Im(\sigma)$ to the frequency ω' of the disturbance in the original reference frame? We have to account for the coordinate transformation and the Doppler effect. We start by equating the exponents of the perturbations in the different coordinate systems. In the original frame, perturbations F' are given by

$$F' = \textstyle\sum_{n=-\mathcal{N}}^{\mathcal{N}} F_n \exp[iK'_X X + iK'_Y Y + iK'_Z Z + ST].$$

In the transformed frame, perturbations f' are given by

$$f' = \textstyle\sum_{n=-\mathcal{N}}^{\mathcal{N}} f_n \exp[i\alpha x + i\beta y + i(\gamma + n)z + \sigma t].$$

If we equate exponents for any n then

$$i\boldsymbol{k'} \cdot \boldsymbol{x} + \sigma t = i\boldsymbol{K'} \cdot \boldsymbol{X} + ST,$$

where the disturbance wavevectors are defined as

$$\begin{aligned} \boldsymbol{k}' &\coloneqq \alpha\hat{\boldsymbol{x}} + \beta\hat{\boldsymbol{y}} + (\gamma + n)\hat{\boldsymbol{z}}, \\ \boldsymbol{K}' &\coloneqq K'_X\hat{\boldsymbol{X}} + K'_Y\hat{\boldsymbol{Y}} + K'_Z\hat{\boldsymbol{Z}}. \end{aligned}$$

We can replace transformed variables with original variables:

$$i\alpha(K_Z X - K_Z Z) + i\beta Y + i(\gamma + n)(\boldsymbol{K} \cdot \boldsymbol{X} - \omega T) + \sigma NT = i\boldsymbol{K'} \cdot \boldsymbol{X} + ST.$$

Equating coefficients of T yields

$$S = N\sigma - i\omega(\gamma + n). \tag{4.47}$$

Hence the numerical disturbance frequencies in the original frame are given by

$$\omega' := -\Im(S) = -\Im[N\sigma - i\omega(\gamma + n)] = \omega(\gamma + n) - N\Im(\sigma).$$

The dimensionless analogue of this equation is

$$\frac{\omega'}{N} = \frac{\omega}{N}(\gamma + n) - \Im(\sigma). \tag{4.48}$$

4.2.1 Characterising the Instability

Figure 4.2 depicts the growth rate of the most unstable mode of disturbance at each point on a grid of (α, β) values for IGWs with $a = 0.1$ and $\theta = \pi/4$. This reproduces a result originally found by LR96. The most unstable modes appear along the line $\beta = 0$, which corresponds with the (X, Z)-plane to which the primary wavevector is confined. There are many other unstable modes of disturbance with non-zero β which lie outside of this plane. Unstable modes are grouped into bands which we call 'tongues'.

The 'tongue' formation of instability bands that appears is characteristic of parametric instability and such contours are commonplace in associated research literature, often when a Mathieu equation is involved. McEwan and Robinson (1975) were the first to study parametric instabilities of IGWs by solving a Mathieu equation. The tongue formation also appears when studying growth rates of parametric instabilities of other types of waves, such as kink modes in the solar corona (e.g Hillier et al., 2019).

The central curve traversing each tongue represents a centre of exact resonance for the parametric instability. The edges of each tongue represent the bounds for each resonance. In Figure 4.3 we explain what each of these 'tongues' of instability correspond to mathematically.

Figure 4.3 reveals that progressively adding an additional term either side of zero in the truncated Fourier series representation (4.46) for disturbances f' produces a single new band of instability in (α, β)-space. Through the theory of Chapter 3 we may specify the exact nature of the resonant interaction which occurs to produce each of these bands of instability. It turns out that each band of instability visible in Figure 4.2 is produced by a resonant triad of IGWs (LR96).

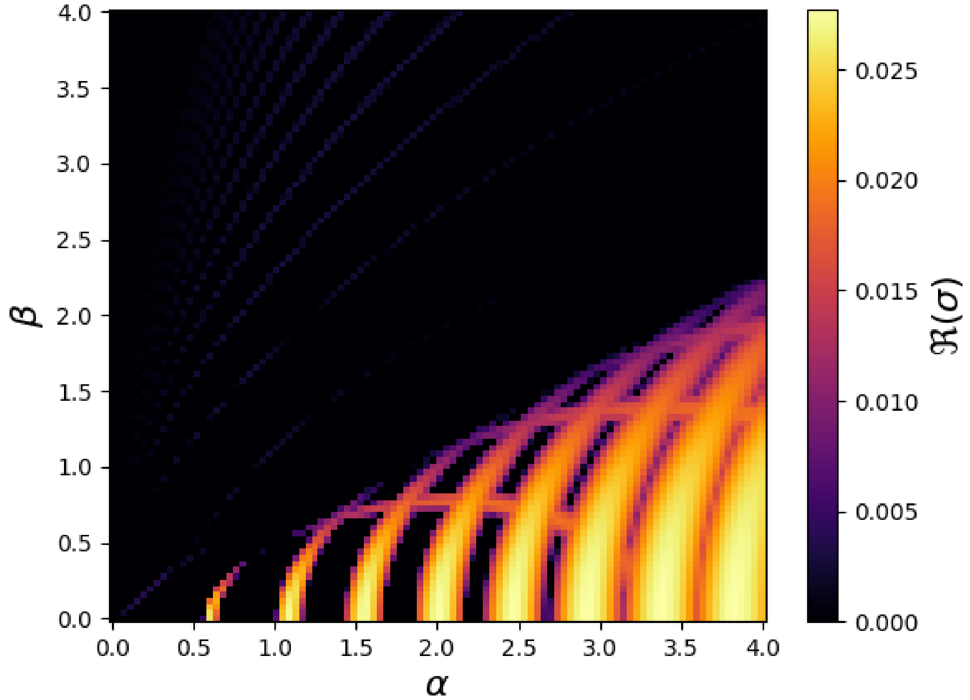

Figure 4.2: Contouring the growth rate of instabilities of an IGW in (α, β)-space. Parameter values: $a = 0.1$, $\theta = \pi/4$, $\gamma = 0$ and $\mathrm{Re} = \mathrm{Pe} = 10^6$. Resolution: $\mathcal{N} = 10$, $n_\alpha = n_\beta = 100$.

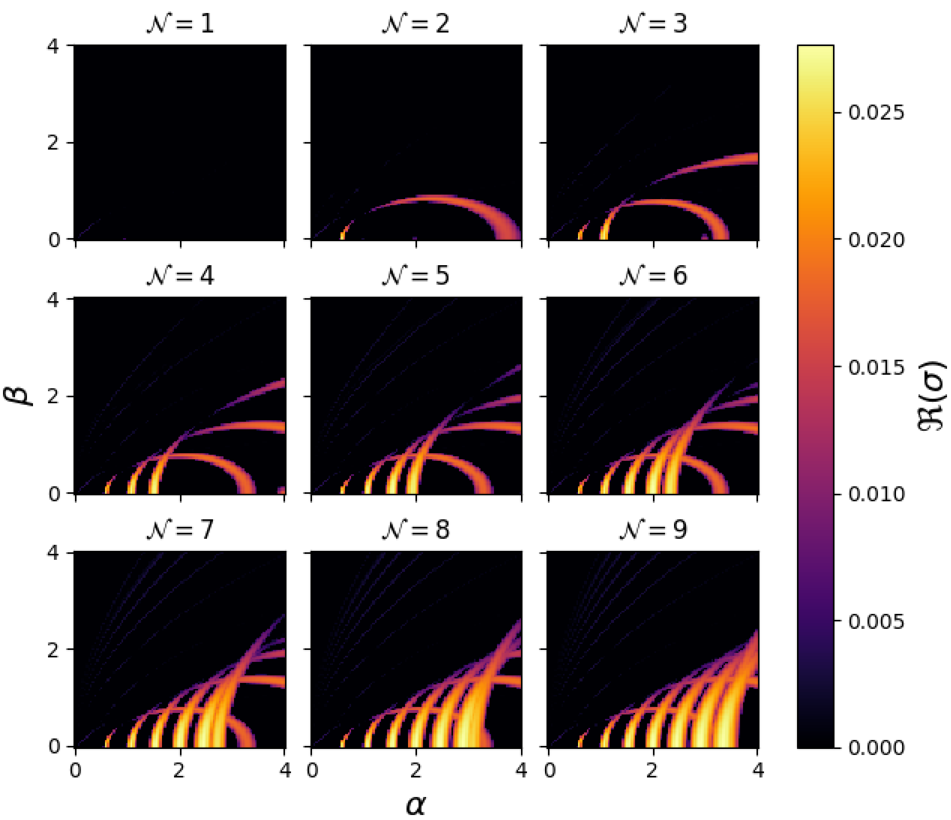

Figure 4.3: Relationship between the truncation point $\mathcal{N}$ of the Fourier series and the number of centres of exact resonance in (α, β)-space. Parameter values are identical to those used in Figure 4.2.

Exact Resonances in the Transformed Frame

Recall from Section 3.2 that resonant triads are represented by

$$\boldsymbol{k} + \boldsymbol{k}_A - \boldsymbol{k}_B = 0, \tag{4.49}$$
$$\omega + \omega_A - \omega_B = 0. \tag{4.50}$$

where A and B are two Fourier components of the Floquet solution. Define the disturbance wavevector $\boldsymbol{k}_n$ as

$$\boldsymbol{k}_n := \alpha\hat{\boldsymbol{x}} + \beta\hat{\boldsymbol{y}} + (\gamma + n)\hat{\boldsymbol{z}}.$$

In the transformed frame, recall that the primary wavevector is just

$$\boldsymbol{k} = \hat{\boldsymbol{z}}.$$

Notice that

$$\boldsymbol{k} - \boldsymbol{k}_n + \boldsymbol{k}_{n-1} = \begin{pmatrix} 0 \\ 0 \\ 1 \end{pmatrix} - \begin{pmatrix} \alpha \\ \beta \\ \gamma + n \end{pmatrix} + \begin{pmatrix} \alpha \\ \beta \\ \gamma + n - 1 \end{pmatrix} = 0,$$

and that

$$\boldsymbol{k} + \boldsymbol{k}_n - \boldsymbol{k}_{n+1} = \begin{pmatrix} 0 \\ 0 \\ 1 \end{pmatrix} + \begin{pmatrix} \alpha \\ \beta \\ \gamma + n \end{pmatrix} - \begin{pmatrix} \alpha \\ \beta \\ \gamma + n + 1 \end{pmatrix} = 0.$$

So there are two ways in which (4.49) is naturally satisfied by two adjacent Fourier modes interacting with the primary wave:

$$\boldsymbol{k}_A = -\boldsymbol{k}_n \quad \text{and} \quad \boldsymbol{k}_B = -\boldsymbol{k}_{n-1}, \tag{4.51}$$
$$\boldsymbol{k}_A = +\boldsymbol{k}_n \quad \text{and} \quad \boldsymbol{k}_B = +\boldsymbol{k}_{n+1}. \tag{4.52}$$

Numerical evidence for this conclusion is supplied by Figure 4.3, where we can visualise how each successive n-th Fourier mode is interacting with the Fourier mode adjacent to it in order to produce a single band of parametric resonance in (α, β)-space.

To find resonant values of α, we find $\boldsymbol{k}_A$ and $\boldsymbol{k}_B$ using either (4.51) or (4.52) and plot the corresponding value of $|\omega + \omega_A - \omega_B|$ against α. The values of α at which this quantity reaches zero are the resonant values of α.

Resonance Curves

We want to find modes satisfying triadic resonances, so we seek curves in (α, β)-space satisfying the resonance conditions (4.49) and (4.50). The dimensionless daughter wave frequencies are given by

$$\frac{\omega_A}{N} = -\frac{K_{A\perp}}{K_A}, \quad \frac{\omega_B}{N} = \frac{K_{B\perp}}{K_B}, \tag{4.53}$$

where

$$K_{A\perp} := \sqrt{K_{AX}^2 + K_{AY}^2}, \quad K_{B\perp} := \sqrt{K_{BX}^2 + K_{BY}^2}.$$

We must choose one of the two options (4.51) and (4.52) in order to satisfy (4.49). If we choose (4.52), the daughter waves A and B respectively represent the disturbance corresponding to dimensionless wavevectors $\boldsymbol{k}_n$ and $\boldsymbol{k}_{n+1}$:

$$\begin{aligned}\boldsymbol{k}_A &= \alpha\hat{\boldsymbol{x}} + \beta\hat{\boldsymbol{y}} + (\gamma+n)\hat{\boldsymbol{z}},\\ \boldsymbol{k}_B &= \alpha\hat{\boldsymbol{x}} + \beta\hat{\boldsymbol{y}} + (\gamma+n+1)\hat{\boldsymbol{z}},\end{aligned}$$

in transformed coordinates. Hence, we apply the reverse coordinate transformation to get the corresponding wavevectors $\boldsymbol{K}_A$ and $\boldsymbol{K}_B$ in the original coordinates.

$$K_{AX} = (\gamma+n)K_X + \alpha K_Z, \tag{4.54}$$
$$K_{AY} = \beta K, \tag{4.55}$$
$$K_{AZ} = (\gamma+n)K_Z - \alpha K_X, \tag{4.56}$$
$$K_{BX} = (\gamma+n+1)K_X + \alpha K_Z, \tag{4.57}$$
$$K_{BY} = \beta K, \tag{4.58}$$
$$K_{BZ} = (\gamma+n+1)K_Z - \alpha K_X. \tag{4.59}$$

In terms of frequencies, the resonance condition we seek is

$$\omega + \omega_A - \omega_B = 0. \tag{4.60}$$

To find the regions of (α,β)-space satisfying condition (4.60), we calculate

$$\Omega := |\omega + \omega_A - \omega_B|/N, \tag{4.61}$$

at each point on a grid of (α,β) values in Figure 4.4. The values of ω_A and ω_B in (4.61) are computed using (4.53) and (4.54)-(4.59). To draw attention to the regions of (α,β)-space where resonance criterion (4.60) is approximately or exactly satisfied, we plot only values of Ω smaller than some threshold value and omit any values falling outside of this threshold. This then allows for easy comparison with the numerical growth rate contours in (α,β)-space.

Disturbance Frequencies

Using (4.53) and (4.54)-(4.56) we can derive a formula for the daughter wave frequency ω_A/N:

$$\frac{\omega_A}{N} = -\sqrt{\frac{[(\gamma+n)\cos\theta + \alpha\sin\theta]^2 + \beta^2}{\alpha^2+\beta^2+(\gamma+n)^2}}. \tag{4.62}$$

Using (4.53) and (4.57)-(4.59) we can derive a formula for the daughter wave frequency ω_B/N:

$$\frac{\omega_B}{N} = +\sqrt{\frac{[(\gamma+n+1)\cos\theta + \alpha\sin\theta]^2 + \beta^2}{\alpha^2+\beta^2+(\gamma+n+1)^2}}. \tag{4.63}$$

Formulae (4.62) and (4.63) for ω_A/N and ω_B/N represent the disturbance frequencies in the original coordinate frame (X, Y, Z). To find the corresponding frequencies $\Im(\sigma_A)$ and $\Im(\sigma_B)$ in the transformed coordinate frame (x, y, z), we must take into account the Doppler shift, as discussed earlier in this section. According to formula (4.48), for any daughter wave A we have

$$\Im(\sigma_A) = \frac{\omega}{N}(\gamma+n_A) - \frac{\omega_A}{N}, \tag{4.64}$$

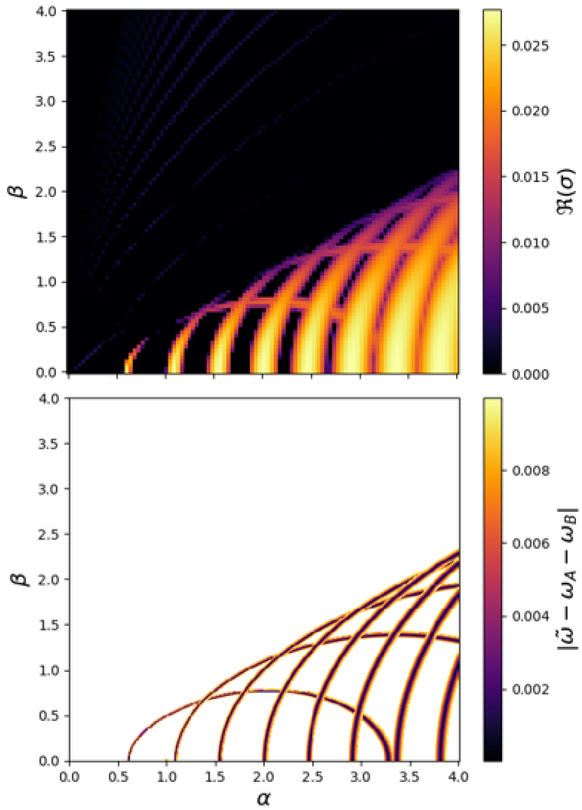

Figure 4.4: (Top) Growth rate contours in wavenumber space for instabilities of a pure internal gravity wave. Parameter values: $a = 0.1$, $\theta = \pi/4$, $\gamma = 0$, $\mathrm{Re} = \mathrm{Pe} = 10^6$. Resolution: $\mathcal{N} = 8$, $n_\alpha = n_\beta = 500$. (Bottom) Curves Ω representing the distance to exact triadic resonance corresponding to pure internal gravity waves for different Fourier modes. Parameter values: $\theta = \pi/4$, $\gamma = 0$. Resolution: $n_\alpha = n_\beta = 500$. Values of Ω greater than 0.01 have been omitted for ease of visibility.

where n_A is the Fourier mode associated with daughter wave A and σ_A is the complex growth rate associated with daughter wave A. The corresponding coupled daughter wave must satisfy

$$\Im(\sigma_B) = \frac{\omega}{N}(\gamma + n_A + 1) - \frac{\omega_B}{N}, \tag{4.65}$$

since $n_B = n_A + 1$. Subtracting (4.64) from (4.65) yields

$$\Im(\sigma_B) - \Im(\sigma_A) = \frac{\omega + \omega_A - \omega_B}{N},$$

which is the triadic resonance condition we expect, given that $\Im(\sigma_A) = \Im(\sigma_B)$ (both A and B are coupled to the same disturbance). In other words $\Im(\sigma_n) = \Im(\sigma_{n+1})$ for any singular value α_n. It is important to recognise that the value of $\Im(\sigma_{n+1})$ calculated at α_n is not the same as the value of $\Im(\sigma_{n+1})$ calculated at α_{n+1}. We state the values of ω_A/N and $\Im(\sigma_A)$ for a selection of triadic resonance instabilities in Table 4.1.

Triad Database

Table 4.1 lists values of quantities associated with resonant triads which occur along the line $\beta = 0$ in Figure 4.4. Figure 4.4 captures only half of the interactions in Table 4.1. Table 4.1 shows how the symmetries in α and the spectrum of Fourier modes relate to one another. Throughout the thesis, we have considered only positive values of α and β, a decision justified by symmetry arguments which are explained in Appendix A.2.2. Negative modes n and $n+1$ resonantly interact with the primary wave to produce instability for positive α. For negative α, it is the positive modes n and $n+1$ that are responsible for TRI. In particular, the resonant interaction takes the form

$$\boldsymbol{k} + \boldsymbol{k}_n - \boldsymbol{k}_{n+1}.$$

where $\boldsymbol{k}$ is the primary wavevector and $\boldsymbol{k}_n = (\alpha, \beta, \gamma + n)$ in the transformed coordinate system. In future work, it would be useful to find a way to explain why this relationship between the sign of n and the sign of α occurs. In Table 4.1, the values $\Im(\sigma_A)$ found by the ideal numerical Floquet solver are an exact match with the values we obtain by Doppler-shifting the original frame frequencies ω_A/N computed using (4.62), as we expect.

n	$n+1$	α_n	ω_A/N	$\Im(\sigma_A)$
-6	-5	$+2.4643$	-0.3854	-3.8572
-5	-4	$+2.0087$	-0.3925	-3.1430
-4	-3	$+1.5508$	-0.4037	-2.4247
-3	-2	$+1.0877$	-0.4237	-1.6976
-2	-1	$+0.6085$	-0.4706	-0.9436
$+1$	$+2$	-0.6085	-0.2365	$+0.9436$
$+2$	$+3$	-1.0877	-0.2834	$+1.6976$
$+3$	$+4$	-1.5508	-0.3034	$+2.4247$
$+4$	$+5$	-2.0087	-0.3146	$+3.1430$
$+5$	$+6$	-2.4643	-0.3217	$+3.8572$

Table 4.1: Pairs of Fourier modes n and $n+1$ which resonantly interact with the primary wave to produce a TRI at the stated α values, along with frequencies ω_A/N pertaining to each mode of disturbance n computed using formula (4.62). For each pair, we state the imaginary part of the complex growth rate $\Im(\sigma_A)$ found using the ideal form of the Floquet solver. Parameter values: $a = 10^{-4}$, $\theta = \pi/4$, $\beta = 0$, $\gamma = 0$. Resolution for Floquet solver: $\mathcal{N} = 40$.

4.2.2 Influence of Parameters

Influence of Primary Wave Amplitude

We begin by observing the dependence on wave amplitude of the growth rate of IGW instabilities in the small-amplitude limit. We know from Mied (1976), Drazin (1977), Klostermeyer (1982, 1983, 1991) and others to expect perturbations to be unstable to TRIs in this small-amplitude limit. We are interested in seeing what changes about the stability of the wave upon incremental adjustments of the amplitude parameter a. Figure 4.5 depicts instability growth rates in (α, β)-space of IGWs with $\theta = \pi/4$, for a selection of different a values. It is clear that the proportion of (α, β)-space which is unstable to resonant triads increases with increasing a. More precisely, the resonance bands increase in width, reducing the space between them. Additionally, the proportion of parameter space which is occupied by unstable modes of disturbance increases as a increases, regardless of whether the instabilities observed are induced by resonant triads or even parametric resonance in general. The second obvious conclusion to draw is an increase in the maximum growth rate observed in this region of wavenumber space as a is increased.

LR96 demonstrated that there is no obvious qualitative difference between contours calculated below the overturning threshold ($a < 1$) and those calculated above the overturning

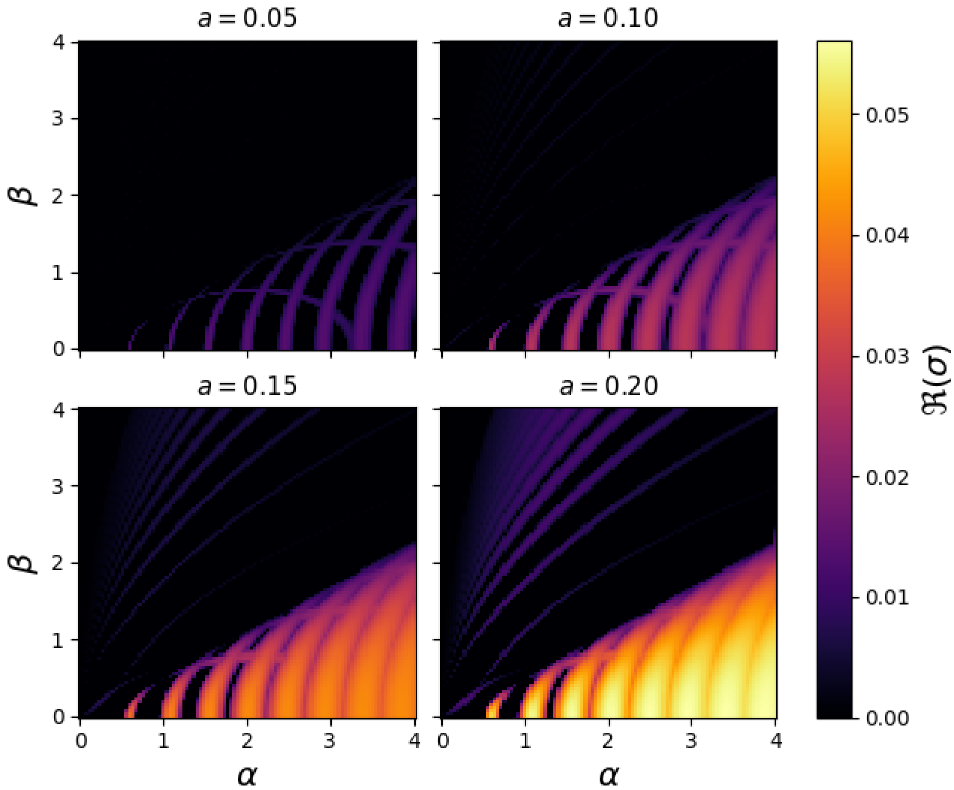

Figure 4.5: Growth rate contours in (α, β)-space for different values of the amplitude parameter a. Parameter values: $\theta = \pi/4$, $\gamma = 0$, and $\mathrm{Re} = \mathrm{Pe} = 10^6$. Resolution: $\mathcal{N} = 15$, $n_\alpha = n_\beta = 100$.

threshold ($a > 1$). Increasing the amplitude demonstrably introduces new regions of instability in wavenumber space, however. Such results are recreated using the Floquet solver (4.45) in Figure 4.6. Based on Figure 4.6, for the case $a \sim 1$, we divide wavenumber space into three dis-

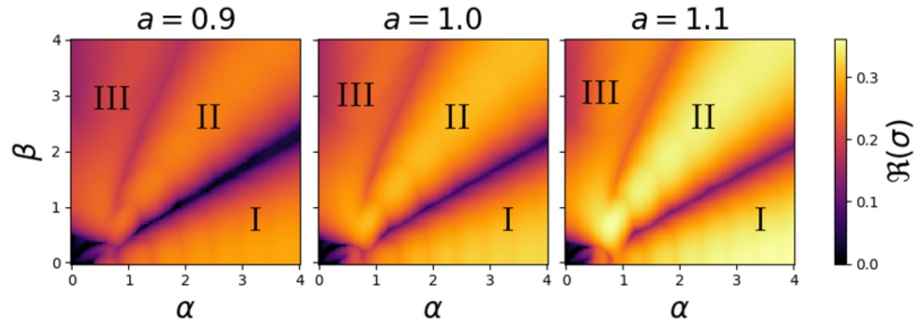

Figure 4.6: Growth rate contours in (α, β)-space for higher values of the amplitude parameter a spanning the overturning threshold $a = 1$. Parameter values: $\theta = \pi/4$, $b_0 = 0$, $\gamma = 0$, and $\mathrm{Re} = \mathrm{Pe} = 10^6$. Resolution: $\mathcal{N} = 40$, $n_\alpha = n_\beta = 100$.

tinct regions going forward: Region I, Region II and Region III. Region I appears to be unstable at all amplitudes observed throughout this chapter, whereas in Regions II and III instabilities only appear to switch on at higher amplitudes. We shall look at the spatial form of the growing modes and how this form differs in each of the three regions later in this chapter.

One of the conclusions which unifies the work of Mied (1976), Drazin (1977), Klostermeyer (1982, 1983, 1991) and others is that at the smallest amplitudes a, instabilities of plane IGWs are approximately two-dimensional, with the fastest-growing modes clinging to the α-axis and with β not playing much of a role. It is only with increasing amplitude a that instabilities become increasingly three-dimensional.

Complex Growth Rates

So far, we have only considered the real part of the complex growth rate σ in the contour plots computed across the (α, β)-plane. At the start of Section 4.2 we stated that values of σ with positive real parts represent direct instability if $\Im(\sigma) = 0$, but if $\Im(\sigma) \neq 0$ then the mode is said to be overstable. Here, we determine which of these two categories the instabilities fall into. We do so by plotting $|\Im(\sigma)|$ alongside non-negative values of $\Re(\sigma)$. The first examples of these are Figure 4.7 and Figure 4.8. In both of these images, we find that at amplitudes of $O(0.1)$, the instability bands in Region I have lower frequencies than the instability bands in Region III. The latter of which, as proposed by LR96, are associated with higher-order resonant interactions. At amplitudes of $O(1)$, we find that instabilities in Regions I and II are overstable, whereas the instabilities in Region III are predominantly direct. We also see that the disturbance frequency increases incrementally between each successive parametric resonance band as we increase α. This can be explained mathematically in the following way. Earlier in this chapter we saw that

$$\Im(\sigma_n) = \frac{\omega}{N}(\gamma + n) - \frac{\omega_n'}{N}.$$

But in the limit of parametric subharmonic instability, $\omega' \sim \omega/2$, so we get

$$\Im(\sigma_n) \approx \frac{\omega}{N}\left(\gamma + n - \frac{1}{2}\right) = \cos\theta \left(\gamma + n - \frac{1}{2}\right).$$

So at fixed values of θ and γ, $|\Im(\sigma_n)|$ increases with n. Since the resonance bands along the α-axis are associated with consecutive integers n, we encounter the following recurrence relation (4.66) for PSI between IGWs:

$$|\Im(\sigma_{n+1})| = |\Im(\sigma_n)| + 1. \tag{4.66}$$

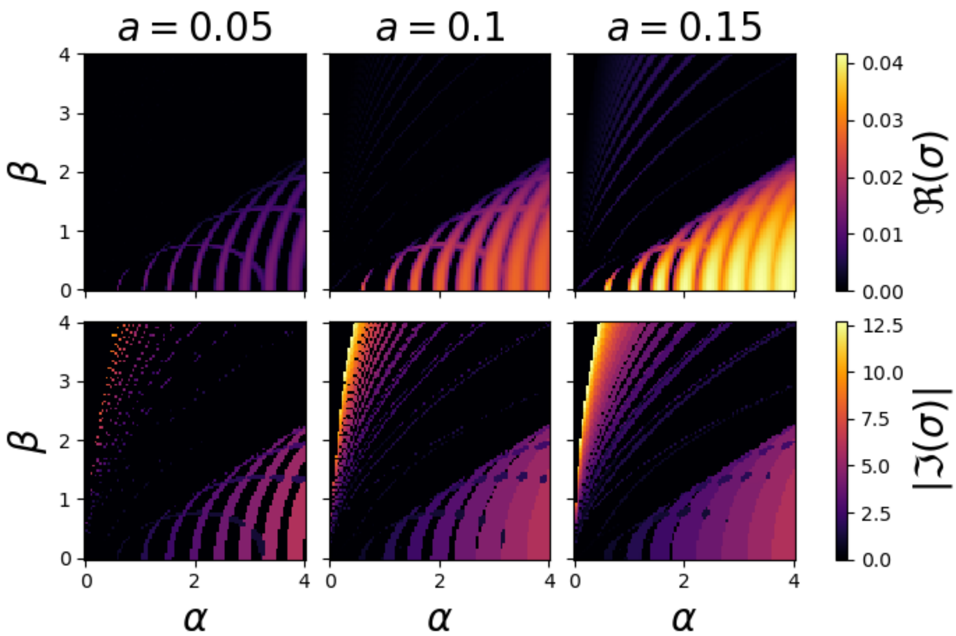

Figure 4.7: Real and imaginary parts of the complex growth rate contoured in wavenumber space for different values of the amplitude parameter a. Parameter values: $\theta = \pi/4$, $\gamma = 0$, $\mathrm{Re} = \mathrm{Pe} = 10^6$. Resolution: $\mathcal{N} = 20$, $n_\alpha = n_\beta = 100$.

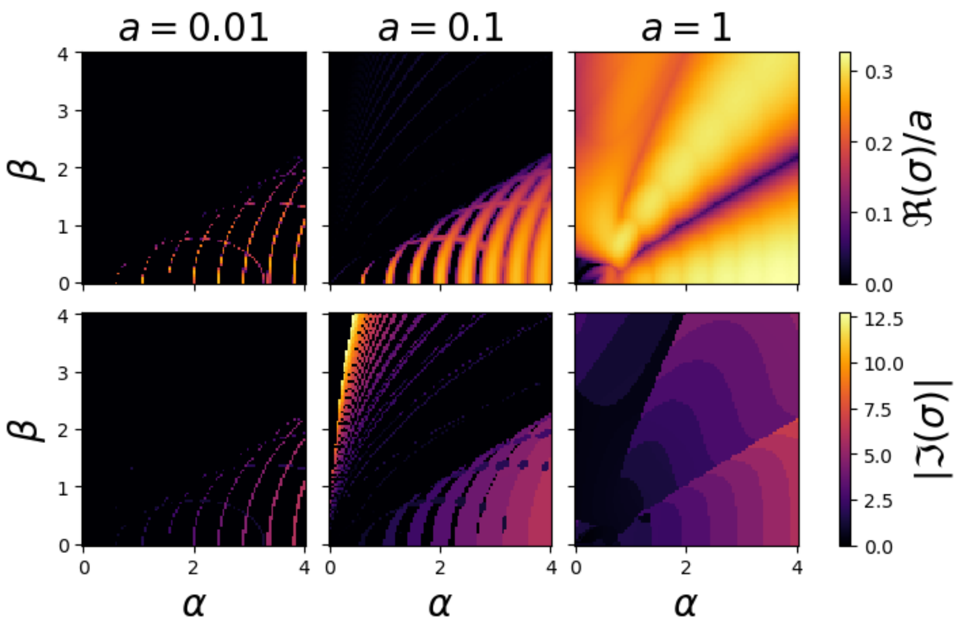

Figure 4.8: Real and imaginary parts of the complex growth rate contoured in wavenumber space for different values of the amplitude parameter a. Real parts are scaled by $1/a$. Parameter values: $\theta = \pi/4$, $\gamma = 0$, $\mathrm{Re} = \mathrm{Pe} = 10^6$. Resolution: $\mathcal{N} = 40$, $n_\alpha = n_\beta = 100$.

Influence of Primary Wave Orientation

We wish to determine what impact the orientation of the primary wavevector has on the instability growth rates. We do so by varying the angle θ, which uniquely determines the wavevector $\boldsymbol{k}$ since we use units such that $k = 1$.

Mied (1976) considered just a single value of θ in detail in his stability analysis ($\theta = \pi/6$). In the literature that followed, different values of θ were compared (Klostermeyer, 1982, 1983, 1991), but a strong conclusion regarding its influence on IGW instability growth rates is lacking. We therefore continue to explore this research question through the numerical solution of (4.45).

Given that for IGWs our dimensionless dispersion relation is $\omega/N = \cos\theta$, varying the propagation angle is equivalent to varying the frequency of the primary wave. The limit in which $\theta \to \pi/2$ gives us the lowest frequency primary wave ($\omega/N \to 0$) and the limit in which $\theta \to 0$ gives us the highest frequency primary wave ($\omega/N \to 1$). It is important to recognise that an exact value of $\theta = \pi/2$ corresponds to a solution which is no longer a wave (since it has zero frequency). Instead, it corresponds to uniform horizontal flow in the X-direction. To see why this is true, we note that the solenoidal constraint for the primary wave takes the form $k_x\tilde{u}_x + k_z\tilde{u}_z = 0$. If $\theta = \pi/2$ then $k_x = 0$ since $k_x = \cos\theta$. It would make no sense for us to consider a wavevector satisfying $k_x = k_z = 0$, i.e. we must have $k_z \neq 0$, which implies that $\tilde{u}_z = 0$, giving us a horizontal flow.

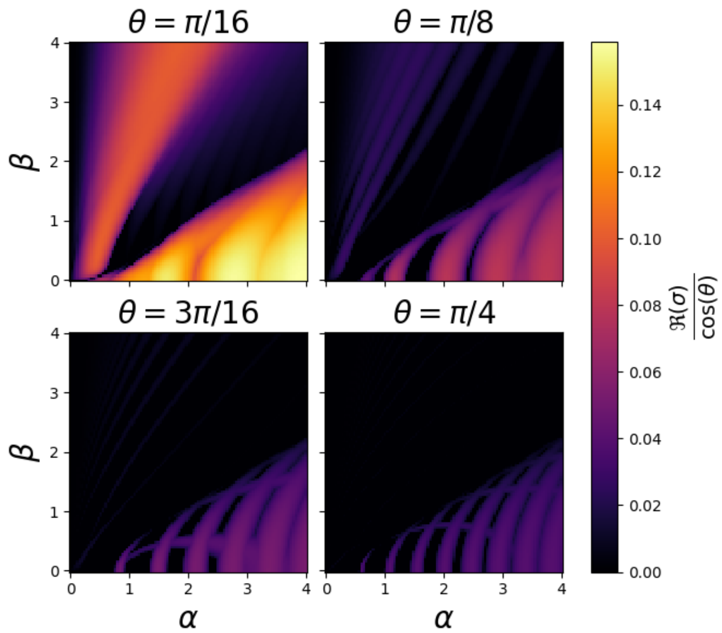

Figure 4.9: Growth rate contours in (α, β)-space for different values of the wave propagation angle θ, scaled with the dimensionless primary wave frequency $\omega/N = \cos\theta$. Parameter values: $a = 0.1$, $\gamma = 0$, and $\mathrm{Re} = \mathrm{Pe} = 10^6$. Resolution: $\mathcal{N} = 25$, $n_\alpha = n_\beta = 100$.

We plot growth rates in (α, β)-space for an IGW with $a = 0.1$ at a selection of different wavevector angles θ in Figures 4.9 and 4.10. To improve the visibility of instability bands when plotting them with a shared colourbar, we scale growth rates in Figures 4.9 and 4.10 with the dimensionless frequency $\omega/N = \cos\theta$. When starting from an angle of $\theta = \pi/16$ with respect to the horizontal X-axis and rotating it towards $\theta = \pi/4$ in Figure 4.9, we observe a reduction in the scaled growth rate overall. In Figure 4.10, we reduce the size of the (α, β) domain considered to reduce the resolution in α and β required to easily visualise the trends on display. We find that for $\theta \in [\pi/4, \pi/2)$, the scaled growth rate also gets smaller as we increase θ. In other words, the scaled growth rate decreases as the frequency of the primary wave decreases. To quantify exactly how much the unscaled growth rate decreases with increasing θ, we plot the maximum observed growth rate as a function of wavevector angle θ later in Figure 4.34. In Figures 4.9 and 4.10, the widths of the bands of parametric resonance decrease as we decrease the primary wave frequency. More bands occupy the same amount of wavenumber space as we increase θ within this domain. Evidently, a higher frequency primary wave reduces the spatial density of parametric resonance bands.

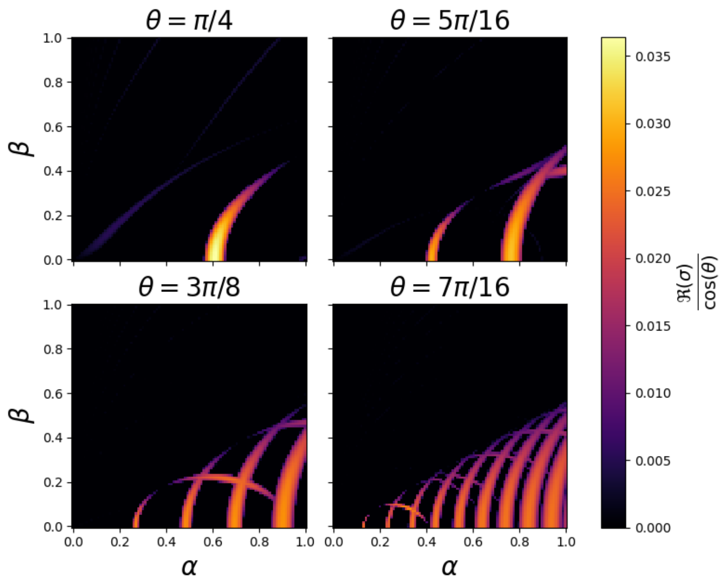

Figure 4.10: Growth rate contours in (α, β)-space for more values of the wave propagation angle θ, scaled with the dimensionless primary wave frequency $\omega/N = \cos\theta$. Parameter values: $a = 0.1$, $b_0 = 0$, $\gamma = 0$, and $\mathrm{Re} = \mathrm{Pe} = 10^6$. Resolution: $\mathcal{N} = 25$, $n_\alpha = n_\beta = 100$.

Influence of Floquet Modulation Parameter

Here we demonstrate what happens to instability growth rates as the parameter γ changes. This constitutes an extension of work attempted in existing literature, namely the work of LR96 and the work of Klostermeyer (1991). LR96 chose to keep γ fixed at $\gamma = 0$, for the sole purpose of restricting the overwhelming amount of parameter space potentially explorable. Klostermeyer (1991) included variations in γ in his work but chose to impose restrictions on the perturbation wavevector component α. Since we do not make such severe restrictions on α, this segment also serves as an extension of the work of Klostermeyer (1991).

It is important to say a little about the physical significance of the parameter γ. It represents the periodicity of the perturbations f' relative to the periodicity of the primary wave solution $\tilde{f}$ (which is 2π-periodic with respect to the z-axis). More precisely, a value of $\gamma = 0$ represents a perturbation with an identical periodicity to the primary wave.

We also find that growth rates are 1-periodic with respect to γ. To see why this is an expected result, we note that due to the infinite nature of the expansion for perturbations, the following holds for any integer $m \in \mathbb{Z}$.

$$\begin{aligned} f'(\boldsymbol{x}, t) &= \textstyle\sum_{n=-\infty}^{\infty} f_n \exp[i\alpha x + i\beta y + i(\gamma + n)z + \sigma t] \\ &= \textstyle\sum_{n=-\infty}^{\infty} f_{n+m} \exp[i\alpha x + i\beta y + i(\gamma + n + m)z + \sigma t]. \end{aligned}$$

In other words, as expressed by LR96, the expansion is invariant under the transformation $\gamma \to \gamma + m$ for any integer $m \in \mathbb{Z}$. This allows us to conclude that at fixed α and β, any pair of adjacent integer values of γ have the same eigenvalues and eigenvectors as each other. This symmetry property allows us to restrict our range of γ to $\gamma \in (-1/2, 1/2]$ on the grounds that no additional information would be gained by widening the interval. We are free to choose to centre this interval wherever we like. We choose to centre it at zero. Only the length of the interval is constrained.

In Figures 4.11 and 4.12, we plot growth rates of IGW instabilities as a function of disturbance wavenumber α for several different values of the Floquet modulation parameter γ.

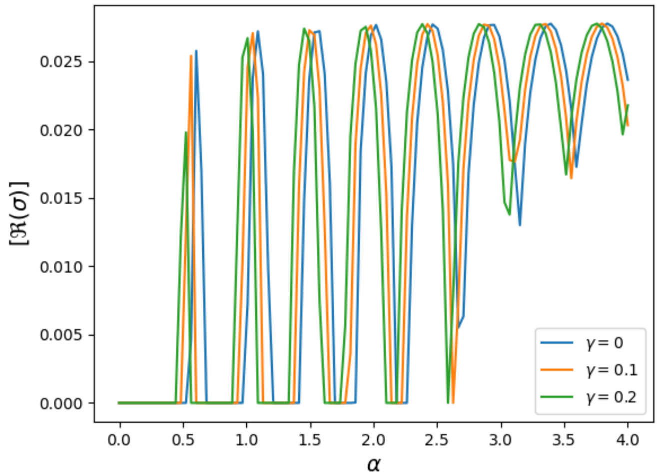

Figure 4.11: Growth rate as a function of α, for a different range of γ values. Calculated at $\beta = 0$, with truncation point $\mathcal{N} = 81$, $n_\alpha = 100$, $\theta = \pi/4$ and $\mathrm{Re} = \mathrm{Pe} = 10^6$.

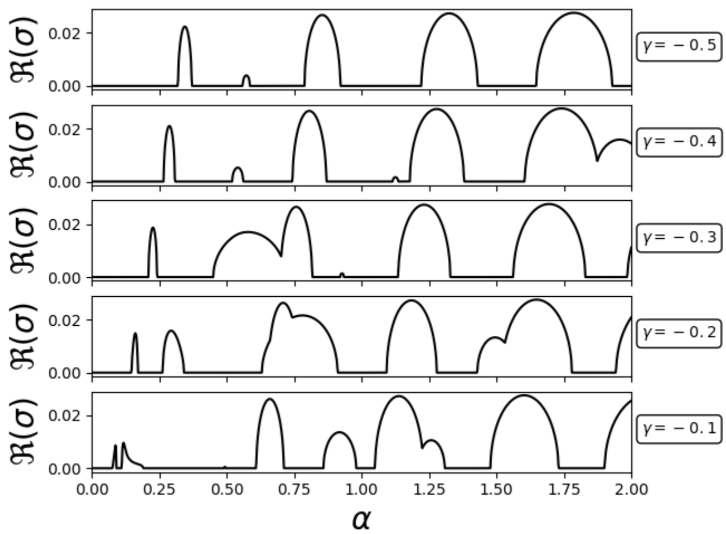

Figure 4.12: Growth rate contours in wavenumber space for different values of the Floquet modulation parameter γ. Parameter values: $a = 0.1, \theta = \pi/4, \beta = 0, \mathcal{N} = 20, \mathrm{Re} = \mathrm{Pe} = 10^6$. Resolution: $n_\alpha = 1000$.

From Figure 4.11 it is clear that the centres of exact resonance for parametric instability get shifted laterally along the α axis as we vary γ. But the maximum growth rate observed in this region of wavenumber space is independent of γ. At larger α, the curves plateau at the same value of $\Re(\sigma)$, regardless of the value of γ. The growth rate of instabilities at small α is impacted by γ, however. For the smallest resonant value of α observed in Figure 4.11, we find that the growth rate pertaining to this resonance decreases with increasing γ.

Figure 4.12 demonstrates the same trends as Figure 4.11, but also reveals that the growth rates within any individual region of resonance can be affected quite significantly by γ. Figure 4.12 makes it even more apparent that the growth rate pertaining to the resonance with the lowest α value decreases with increasing γ. The main conclusion to be drawn from both 4.11 and 4.12 is that changing the periodicity of the disturbance relative to the primary wave changes the values of the disturbance wavenumber α at which triadic resonance occurs. We have studied the influence of γ on growth rates for 2D disturbances (for which $\beta = 0$) but not for 3D disturbances (for which $\beta \neq 0$). In future work, it would be useful to gain an understanding of how γ influences the growth rates of 3D disturbances.

Influence of Thermal Péclet Number

Much of the previous work on instabilities of IGWs in Boussinesq fluids has been in the absence of viscosity and thermal diffusion (e.g. Mied, 1976; Klostermeyer, 1982). Klostermeyer (1983) studied the influence of non-zero viscosity in the problem, finding that adding viscosity increases the length scale of the fastest-growing modes of disturbance when compared with the ideal problem. The influence of thermal diffusion has not been studied, however.

So far, the work presented in this chapter has described instabilities of IGWs in the presence of very weak viscosity and thermal diffusion, which has had little impact on the growth rates observed. One of our applications of interest is the interiors of stars, in which $\mathrm{Pr} \ll 1$. Given that $\mathrm{Pe} = \mathrm{RePr}$, at fixed $\mathrm{Re} = 10^6$ the value $\mathrm{Pe} = 10^6$ is not a realistic Péclet number in stellar interiors. It is therefore of interest to consider smaller values of Pe, as they are particularly relevant for stellar interiors.

Here we visualise the damping of instabilities by thermal diffusion. In Figures 4.13 and 4.14 we plot growth rates in (α, β) space for IGWs in the presence of a range of different Pe values. We find that as thermal diffusivity is increased, a greater proportion of the visible instability bands are damped. For the range of (α, β) shown, thermal diffusion has almost entirely wiped out any instability bands in this region of parameter space by the time we reduce it as far as $\mathrm{Pe} = 100$ in Figure 4.13.

In Figure 4.14 we reduce the interval between Pe values to more easily visualise the damping effect of thermal diffusion on the growth rate. Figure 4.14 reveals that TRIs are essentially removed one-by-one as we increase thermal diffusion, with the TRIs at higher wavenumbers disappearing first. In Section 4.5.1, we find that this progressive vanishing of TRIs with decreasing Pe is accounted for by a small extension of the theoretical framework for TRIs of IGWs presented in Chapter 3. We do so by adjusting the value obtained by the ideal growth rate formula (3.61) by the decay rate due to thermal diffusion (2.91).

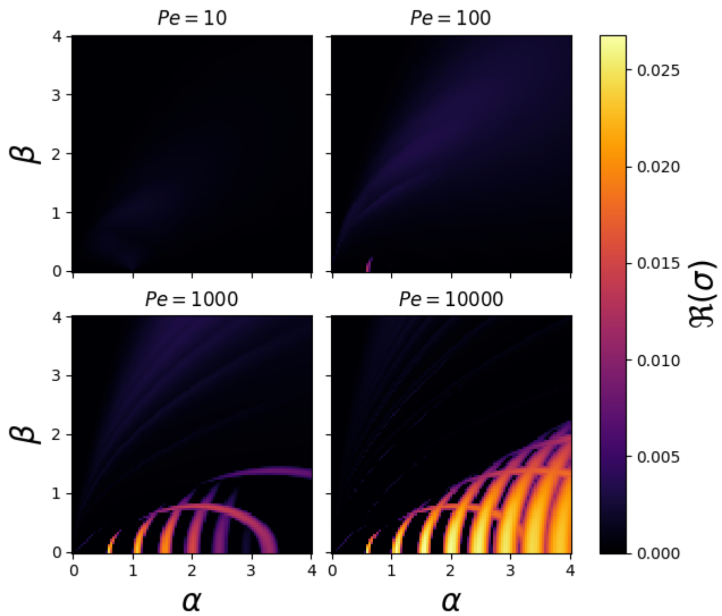

Figure 4.13: Growth rate contours in wavenumber space for different values of the thermal Péclet number Pe. Parameter values: $a = 0.1, \theta = \pi/4, \gamma = 0, \mathcal{N} = 40, \mathrm{Re} = 10^6$.

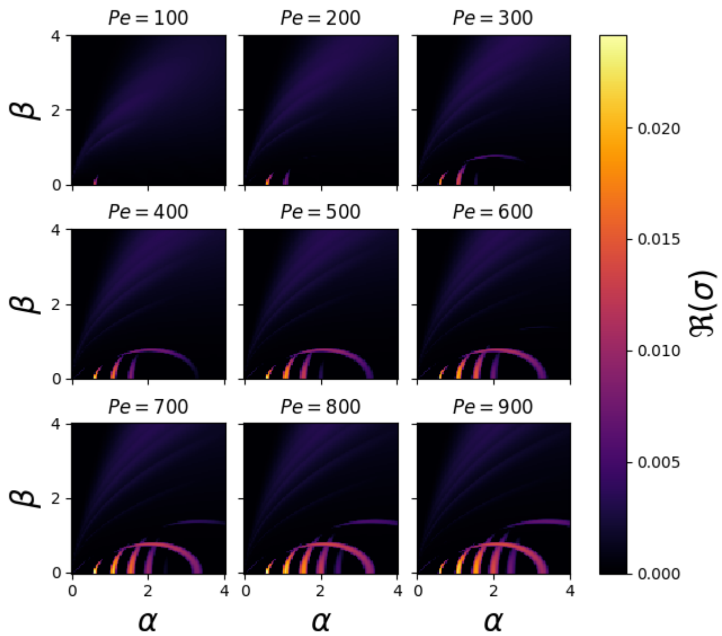

Figure 4.14: Growth rate contours in wavenumber space for different values of the thermal Péclet number Pe. Parameter values: $a = 0.1, \theta = \pi/4, \gamma = 0, \mathcal{N} = 40, \mathrm{Re} = 10^6$.

Thermal Diffusion at Overturning Amplitude

So far, we have determined the influence of varying the thermal Péclet number on the growth rate of instabilities of small-amplitude IGWs. It is interesting to consider how thermal diffusion affects instabilities of IGWs with amplitudes sufficiently large that the IGW is statically unstable. We could speculate that at such amplitudes, increasing thermal diffusion may introduce new instabilities, e.g. shear instabilities enabled by thermal diffusion. This speculation is our primary motivation for studying the impact of thermal diffusion on instabilities of statically-unstable IGWs. To determine whether this occurs, we view the impact thermal diffusion has on a primary wave with amplitude at the overturning amplitude $a = 1$.

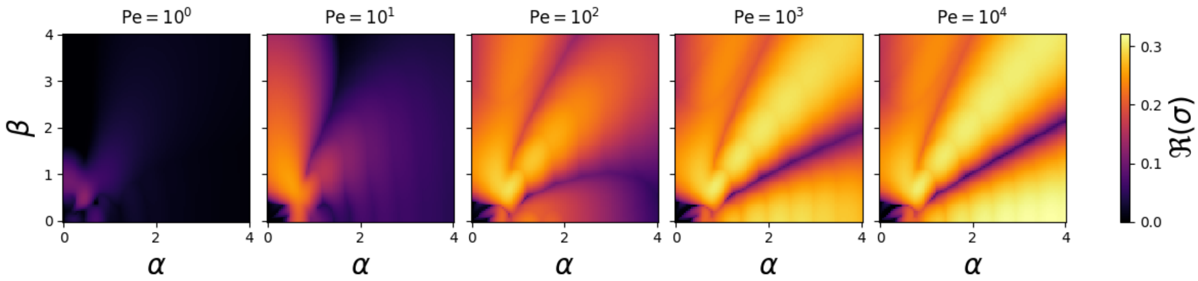

Figure 4.15: Growth rate contours in wavenumber space for different values of the thermal Péclet number Pe. Parameter values: $a = 1, \theta = \pi/4, \gamma = 0, \mathcal{N} = 20, \mathrm{Re} = 10^6$.

In Figures 4.15 and 4.16, we plot growth rates for instabilities of IGWs with amplitudes at the overturning threshold $a = 1$ for a selection of different Pe values. The growth rates in each of Regions I, II and III are progressively damped as we reduce the value of Pe. Region I of instability is eventually eradicated entirely by thermal diffusion by the time we reach $\mathrm{Pe} = 1$ in Figure 4.15. We take a closer look at this process by reducing the size of the interval in Pe between each panel in Figure 4.16. As was the case at lower amplitude, Region I disappears gradually with decreasing Pe such that instabilities at higher values of α are eliminated first. Neither of Figures 4.15 and 4.16 provide any evidence to suggest that new varieties of instability are switched on by introducing thermal diffusion.

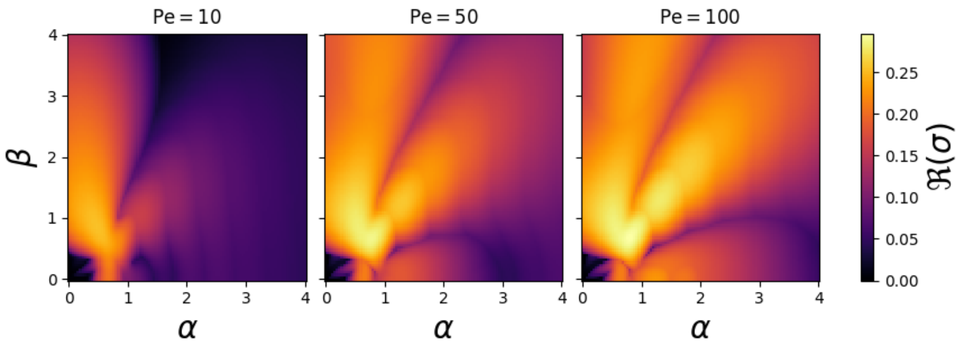

Figure 4.16: Growth rate contours in wavenumber space for different values of the thermal Péclet number Pe. Parameter values: $a = 1, \theta = \pi/4, \gamma = 0, \mathcal{N} = 20, \mathrm{Re} = 10^6$.

4.3 Eigenfunctions

In Section 4.2 we studied growth rates of IGW instabilities. This allowed us to determine which modes of disturbance are unstable, and to determine which of the unstable modes are the fastest-growing. To better understand the disturbances, it is useful to determine what they look like in (X, Z)-space. In other words, we make plots of $\boldsymbol{U'}$ and ρ' as functions of X and Z.

Method of Implementation

In the numerical solution of eigenvalue problem (4.45), $\boldsymbol{v}$ is a vector of length $6N + 3$ and M is a matrix of size $(6\mathcal{N} + 3) \times (6\mathcal{N} + 3)$. After solving the $(6\mathcal{N} + 3) \times (6\mathcal{N} + 3)$ eigenvalue problem with $2\mathcal{N} + 1$ Fourier modes, we get $6\mathcal{N} + 3$ eigenvalues σ and $6\mathcal{N} + 3$ eigenvectors, each of length $6N+3$. We then record the eigenvector $\boldsymbol{v}$ of length $6\mathcal{N}+3$ corresponding to the eigenvalue σ with the maximum real part (the fastest-growing mode). We split this particular eigenvector into 3 vectors each of length $2\mathcal{N}+1$ of the form

$$\boldsymbol{v}_1 := (u^x_{-\mathcal{N}}, \dots, u^x_0, \dots, u^x_{\mathcal{N}}), \tag{4.67}$$
$$\boldsymbol{v}_2 := (u^z_{-\mathcal{N}}, \dots, u^z_0, \dots, u^z_{\mathcal{N}}), \tag{4.68}$$
$$\boldsymbol{v}_3 := (\varrho_{-\mathcal{N}}, \dots, \varrho_0, \dots, \varrho_{\mathcal{N}}). \tag{4.69}$$

We can then find the value of u^y_n which was omitted from the eigenvalue problem using the rearranged divergence-free constraint:

$$u^y_n = -\frac{\alpha u^x_n + (\gamma + n)u^z_n}{\beta}.$$

From this formula we get a vector of length $2\mathcal{N}+1$ of the form

$$\boldsymbol{v}_4 := (u^y_{-\mathcal{N}}, \dots, u^y_0, \dots, u^y_{\mathcal{N}}). \tag{4.70}$$

We can then record an eigenfunction for each of our seven variables corresponding to the fastest-growing eigenvalue.

$$f'(x,y,z,t) = \textstyle\sum_{n=-\mathcal{N}}^{\mathcal{N}} f_n \exp\left[i\alpha x + i\beta y + i(n+\gamma)z + \sigma t\right] \quad \text{for} \quad f \in \{\boldsymbol{u}, \varrho\}.$$

The computed eigenfunctions are transformed into the original coordinate system and plotted in the original (X,Z)-plane. We restrict this to the (X,Z)-plane on the basis that the direction of the Y axis is unchanged by the coordinate rotation (only its magnitude changes in order to render it dimensionless).

Resolution

The Floquet calculation takes a Fourier series of infinitely many terms and approximates it numerically using a finite truncation of the series with $2\mathcal{N}+1$ terms. How can we be confident that there are sufficiently many terms in our finite truncation to accurately represent the behaviour of the infinite series and capture all instabilities present? We would like some kind of measure of how *resolved* the calculation is, i.e. whether the chosen $\mathcal{N}$ value is sufficiently high for the calculation. To do so, we use (4.67)-(4.70) to find the *spectral energy density* for each Fourier mode n:

$$E_n := |u^x_n|^2 + |u^y_n|^2 + |u^z_n|^2 + |\varrho_n|^2 k^2/k_z^2. \tag{4.71}$$

We calculate $2\mathcal{N}+1$ values of E_n associated with the fastest-growing eigenvalue σ for each use of the Floquet solver. We then calculate the following ratio:

$$\Lambda := \frac{\max(E_n)}{\max(E_{-\mathcal{N}}, E_{\mathcal{N}})}.$$

Λ is our measure of how resolved the calculation is. We get one value of Λ for each use of the eigenvalue solver. We regard calculations with $\Lambda > 10^6$ as being sufficiently resolved.

Varying the Amplitude Parameter

Here, we investigate the impact of varying a on the disturbance. We take the range of values of a from Figure 4.5. For a location at which to plot the disturbance, we choose a point in (α, β)-space which is unstable at all four values of a. The point we choose is $(\alpha, \beta) = (2, 0)$. We plot eigenfunctions corresponding to each panel in Figure 4.5 and present them in Figure 4.17. We present the accompanying growth rate for the unstable mode corresponding to each panel in Table 4.2.

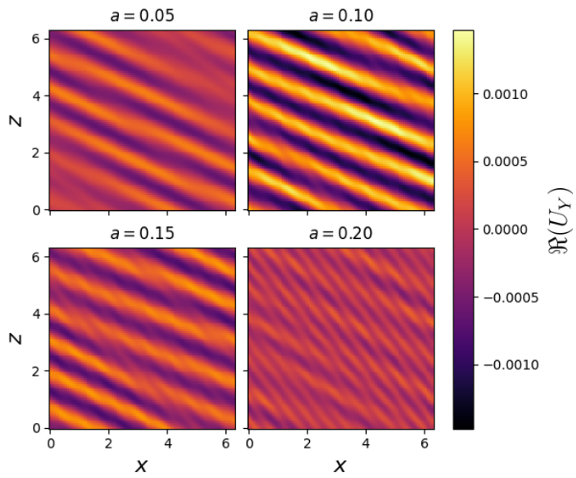

Figure 4.17: Real parts of the perturbations U'_Y in (X, Z) space for different values of the amplitude parameter a. Parameter values: $\theta = \pi/4$, $\alpha = 2$, $\beta = 0$,$\gamma = 0$, and $\mathrm{Re} = \mathrm{Pe} = 10^6$. Resolution: $\mathcal{N} = 15$, $n_X = n_Z = 100$.

In Figure 4.17 we see that, out of the four values of a shown, the size of the perturbations $\Re(U'_Y)$ is maximised at $a = 0.1$. There is no obvious reason why this panel contains the largest value of $|\Re(U'_Y)|$. These eigenfunctions correspond to the point $(\alpha, \beta) = (2, 0)$ in Figure 4.5. Table 4.2 demonstrates a linear relationship between the growth rate and the wave amplitude, which was first identified by McEwan and Robinson (1975). As we increase a in the eigenfunctions of Figure 4.17, we find that the structural complexity of the eigenfunction increases. By this, we mean that a greater number of disturbance wavevector directions appear as we increase a. This is because as we increase a, a greater number of couplings occur between different Fourier modes n. We choose not to show disturbances U'_X, U'_Z, P' and ϱ' here, since varying a in this domain makes virtually no difference to these these variables.

Table 4.2: Growth rates at $(\alpha, \beta) = (2, 0)$ corresponding to Figure 4.5.

a	σ_r
0.05	1.37×10^{-2}
0.10	2.77×10^{-2}
0.15	4.16×10^{-2}
0.20	5.57×10^{-2}

Varying the Wave Propagation Angle

We now investigate the influence of θ on the disturbance. We take values of θ from each panel of Figure 4.9. For a location at which to plot the disturbance, we choose a point in (α, β) space which is unstable at all four values of θ. The point $(\alpha, \beta) = (2, 0)$ is chosen again. We plot eigenfunctions corresponding to each panel of Figure 4.9 in Figure 4.18. The growth rate of the disturbance in each panel of Figure 4.18 is stated in Table 4.3. In Figure 4.18, the amplitude of

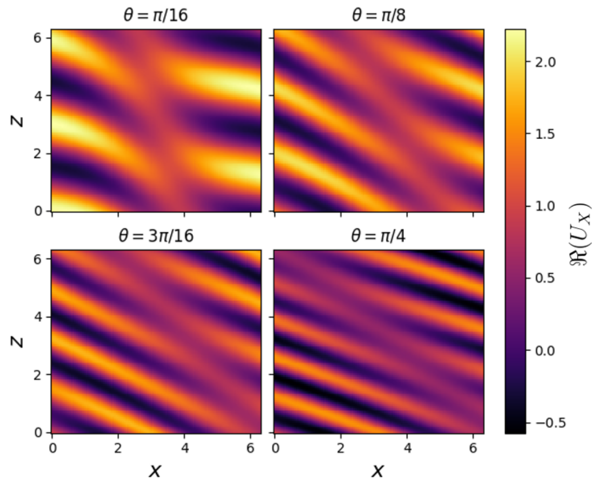

Figure 4.18: Real parts of the perturbations U'_X in (X, Z) space for different values of the wavevector orientation θ. Parameter values: $a = 0.1$, $\alpha = 2$, $\beta = 0$, $\gamma = 0$, and $\mathrm{Re} = \mathrm{Pe} = 10^6$. Resolution: $\mathcal{N} = 25$, $n_X = n_Z = 100$.

the disturbance decreases with increasing θ. The number of disturbance crests occupying this spatial domain increases each time we increase the primary wavevector angle θ. This means that the number of visible crests increases as we reduce the frequency of the primary wave. Table 4.3 shows that the growth rate gets smaller as we reduce the primary wave frequency.

Table 4.3: Growth rates and frequencies at $(\alpha, \beta) = (2, 0)$ corresponding to Figure 4.9 and Figure 4.18.

θ	σ_r
$\pi/16$	1.14×10^{-1}
$\pi/8$	7.21×10^{-2}
$3\pi/16$	3.74×10^{-2}
$\pi/4$	2.77×10^{-2}

Varying the Floquet Modulation Parameter

We wish to see whether the eigenfunctions change qualitatively as we vary γ. To do so, we compute eigenfunctions at a point of exact triadic resonance, namely the point associated with the $n = -2$ mode. This mode generates a growth rate peak which moves in the negative α direction every time we increase γ. We demonstrated how varying γ changes the location of resonant values of α in Figure 4.12 from Section 4.2.

We record the changing value of this resonant α value associated with the $n = -2$ mode for each value of γ we consider in Table 4.4. We plot the associated eigenfunctions for each value of γ at the relevant resonant value of α, i.e. we plot eigenfunctions for each row of Table 4.4. We present the eigenfunctions for $\gamma = -0.5$ in Figure 4.19, for $\gamma = 0$ in Figure 4.20 and for $\gamma = 0.5$ in Figure 4.21. We find that there are no obvious differences between the eigenfunctions at any of the γ values considered. The number of crests occupying this (X, Z) domain is unchanged by varying γ, and so is the amplitude of the disturbance in general.

Table 4.4: Values of α at which a TRI of IGWs occurs corresponding to the $n = -2$ Fourier mode for a selection of values of γ. Parameter values: $\theta = \pi/4$, $\beta = 0$.

γ	α
-5	0.85164528
0	0.60854561
5	0.3471065

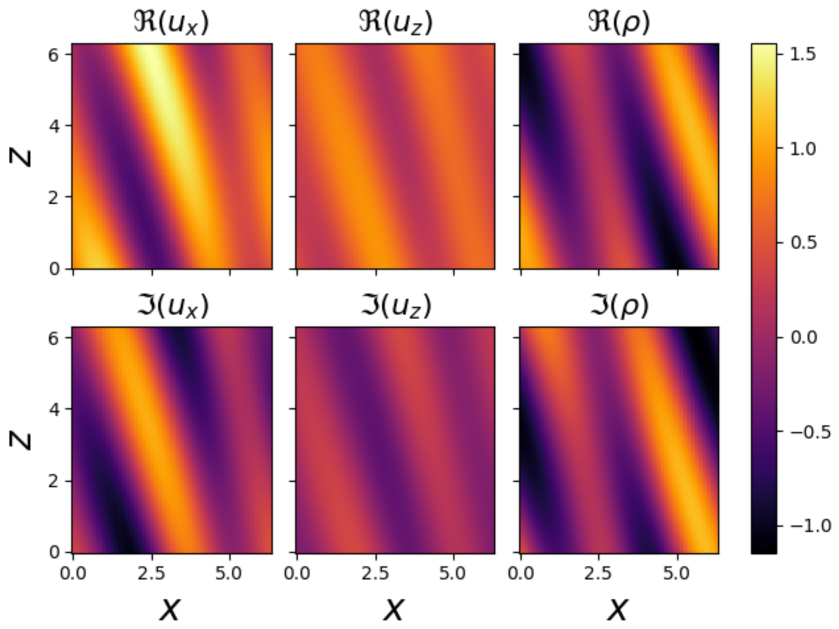

Figure 4.19: Eigenfunctions computed at the resonant α value corresponding to the $n = -2$ mode. Parameter values: $a = 0.1, \theta = \pi/4$, $\alpha = 0.85164528$, $\beta = 0$, $\gamma = -0.5$, $\mathcal{N} = 20$, $\mathrm{Re} = \mathrm{Pe} = 10^6$. Resolution: $n_X = n_Z = 100$.

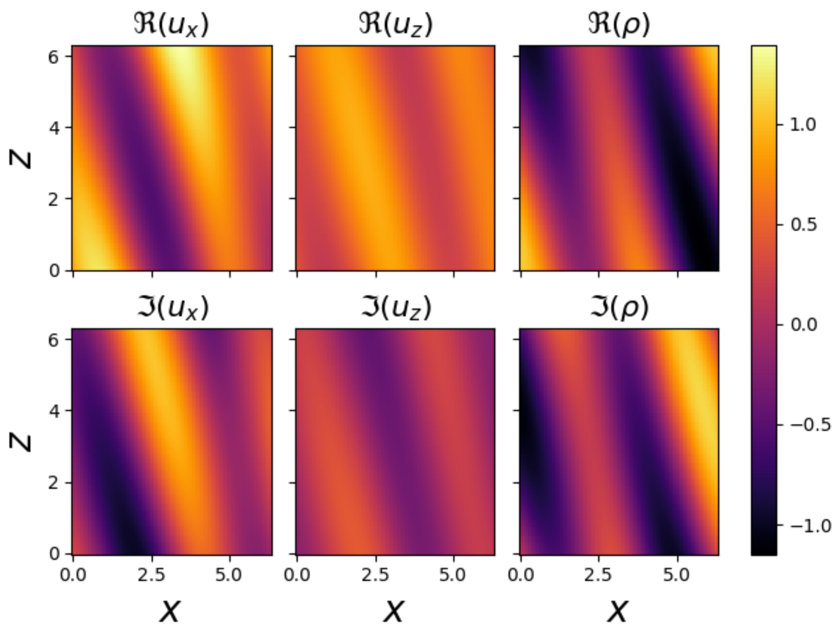

Figure 4.20: Eigenfunctions computed at the resonant α value corresponding to the $n = -2$ mode. Parameter values: $a = 0.1, \theta = \pi/4$, $\alpha = 0.60854561$, $\beta = 0$, $\gamma = 0$, $\mathcal{N} = 20$, $\mathrm{Re} = \mathrm{Pe} = 10^6$. Resolution: $n_X = n_Z = 100$.

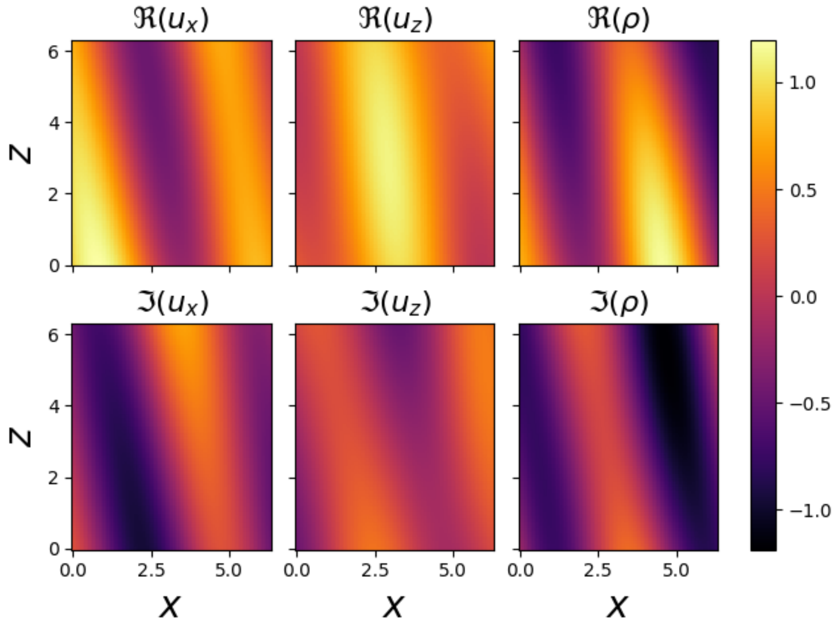

Figure 4.21: Eigenfunctions computed at the resonant α value corresponding to the $n = -2$ mode. Parameter values: $a = 0.1, \theta = \pi/4$, $\alpha = 0.3471065$, $\beta = 0$, $\gamma = 0.5$, $\mathcal{N} = 20$, $\mathrm{Re} = \mathrm{Pe} = 10^6$. Resolution: $n_X = n_Z = 100$.

4.4 Energetics

So far in this chapter we have provided numerical evidence of IGW instabilities for a range of different parameters. We wish to gain some some sense of what is driving these instabilities physically. One way to do that is to derive an evolution equation for the energy density of the disturbance. Within the evolution equation for the energy density are two important terms, each of which represent the contribution of a particular physical process towards driving instability in the system. The exact nature of each of these terms will be revealed momentarily. The energetic equations we present are based on those derived by LR96.

Finding the energy density serves another purpose, too. It provides a means of verifying the implementation of the Floquet solver. The energetic equations yield a formula for the growth rate σ_r. We can check that its value matches the value of $\Re(\sigma)$ to a suitable degree of accuracy, where $\Re(\sigma)$ is the value outputted by the Floquet solver.

4.4.1 Deriving a Formula for the Total Energy Density

In a stably-stratified Boussinesq fluid, we must consider two types of energy: kinetic and potential. To derive an evolution equation for the total energy density of the disturbance, we must first derive an evolution equation for each of these two types of energy density individually. We can derive both of these equations from system (4.32)-(4.34).

Kinetic Energetics

We define the *kinetic energy density* E_K of the disturbance as

$$E_K := |\hat{u}_x|^2 + |\hat{u}_y|^2 + |\hat{u}_z|^2. \tag{4.72}$$

The momentum equation (4.32) in component form is

$$\hat{u}_z \frac{\mathrm{d}\tilde{u}_x}{\mathrm{d}z} + C\hat{u}_x = \frac{L\hat{u}_x}{\mathrm{Re}} - i\alpha\hat{P} + \frac{k_x\hat{\varrho}}{k_z}, \tag{4.73}$$

$$C\hat{u}_y = \frac{L\hat{u}_y}{\mathrm{Re}} - i\beta\hat{P}, \tag{4.74}$$

$$C\hat{u}_z = \frac{L\hat{u}_z}{\mathrm{Re}} - \left(i\gamma + \frac{\mathrm{d}}{\mathrm{d}z}\right)\hat{P} - \hat{\varrho}. \tag{4.75}$$

We use the identity $z^*z \equiv |z|^2$ and the identity $(z + z^*)/2 \equiv \Re(z)$ for any $z \in \mathbb{C}$ to get an equation for the kinetic energy density E_K. We start by taking $[\hat{u}_x^*(4.73) + (4.73)^*\hat{u}_x]/2$:

$$\left(\sigma_r + \frac{\tilde{u}_z}{2}\frac{\mathrm{d}}{\mathrm{d}z}\right)|\hat{u}_x|^2 + \Re(\hat{u}_x^*\hat{u}_z)\frac{\mathrm{d}\tilde{u}_x}{\mathrm{d}z} = \frac{\Re(\hat{u}_x^* L\hat{u}_x)}{\mathrm{Re}} + \Re(i\alpha\hat{P}^*\hat{u}_x) + \frac{k_x\Re(\hat{u}_x^*\hat{\varrho})}{k_z}, \tag{4.76}$$

where σ_r is defined as the real part of σ:

$$\sigma_r := \Re(\sigma).$$

Next we take $[\hat{u}_y^*(4.74) + (4.74)^*\hat{u}_y]/2$:

$$\left(\sigma_r + \frac{\tilde{u}_z}{2}\frac{\mathrm{d}}{\mathrm{d}z}\right)|\hat{u}_y|^2 = \frac{\Re(\hat{u}_y^* L\hat{u}_y)}{\mathrm{Re}} + \Re(i\beta\hat{P}^*\hat{u}_y). \tag{4.77}$$

We then take $[\hat{u}_z^*(4.75) + (4.75)^*\hat{u}_z]/2$:

$$\left(\sigma_r + \frac{\tilde{u}_z}{2}\frac{\mathrm{d}}{\mathrm{d}z}\right)|\hat{u}_z|^2 = \frac{\Re(\hat{u}_z^* L\hat{u}_z)}{\mathrm{Re}} + \Re(i\gamma \hat{P}^*\hat{u}_z) - \Re(\hat{u}_z^*\hat{\varrho}) + \Re\left(\hat{u}_z\frac{\mathrm{d}\hat{p}^*}{\mathrm{d}z}\right). \tag{4.78}$$

By manipulating the pressure terms using mass continuity, their sum simplifies to

$$\left(\sigma_r + \frac{\tilde{u}_z}{2}\frac{\mathrm{d}}{\mathrm{d}z}\right)E_K = \Re\left[-(\hat{u}_x^*\hat{u}_z)\frac{\mathrm{d}\tilde{u}_x}{\mathrm{d}z} - \frac{\mathrm{d}}{\mathrm{d}z}\left(\hat{P}^*\hat{u}_z\right) + \frac{\hat{\boldsymbol{u}}_x^*\cdot L\hat{\boldsymbol{u}}_x^*}{\mathrm{Re}} + \left(\frac{k_x\hat{u}_x^*}{k_z} - \hat{u}_z^*\right)\hat{\varrho}\right]. \tag{4.79}$$

Equation (4.79) is an evolution equation for the kinetic energy density of the disturbance. Note the presence of the term $(k_x\hat{u}_x^*/k_z - \hat{u}_z^*)\hat{\varrho}$. This term represents the buoyancy flux of the disturbance. This is a means of converting between kinetic and potential energy in the system.

Potential Energetics

We define the *potential energy density* E_P of the disturbance as

$$E_P \coloneqq (k^2/k_z^2)|\hat{\varrho}|^2. \tag{4.80}$$

To form an equation for E_P, we begin with the internal energy equation (4.33). Taking $[\hat{\varrho}^*(4.33)+(4.33)^*\hat{\varrho}]/2$ and multiplying throughout by k^2/k_z^2 yields

$$\left(\sigma_r + \frac{\tilde{u}_z}{2}\frac{\mathrm{d}}{\mathrm{d}z}\right)E_P = \Re\left[-(\hat{u}_z^*\hat{\varrho})\frac{\mathrm{d}\tilde{\varrho}}{\mathrm{d}z}\frac{k^2}{k_z^2} + \frac{\hat{\varrho}^* L\hat{\varrho}}{\mathrm{Pe}}\frac{k^2}{k_z^2} + \left(\hat{u}_z^* - \frac{k\hat{u}_x^*}{k_z}\right)\hat{\varrho}\right]. \tag{4.81}$$

Equation (4.81) is an evolution equation for the potential energy density of the disturbance. Note that this equation also includes the buoyancy flux term $(k_x\hat{u}_x^*/k_z - \hat{u}_z^*)\hat{\varrho}$ which appeared in (4.79).

Combined Energetics

We define the *total energy density* as

$$E \coloneqq E_K + E_P. \tag{4.82}$$

We can combine the evolution equations (4.79) and (4.81) for the kinetic and potential energy densities E_K and E_P to get an evolution equation for the total energy density E.

$$\left(\sigma_r + \frac{\tilde{u}_z}{2}\frac{\mathrm{d}}{\mathrm{d}z}\right)E = \Re\left[-(\hat{u}_x^*\hat{u}_z)\frac{\mathrm{d}\tilde{u}_x}{\mathrm{d}z} - (\hat{u}_z^*\hat{\varrho})\frac{\mathrm{d}\tilde{\varrho}}{\mathrm{d}z}\frac{k^2}{k_z^2} - \frac{\mathrm{d}}{\mathrm{d}z}\left(\hat{P}^*\hat{u}_z\right) + \frac{\hat{\boldsymbol{u}}_x^*\cdot L\hat{\boldsymbol{u}}_x}{\mathrm{Re}} + \frac{\hat{\varrho}^* L\hat{\varrho}}{\mathrm{Pe}}\frac{k^2}{k_z^2}\right].$$

When adding the kinetic and potential equations together, the buoyancy flux terms from each cancel each other out. This is consistent with the idea that the buoyancy flux term represents conversion between kinetic and potential energy in either direction. Upon integration over one period of the primary wave, two of these terms vanish due to the 2π-periodicity of $\hat{f}$ variables. We call these *conservative* terms. We are left with

$$\sigma_r\int_0^{2\pi} E\mathrm{d}z = \int_0^{2\pi}\Re\left[-(\hat{u}_x^*\hat{u}_z)\frac{\mathrm{d}\tilde{u}_x}{\mathrm{d}z} - (\hat{u}_z^*\hat{\varrho})\frac{\mathrm{d}\tilde{\varrho}}{\mathrm{d}z}\frac{k^2}{k_z^2} + \frac{\hat{\boldsymbol{u}}_x^*\cdot L\hat{\boldsymbol{u}}_x}{\mathrm{Re}} + \frac{\hat{\varrho}^* L\hat{\varrho}}{\mathrm{Pe}}\frac{k^2}{k_z^2}\right].$$

We arrive at a formula for σ_r:

$$\sigma_r = \mathcal{E}_K + \mathcal{E}_P + \mathcal{D}_\nu + \mathcal{D}_\kappa. \tag{4.83}$$

We can compare the value for σ_r that (4.83) produces with the value of σ_r found by the numerical Floquet solver. This new formula for σ_r contains four terms, two of which can potentially drive the instabilities we study.

We define the contribution of *shear production* to the growth rate ($\mathcal{E}_K$) as:

$$\mathcal{E}_K := -\frac{1}{I_E}\int_0^{2\pi} \Re\left[(\hat{u}_x^* \hat{u}_z)\frac{\mathrm{d}\tilde{u}_x}{\mathrm{d}z}\right]\mathrm{d}z,$$

and the contribution of *buoyancy production* to the growth rate ($\mathcal{E}_P$) as:

$$\mathcal{E}_P := -\frac{k^2}{k_z^2 I_E}\int_0^{2\pi} \Re\left[(\hat{u}_z^* \hat{\varrho})\frac{\mathrm{d}\tilde{\varrho}}{\mathrm{d}z}\right]\mathrm{d}z, \tag{4.84}$$

where I_E is the integral of the total energy density:

$$I_E := \int_0^{2\pi} E\mathrm{d}z = 2\pi \sum_{n=-\infty}^{\infty}\left(|||\boldsymbol{u}_n|||^2 + \frac{k^2}{k_z^2}|\varrho_n|^2\right).$$

The shear production term is a means of transferring kinetic energy between the primary wave fluctuation in velocity and the velocity disturbance. The energy transfer can be in either direction and is induced by the disturbance interacting with shear in the velocity field. Conversely, the buoyancy production term is a means of transferring potential energy between the primary wave and the disturbance. It contains the nonlinear interaction between the disturbance and basic fluctuation in density. Importantly, the growth rate σ_r is predominantly the combination of the shear production term $\mathcal{E}_K$ and the buoyancy production term $\mathcal{E}_P$. The terms $\mathcal{E}_K$ and $\mathcal{E}_P$ can only drive instability if they have a positive non-zero value.

The terms $\mathcal{D}_\nu$ and $\mathcal{D}_\kappa$ represent energy losses due to viscous and thermal dissipation. Such energy losses reduce the growth rate. At the values of Re and Pe we consider, the magnitudes of $\mathcal{D}_\nu$ and $\mathcal{D}_\kappa$ are typically expected to be negligible in comparison to that of $\mathcal{E}_K$ and $\mathcal{E}_P$. The dissipation terms are defined as

$$\mathcal{D}_\nu := \frac{1}{I_E}\int_0^{2\pi}\frac{\hat{\boldsymbol{u}}_x^* \cdot L\hat{\boldsymbol{u}}_x}{\mathrm{Re}}\mathrm{d}z,$$
$$\mathcal{D}_\kappa := \frac{1}{I_E}\int_0^{2\pi}\frac{k^2}{k_z^2}\frac{\hat{\varrho}^* L\hat{\varrho}}{\mathrm{Pe}}\mathrm{d}z.$$

These can be computed exactly from the numerical eigenfunctions f_n via the formulae

$$\mathcal{D}_\nu = \frac{2\pi}{I_E}\sum_{n=-\infty}^{\infty} L_n\left(\frac{|u_n^x|^2 + |u_n^y|^2 + |u_n^z|^2}{\mathrm{Re}}\right), \tag{4.85}$$

$$\mathcal{D}_\kappa = \frac{2\pi}{I_E}\sum_{n=-\infty}^{\infty}\frac{k^2}{k_z^2}L_n\left(\frac{|\varrho_n|^2}{\mathrm{Pe}}\right). \tag{4.86}$$

Lombard and Riley (1996) provide a summary of the various means of transferring energy, which we reproduce in Figure 4.22.

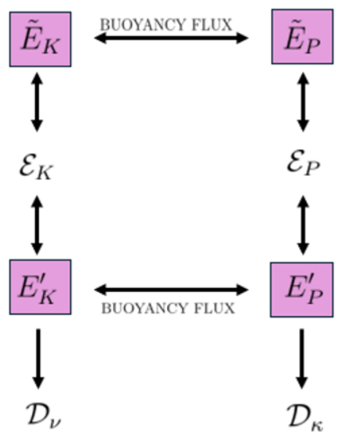

Figure 4.22: Schematic depicting processes of energy transfer inspired by Lombard and Riley (1996). $\tilde{E}_K$ and $\tilde{E}_P$ denote the primary wave energy densities of the kinetic and potential varieties respectively. E'_K and E'_P represent the corresponding energy densities associated with the disturbance.

Implementation

We wish to calculate the value of $\mathcal{E}_K$ and the value of $\mathcal{E}_P$ corresponding to the fastest-growing mode at each point on the (α, β) grid. At each grid point, we have a complex eigenvalue σ with maximal real part σ_r. We calculate the integrals from each of $\mathcal{E}_K$ and $\mathcal{E}_P$ using the trapezoidal rule. To do so, we define functions representing the integrand in each case:

$$F_K(z) = \Re[\hat{u}_x^*(z)\hat{u}_z(z)\partial_z\tilde{u}_x(z)],$$
$$F_P(z) = \Re[\hat{u}_z^*(z)\hat{\varrho}(z)\partial_z\tilde{\varrho}(z)].$$

We can calculate the individual functions $\hat{f}(z)$ within via (4.44). Fourier coefficients f_n are extracted from eigenvector components within (4.67)-(4.70). We can thus calculate $\mathcal{E}_K$ and $\mathcal{E}_P$ numerically via

$$\mathcal{E}_K = -1/I_E \int_0^{2\pi} F_K(z)\mathrm{d}z,$$
$$\mathcal{E}_P = -k^2/(k_z^2 I_E) \int_0^{2\pi} F_P(z)\mathrm{d}z,$$

where I_E is computed via

$$I_E = 2\pi \sum_{n=-\mathcal{N}}^{\mathcal{N}} (|u_n^x|^2 + |u_n^y|^2 + |u_n^z|^2 + k^2/k_z^2|\varrho_n|^2).$$

Energy Balance

Here, we check that the numerically-obtained growth rates match up to those computed using formula (4.83) for σ_r. On top of approximating $\mathcal{E}_K$ and $\mathcal{E}_P$ via the trapezoidal rule, such a check requires the computation of values for $\mathcal{D}_\nu$ and $\mathcal{D}_\kappa$. This is achieved through formulae (4.85) and (4.86). At each point in parameter space we check, we compute the values of $\mathcal{E}_K$, $\mathcal{E}_P$, $\mathcal{D}_\nu$ and $\mathcal{D}_\kappa$ using the functions $\hat{f}(z)$ corresponding to the eigenvalue σ with maximum real part found by solving (4.45) at that point.

In particular, we check that the following is satisfied to a suitable degree of accuracy:

$$\sigma_r = \Re(\sigma), \tag{4.87}$$

where σ_r is given by formula (4.83) and σ is the eigenvalue with the maximum real part of the eigenvalue problem (4.45) constituting the numerical Floquet solver. Below we present values detailing the degree of accuracy to which the relationship (4.87) is preserved by the implementation. We do this by fixing $\beta = 0$ and calculating the relevant quantities at a selection of α values which exactly satisfy the triadic resonance criterion (4.49). Table 4.5 below confirms that energetic balance is sufficiently satisfied by the implementation.

α	$\mathcal{E}_K$	$\mathcal{E}_P$	σ_r	$\Re(\sigma)$
0.60854561	0.01215112	0.01372035	0.02586813	0.02586813
1.08768148	0.01285909	0.01430847	0.02715939	0.02715939
1.55082784	0.01301628	0.01449587	0.02749678	0.02749678
2.00873507	0.01308067	0.01457225	0.02762794	0.02762794
2.46427470	0.01311317	0.01461071	0.02768689	0.02768690
2.91854292	0.01313180	0.01463277	0.02771317	0.02771318
3.37204945	0.01314343	0.01464658	0.02772180	0.02772182
3.82506357	0.01315110	0.01465573	0.02771939	0.02771956

Table 4.5: Values of energetic quantities calculated at values of α satisfying exact triadic resonance. Parameter values: $a = 0.1, \theta = \pi/4, \beta = 0, \gamma = 0, \mathrm{Re} = \mathrm{Pe} = 10^6$. Resolution: $\mathcal{N} = 20$, $n_\alpha = n_\beta = 100$.

4.4.2 Decomposing the Growth Rate

To determine what is driving IGW instabilities energetically, we contour $\mathcal{E}_K$ and $\mathcal{E}_P$ in (α, β)-space and compare the results side-by-side with contours of σ_r in (α, β)-space. This allows us to visually deduce the relative contributions of $\mathcal{E}_K$ and $\mathcal{E}_P$ to σ_r. Since the values of Re, Rm and Pe we consider in Section 4.4.2 are fixed at 10^6, the dissipation terms $\mathcal{D}_\nu$ and $\mathcal{D}_\kappa$ have a negligible contribution to σ_r. The growth rate is therefore approximately equal to the sum of $\mathcal{E}_K$ and $\mathcal{E}_P$.

Small-Amplitude Primary Wave

We plot the contributions $\mathcal{E}_K$ and $\mathcal{E}_P$ to the growth rates alongside the growth rates themselves for a small-amplitude primary wave with $a = 0.1$ and $\theta = \pi/4$ in Figure 4.23. Any negative values of $\mathcal{E}_K$ and $\mathcal{E}_P$ are set to zero in Figure 4.23 to improve the visibility of unstable modes of disturbance. The same applies to σ_r, which is always the case for any plots of the real part of the complex growth rate in this thesis. It is clear that the instability tongues pointing in the negative α direction are predominantly driven by buoyancy production, whereas the instability tongues pointing in the positive β direction are driven roughly as much by shear production as they are by buoyancy production. We now consider two points in (α, β)-space: one which occupies a tongue pointing in the positive β direction and one which occupies a tongue pointing in the negative α direction. We compare the eigenfunctions computed at each point to determine whether there are any fundamental differences between the two.

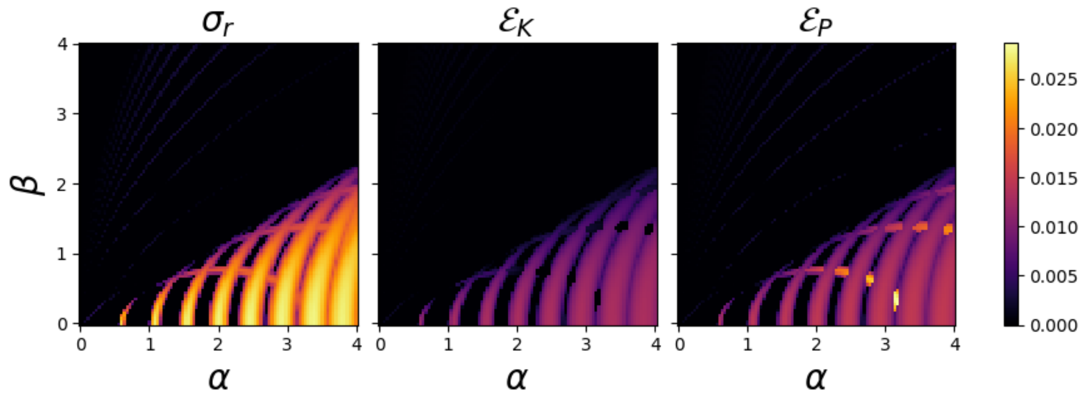

Figure 4.23: Shear production $\mathcal{E}_K$ and buoyancy production $\mathcal{E}_P$ alongside growth rate for a range of α and β values. Negative values of σ_r, $\mathcal{E}_K$ and $\mathcal{E}_P$ have been set to zero. Parameter values: $a = 0.1$, $\theta = \pi/4, \gamma = 0, \mathrm{Re} = \mathrm{Pe} = 10^6$. Resolution: $\mathcal{N} = 20$, $n_\alpha = n_\beta = 100$.

Eigenfunctions at $(\alpha, \beta) = (0.608, 0)$

We start by plotting eigenfunctions computed at the point $(\alpha, \beta) = (0.608, 0)$, which occupies a tongue pointing in the positive β direction. Here, the instability is driven by both shear and buoyancy in approximately equal measure. The resulting eigenfunctions, along with all parameter values used to plot them, are identical to those which feature in Figure 4.20 from Section 4.3, so we do not reproduce the plot here.

Eigenfunctions at $(\alpha, \beta) = (2.778, 0.650)$

We now plot eigenfunctions computed at the point $(\alpha, \beta) = (2.778, 0.650)$, which occupies a tongue pointing in the negative α direction. Here, the instability is driven purely by buoyancy. The results are shown in Figure 4.24.

There is one obvious difference between the disturbances at $(\alpha, \beta) = (0.608, 0)$ and those at $(\alpha, \beta) = (2.778, 0.650)$. The orientation of the wavevector of the disturbance differs significantly between the two. We speculate that this in keeping with the fact that the latter is driven purely by potential energy transfers, and that the former is driven by a combination of kinetic and potential energy transfers.

In Figures 4.20 and 4.24 we have deliberately chosen two resonance bands which are produced by the same Fourier mode coupling: the coupling between the $n = -2$ mode and the $n = -1$ mode. It is interesting that two bands of instability produced by the same exact resonant coupling can have such differences in the way that the instability is driven energetically.

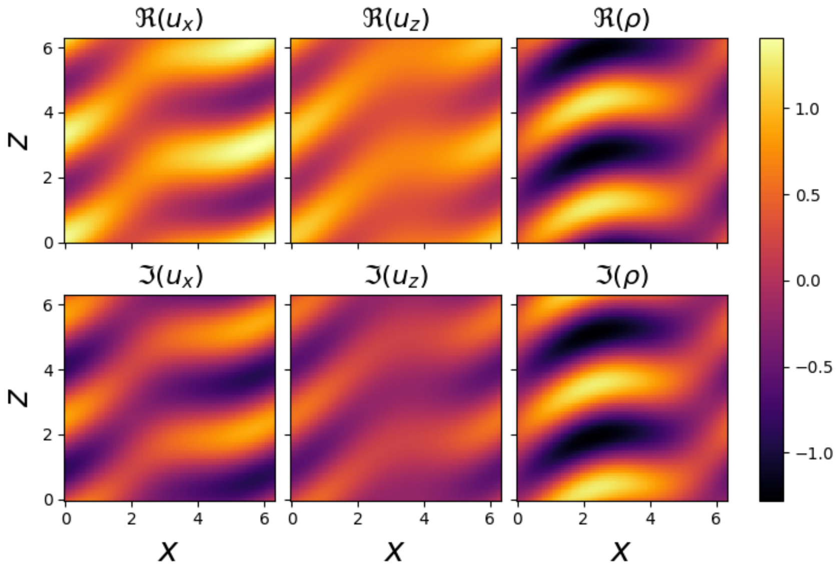

Figure 4.24: Perturbations corresponding to an instability from Figure 4.23 driven by both shear and buoyancy. Parameter values: $a = 0.1$, $\theta = \pi/4$, $\alpha = 2.778$, $\beta = 0.650$, $\gamma = 0$, $\mathrm{Re} = \mathrm{Pe} = 10^6$. Resolution: $\mathcal{N} = 20$, $n_X = n_Z = 100$.

Overturning Amplitude Primary Wave

In Figure 4.25 we present the energetic quantities for instabilities of IGWs with amplitude $a = 1$, the threshold for the onset of overturning. Again, any negative values of $\mathcal{E}_K$ and $\mathcal{E}_P$ are set to zero in Figure 4.25 to improve the visibility of unstable modes of disturbance. Recall that parameter space divides itself into three distinct regions of instability, labelled I, II and III respectively. Each region is labelled in Figure 4.25. We find that the instabilities in Region I are almost entirely driven by buoyancy as opposed to by shear. This makes sense because $a = 1$ is the critical value at which we expect static convective instability to switch on. Instabilities in Region III are predominantly driven by shear, whereas instabilities in Region II are driven slightly more by buoyancy than they are by shear. We now investigate whether there are any obvious differences between the eigenfunctions computed in each of these regions.

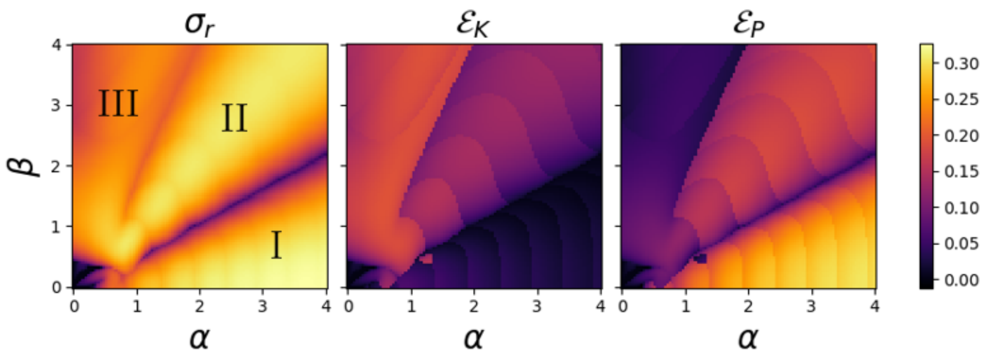

Figure 4.25: Shear production $\mathcal{E}_K$ and buoyancy production $\mathcal{E}_P$ alongside growth rate for a range of α and β values. Labels I, II, and III represent divisions of wavenumber space according to regions of instability. Parameter values: $a = 1$, $\theta = \pi/4, \gamma = 0, \mathrm{Re} = \mathrm{Pe} = 10^6$. Resolution: $\mathcal{N} = 20$, $n_\alpha = n_\beta = 100$.

Eigenfunctions in Region I

In Figure 4.26 we plot the real and imaginary parts of the disturbance quantities U_X', U_Z' and ρ' computed at the point $(\alpha, \beta) = (3, 0)$, which lies in Region I of Figure 4.25. We find that there are approximately three crests spanning the domain $Z \in [0, 2\pi)$. Instabilities in Region I are almost entirely driven by buoyancy as opposed to shear as shown in Figure 4.25, though it is not clear whether this can explain the behaviour exhibited by the eigenfunctions in Region I.

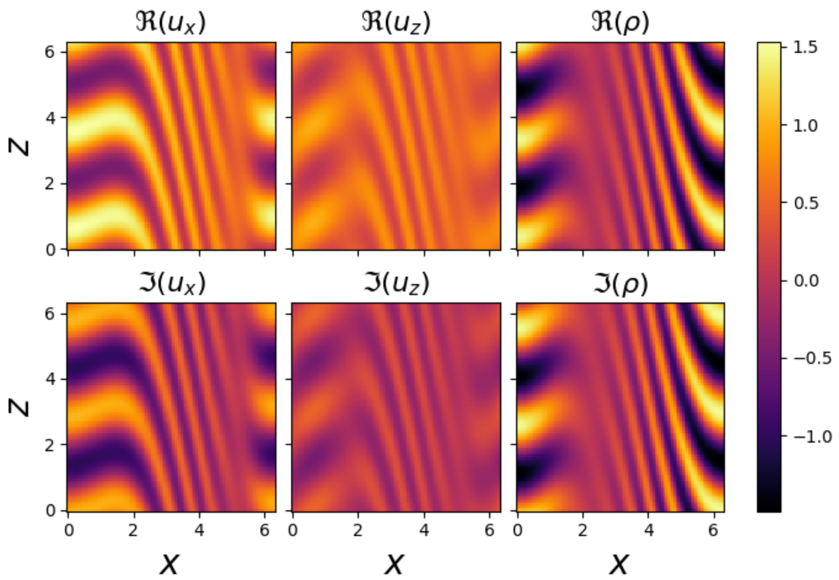

Figure 4.26: Perturbations corresponding to an instability from Region I in Figure 4.25. Parameter values: $a = 1$, $\theta = \pi/4$, $\alpha = 3$, $\beta = 0$, $\gamma = 0$, $\mathrm{Re} = \mathrm{Pe} = 10^6$. Resolution: $\mathcal{N} = 40$, $n_X = n_Z = 100$.

Eigenfunctions in Region II

In Figure 4.27 we plot the real and imaginary parts of the disturbance quantities U_X', U_Z' and ρ' computed at the point $(\alpha, \beta) = (2, 2)$, which lies in Region II of Figure 4.25. As shown in Figure 4.25, instabilities are driven slightly more by buoyancy than they are by shear in Region II, though the contribution of both $\mathcal{E}_K$ and $\mathcal{E}_P$ is significant. We find that there are fewer crests occupying the same domain in Z compared with the eigenfunctions computed in Region I. The wavelength of the disturbance is greater in Region II than it is in Region I.

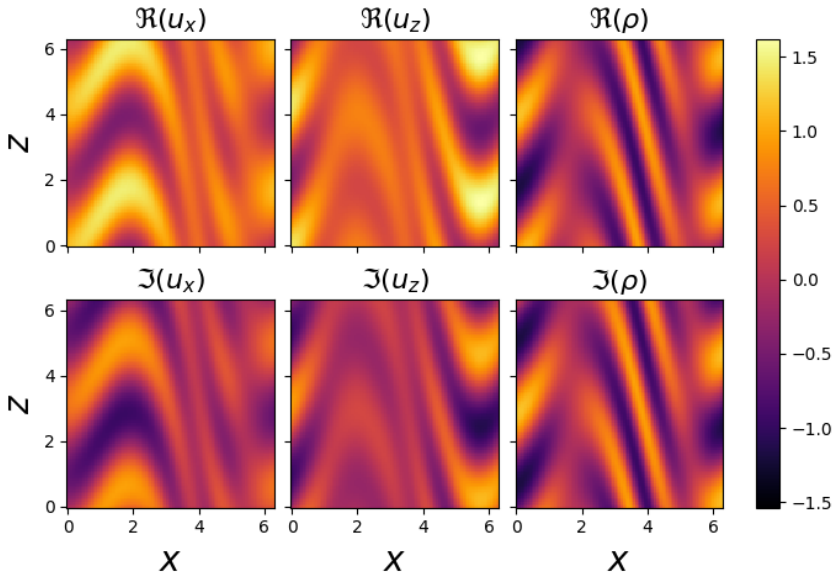

Figure 4.27: Perturbations corresponding to an instability from Region I in Figure 4.25. Parameter values: $a = 1$, $\theta = \pi/4$, $\alpha = 2$, $\beta = 2$, $\gamma = 0$, $\mathrm{Re} = \mathrm{Pe} = 10^6$. Resolution: $\mathcal{N} = 40$, $n_X = n_Z = 100$.

Eigenfunctions in Region III

In Figure 4.28 we plot the real and imaginary parts of the disturbance quantities U_X', U_Z' and ρ' computed at the point $(\alpha, \beta) = (0, 3)$, which lies in Region III of Figure 4.25. As shown in Figure 4.25, instabilities in Region III are predominantly driven by shear. We find that the behaviour of the disturbance in Region III is very different to the behaviour observed in Region I and Region II. In Region III, the disturbance wavevector is oriented approximately in the horizontal X-direction. The same can certainly not be said of the disturbance in Region I and Region II.

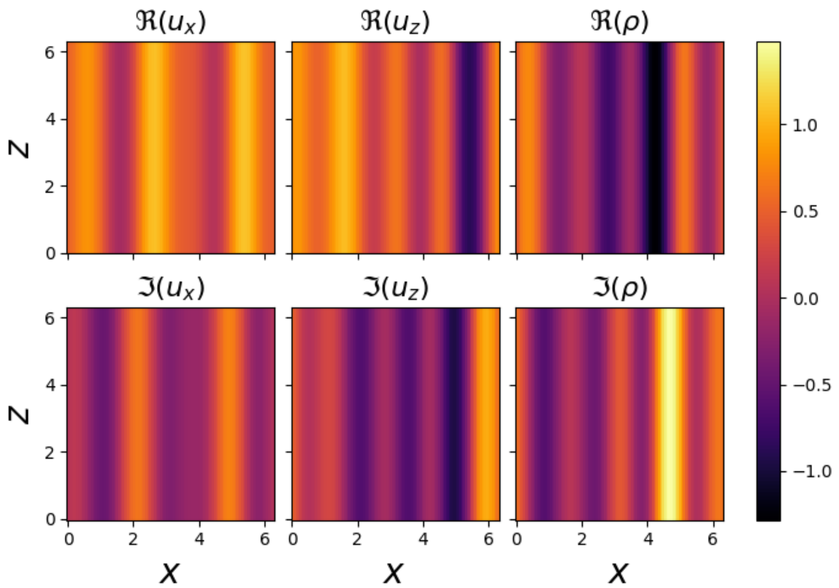

Figure 4.28: Perturbations corresponding to an instability from Region I driven by both shear and buoyancy. Parameter values: $a = 1$, $\theta = \pi/4$, $\alpha = 0$, $\beta = 3$, $\gamma = 0$, $\mathrm{Re} = \mathrm{Pe} = 10^6$. Resolution: $\mathcal{N} = 40$, $n_X = n_Z = 100$.

Influence of Primary Wavevector Angle

We finish our analysis of the energetics of IGWs in Boussinesq fluids by investigating the influence of primary wavevector angle θ on $\mathcal{E}_K$ and $\mathcal{E}_P$. In Figures 4.29 and 4.30 we plot energetic quantities alongside the growth rate for a selection of different orientations of the primary wavevector in the domain $\theta \in [0, \pi/2)$. Unlike Figures 4.23 and 4.25, we have not set negative values of $\mathcal{E}_K$ and $\mathcal{E}_P$ to zero here. In this domain for θ, the primary wave frequency gets smaller as we increase the size of θ. At the highest primary wave frequency we consider $\theta = \pi/16$, instabilities in Region I are driven predominantly by buoyancy, however the contribution of shear is not negligible. At the lowest primary wave frequencies, instabilities are driven fairly equally by shear and buoyancy. Energy is essentially equipartitioned. How do we interpret this physically? As $\theta \to \pi/2$, $\cos\theta \to 0$, i.e the primary wave frequency tends to zero. In this limit, the primary wave approaches a propagation direction of the positive Z-axis, the direction of stratification. So instabilites of IGWs with wavevectors aligned with the direction of gravity are driven by shear and buoyancy in equal measure.

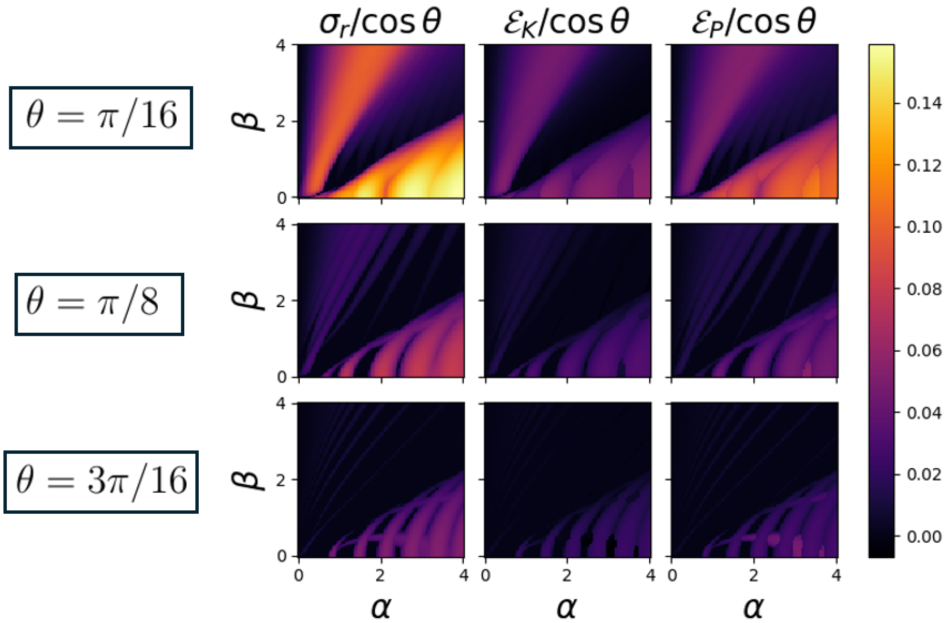

Figure 4.29: Shear production $\mathcal{E}_K$ and buoyancy production $\mathcal{E}_P$ alongside growth rate for a range of α and β values. Parameter values: $a = 0.1$, $\gamma = 0$, $\mathrm{Re} = \mathrm{Pe} = 10^6$. Resolution: $\mathcal{N} = 25$, $n_\alpha = n_\beta = 100$.

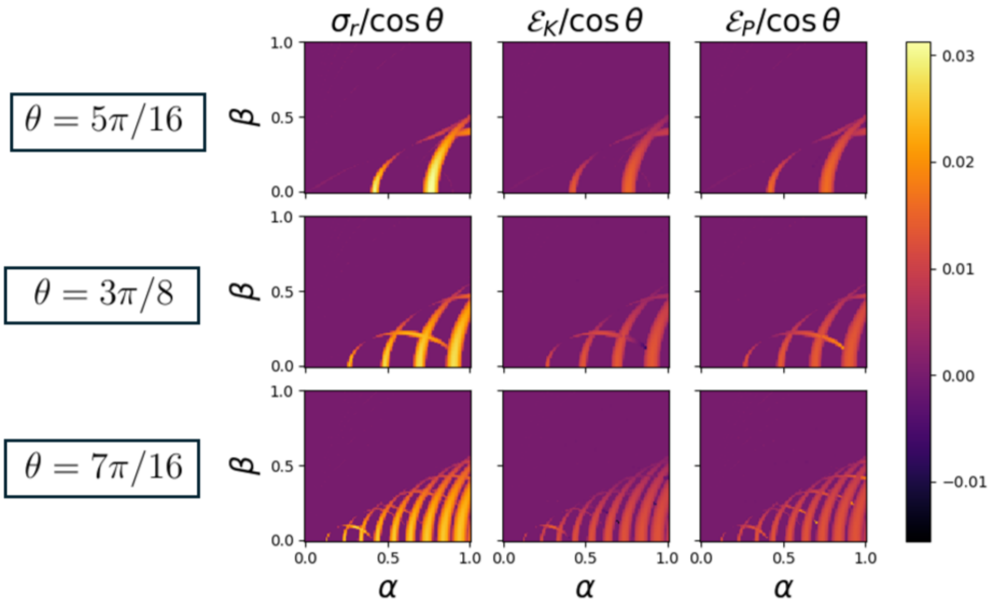

Figure 4.30: Shear production $\mathcal{E}_K$ and buoyancy production $\mathcal{E}_P$ alongside growth rate for a range of α and β values. Parameter values: $a = 0.1, \gamma = 0, \mathrm{Re} = \mathrm{Pe} = 10^6$. Resolution: $\mathcal{N} = 25, n_\alpha = n_\beta = 100$.

4.5 Comparing Numerical and Theoretical Growth Rates

In Chapter 3 we derived a theoretical framework for predicting the growth rates of TRIs for IGWs at points in wavenumber space where the triadic resonance conditions are satisfied exactly. In Chapter 4, so far we have used a numerical Floquet eigenvalue solver to compute growth rates of IGWs. It is now time to bridge the gap between these two avenues of investigation. We wish to test the agreement between the two for instabilities of small-amplitude IGWs which can be attributed to TRIs between IGWs.

4.5.1 Exact Resonances

Here we seek to identify α values at which exact triadic resonance occurs by finding resonant α as a function of n along the $\beta = 0$ axis at $\gamma = 0$. The daughter wave frequencies, now treated as functions of α, are given by (4.53). For each Fourier mode n that we consider, we fix $\boldsymbol{K}$ and treat $\boldsymbol{K}_A$ and $\boldsymbol{K}_B$ as functions of α. To ensure that the wavevector resonance condition (4.49) is satisfied, we compute $\boldsymbol{K}_A$ and $\boldsymbol{K}_B$ using formulae (4.54)-(4.59) from earlier in this chapter.

The frequency resonance condition (4.50) amounts to $\Omega(\alpha) = 0$, where

$$\Omega(\alpha) := [\omega + \omega_A(\alpha) - \omega_B(\alpha)]/N.$$

Finding the root α of this function $\Omega(\alpha)$ gives us the α value satisfying exact parametric resonance for each Fourier mode n. We use the Python routine `scipy.optimize.fsolve` with initial value $\alpha_0 = 0.1$ to retrieve these α values.

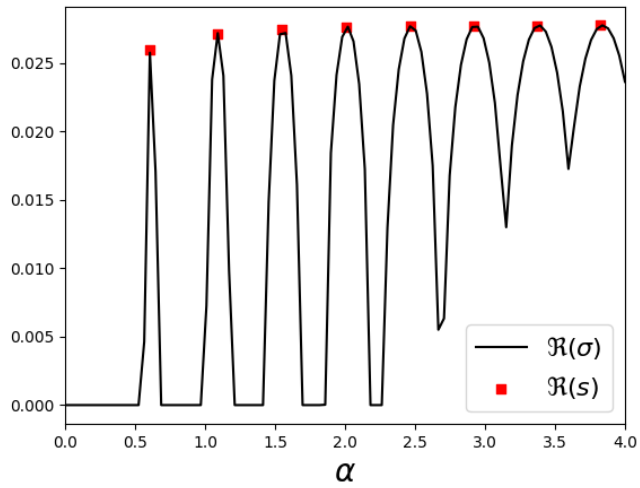

Figure 4.31: Growth rates $\Re(\sigma)$ computed by the ideal form of the Floquet solver for a range of α values, along with growth rates $\Re(s)$ found using formula (4.88) calculated at values of α satsifying exact triadic resonance. Each resonant value of α corresponds to a Fourier mode n from the set $n \in [-9, -2]$. Parameter values: $a = 0.1$, $\theta = \pi/4$, $\beta = 0$, $\gamma = 0$. Resolution: $\mathcal{N} = 20$, $n_\alpha = 100$.

Growth Rates at Points of Exact Resonance

Now that we have a way of finding a value of α at which a resonant triad appears for each Fourier mode n at fixed β, the natural next step is to use the formula for s to predict the growth rate at these points and determine how well they agree with the growth rates $\Re(\sigma)$ found by the numerical Floquet solver. For theoretical growth rates, we calculate

$$s(\alpha) = a\sqrt{\frac{c_2(\alpha)c_4(\alpha)}{c_1(\alpha)c_3(\alpha)}}, \tag{4.88}$$

where the coefficient functions c_i are given by formulae (3.55)-(3.58), at resonant values of α found by solving $\Omega(\alpha) = 0$. The results of comparing the two methods of finding the growth rate are shown in Figure 4.31. This confirms that the instabilities in Region 1 are induced by resonant triads composed of three IGWs.

Expectedly, the asymptotic predictions made using the general formula for s get increasingly accurate the smaller the value of a. We quantify the agreement between these asymptotic predictions for the growth rate and the numerical growth rates by considering the relative error in the approximation later in this section.

Influence of Thermal Diffusion

Earlier in Section 4.2.2 we viewed what the impact of thermal diffusion was on the numerical Floquet contours. We saw that reducing the thermal Péclet number progressively removes resonant triads from the region of parameter space observed. We can quantify exactly how much impact reducing Pe has on the growth rate using the linear decay rate due to thermal diffusion, which was derived in Section 2.3.4. We derived this under the assumption that $\mathrm{Pr} \ll 1$, which means that we can neglect viscosity in favour of thermal diffusion. This assumption is relevant for stellar interiors. We found that, under the influence of thermal diffusion, frequencies are given by

$$\omega = \omega_{\text{ideal}} - i\kappa k^2/2 \tag{4.89}$$

to leading order in κ, where $\omega_{\text{ideal}} = NK_X/K$. The dimensionless equivalent of this solution is

$$\frac{\omega}{N} = \frac{\omega_{\text{ideal}}}{N} - \frac{i}{2\text{Pe}}.$$

The growth rate is just the imaginary part of this frequency:

$$\Im\left(\frac{\omega}{N}\right) = -\frac{1}{2\text{Pe}}.$$

The term on the right hand side represents the leading order decay rate due to thermal diffusion. For the primary wave, $\Im(\omega/N)$ is uniformly negative since the ideal primary wave does not grow. For disturbances, the equivalent growth rate formula is

$$\Re(\sigma) = \Re(\sigma_{\text{ideal}}) - \frac{k_A^2}{2\text{Pe}},$$

where k_A is the norm of the dimensionless disturbance wavector $\boldsymbol{k}_A := \boldsymbol{K}_A/K$. The second term on the right hand side represents the linear decay rate due to thermal diffusion. We label it as Λ_κ:

$$\Lambda_\kappa := \frac{k_A^2}{2\text{Pe}}.$$

Here, the wavevector components are determined (4.54)-(4.56). This was derived at leading order in κ. We can assess how well Λ_κ predicts the damping rates due to thermal dissipation by subtracting it from the ideal theoretical growth rate $\Re(s)$ and comparing this value with the corresponding numerical Floquet values at points of exact triadic resonance. We perform this in Figures 4.32 and 4.33. We observe good agreement between $\Re(\sigma)$ and $\Re(s) - \Delta_\kappa$ for larger growth rates but Δ_κ overestimates the extent of the dissipation for smaller growth rates.

In the $\text{Pe} = 10^3$ panel of Figure 4.33, an adjustment has been made to the plotting procedure. For all other panels, the mapping from n values to corresponding resonant α values at which resonant peaks in growth rate appear is one-to-one. For any integer m, the m-th value of n corresponds to the m-th value of α. However, at $\text{Pe} = 10^3$, the Fourier mode $n = -2$ possesses two values of α in this range which lead to a visible TRI peak in growth rate: $\alpha \approx 0.61$ and $\alpha \approx 3.28$. As a result, for the the $\text{Pe} = 10^3$ panel we plot nine theoretical growth rates instead of eight. Two of these correspond to the $n = -2$ mode and each of the remaining seven correspond to one of the modes from the set $n \in \{-9, -8, ..., -3\}$.

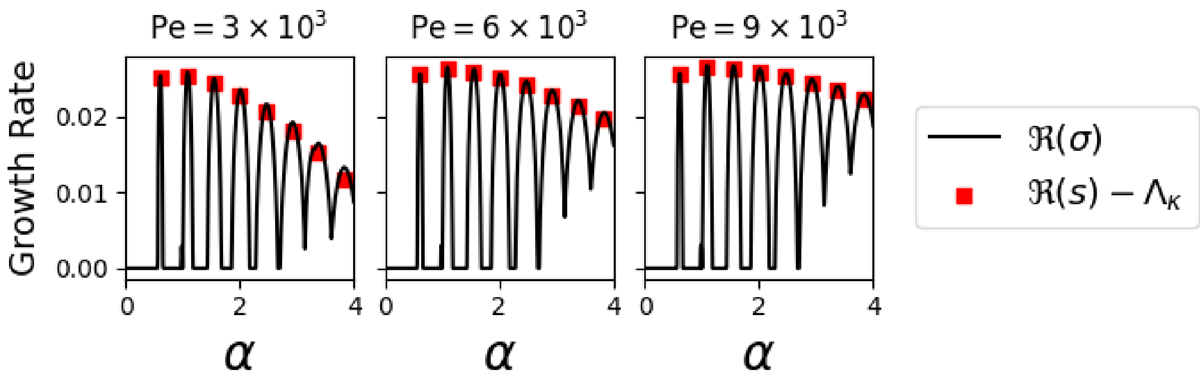

Figure 4.32: Growth rates $\Re(\sigma)$ calculated by the Floquet solver alongside growth rates $\Re(s)$ computed using (4.88) and adjusted by the decay rate correction Λ_κ due to thermal diffusion for different values of the thermal Péclet number Pe. Any negative growth rates obtained by either method have been set to zero. Parameter values: $a = 0.1$, $\theta = \pi/4$, $\beta = 0$, $\gamma = 0$, $\mathcal{N} = 20$. The Fourier modes used for the theoretical calculation of s are $n \in \{-2, -3, ..., -9\}$.

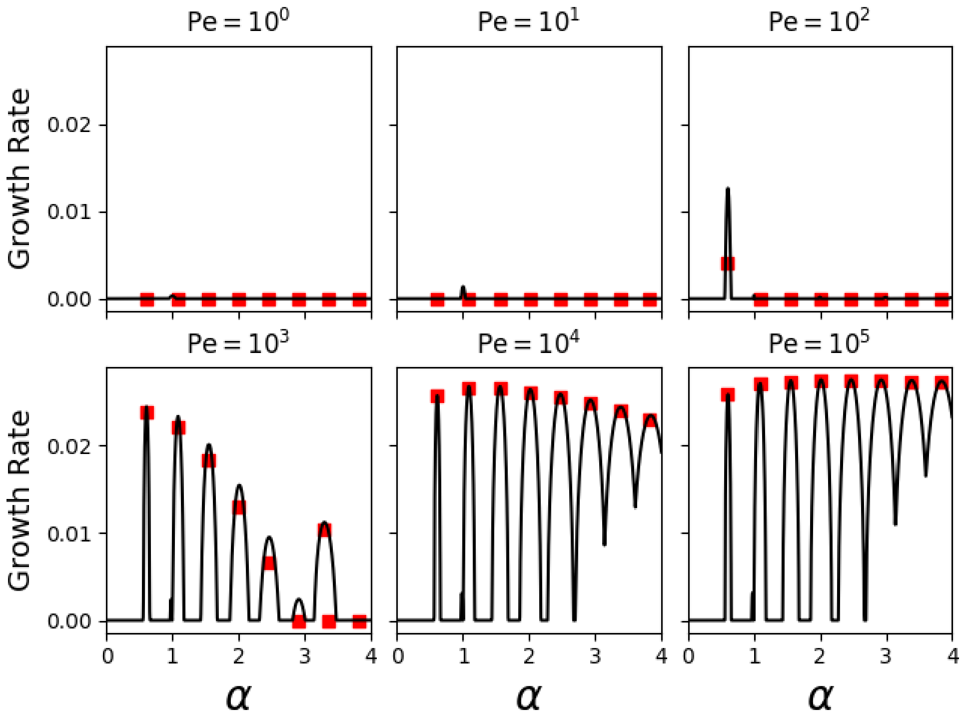

Figure 4.33: Growth rates $\Re(\sigma)$ calculated by the Floquet solver alongside growth rates $\Re(s)$ computed using (4.88) and adjusted by the decay rate correction Λ_κ due to thermal diffusion for different values of the thermal Péclet number Pe. Any negative growth rates obtained by either method have been set to zero. Parameter values: $a = 0.1$, $\theta = \pi/4$, $\beta = 0$, $\gamma = 0$, $\mathcal{N} = 20$. The Fourier modes used for the theoretical calculation of s are $n \in \{-9, -8, ..., -2\}$.

4.5.2 Short Wavelength Limit

At the end of Chapter 3 we demonstrated how the asymptotically predicted formula for s simplifies in the limit in which the wavelengths of the disturbances (the daughter waves) are much shorter than that of the primary wave. We expressed this as

$$k_A \gg k, \quad k_B \gg k.$$

This limit is known as the parametric subharmonic instability, characterised by the relationship

$$\omega_A \approx -\omega/2, \quad \omega_B \approx \omega/2. \tag{4.90}$$

Prior to making this assumption, the formula for s took the form

$$s = s(a, \theta, \alpha, \beta, \gamma, n).$$

We showed that when taking the PSI limit, the formula for s collapses to a function of primary wave parameters a and θ only:

$$s(a, \theta) = \frac{a}{16} \frac{\cos\theta}{\sin\theta} \left[\pm 2\sin^3\theta + (1 + 2\cos^2\theta)\sqrt{4 - \cos^2\theta} \right]. \tag{4.91}$$

This formula was originally derived by Sonmor and Klaassen (1997). Throughout this chapter we have computed numerical growth rates $\Re(\sigma)$ using roots of the Floquet eigenvalue problem (4.45). In Figure 4.34 we find the roots σ of equation (4.45) as a function of a and θ. For each a and each θ, we maximise $\Re(\sigma)$ over the range of (α, β) we used in this chapter, i.e. $(\alpha, \beta) \in [0, 4] \times [0, 4]$. Alongside these values we plot the output of the function $s(a, \theta)$ evaluated at the relevant a and θ values. We find that when varying θ there is very good agreement between the two methods, suggesting that the PSI estimate $s(\theta)$ reliably predicts the fastest-growing instabilities for any primary wave. When varying a the agreement is only strong for the smallest amplitudes. This is expected considering a is the ordering parameter we used to expand the variables in the asymptotic calculation. The theoretical framework is valid under the assumption that $a \ll 1$. It is surprising that even at $a = 1$, the value of $s(a)$ is of a similar size to the value of $\Re(\sigma)$ in Figure 4.34, despite the assumption $a \ll 1$ being violated. This

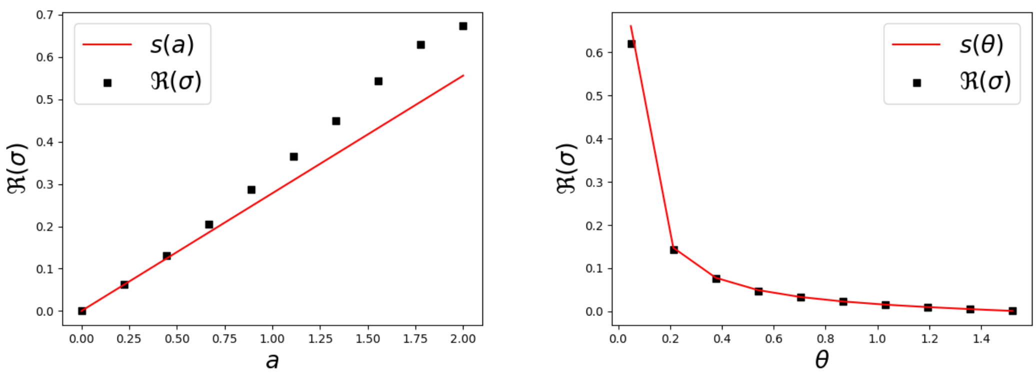

Figure 4.34: (Black squares) Numerical growth rate calculated via the ideal form of (4.45) maximised over (α, β) as a function of primary wave amplitude a (left panel) and as a function of primary wave orientation θ (right panel). (Red line) Theoretical prediction for the growth rate in the short wavelength limit calculated via (4.91). Parameter values: $a = 0.1$ (right panel), $\theta = \pi/4$ (left panel), $\gamma = 0$. Resolution: $\mathcal{N} = 40$.

linear relationship between amplitude a and the maximum growth rate $\Re(\sigma)$ observed is a result originally obtained by McEwan and Robinson (1975), who studied parametric instabilities of IGWs through a Mathieu equation.

4.5.3 Absolute Error and Relative Error

It is visually apparent that the theoretical and numerical growth rates agree, but we should have some way of quantifying to what extent the two values agree. We need an expression for the error in the approximation.

The asymptotic expansion for the growth rate σ can be written as

$$\sigma = \sigma_0 + \sigma_1 + \sigma_2 + \ldots \tag{4.92}$$

where σ_i represents the growth rate at the i-th order in a.

From this we find the absolute disagreement δ between the numerical growth rate σ and the leading order asymptotic growth rate σ_0 to be

$$\delta := |\sigma - \sigma_0| \,.$$

The relative disagreement δ between the numerical growth rate σ and the leading order asymptotic growth rate σ_0 is therefore

$$\Delta := \left| \frac{\sigma - \sigma_0}{\sigma_0} \right| .$$

From (4.92) it is clear that we should observe $\Delta \to 0$ as $a \to 0$, since each successive σ_i is proportional to a higher power of a. To test this numerically, we calculate

$$\delta(a) := |\sigma(a) - \sigma_0(a)| \,, \quad \Delta(a) := \left| \frac{\sigma(a) - \sigma_0(a)}{\sigma_0(a)} \right| ,$$

for a series of descending values of a. σ is the value computed by the numerical eigenvalue problem and $\sigma_0 = \Re(s)$ is calculated from (3.61), the main result of Chapter 3.

This calculation is performed at a single value of α satisfying exact resonance. The asymptotics are performed in the absence of any diffusion, so we must use the ideal form of the Floquet solver to properly show the relationship between the amplitude and the error, assuming that numerical results are accurate to machine precision. We now provide each of the

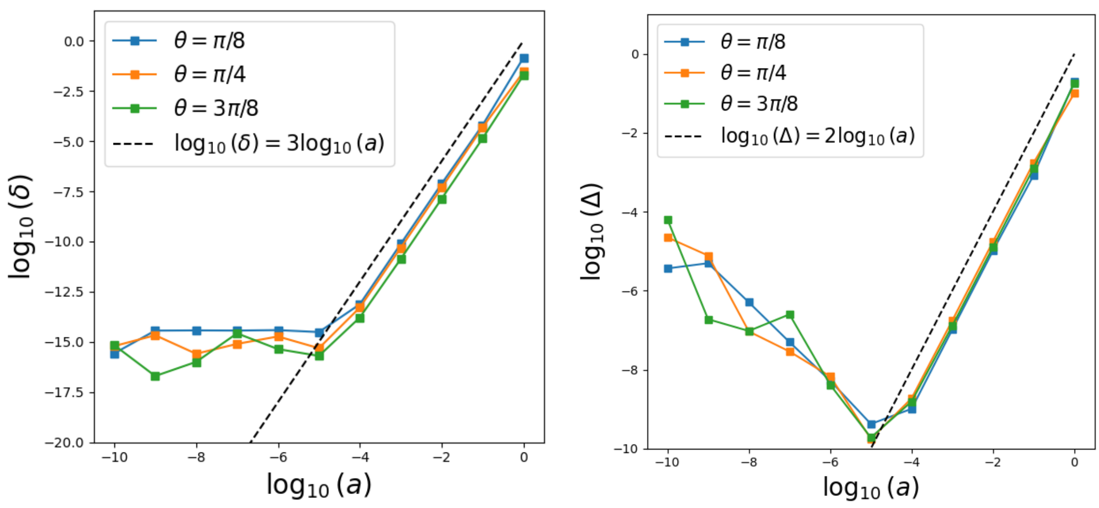

Figure 4.35: Absolute error δ and relative error Δ in the growth rate as a function of amplitude a calculated at a resonant value of α corresponding to Fourier mode $n = -5$ for a selection of primary wavevector angles θ. Parameter values: $a \in (10^{-10}, 1)$, $\alpha \approx 0.20087$, $\beta = 0$, $\gamma = 0$. Resolution: $n_a = 10$, $\mathcal{N} = 50$.

numerical values for the above plots, along with corresponding growth rate values, to better understand the trends on show. In Figure 4.35, for the largest values of a, we observe a linear

a	δ	Δ	σ_r
10^{-10}	1.5766×10^{-15}	5.7114×10^{-5}	2.7605×10^{-11}
10^{-9}	2.8597×10^{-15}	1.0360×10^{-5}	2.7605×10^{-10}
10^{-8}	1.6421×10^{-15}	5.9488×10^{-7}	2.7605×10^{-9}
10^{-7}	1.4067×10^{-15}	5.0960×10^{-8}	2.7605×10^{-8}
10^{-6}	1.6700×10^{-15}	6.0499×10^{-9}	2.7605×10^{-7}
10^{-5}	1.2514×10^{-15}	4.5333×10^{-10}	2.7605×10^{-6}
10^{-4}	5.0379×10^{-14}	1.8250×10^{-9}	2.7605×10^{-5}
10^{-3}	4.8236×10^{-11}	1.7474×10^{-7}	2.7605×10^{-4}
10^{-2}	4.8235×10^{-8}	1.7474×10^{-5}	2.7605×10^{-3}
10^{-1}	4.8034×10^{-5}	1.7401×10^{-3}	2.7605×10^{-2}
10^{0}	2.7888×10^{-2}	1.0103×10^{-1}	2.7605×10^{-1}

Table 4.6: Errors alongside corresponding amplitudes and growth rates calculated at a resonant value of α corresponding to Fourier mode $n = -5$. Parameter values: $a \in (10^{-10}, 1)$, $\theta = \pi/4$, $\alpha = 0.20087$, $\beta = 0$, $\gamma = 0$. Resolution: $n_a = 10$.

relationship between the logarithm of a and the logarithms of both δ and Δ. The gradients of these linear relationships are illustrated by the black dashed lines which are overlaid. We find that $\log_{10}(\Delta)$ decreases linearly with $\log_{10}(a)$ until it reaches $a = 10^{-5}$, below which $\log_{10}(\Delta)$ starts increasing. This is explained by a combination of two things:

1. δ reaches machine precision at $a = 10^{-5}$.

2. σ_r continues to decrease by an order of magnitude each time we decrease a.

This means that with each progressively smaller value of a, an approximately constant value of δ is divided by a progressively smaller value of σ_r and therefore Δ increases.

Quantifying the Rate of Convergence

We can use Table 4.6 to quantify the rate at which the theoretical prediction for the growth rate converges towards the numerical Floquet value. If a decreases by a factor of 10^{-1}, then $\delta = |\sigma - \sigma_0|$ decreases by a factor of 10^{-3} until machine precision is reached. This would suggest that

$$\sigma_n = O(a^{2n+1}) \quad \text{for} \quad n \in \mathbb{N}.$$

If we write expansion (4.92) as

$$\sigma = a\check{\sigma}_0 + a^3\check{\sigma}_1 + a^5\check{\sigma}_2 + \ldots,$$

where $\check{\sigma}_i$ are of size $O(1)$, then it follows naturally that

$$\Delta = \frac{\sigma - \sigma_0}{\sigma_0} = \frac{\sigma - a\hat{\sigma}_0}{a\hat{\sigma}_0} = \frac{a^3\hat{\sigma}_1 + \ldots}{a\hat{\sigma}_0} = O(a^2).$$

This is consistent with a second conclusion we can draw from Table 4.6, namely that as we decrease a by a factor of 10^{-1}, Δ decreases by a factor of 10^{-2}.

Summary

In this chapter we studied instabilities of IGWs propagating through a stably-stratified Boussinesq fluid with constant buoyancy frequency N in the absence of a magnetic field. We did so by linearising the equations of motion and using a Floquet method to construct an eigenvalue problem with eigenvalue σ, the complex growth rate. Because the plane wave solution is an exact solution of the nonlinear equations of motion, the eigenvalue problem in this chapter can be used to study instabilities of IGWs for any amplitude a. We solved this eigenvalue problem numerically to contour the growth rate in wavenumber space. On top of this, we presented equations for the energetics of the instabilities which allowed us to determine the relative contributions of two physical processes to the instabilities: shear and buoyancy production. Finally, we demonstrated agreement between the growth rates predicted by the asymptotic framework for small-amplitude IGW instabilities presented in Chapter 3 and the numerically computed growth rates.

The construction of the eigenvalue problem and the derivation of the energetic equations reproduces the work of LR96, but we used their framework to produce original results. Namely, we computed eigenfunctions to produce an image of the disturbances in (X, Z)-space and studied the influence of varying the Floquet modulation parameter γ on IGW instabilities. We also studied the effects of thermal diffusion on IGW instabilities. Through these results, we built upon the existing body of work performed within this problem, which has been studied by Mied (1976); Drazin (1977); Klostermeyer (1982, 1983, 1991); Sonmor and Klaassen (1997) amongst other authors. Our results reinforce the unifying conclusion of these works: that plane IGWs in a stably-stratified Boussinesq fluid are unstable for any wave amplitude. Courtesy of these authors, it is a known result that instabilities of small-amplitude plane IGWs in a Boussinesq fluid can be attributed to TRIs between three coupled IGWs. We showed how this conclusion can be verified by plotting resonance curves of the quantity Ω to reveal locations in parameter space where TRIs can be expected. Importantly, this chapter presents a method which can be extended to study instabilities of AGWs propagating through a Boussinesq fluid permeated by a uniform background magnetic field. This has not previously been done in the research literature. We tackle this problem in Chapter 6.

Chapter 5

MHD Triadic Resonance Interactions

The aim of this chapter is to take the same asymptotic procedure seen in Chapter 3 and apply it to a stably-stratified Boussinesq fluid permeated by a uniform background magnetic field. This allows us to study how the stability of an IGW is modified by the presence of a magnetic field, which is an important feature of many of our applications of interest. We derive an analytical formula for predicting the growth rate of AGW instabilities under circumstances in which the criteria for a TRI are exactly satisfied. Naturally, incorporating a magnetic field in the governing equations produces a much richer array of interactions. In Chapters 3 and 4 our system permitted one type of wave: IGWs. For the remainder of this thesis, our system permits two types of wave: AGWs and AWs.

The primary wave is now defined by four parameters: the amplitude a, the wavevector angle θ, the background magnetic field angle ζ and the background magnetic field strength B_0. In this chapter, we restrict our attention to magnetic fields which are coplanar with the primary wavevector (i.e. $B_{0Y} = 0$). The theoretical framework derived in this chapter is therefore applicable to 2D background magnetic fields only. Having explored the influence of a and θ in Chapters 3 and 4 on hydrodynamic instabilities of a primary IGW, we now also focus on the influence of ζ and B_0 on magnetohydrodynamic instabilities of a primary AGW in Chapters 5 and 6.

5.1 MHD Resonant Triads

In this section we outline the different types of TRI which are possible in a stably-stratified Boussinesq fluid permeated by a uniform background magnetic field. Recall that, without loss of generality, the triadic resonance conditions we consider are

$$\boldsymbol{K} + \boldsymbol{K}_A - \boldsymbol{K}_B = 0, \tag{5.1}$$

$$\omega + \omega_A - \omega_B = 0. \tag{5.2}$$

In this chapter we only consider interactions in which the primary wave is a hybrid Alfvén-gravity wave. The frequency of the primary wave is therefore given by

$$\omega = \pm\sqrt{\frac{N^2 K_X^2}{K^2} + \frac{(\boldsymbol{K} \cdot \boldsymbol{B}_0)^2}{\mu_0 \rho_0}}. \tag{5.3}$$

We allow each of the daughter waves A and B to be either hybrid Alfvén-gravity waves or pure Alfvén waves. Table 5.1 below lists all of the possible wave type combinations we consider when forming triads. An AGW is approximately an IGW in the limit in which $b_0 \ll 1$, but such waves become increasingly Alfvénic in character as we increase the field strength.

Primary Wave	Daughter Wave A	Daughter Wave B
Alfvén-gravity	Alfvén-gravity	Alfvén-gravity
Alfvén-gravity	Alfvén-gravity	Alfvén
Alfvén-gravity	Alfvén	Alfvén

Table 5.1: Possible resonant interactions in the MHD system between two daughter waves and a primary wave of hybrid Alfvén-gravity character.

We have distinct formulae for ω_A and ω_B depending on which type of wave we consider. Both the Alfvén-gravity wave dispersion relation and the Alfvén wave dispersion relation are quadratic, so we must select either the positive or negative root in either case.

When A and B are both pure Alfvén waves, we make the choice

$$\omega_A = +\frac{\boldsymbol{K}_A \cdot \boldsymbol{B}_0}{\sqrt{\mu_0 \rho_0}}, \tag{5.4}$$

$$\omega_B = -\frac{\boldsymbol{K}_B \cdot \boldsymbol{B}_0}{\sqrt{\mu_0 \rho_0}}. \tag{5.5}$$

When A and B are both hybrid Alfvén-gravity waves, we make the choice

$$\omega_A = -\sqrt{\frac{N^2 K_{A\perp}^2}{K_A^2} + \frac{(\boldsymbol{K}_A \cdot \boldsymbol{B}_0)^2}{\mu_0 \rho_0}}, \tag{5.6}$$

$$\omega_B = +\sqrt{\frac{N^2 K_{B\perp}^2}{K_B^2} + \frac{(\boldsymbol{K}_B \cdot \boldsymbol{B}_0)^2}{\mu_0 \rho_0}}. \tag{5.7}$$

These sign choices are necessary to satisfy the conditions (5.1) and (5.2) for positive $\boldsymbol{K}_A$ and $\boldsymbol{K}_B$ in the region of parameter space we consider. All possible sign conventions have been explored to ensure that no instabilities are left unaccounted for.

AGW-AGW-AGW Resonance Curves

Here we consider the case with disturbances with no Y-component and produce 2D curves in wavenumber space along which we can expect to find triadic resonance between three AGWs. The frequency resonance condition for AGW-AGW-AGW interactions is (5.2), where ω is given by formula (5.3) and ω_A and ω_B are given by

$$\omega_A = -\sqrt{\frac{N^2 K_{AX}^2}{K_A^2} + \frac{(\boldsymbol{K}_A \cdot \boldsymbol{B}_0)^2}{\mu_0 \rho_0}},$$

$$\omega_B = +\sqrt{\frac{N^2 K_{BX}^2}{K_B^2} + \frac{(\boldsymbol{K}_B \cdot \boldsymbol{B}_0)^2}{\mu_0 \rho_0}}.$$

Since we are interested in triadic resonance described by (5.1) and (5.2), we can re-express ω_B in terms of the primary wave and daughter wave A:

$$\omega_B = \sqrt{\frac{N^2(K_{AX}+K_X)^2}{(K_{AX}+K_X)^2+(K_{AZ}+K_Z)^2} + \frac{[(\boldsymbol{K}_A+\boldsymbol{K})\cdot\boldsymbol{B}_0]^2}{\mu_0\rho_0}}.$$

We again define dimensionless wavenumbers

$$k_{AX} := K_{AX}/K_X, \quad k_{AZ} := K_{AZ}/K_Z. \tag{5.8}$$

Recall that

$$K_X = K\cos\theta, \quad K_Z = K\sin\theta, \tag{5.9}$$

which means

$$K_Z/K_X = \tan\theta. \tag{5.10}$$

The magnetic field components can be written in terms of field strength B_0 and orientation ζ:

$$B_{0X} = B_0\cos\zeta, \quad B_{0Z} = B_0\sin\zeta. \tag{5.11}$$

In the stably-stratified MHD system, the dimensionless magnetic field strength b_0 is given by

$$b_0 = \frac{KB_0}{N\sqrt{\mu_0\rho_0}}. \tag{5.12}$$

Using (5.8)-(5.12), equation (5.3) for the primary wave frequency ω becomes

$$\omega^2/N^2 = \cos^2\theta + b_0^2(\cos\theta\cos\zeta+\sin\theta\sin\zeta)^2. \tag{5.13}$$

The daughter wave frequencies become

$$\frac{\omega_A^2}{N^2} = \frac{k_{AX}^2}{k_{AX}^2+(\tan^2\theta)k_{AZ}^2} + b_0^2(k_{AX}\cos\theta\cos\zeta + k_{AZ}\sin\theta\sin\zeta)^2, \tag{5.14}$$

$$\begin{aligned}\frac{\omega_B^2}{N^2} = &\frac{(1+k_{AX})^2}{(1+k_{AX})^2+(\tan^2\theta)(1+k_{AZ})^2} \\ &+ b_0^2[(1+k_{AX})\cos\theta\cos\zeta+(1+k_{AZ})\sin\theta\sin\zeta]^2.\end{aligned} \tag{5.15}$$

We can use equations (5.13)-(5.15), together with (5.2) to plot resonance curves in (k_{AX}, k_{AZ}) space for AGW-AGW-AGW interactions at fixed values of θ, ζ and b_0. We plot this in Figure 5.1 for different orientations of the background magnetic field, revealing which pairs of (k_{AX}, k_{AZ}) values are resonant when $k_{AY} = 0$. In Figures 5.2 and 5.3 we plot resonance curves for different magnetic field strengths. We find that at $b_0 = 0.2$, we start to observe pairs of resonant wavenumbers in which $|k_{AZ}| \gg |k_{AX}|$. As was the case for IGW-IGW-IGW interactions in Chapter 3, there is a threshold for $|k_{AZ}|$ below which resonance does not occur.

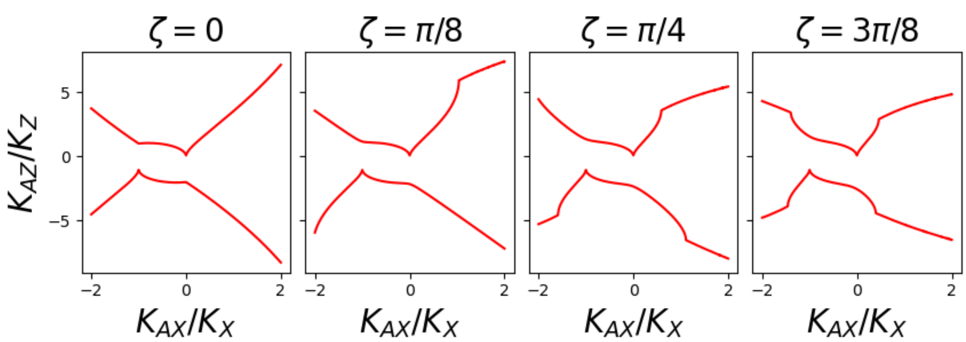

Figure 5.1: Pairs of (k_{AX}, k_{AZ}) values which produce resonant triads between AGWs when $k_{AY} = 0$. Parameter values: $\theta = \pi/4$, $b_0 = 0.1$.

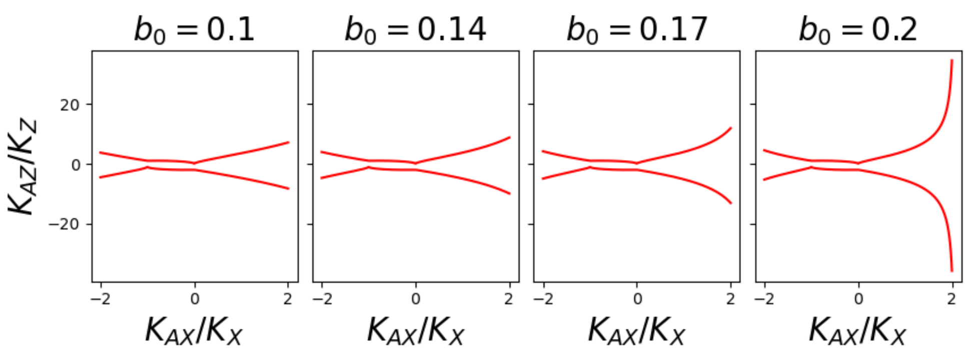

Figure 5.2: Pairs of (k_{AX}, k_{AZ}) values which produce resonant triads between AGWs when $k_{AY} = 0$. Parameter values: $\theta = \pi/4$, $\zeta = 0$.

AGW-AW-AW Resonance Curves

We can produce similar resonance curves for AGW-AW-AW interactions. The frequency resonance condition for AGW-AW-AW interactions is (5.2), where ω is given by formula (5.3) and ω_A and ω_B are given by

$$\omega_A = +\frac{\boldsymbol{K}_A \cdot \boldsymbol{B}_0}{\mu_0 \rho_0}, \quad \omega_B = -\frac{\boldsymbol{K}_B \cdot \boldsymbol{B}_0}{\mu_0 \rho_0}.$$

Using the wavenumber resonance condition (5.1), we can rewrite ω_B as

$$\omega_B = -\frac{(\boldsymbol{K}_X + \boldsymbol{K}_A) \cdot \boldsymbol{B}_0}{\mu_0 \rho_0}.$$

Using (5.8)-(5.12) the daughter wave frequencies become

$$\omega_A/N = +(b_0 \cos\theta \cos\zeta) k_{AX} + (b_0 \sin\theta \sin\zeta) k_{AZ}, \tag{5.16}$$
$$\omega_B/N = -(b_0 \cos\theta \cos\zeta)(1 + k_{AX}) - (b_0 \sin\theta \sin\zeta)(1 + k_{AZ}). \tag{5.17}$$

Using (5.16)-(5.17), the dimensionless form of the frequency resonance condition (5.2) becomes

$$\omega/N + b_0 \cos\theta \cos\zeta (1 + 2k_{AX}) + b_0 \sin\theta \sin\zeta (1 + 2k_{AZ}) = 0, \tag{5.18}$$

where ω/N is given by (5.13). We find that k_{AZ} is a linear function of k_{AX} for AGW-AW-AW resonances when $k_{AY} = 0$. Curves of k_{AZ} against k_{AX} could also be derived for AGW-AGW-AW interactions in future work.

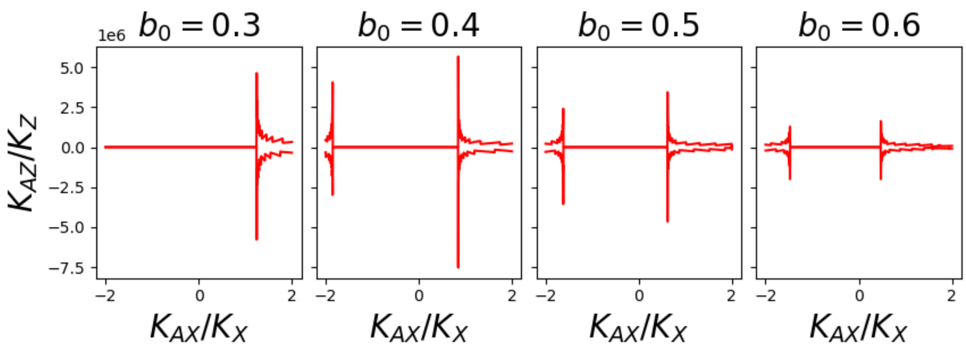

Figure 5.3: Pairs of (k_{AX}, k_{AZ}) values which produce resonant triads between AGWs when $k_{AY} = 0$. Parameter values: $\theta = \pi/4$, $\zeta = 0$.

5.2 Asymptotics

5.2.1 Growth Rate at Points of Exact Resonance

In this section we present the asymptotic derivation of a formula for the growth rate under the conditions where triadic resonance is exactly satisfied, this time in the presence of a magnetic field. We again follow the approach used in Chapter 3, which was based on the method of Cui and Latter (2022).

In the following derivation, we use the wave amplitude a as a small ordering parameter. We again expand perturbations in terms of powers of a. We consider a 'slow' timescale τ related to the original 'fast' timescale T by $\tau = aT$. The fast timescale is the timescale on which the waves oscillate. The slow timescale is the timescale on which the amplitude of any unstable disturbances grow. Multiple scale analysis enables us to obtain analytical results for growth rates of instabilities which grow slowly relative to the oscillation timescale.

Linearising the Governing Equations

Similarly to Chapter 3, we temporarily redefine the following variables for the rest of this chapter to simplify the algebra:

$$\frac{\rho g}{\rho_0} \to \rho, \qquad \frac{P}{\rho_0} \to P, \qquad \frac{\boldsymbol{B}}{\sqrt{\mu_0 \rho_0}} \to \boldsymbol{B}. \tag{5.19}$$

As a result, the variables ρ, P and $\boldsymbol{B}$ do not have dimensions of density, pressure and a magnetic field respectively in this chapter. At the end of this chapter, the interpretations of P and ρ are reset according to how they appeared in Chapters 2 and 4.

Here, we develop theory pertaining to ideal AGWs, which means we take the following limits regarding the dimensionless numbers:

$$\mathrm{Re} \to \infty, \qquad \mathrm{Rm} \to \infty, \qquad \mathrm{Pe} \to \infty. \tag{5.20}$$

We treat viscosity ν, Ohmic diffusion η and thermal diffusion κ as negligible in this chapter as a result.

We begin with the ideal Boussinesq MHD equations for a stably-stratified fluid with constant buoyancy frequency N permeated by a uniform background magnetic field, which first appeared in Chapter 2 as equations (2.32)-(2.36) (but now with the interpretations of ρ, P and $\boldsymbol{B}$ temporarily modified by (5.19):

$$\frac{\mathrm{D}\boldsymbol{U}}{\mathrm{D}T} = \boldsymbol{B}\cdot\nabla\boldsymbol{B} - \nabla P - \rho\hat{\boldsymbol{Z}}, \tag{5.21}$$
$$\frac{\mathrm{D}\boldsymbol{B}}{\mathrm{D}T} = \boldsymbol{B}\cdot\nabla\boldsymbol{U}, \tag{5.22}$$
$$\frac{\mathrm{D}\rho}{\mathrm{D}T} = N^2 U_Z, \tag{5.23}$$
$$\nabla\cdot\boldsymbol{U} = 0, \tag{5.24}$$
$$\nabla\cdot\boldsymbol{B} = 0. \tag{5.25}$$

To incorporate both timescales into the problem, we write

$$\frac{\partial}{\partial T} \to \frac{\partial}{\partial T} + a\frac{\partial}{\partial \tau}. \tag{5.26}$$

We now write dependent variables as

$$\boldsymbol{U}(\boldsymbol{X},T,\tau) = \tilde{\boldsymbol{U}}(X,Z,T) + \boldsymbol{U'}(\boldsymbol{X},T,\tau), \tag{5.27}$$
$$\boldsymbol{B}(\boldsymbol{X},T,\tau) = \tilde{\boldsymbol{B}}(X,Z,T) + \boldsymbol{B'}(\boldsymbol{X},T,\tau) + \boldsymbol{B}_0, \tag{5.28}$$
$$P(\boldsymbol{X},T,\tau) = \tilde{P}(X,Z,T) + P'(\boldsymbol{X},T,\tau), \tag{5.29}$$
$$\rho(\boldsymbol{X},T,\tau) = \tilde{\rho}(X,Z,T) + \rho'(\boldsymbol{X},T,\tau). \tag{5.30}$$

Tilde notation denotes primary wave quantities. Prime notation denotes disturbances with respect to the primary wave. To make the dependence of $\tilde{\boldsymbol{U}}$, $\tilde{\boldsymbol{B}}$ and $\tilde{\rho}$ on the ordering parameter a explicit, we define $\breve{\boldsymbol{U}}$, $\breve{\boldsymbol{B}}$ and $\breve{\rho}$ via

$$\tilde{\boldsymbol{U}} = a\breve{\boldsymbol{U}}, \quad \tilde{\boldsymbol{B}} = a\breve{\boldsymbol{B}}, \quad \tilde{\rho} = a\breve{\rho}. \tag{5.31}$$

We substitute (5.26)-(5.30) and (5.31) into (5.21)-(5.25). Noting that the nonlinear equations satisfied by the primary wave are

$$\frac{\mathrm{D}\tilde{\boldsymbol{U}}}{\mathrm{D}T} = \boldsymbol{B}_0\cdot\nabla\tilde{\boldsymbol{B}} - \nabla\tilde{P} - \rho\hat{\boldsymbol{Z}}, \tag{5.32}$$
$$\frac{\mathrm{D}\tilde{\boldsymbol{B}}}{\mathrm{D}T} = \boldsymbol{B}_0\cdot\nabla\tilde{\boldsymbol{U}}, \tag{5.33}$$
$$\frac{\mathrm{D}\tilde{\rho}}{\mathrm{D}T} = N^2\tilde{U}_Z, \tag{5.34}$$
$$\nabla\cdot\tilde{\boldsymbol{U}} = 0, \tag{5.35}$$
$$\nabla\cdot\tilde{\boldsymbol{B}} = 0, \tag{5.36}$$

the linearised forms of equations (5.21)-(5.24) with respect to disturbances are

$$\frac{\partial\boldsymbol{U'}}{\partial T} + a\Phi_U = \boldsymbol{B}_0\cdot\nabla\boldsymbol{B'} - \nabla P' - \rho'\hat{\boldsymbol{Z}}, \tag{5.37}$$
$$\frac{\partial\boldsymbol{B'}}{\partial T} + a\Phi_B = \boldsymbol{B}_0\cdot\nabla\boldsymbol{U'}, \tag{5.38}$$
$$\frac{\partial\rho'}{\partial T} + a\Phi_\rho = N^2 U'_Z, \tag{5.39}$$
$$\nabla\cdot\boldsymbol{U'} = 0, \tag{5.40}$$
$$\nabla\cdot\boldsymbol{B'} = 0, \tag{5.41}$$

where Φ_U, Φ_B and Φ_ρ are defined via

$$\Phi_U := \frac{\partial \boldsymbol{U'}}{\partial \tau} + \check{\boldsymbol{U}} \cdot \nabla \boldsymbol{U'} + \boldsymbol{U'} \cdot \nabla \check{\boldsymbol{U}} - \check{\boldsymbol{B}} \cdot \nabla \boldsymbol{B'} - \boldsymbol{B'} \cdot \nabla \check{\boldsymbol{B}},$$
$$\Phi_B := \frac{\partial \boldsymbol{B'}}{\partial \tau} + \check{\boldsymbol{U}} \cdot \nabla \boldsymbol{B'} + \boldsymbol{U'} \cdot \nabla \check{\boldsymbol{B}} - \check{\boldsymbol{B}} \cdot \nabla \boldsymbol{U'} - \boldsymbol{B'} \cdot \nabla \check{\boldsymbol{U}},$$
$$\Phi_\rho := \frac{\partial \rho'}{\partial \tau} + \check{\boldsymbol{U}} \cdot \nabla \rho' + \boldsymbol{U'} \cdot \nabla \check{\rho}.$$

We consider asymptotic expansions of the form

$$F' = F_0' + aF_1' + a^2 F_2' + O(a^3) \quad \text{for} \quad F \in \{\boldsymbol{U}, \boldsymbol{B}, P, \rho\}. \tag{5.42}$$

We put (5.42) into the linearised equations (5.37)-(5.41) and collect terms at each order in a.

Equations at $O(a^0)$

Using the fact that any terms containing appearances of $\tilde{F}$ are at most $O(a^1)$, from (5.37)-(5.41) we retain only the following at $O(a^0)$:

$$\frac{\partial \boldsymbol{U}_0'}{\partial T} = \boldsymbol{B}_0 \cdot \nabla \boldsymbol{B}_0' - \nabla P_0' - \rho_0' \hat{\boldsymbol{Z}}, \tag{5.43}$$
$$\frac{\partial \boldsymbol{B}_0'}{\partial T} = \boldsymbol{B}_0 \cdot \nabla \boldsymbol{U}_0', \tag{5.44}$$
$$\frac{\partial \rho_0'}{\partial T} = N^2 U_{0Z}', \tag{5.45}$$
$$\nabla \cdot \boldsymbol{U}_0' = 0, \tag{5.46}$$
$$\nabla \cdot \boldsymbol{B}_0' = 0. \tag{5.47}$$

The constant background magnetic field $\boldsymbol{B}_0$ should not be confused with the $O(1)$ perturbation quantity $\boldsymbol{B}_0'$. Taking $\nabla \times \nabla \times$ (5.43) yields

$$\frac{\partial}{\partial T}(\nabla \times \nabla \times \boldsymbol{U}_0') = \boldsymbol{B}_0 \cdot \nabla(\nabla \times \nabla \times \boldsymbol{B}_0') - \nabla \times \nabla \times \left(\rho_0' \hat{\boldsymbol{Z}}\right).$$

Applying the vector identity $\nabla \times \nabla \times \boldsymbol{v} \equiv \nabla(\nabla \cdot \boldsymbol{v}) - \nabla^2 \boldsymbol{v}$ together with (5.46)-(5.47) gives

$$\frac{\partial}{\partial T}(\nabla^2 \boldsymbol{U}_0') = \boldsymbol{B}_0 \cdot \nabla(\nabla^2 \boldsymbol{B}_0') + \nabla \left(\frac{\partial \rho_0'}{\partial Z}\right) - (\nabla^2 \rho_0') \hat{\boldsymbol{Z}}.$$

We then differentiate by T, use (5.45) to replace $\partial_T \rho_0'$ and use (5.44) to replace $\partial_T \boldsymbol{B}_0'$.

We get the following PDE in terms of $\boldsymbol{U}_0'$:

$$\left[\frac{\partial^2}{\partial T^2} - (\boldsymbol{B}_0 \cdot \nabla)^2\right](\nabla^2 \boldsymbol{U}_0') + N^2 \left(\hat{\boldsymbol{Z}} \nabla^2 - \nabla \frac{\partial}{\partial Z}\right) U_{0Z}' = 0. \tag{5.48}$$

We now have an equation entirely in terms of the leading order velocity variable. This is the end point of deriving a leading order equation describing daughter waves. Its Z-component (5.49) gives us the AGW dispersion relation we expect when we insert a plane wave solution:

$$\frac{\partial^2}{\partial T^2}\left(\nabla^2 U_{0Z}'\right) - (\boldsymbol{B}_0 \cdot \nabla)^2 \nabla^2 U_{0Z}' + N^2 \nabla_\perp^2 U_{0Z}' = 0, \tag{5.49}$$

where $\nabla_\perp^2 := \partial_X^2 + \partial_Y^2$.

General Solution

Since we are concerned with resonant triads involving two daughter waves A and B, the general solution we need to consider to this order is

$$\begin{aligned}\boldsymbol{U}_0' =& A(\tau)\boldsymbol{U}_A E_A + A^*(\tau)\boldsymbol{U}_A^* E_{-A} + \\ & B(\tau)\boldsymbol{U}_B E_B + B^*(\tau)\boldsymbol{U}_B^* E_{-B},\end{aligned}$$

where $E_{\pm C}$ for any wave C is defined via

$$E_{\pm C} := \exp[i(\pm \boldsymbol{K}_C \cdot \boldsymbol{X} \mp \omega_C T)].$$

We consider a similar general solution for the other dependent variables $\boldsymbol{B}_0'$, P_0' and ρ_0'. For each daughter wave we must consider the superposition of two complex conjugate exponential solutions, since $\boldsymbol{U}_0'$ must be purely real. The vectors $\boldsymbol{U}_A$ and $\boldsymbol{U}_B$ are eigenvectors of equation (5.48), with eigenvalues ω_A and ω_B respectively. Their magnitudes are free to be chosen at our convenience. A and B are the amplitudes of each daughter wave. The amplitudes of the disturbance vary on the slow timescale τ, so it makes sense physically for these quantities to have τ-dependence.

Eigenvector Components

We want to find equations relating the eigenvector components for daughter wave A, so we first seek solutions to the $O(a^0)$ equations (5.43)-(5.47) of the form

$$F_0'(\boldsymbol{X}, T) = F_A \exp(i\boldsymbol{K}_A \cdot \boldsymbol{X} - i\omega_A T) \quad \text{for} \quad F \in \{\boldsymbol{U}, \boldsymbol{B}, P, \rho\}.$$

Putting this solution form into the $O(a^0)$ equations (5.43)-(5.47) produces

$$\omega_A U_{AX} = -(\boldsymbol{K}_A \cdot \boldsymbol{B}_0)B_{AX} + K_{AX}P_A, \tag{5.50}$$
$$\omega_A U_{AY} = -(\boldsymbol{K}_A \cdot \boldsymbol{B}_0)B_{AY} + K_{AY}P_A, \tag{5.51}$$
$$\omega_A U_{AZ} = -(\boldsymbol{K}_A \cdot \boldsymbol{B}_0)B_{AZ} + K_{AZ}P_A - i\rho_A, \tag{5.52}$$
$$\omega_A B_{AX} = -(\boldsymbol{K}_A \cdot \boldsymbol{B}_0)U_{AX}, \tag{5.53}$$
$$\omega_A B_{AY} = -(\boldsymbol{K}_A \cdot \boldsymbol{B}_0)U_{AY}, \tag{5.54}$$
$$\omega_A B_{AZ} = -(\boldsymbol{K}_A \cdot \boldsymbol{B}_0)U_{AZ}, \tag{5.55}$$
$$\omega_A \rho_A = iN^2 U_{AZ}, \tag{5.56}$$
$$\boldsymbol{K}_A \cdot \boldsymbol{U}_A = 0, \tag{5.57}$$
$$\boldsymbol{K}_A \cdot \boldsymbol{B}_A = 0. \tag{5.58}$$

From this set of equations, we want to get a set of equations relating the components of the amplitudes F_A to one another. To do so, we start by taking K_{AX}(5.50) + K_{AY}(5.51) + K_{AZ}(5.52), which yields

$$P_A = \left(\frac{iK_{AZ}}{K_A^2}\right)\rho_A.$$

We then use (5.56) to replace ρ_A:

$$P_A = -\left(\frac{N^2 K_{AZ}}{\omega_A K_A^2}\right)U_{AZ}. \tag{5.59}$$

The process of determining the remaining amplitudes F_A from here differs depending on whether A is an Alfvén wave or an Alfvén-gravity wave.

Alfvén Waves

We saw in Section 2.3.3 that pure Alfvén waves A can only exist in a system with density stratification if they are associated with purely horizontal disturbances (i.e. confined to the (X, Y)-plane). Mathematically, they must have $U_{AZ} = B_{AZ} = P_A = \rho_A = 0$. The system of equations (5.50)-(5.58) describing the eigenvector components reduces to

$$\begin{aligned}
\omega_A U_{AX} &= -(\boldsymbol{K}_A \cdot \boldsymbol{B}_0) B_{AX}, \\
\omega_A U_{AY} &= -(\boldsymbol{K}_A \cdot \boldsymbol{B}_0) B_{AY}, \\
\omega_A B_{AX} &= -(\boldsymbol{K}_A \cdot \boldsymbol{B}_0) U_{AX}, \\
\omega_A B_{AY} &= -(\boldsymbol{K}_A \cdot \boldsymbol{B}_0) U_{AY}, \\
0 &= K_{AX} U_{AX} + K_{AY} U_{AY}, \\
0 &= K_{AX} B_{AX} + K_{AY} B_{AY}.
\end{aligned}$$

The equations pertaining to daughter wave B are analogous. From these relations it is straightforward to see that the eigenvector components are

$$\begin{aligned}
(U_{AX}, U_{AY}, B_{AX}, B_{AY}) &= \left(1, -\frac{K_{AX}}{K_{AY}}, -\frac{(\boldsymbol{K}_A \cdot \boldsymbol{B}_0)}{\omega_A}, \frac{(\boldsymbol{K}_A \cdot \boldsymbol{B}_0)}{\omega_A} \frac{K_{AX}}{K_{AY}}\right) U_{AX}, \\
(U_{BX}, U_{BY}, B_{BX}, B_{BY}) &= \left(1, -\frac{K_{BX}}{K_{BY}}, -\frac{(\boldsymbol{K}_A \cdot \boldsymbol{B}_0)}{\omega_B}, \frac{(\boldsymbol{K}_B \cdot \boldsymbol{B}_0)}{\omega_B} \frac{K_{BX}}{K_{BY}}\right) U_{BX}.
\end{aligned}$$

When A and B are both pure Alfvén waves, we make the choice

$$\omega_A = +\boldsymbol{K}_A \cdot \boldsymbol{B}_0, \quad \omega_B = -\boldsymbol{K}_B \cdot \boldsymbol{B}_0.$$

A convenient choice of arbitrary amplitude is $U_{AX} = K_{AY}$ and $U_{BX} = K_{BY}$, giving

$$(U_{AX}, U_{AY}, B_{AX}, B_{AY}) = (K_{AY}, -K_{AX}, -K_{AY}, K_{AX}), \tag{5.60}$$

$$(U_{BX}, U_{BY}, B_{BX}, B_{BY}) = (K_{BY}, -K_{BX}, K_{BY}, -K_{BX}). \tag{5.61}$$

Alfvén-Gravity Waves

Here, we no longer assume that $U_{AZ} = B_{AZ} = P_A = \rho_A = 0$ and proceed with

$$P_A = -\left(\frac{N^2 K_{AZ}}{\omega_A K_A^2}\right) U_{AZ}. \tag{5.62}$$

One by one, we choose to express each variable F_A in terms of U_{AZ}. To get an expression for U_{AX}, we take ω_A(5.50), use (5.53) to replace B_{AX} and use (5.62) to replace P_A. This gives

$$U_{AX} = \left(\frac{N^2 K_{AX} K_{AZ}}{K_A^2[(\boldsymbol{K}_A \cdot \boldsymbol{B}_0)^2 - \omega_A^2]}\right) U_{AZ}.$$

Similarly, from (5.51) we obtain

$$U_{AY} = \left(\frac{N^2 K_{AY} K_{AZ}}{K_A^2[(\boldsymbol{K}_A \cdot \boldsymbol{B}_0)^2 - \omega_A^2]}\right) U_{AZ}.$$

It is then straightforward to obtain eigenvector components B_{AX}, B_{AY} using (5.53) and (5.54):

$$B_{AX} = \left(\frac{N^2 K_{AX} K_{AZ} (\boldsymbol{K}_A \cdot \boldsymbol{B}_0)}{\omega_A K_A^2 [\omega_A^2 - (\boldsymbol{K}_A \cdot \boldsymbol{B}_0)^2]} \right) U_{AZ},$$
$$B_{AY} = \left(\frac{N^2 K_{AY} K_{AZ} (\boldsymbol{K}_A \cdot \boldsymbol{B}_0)}{\omega_A K_A^2 [\omega_A^2 - (\boldsymbol{K}_A \cdot \boldsymbol{B}_0)^2]} \right) U_{AZ}.$$

We already have the remaining components B_{AZ} and ρ_A in terms of U_{AZ}. Recall that for Alfvén-gravity waves A, the squared frequency ω_A^2 is given by the square of (5.6). As a result, the eigenvector components reduce to

$$\boldsymbol{U}_A = \left(-\frac{K_{AX} K_{AZ}}{K_{A\perp}^2} \hat{\boldsymbol{X}} - \frac{K_{AY} K_{AZ}}{K_{A\perp}^2} \hat{\boldsymbol{Y}} + \hat{\boldsymbol{Z}} \right) U_{AZ},$$
$$\boldsymbol{B}_A = \left(\frac{K_{AX} K_{AZ}}{K_{A\perp}^2} \hat{\boldsymbol{X}} + \frac{K_{AY} K_{AZ}}{K_{A\perp}^2} \hat{\boldsymbol{Y}} - \hat{\boldsymbol{Z}} \right) \frac{(\boldsymbol{K}_A \cdot \boldsymbol{B}_0)}{\omega_A} U_{AZ},$$
$$P_A = -\left(\frac{N^2 K_{AZ}}{\omega_A K_A^2} \right) U_{AZ},$$
$$\rho_A = \left(\frac{i N^2}{\omega_A} \right) U_{AZ}.$$

A sensible choice for the arbitrary amplitude U_{AZ} is $U_{AZ} = K_{A\perp}^2$, giving

$$\boldsymbol{U}_A = -K_{AX} K_{AZ} \hat{\boldsymbol{X}} - K_{AY} K_{AZ} \hat{\boldsymbol{Y}} + K_{A\perp}^2 \hat{\boldsymbol{Z}},$$
$$\boldsymbol{B}_A = \left(K_{AX} K_{AZ} \hat{\boldsymbol{X}} + K_{AY} K_{AZ} \hat{\boldsymbol{Y}} - K_{A\perp}^2 \hat{\boldsymbol{Z}} \right) \frac{(\boldsymbol{K}_A \cdot \boldsymbol{B}_0)}{\omega_A},$$
$$P_A = -\frac{N^2 K_{AZ} K_{A\perp}^2}{\omega_A K_A^2},$$
$$\rho_A = \frac{i N^2 K_{A\perp}^2}{\omega_A}.$$

The eigenvector components for daughter wave B are analogous. We must stress that daughter waves A and B need not be of the same type. The case where A is an AGW and B is an AW (or vice versa) is also a class of interaction observed later in the numerical results of Chapter 6. The objective now is to obtain a second order PDE with $\boldsymbol{U}_1'$ as the dependent variable at $O(a^1)$, from which we can produce solvability conditions which allow us to obtain a formula for the growth rate.

Equations at $O(a^1)$

At $O(a^1)$, from equations (5.37)-(5.41) we retain

$$\frac{\partial \boldsymbol{U}_1'}{\partial T} - \boldsymbol{B}_0 \cdot \nabla \boldsymbol{B}_1' + \nabla P_1' + \rho_1' \hat{\boldsymbol{Z}} = -\boldsymbol{F}_U, \tag{5.63}$$
$$\frac{\partial \boldsymbol{B}_1'}{\partial T} - \boldsymbol{B}_0 \cdot \nabla \boldsymbol{U}_1' = -\boldsymbol{F}_B, \tag{5.64}$$
$$\frac{\partial \rho_1'}{\partial T} - N^2 U_{1Z}' = -F_\rho, \tag{5.65}$$
$$\nabla \cdot \boldsymbol{U}_1' = 0, \tag{5.66}$$
$$\nabla \cdot \boldsymbol{B}_1' = 0. \tag{5.67}$$

The forcing terms $\boldsymbol{F}_U$, $\boldsymbol{F}_B$ and F_ρ are defined as

$$\boldsymbol{F}_U := \frac{\partial \boldsymbol{U}_0'}{\partial \tau} + \check{\boldsymbol{U}} \cdot \nabla \boldsymbol{U}_0' + \boldsymbol{U}_0' \cdot \nabla \check{\boldsymbol{U}} - \check{\boldsymbol{B}} \cdot \nabla \boldsymbol{B}_0' - \boldsymbol{B}_0' \cdot \nabla \check{\boldsymbol{B}}, \tag{5.68}$$

$$\boldsymbol{F}_B := \frac{\partial \boldsymbol{B}_0'}{\partial \tau} + \check{\boldsymbol{U}} \cdot \nabla \boldsymbol{B}_0' + \boldsymbol{U}_0' \cdot \nabla \check{\boldsymbol{B}} - \check{\boldsymbol{B}} \cdot \nabla \boldsymbol{U}_0' - \boldsymbol{B}_0' \cdot \nabla \check{\boldsymbol{U}}, \tag{5.69}$$

$$F_\rho := \frac{\partial \rho_0'}{\partial \tau} + \check{\boldsymbol{U}} \cdot \nabla \rho_0' + \boldsymbol{U}_0' \cdot \nabla \check{\rho}. \tag{5.70}$$

To get a second order PDE with $\boldsymbol{U}_1'$ as the dependent variable, we take $\nabla \times \nabla \times \partial_T$(5.63) and again apply the vector identity $\nabla \times \nabla \times \boldsymbol{v} \equiv \nabla(\nabla \cdot \boldsymbol{v}) - \nabla^2 \boldsymbol{v}$. This gives

$$\frac{\partial^2}{\partial T^2}(\nabla^2 \boldsymbol{U}_1') - (\boldsymbol{B}_0 \cdot \nabla)\left(\nabla^2 \frac{\partial \boldsymbol{B}_1'}{\partial T}\right) - \left(\frac{\partial}{\partial Z}\nabla - \hat{\boldsymbol{Z}}\nabla^2\right)\left(\frac{\partial \rho_1'}{\partial T}\right) = \nabla \times \nabla \times \left(\frac{\partial \boldsymbol{F}_U}{\partial T}\right).$$

We then use (5.64) to replace $\partial_T \boldsymbol{B}_1'$ and use (5.65) to replace $\partial_T \rho_1'$. The end result is

$$\left[\frac{\partial^2}{\partial T^2} - (\boldsymbol{B}_0 \cdot \nabla)^2\right](\nabla^2 \boldsymbol{U}_1') + N^2\left(\hat{\boldsymbol{Z}}\nabla^2 - \nabla \frac{\partial}{\partial Z}\right) U_{1Z}' = \boldsymbol{G}, \tag{5.71}$$

where the vector $\boldsymbol{G}$ is defined as

$$\boldsymbol{G} := \nabla \times \nabla \times \left(\frac{\partial \boldsymbol{F}_U}{\partial T}\right) - (\boldsymbol{B}_0 \cdot \nabla)(\nabla^2 \boldsymbol{F}_B) + \left(\hat{\boldsymbol{Z}}\nabla^2 - \nabla \frac{\partial}{\partial Z}\right) F_\rho. \tag{5.72}$$

Deriving Solvability Conditions in Matrix Form

To derive solvability conditions, we use all three components of the PDE (5.71) to construct a matrix equation. We start from the corresponding homogeneous PDE (5.48):

$$\left[\frac{\partial^2}{\partial T^2} - (\boldsymbol{B}_0 \cdot \nabla)^2\right](\nabla^2 \boldsymbol{U}_0') + N^2\left(\hat{\boldsymbol{Z}}\nabla^2 - \nabla \frac{\partial}{\partial Z}\right) U_{0Z}' = 0.$$

In matrix form, this reads

$$\mathcal{L}\boldsymbol{U}_0' = 0, \tag{5.73}$$

where the linear operator $\mathcal{L}$ is defined as

$$\mathcal{L} = \begin{pmatrix} [\partial_T^2 - (\boldsymbol{B}_0 \cdot \nabla)^2]\nabla^2 & 0 & -N^2 \partial_Z \partial_X \\ 0 & [\partial_T^2 - (\boldsymbol{B}_0 \cdot \nabla)^2]\nabla^2 & -N^2 \partial_Z \partial_Y \\ 0 & 0 & [\partial_T^2 - (\boldsymbol{B}_0 \cdot \nabla)^2]\nabla^2 + N^2 \nabla_\perp^2 \end{pmatrix}.$$

At $O(a)$ the analogous PDE (5.71) can be expressed as

$$\mathcal{L}\boldsymbol{U}_1' = \boldsymbol{G}, \tag{5.74}$$

where the vector G is defined as

$$\boldsymbol{G} := \nabla\left(\nabla \cdot \frac{\partial \boldsymbol{F}_U}{\partial T}\right) - \nabla^2 \frac{\partial \boldsymbol{F}_U}{\partial T} - (\boldsymbol{B}_0 \cdot \nabla)(\nabla^2 \boldsymbol{F}_B) + \left(\hat{\boldsymbol{Z}}\nabla^2 - \nabla \frac{\partial}{\partial Z}\right) F_\rho.$$

We write $\boldsymbol{G}$ as

$$\boldsymbol{G} = \boldsymbol{G}_A E_A + \boldsymbol{G}_B E_B + \ldots$$

where the ellipsis contains terms which are proportional to exponential factors other than E_A and E_B, as well as the relevant complex conjugates. When considering solutions of the form

$$\boldsymbol{U}_0'(\boldsymbol{X}, T) = \boldsymbol{U}_A \exp(i\boldsymbol{K}_A \cdot \boldsymbol{X} - i\omega_A T),$$

the $O(1)$ PDE (5.73) becomes

$$(M_A - \omega_A^2 I)\boldsymbol{U}_A = 0, \tag{5.75}$$

where I is the 3×3 identity matrix and the matrix M_A is given by

$$M_A := \begin{pmatrix} (\boldsymbol{K}_A \cdot \boldsymbol{B}_0)^2 & 0 & -N^2 K_{AZ} K_{AX}/K_A^2 \\ 0 & (\boldsymbol{K}_A \cdot \boldsymbol{B}_0)^2 & -N^2 K_{AZ} K_{AY}/K_A^2 \\ 0 & 0 & (\boldsymbol{K}_A \cdot \boldsymbol{B}_0)^2 + N^2 K_{A\perp}^2/K_A^2 \end{pmatrix}.$$

At $O(a)$, the component of the PDE (5.74) proportional to $\exp(i\boldsymbol{K}_A \cdot \boldsymbol{X} - i\omega_A^2 T)$ is

$$(M_A - \omega_A^2 I)\boldsymbol{U}_{1A} = \boldsymbol{G}_A. \tag{5.76}$$

We can think of $\boldsymbol{U}_A$ as a right eigenvector for the matrix M_A. Consider the corresponding left eigenvector $\hat{\boldsymbol{U}}_A$, which must satisfy

$$\hat{\boldsymbol{U}}_A^\top (M_A - \omega_A^2 I) = 0, \tag{5.77}$$

where $\boldsymbol{U}_A^\top$ denotes the transpose of $\boldsymbol{U}_A$. We multiply (5.76) by the left eigenvector $\boldsymbol{U}_A^\top$ on the left to get

$$\hat{\boldsymbol{U}}_A^\top \boldsymbol{G}_A = 0. \tag{5.78}$$

This is the desired solvability condition for daughter wave A. Similarly, we find that the solvability condition for daughter wave B is

$$\hat{\boldsymbol{U}}_B^\top \boldsymbol{G}_B = 0. \tag{5.79}$$

We may write (5.78) and (5.79) as a system of ODEs (the amplitude equations).

$$\frac{\mathrm{d}A}{\mathrm{d}\tau} = -\frac{c_2}{c_1} B \quad \text{and} \quad \frac{\mathrm{d}B}{\mathrm{d}\tau} = -\frac{c_4}{c_3} A. \tag{5.80}$$

The expressions for the coefficients c_i are given in the next section. From this coupled system we can again form a second order ODE in terms of A, which reads

$$\frac{\mathrm{d}^2 A}{\mathrm{d}\tau^2} = \left(\frac{c_2 c_4}{c_1 c_3}\right) A.$$

Suppose solutions take the form $A \propto \exp(s_\tau \tau)$. The complex growth rate in τ is thus calculated via

$$s_\tau = \pm\sqrt{\frac{c_2 c_4}{c_1 c_3}}. \tag{5.81}$$

The corresponding growth rate in T is

$$s = \pm a\sqrt{\frac{c_2 c_4}{c_1 c_3}}. \tag{5.82}$$

Equation (5.82) can be implemented numerically to predict instability growth rates at points in parameter space which exactly satisfy the resonance conditions (5.1) and (5.2).

Expectedly, the three eigenvalues ω_A^2 of M_A satisfy the dispersion relations for Alfvén-gravity waves (5.83) and Alfvén waves (5.84):

$$\omega_{A1}^2 = (\boldsymbol{K}_A \cdot \boldsymbol{B}_0)^2 + N^2 K_{A\perp}^2 / K_A^2, \tag{5.83}$$
$$\omega_{A2}^2 = (\boldsymbol{K}_A \cdot \boldsymbol{B}_0)^2. \tag{5.84}$$

Eigenvalue (5.83) has multiplicity one and eigenvalue (5.84) has multiplicity two. We find different explicit solvability conditions depending on whether the daughter waves are of hybrid Alfvén-gravity character or of pure Alfvén character.

5.2.2 Explicit Solvability Conditions

In equation (3.61), the values of c_i differ depending on whether the daughter waves are AGWs or AWs. We derive expressions for c_i in each case.

Alfvén-Gravity Waves

The eigenvalue of (5.75) and (5.77) pertaining to AGWs is (5.83).

Its associated right eigenvector is

$$\boldsymbol{U}_A = -K_{AZ} K_{AX} \hat{\boldsymbol{X}} - K_{AZ} K_{AY} \hat{\boldsymbol{Y}} + K_{A\perp}^2 \hat{\boldsymbol{Z}},$$

which we saw in Chapter 3. Its associated left eigenvector is

$$\hat{\boldsymbol{U}}_A = \hat{\boldsymbol{Z}}.$$

The solvability conditions for each daughter wave A and B are

$$\hat{\boldsymbol{U}}_A^\top \boldsymbol{G}_A = 0, \quad \hat{\boldsymbol{U}}_B^\top \boldsymbol{G}_B = 0.$$

When the daughter waves are AGWs, these solvability conditions reduce to

$$G_{AZ} = 0, \quad G_{BZ} = 0,$$

where G_{AZ} and G_{BZ} are the Z components of $\boldsymbol{G}_A$ and $\boldsymbol{G}_B$ respectively. Their explicit formulae are provided in Appendix A.3.2. These conditions are equivalent to those derived for IGW-IGW-IGW interactions in Chapter 3, in the sense that we can just use the vertical component of the $O(a^1)$ PDE (5.71) alone to produce solvability conditions.

To find the amplitude equations, we express the coefficients G_{AZ} and G_{BZ} as

$$
\begin{aligned}
G_{AZ} &= c_1 \frac{\mathrm{d}A}{\mathrm{d}\tau} + c_2 B, \\
G_{BZ} &= c_3 \frac{\mathrm{d}B}{\mathrm{d}\tau} + c_4 A.
\end{aligned}
$$

The coefficients c_1 and c_3 are given by

$$
\begin{aligned}
c_1 &= -2i\omega_A K_{A\perp}^2 K_A^2, \\
c_3 &= -2i\omega_B K_{B\perp}^2 K_B^2.
\end{aligned}
$$

Let $\boldsymbol{K}_W \coloneqq \boldsymbol{K}$. The coefficient c_2 is given by

$$
\begin{aligned}
c_2 = &+ B(\boldsymbol{K}_B \cdot \boldsymbol{U}_W)[\omega_A(\boldsymbol{U}_A \cdot \boldsymbol{U}_B) - (\boldsymbol{K}_A \cdot \boldsymbol{B}_0) K_A^2 B_{BZ} - iK_{A\perp}^2 \rho_B] \\
&- B(\boldsymbol{K}_W \cdot \boldsymbol{U}_B)[\omega_A(\boldsymbol{U}_A \cdot \boldsymbol{U}_W) - (\boldsymbol{K}_A \cdot \boldsymbol{B}_0) K_A^2 B_{WZ} + iK_{A\perp}^2 \rho_W] \\
&- B(\boldsymbol{K}_B \cdot \boldsymbol{B}_W)[\omega_A(\boldsymbol{U}_A \cdot \boldsymbol{B}_B) - (\boldsymbol{K}_A \cdot \boldsymbol{B}_0) K_A^2 U_{BZ}] \\
&+ B(\boldsymbol{K}_W \cdot \boldsymbol{B}_B)[\omega_A(\boldsymbol{U}_A \cdot \boldsymbol{B}_W) - (\boldsymbol{K}_A \cdot \boldsymbol{B}_0) K_A^2 U_{WZ}].
\end{aligned}
$$

The coefficient c_4 is given by

$$
\begin{aligned}
c_4 = &+ (\boldsymbol{K}_A \cdot \boldsymbol{U}_W)[\omega_B(\boldsymbol{U}_B \cdot \boldsymbol{U}_A) - (\boldsymbol{K}_B \cdot \boldsymbol{B}_0) K_B^2 B_{AZ} - iK_{B\perp}^2 \rho_A] \\
&+ (\boldsymbol{K}_W \cdot \boldsymbol{U}_A)[\omega_B(\boldsymbol{U}_B \cdot \boldsymbol{U}_W) - (\boldsymbol{K}_B \cdot \boldsymbol{B}_0) K_B^2 B_{WZ} - iK_{B\perp}^2 \rho_W] \\
&- (\boldsymbol{K}_A \cdot \boldsymbol{B}_W)[\omega_B(\boldsymbol{U}_B \cdot \boldsymbol{B}_A) - (\boldsymbol{K}_B \cdot \boldsymbol{B}_0) K_B^2 U_{AZ}] \\
&- (\boldsymbol{K}_W \cdot \boldsymbol{B}_A)[\omega_B(\boldsymbol{U}_B \cdot \boldsymbol{B}_W) - (\boldsymbol{K}_B \cdot \boldsymbol{B}_0) K_B^2 U_{WZ}].
\end{aligned}
$$

The derivations for coefficients c_i are provided in Appendix A.3.2. The growth rate s is then evaluated numerically.

Alfvén Waves

We now derive solvability conditions for daughter waves of pure Alfvén character instead. The eigenvalue of (5.75) and (5.77) pertaining to AWs is (5.84). This eigenvalue has multiplicity two.

As a consequence, its associated right eigenvector has a two-parameter solution form:

$$
\begin{pmatrix} U_{AX} \\ U_{AY} \\ U_{AZ} \end{pmatrix} = \begin{pmatrix} 1 \\ 0 \\ 0 \end{pmatrix} U_{AX} + \begin{pmatrix} 0 \\ 1 \\ 0 \end{pmatrix} U_{AY}.
$$

Its associated left eigenvector also has a two-parameter solution form:

$$
\begin{pmatrix} \hat{U}_{AX} \\ \hat{U}_{AY} \\ \hat{U}_{AZ} \end{pmatrix} = \begin{pmatrix} K_{A\perp}^2 \\ 0 \\ K_{AZ} K_{AX} \end{pmatrix} \mathcal{U}_{AX} + \begin{pmatrix} 0 \\ K_{A\perp}^2 \\ K_{AZ} K_{AY} \end{pmatrix} \mathcal{U}_{AY}.
$$

The solvability conditions for each daughter wave A and B are

$$
\hat{\boldsymbol{U}}_A^\top \boldsymbol{G}_A = 0, \quad \hat{\boldsymbol{U}}_B^\top \boldsymbol{G}_B = 0.
$$

The simplest choices for this two parameter solution are

$$\mathcal{U}_{AX} = 1 \quad \text{and} \quad \mathcal{U}_{AY} = 0, \tag{5.85}$$
$$\mathcal{U}_{AX} = 0 \quad \text{and} \quad \mathcal{U}_{AY} = 1. \tag{5.86}$$

The solvability conditions corresponding to each of the choices (5.85) and (5.86) for the two-parameter solution associated with daughter wave A are

$$K_{A\perp}^2 G_{AX} + K_{AZ}K_{AX}G_{AZ} = 0, \tag{5.87}$$
$$K_{A\perp}^2 G_{AY} + K_{AZ}K_{AY}G_{AZ} = 0. \tag{5.88}$$

The equivalent conditions for daughter wave B are

$$K_{B\perp}^2 G_{BX} + K_{BZ}K_{BX}G_{BZ} = 0, \tag{5.89}$$
$$K_{B\perp}^2 G_{BY} + K_{BZ}K_{BY}G_{BZ} = 0. \tag{5.90}$$

We can eliminate each of G_{AZ} and G_{BZ} from these equations respectively by taking K_{AY}(5.87)$-$ K_{AX}(5.88) and K_{BY}(5.89)$-K_{BX}$(5.90). Though it is not necessary to eliminate G_{AZ} and G_{BZ} to proceed, the algebra is simplified as a result.

The solvability conditions we obtain for pure AWs are thus

$$K_{AY}G_{AX} - K_{AX}G_{AY} = 0, \quad K_{BY}G_{BX} - K_{BX}G_{BY} = 0. \tag{5.91}$$

Explicit formulae for the components of $\boldsymbol{G}_A$ and $\boldsymbol{G}_B$ are provided in Appendix A.3.2. Equations (5.91) are equivalent to the solvability conditions we would get from taking the vertical component of the vorticity analogue of the $O(a)$ PDE (5.74).

To find the amplitude equations, we write

$$K_{AY}G_{AX} - K_{AX}G_{AY} = c_1\frac{\mathrm{d}A}{\mathrm{d}\tau} + c_2 B,$$
$$K_{BY}G_{BX} - K_{BX}G_{BY} = c_3\frac{\mathrm{d}B}{\mathrm{d}\tau} + c_4 A.$$

where the coefficients (derived in Appendix A.3.2) are given by

$$\begin{aligned}
c_1 &= -2\omega_A K_{A\perp}^2, \\
c_2 &= +2i\omega_A K_{AY}K_{BY}K_{WX}(U_{WX} - B_{WX}), \\
c_3 &= -2\omega_B K_{B\perp}^2, \\
c_4 &= -2i\omega_B K_{AY}K_{BY}K_{WX}(U_{WX} + B_{WX}).
\end{aligned}$$

The explicit form of s is therefore

$$s = \pm\frac{a\beta^2\cos\theta}{2K_{A\perp}K_{B\perp}}. \tag{5.92}$$

Interestingly, this formula for the growth rate of an AGW-AW-AW TRI is independent of b_0 and ζ. It might seem at first that this should not be the case. It is however perfectly reasonable for the formula (5.92) to have no explicit b_0 or ζ dependence, as the influence of the magnetic field parameters manifests itself in the particular resonant combinations of $\boldsymbol{K}_A$ and $\boldsymbol{K}_B$ which arise.

Making assumptions about the sizes of the wavenumbers at this stage does not simplify the expression for s like it does in the case of AGW-AGW-AGW interactions. There is hence nothing to gain by taking the short wavelength limit in the case of AGW-AW-AW interactions.

Formula (5.92) tells us that there are no unstable modes when $\beta = 0$. This means that there are no 2D modes of disturbance which are unstable to AGW-AW-AW resonance.

Summary

In Chapter 5, we derived formulae for the growth rate of instabilities of small-amplitude AGWs under conditions in which criteria (5.1) and (5.2) are satisfied exactly. We have developed a theoretical framework with which to study TRIs of small-amplitude AGWs propagating through Boussinesq fluids permeated by 2D magnetic fields. This allows us to analyse the stability of a small-amplitude primary AGW. We derived explicit growth rate formulae for two classes of TRI: AGW-AGW-AGW interactions and AGW-AW-AW interactions. In future, we could also derive an explicit growth rate formula pertaining to AGW-AGW-AW interactions. AGW parametric instabilities are not limited to three-wave interactions. Any number of waves could potentially interact to produce instabilities.

In Chapter 6 we will analyse the instabilities of AGWs more broadly through the construction of a numerical eigenvalue problem, which serves as a magnetic extension of the eigenvalue problem presented in Chapter 4. Such a task does not require the same strict adherence to TRI critera, or to the assumption $a \ll 1$. At the end of Chapter 6 we will use formula (5.82) to vouch for some of the numerical results acquired. In future work, one could obtain a formula for the growth rate for AGW-AGW-AGW interactions in the short wavelength limit in the same way that we did for IGW-IGW-IGW interactions in Chapter 3. This would allow us to analytically predict the growth rate of the fastest-growing 2D instability for any primary wave (a, θ, ζ, b_0). One could also extend the framework to include non-zero values of B_{0Y}, thereby making the theory applicable to 3D background magnetic fields.

Chapter 6

Instabilities of Finite-Amplitude AGWs

This chapter is primarily motivated by the magnetic fields which typically permeate the radiative zones of stars. We know that IGWs can be excited here via penetrative plumes from the neighbouring convective zone (e.g Pinçon et al., 2016), or by tidal forcing (e.g. Guo et al., 2023). Stability analyses of tidally-forced IGWs in solar-type stars can be found in the literature (e.g Barker and Ogilvie, 2011), but the effects of magnetic fields on such stability analyses have never been studied. It remains to find out exactly what impact adding a magnetic field has on the instabilities of the wave.

We follow the same steps for linear stability analysis we took in Chapter 4, but with the governing equations adapted to account for the presence of a magnetic field. In other words, we build upon the stability analysis of a finite-amplitude plane IGW by incorporating magnetic fields for the first time. It leaves us equipped to study a plane AGW propagating through a magnetised, stably-stratified Boussinesq fluid with no restrictions on the amplitude of the wave. As we saw in Chapter 5, the range of wave interactions on display are now far more diverse.

6.1 Floquet Solver

6.1.1 The Basic State

Before diving into the linear stability analysis, let us clarify exactly what state we are perturbing.

We shall suppose that all dependent variables $F(\boldsymbol{X}, T)$ comprise three parts:

$$F(\boldsymbol{X}, T) = F_b + \tilde{F}(X, Z, T) + F'(X, Y, Z, T) \quad \text{for} \quad F \in \{\boldsymbol{U}, \boldsymbol{B}, P, \rho\}, \tag{6.1}$$

where F_b is a stably-stratified static background state in hydrostatic equilibrium representing fluid at rest permeated by a uniform magnetic field $\boldsymbol{B}_0$ and $\tilde{F}(X, Z, T)$ represents a plane wave solution with arbitrarily large amplitude to the Boussinesq MHD equations in the absence of diffusion. Together, F_b and $\tilde{F}$ comprise the time-dependent and space-dependent basic state for linear stability analysis. F' describes a perturbation with respect to this basic state. The perturbations we consider are three-dimensional and the diffusion acting on them is treated as non-zero.

The static background state F_b is given by

$$\boldsymbol{U}_b = P_b = \rho_b = 0, \quad \boldsymbol{B}_b = \boldsymbol{B}_0. \tag{6.2}$$

Of course, the background hydrostatic equilibrium does not have zero pressure and zero density. P_b and ρ_b are zero here because P and ρ are deviations from the hydrostatic pressure and density respectively. We introduced P and ρ as components of the total pressure $\breve{P}$ and total density $\breve{\rho}$ in Chapter 2 when applying the Boussinesq approximation to the fully compressible MHD equations.

The plane wave solution has the following explicit formulae:

$$\tilde{\boldsymbol{U}}(X,Z,T) = 2a\boldsymbol{U}_W \cos(\boldsymbol{K}\cdot\boldsymbol{X} - \omega T), \tag{6.3}$$
$$\tilde{\boldsymbol{B}}(X,Z,T) = 2a\boldsymbol{B}_W \cos(\boldsymbol{K}\cdot\boldsymbol{X} - \omega T), \tag{6.4}$$
$$\tilde{\rho}(X,Z,T) = 2ia\rho_W \sin(\boldsymbol{K}\cdot\boldsymbol{X} - \omega T), \tag{6.5}$$

where $\boldsymbol{K} := K_X\hat{\boldsymbol{X}} + K_Z\hat{\boldsymbol{Z}} = K\hat{\boldsymbol{K}}$ is its wavevector and ω is its angular frequency.

The coefficients $\boldsymbol{U}_W$, $\boldsymbol{B}_W$ and ρ_W are given by

$$\boldsymbol{U}_W := \frac{\omega}{2}\left(\frac{\hat{\boldsymbol{X}}}{K_X} - \frac{\hat{\boldsymbol{Z}}}{K_Z}\right), \quad \boldsymbol{B}_W := \frac{\boldsymbol{K}\cdot\boldsymbol{B}_0}{2}\left(\frac{\hat{\boldsymbol{Z}}}{K_Z} - \frac{\hat{\boldsymbol{X}}}{K_X}\right), \quad \rho_W := \frac{i}{2K_Z}\frac{\mathrm{d}\bar{\rho}}{\mathrm{d}Z}. \tag{6.6}$$

Solution (6.3)-(6.5) describes an Alfvén-gravity wave restored by both buoyancy and magnetic tension. This wave is approximately an IGW in the limit in which $b_0 \ll 1$, where the dimensionless field strength b_0 is given by

$$b_0 := \frac{KB_0}{N\sqrt{\mu_0\rho_0}}. \tag{6.7}$$

The derivation of these formulae for the amplitudes is provided in Section 2.4.

The uniform background magnetic field is expressed as

$$\boldsymbol{B}_0 = B_{0X}\hat{\boldsymbol{X}} + \boldsymbol{B}_{0Y}\hat{\boldsymbol{Y}} + B_{0Z}\hat{\boldsymbol{Z}}. \tag{6.8}$$

We parameterise $\boldsymbol{B}_0$ in terms of spherical polar coordinates:

$$B_{0X}(\xi,\zeta) = B_0 \sin\xi\cos\zeta,$$
$$B_{0Y}(\xi,\zeta) = B_0 \cos\xi,$$
$$B_{0Z}(\xi,\zeta) = B_0 \sin\xi\sin\zeta.$$

Here, ζ is the angle that the projection of $\boldsymbol{B}_0$ in the (X,Z)-plane makes with the X-axis, whereas ξ is the angle that $\boldsymbol{B}_0$ makes with the Y-axis. In the spherical coordinate system, ξ is the polar angle and ζ is the azimuthal angle. We ignored the Y-component of $\boldsymbol{B}_0$ and the angle ξ in Chapter 2 because the primary wave frequency ω has no B_{0Y}-dependence. A Y-component in B_0 would make no difference to the $\boldsymbol{K}\cdot\boldsymbol{B}_0$ term in the dispersion relation (since there is no K_Y). However a non-zero value of B_{0Y} does make a difference to the perturbation equations

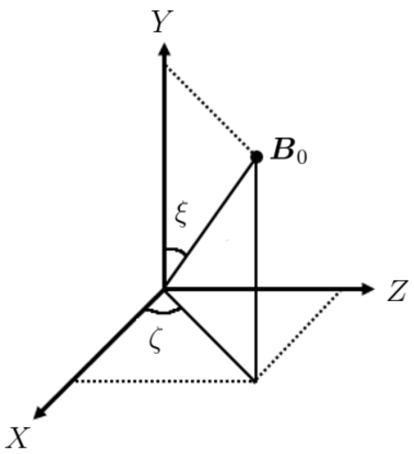

Figure 6.1: Spherical coordinate representation of the background magnetic field $\boldsymbol{B}_0$.

that we shall derive in the MHD linear stability analysis which follows. If we were to include non-zero B_{0Y} in Chapter 5 the perturbation equations in the asymptotic derivation would also be affected. Considering 3D background magnetic fields would serve as a valuable extension to the 2D theoretical framework derived in Chapter 5.

For many of the results in this chapter, we fix the background magnetic field angle ξ at a value of $\xi = \pi/2$ and in doing so confine the background magnetic field to the (X, Z)-plane, which is the plane to which the primary wavevector $\boldsymbol{K}$ is confined. This planar confinement of the background magnetic field comes with some loss in generality. Additional dynamics get introduced if $\boldsymbol{K}$ and $\boldsymbol{B}_0$ are not in the same plane. This is a different problem to the situation in which $\boldsymbol{K}$ and $\boldsymbol{B}_0$ are confined to the same plane. We remove this two-dimensional restriction on $\boldsymbol{B}_0$ later in Chapter 6 and allow fully three-dimensional background magnetic fields, i.e. we consider background fields with a non-zero Y-component.

6.1.2 The Coordinate Transformation

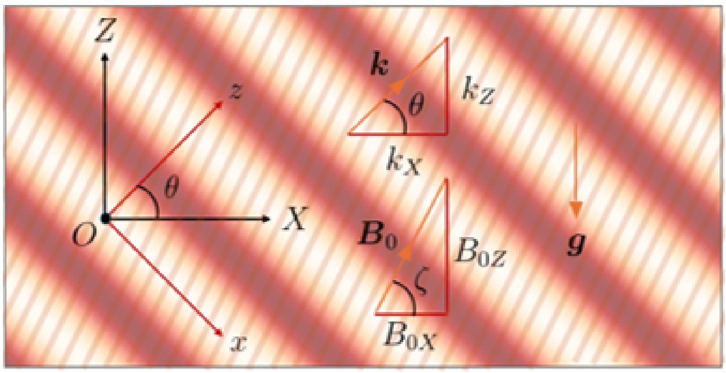

Figure 6.2: Coordinate configuration showing the relative orientations of the (X, Z) and (x, z) frames, along with how they relate to the directions of the primary wavevector $\boldsymbol{k}$ and a cross section of the uniform background magnetic field $\boldsymbol{B}_0$. The Y-axis points directly out of the page.

We apply the same coordinate transformation from Chapter 4 to the dimensional Boussinesq MHD equations for a stably-stratifed fluid with constant buoyancy frequency N and uniform background magnetic field $\boldsymbol{B}_0$, which read

$$\frac{\mathrm{D}\boldsymbol{U}}{\mathrm{D}T} = \nu\nabla^2\boldsymbol{U} + \frac{\boldsymbol{B}\cdot\nabla\boldsymbol{B}}{\mu_0\rho_0} - \frac{\nabla P}{\rho_0} + \frac{\rho\boldsymbol{g}}{\rho_0}, \tag{6.9}$$

$$\frac{\mathrm{D}\boldsymbol{B}}{\mathrm{D}T} = \eta\nabla^2\boldsymbol{B} + \boldsymbol{B}\cdot\nabla\boldsymbol{U}, \tag{6.10}$$

$$\frac{\mathrm{D}\rho}{\mathrm{D}T} = \kappa\nabla^2\rho - U_Z\frac{\mathrm{d}\bar{\rho}}{\mathrm{d}Z}, \tag{6.11}$$

along with the divergence-free constraints

$$\nabla\cdot\boldsymbol{U} = 0, \quad \nabla\cdot\boldsymbol{B} = 0. \tag{6.12}$$

The transformation we apply is depicted in Figure 6.2. As was the case in the hydrodynamic setting of Chapter 4, the spatial coordinate transformation is given by

$$\begin{pmatrix} x \\ y \\ z \end{pmatrix} = \begin{pmatrix} K_Z & 0 & -K_X \\ 0 & K & 0 \\ K_X & 0 & K_Z \end{pmatrix} \begin{pmatrix} X \\ Y \\ Z \end{pmatrix} - \begin{pmatrix} 0 \\ 0 \\ \omega T \end{pmatrix}. \tag{6.13}$$

The fluid velocity component transformation is also unchanged:

$$\begin{pmatrix} u_x \\ u_y \\ u_z \end{pmatrix} = \frac{1}{N}\begin{pmatrix} K_Z & 0 & -K_X \\ 0 & K & 0 \\ K_X & 0 & K_Z \end{pmatrix} \begin{pmatrix} U_X \\ U_Y \\ U_Z \end{pmatrix} - \begin{pmatrix} 0 \\ 0 \\ \omega/N \end{pmatrix}. \tag{6.14}$$

Now that we consider the presence of a magnetic field, we require a transformation analogous to that of the fluid velocity components for the magnetic field components. The proposed transformation for the components of the magnetic field is

$$\begin{pmatrix} b_x \\ b_y \\ b_z \end{pmatrix} = \frac{1}{N\sqrt{\mu_0\varrho_0}}\begin{pmatrix} K_Z & 0 & -K_X \\ 0 & K & 0 \\ K_X & 0 & K_Z \end{pmatrix} \begin{pmatrix} B_X \\ B_Y \\ B_Z \end{pmatrix}. \tag{6.15}$$

The remaining variables to be transformed are also the same as before.

$$\varrho = -\frac{K_Z\rho}{\mathrm{d}\bar{\rho}/\mathrm{d}Z}, \quad p = \frac{K^2P}{\rho_0N^2}, \quad t = NT. \tag{6.16}$$

Note that in this chapter, P and p respectively represent the dimensional and dimensionless sums of the fluid pressure and the magnetic pressure, rather than simply the fluid pressure. The dimensionless plane wavevector components are

$$k_X = K_X/K = \cos\theta, \quad k_Z = K_Z/K = \sin\theta. \tag{6.17}$$

The complete set of governing equations we acquire as a result of applying this transformation to the original governing equations (6.9)-(6.12) is

$$\frac{\mathrm{D}\boldsymbol{u}}{\mathrm{D}t} = \frac{\nabla^2 \boldsymbol{u}}{\mathrm{Re}} + \boldsymbol{b}\cdot\nabla\boldsymbol{b} - \nabla p + \left(\frac{k_x}{k_z}\hat{\boldsymbol{x}} - \hat{\boldsymbol{z}}\right)\varrho, \tag{6.18}$$

$$\frac{\mathrm{D}\boldsymbol{b}}{\mathrm{D}t} = \frac{\nabla^2 \boldsymbol{b}}{\mathrm{Rm}} + \boldsymbol{b}\cdot\nabla\boldsymbol{u}, \tag{6.19}$$

$$\frac{\mathrm{D}\varrho}{\mathrm{D}t} = \frac{\nabla^2 \varrho}{\mathrm{Pe}} + k_z\left(k_z u_z - k_x u_x + \frac{k_z\omega}{N}\right), \tag{6.20}$$

along with the divergence-free constraints

$$\nabla\cdot\boldsymbol{u} = 0, \quad \nabla\cdot\boldsymbol{b} = 0. \tag{6.21}$$

Here Re is the *fluid Reynolds number*, Rm is the *magnetic Reynolds number* and Pe is the *thermal Péclet number*, which were discussed in the introduction. According to our temporal scaling $1/N$ and spatial scaling $1/K$, these have the following formulae in our system:

$$\mathrm{Re} := \frac{N}{\nu K^2}, \quad \mathrm{Rm} := \frac{N}{\eta K^2}, \quad \mathrm{Pe} := \frac{N}{\kappa K^2}. \tag{6.22}$$

The transformed plane wave solution is

$$\tilde{u_x}(z) = 2u_w \cos z, \quad \tilde{u_z} = -\omega/N, \quad \tilde{b}_x(z) = 2b_w \cos z, \quad \tilde{\varrho}(z) = 2\varrho_w \sin z, \tag{6.23}$$

with amplitudes u_w, b_w and ϱ_w given by

$$u_w := \frac{a}{2k_Z k_X}\frac{\omega}{N}, \quad b_w := -\frac{a}{2k_X k_Z}\frac{\omega}{N}, \quad \varrho_w = \frac{a}{2}.$$

In the original coordinate frame, $\tilde{B}_Z$ is nonzero. The z-component $\tilde{b}_z$ of the transformed basic magnetic field fluctuation is identically zero, however.

In the transformed coordinates, the uniform background magnetic field is expressed as

$$\boldsymbol{b}_0 = b_{0x}\hat{\boldsymbol{x}} + b_{0y}\hat{\boldsymbol{y}} + b_{0z}\hat{\boldsymbol{z}}. \tag{6.24}$$

The dimensionless, transformed equivalent of the dispersion relation is

$$\frac{\omega}{N}\left(\frac{\omega^2}{N^2} - b_{0z}^2\right)\left(\frac{\omega^2}{N^2} - k_x^2 - b_{0z}^2\right) = 0. \tag{6.25}$$

6.1.3 Constructing an Eigenvalue Problem

Constructing a System of ODEs

The construction of the eigenvalue problem begins with linearisation. We decompose dependent variables into the static background state, the primary wave and a disturbance.

We express dependent variables as

$$\boldsymbol{u}(x,y,z,t) = \tilde{\boldsymbol{u}}(z) + \boldsymbol{u}'(x,y,z,t), \tag{6.26}$$

$$\boldsymbol{b}(x,y,z,t) = \boldsymbol{b}_0 + \tilde{\boldsymbol{b}}(z) + \boldsymbol{b}'(x,y,z,t), \tag{6.27}$$

$$p(x,y,z,t) = \tilde{p}(z) + p'(x,y,z,t), \tag{6.28}$$

$$\varrho(x,y,z,t) = \tilde{\varrho}(z) + \varrho'(x,y,z,t), \tag{6.29}$$

where f_0,$\tilde{f}$ and f' for $f \in \{\boldsymbol{u}, \boldsymbol{b}, \boldsymbol{p}, \varrho\}$ are the transformed, dimensionless forms of the variables defined in §4.1.1. We apply decompositions (6.26)-(6.29) to (6.18)-(6.21) and linearise the equations with respect to perturbation variables f'. The plane wave $\tilde{f}$ is an exact nonlinear solution of (6.18)-(6.21), so any terms featuring only primary wave variables do not appear in the equations which follow.

$$\frac{\partial \boldsymbol{u}'}{\partial t} + \tilde{\boldsymbol{u}} \cdot \nabla \boldsymbol{u}' + \boldsymbol{u}' \cdot \nabla \tilde{\boldsymbol{u}} = \frac{\nabla^2 \boldsymbol{u}'}{\mathrm{Re}} + (\boldsymbol{b}_0 + \tilde{\boldsymbol{b}}) \cdot \nabla \boldsymbol{b}' + \boldsymbol{b}' \cdot \nabla \tilde{\boldsymbol{b}} - \nabla p' + \Psi \varrho', \tag{6.30}$$

$$\frac{\partial \boldsymbol{b}'}{\partial t} + \tilde{\boldsymbol{u}} \cdot \nabla \boldsymbol{b}' + \boldsymbol{u}' \cdot \nabla \tilde{\boldsymbol{b}} = \frac{\nabla^2 \boldsymbol{b}'}{\mathrm{Rm}} + (\boldsymbol{b}_0 + \tilde{\boldsymbol{b}}) \cdot \nabla \boldsymbol{u}' + \boldsymbol{b}' \cdot \nabla \tilde{\boldsymbol{u}}, \tag{6.31}$$

$$\frac{\partial \varrho'}{\partial t} + \tilde{\boldsymbol{u}} \cdot \nabla \varrho' + \boldsymbol{u}' \cdot \nabla \tilde{\varrho} = \frac{\nabla^2 \varrho'}{\mathrm{Pe}} + k_z(k_z u_z' - k_x u_x'), \tag{6.32}$$

along with the divergence-free constraints

$$\nabla \cdot \boldsymbol{u}' = 0, \quad \nabla \cdot \boldsymbol{b}' = 0, \tag{6.33}$$

where $\Psi \coloneqq (k_x/k_z)\hat{\boldsymbol{x}} - \hat{\boldsymbol{z}}$. In order to use a Floquet method for stability analysis, we must convert the governing system of partial differential equations into a system of ordinary differential equations with periodic coefficients. We choose to make the coefficients periodic in z because z represents the phase of the primary wave. We again separate the z dependence of perturbations from the dependence on the other independent variables x, y and t.

Namely, we introduce the eigenmode decomposition

$$f'(x,y,z,t) = f^\dagger(z)\exp(i\alpha x + i\beta y + \sigma t), \quad \text{for} \quad f \in \{\boldsymbol{u}, \boldsymbol{b}, p, \varrho\}. \tag{6.34}$$

Recall that $\alpha, \beta \in \mathbb{R}$ are the x and y components of the disturbance wavevector $\boldsymbol{k}'$ in the (x, y, z) coordinate system. We define the convective derivative operator c and the Laplacian operator l as

$$c \coloneqq \sigma + i\alpha\tilde{u}_x + \tilde{u}_z\frac{\mathrm{d}}{\mathrm{d}z}, \quad l \coloneqq -\alpha^2 - \beta^2 + \frac{\mathrm{d}^2}{\mathrm{d}z^2}. \tag{6.35}$$

The linearised PDEs (6.30)-(6.33) become a system of ODEs:

$$\begin{aligned} c\boldsymbol{u}^\dagger + u_z^\dagger \frac{\mathrm{d}\tilde{\boldsymbol{u}}}{\mathrm{d}z} = {} & \frac{l\boldsymbol{u}^\dagger}{\mathrm{Re}} + (i\alpha b_{0x} + i\beta b_{0y} + i\alpha\tilde{b}_x)\boldsymbol{b}^\dagger + b_{0z}\frac{\mathrm{d}\boldsymbol{b}^\dagger}{\mathrm{d}z} + b_z^\dagger\frac{\mathrm{d}\tilde{\boldsymbol{b}}}{\mathrm{d}z} \\ & - \left(i\alpha\hat{\boldsymbol{x}} + i\beta\hat{\boldsymbol{y}} + \hat{\boldsymbol{z}}\frac{\mathrm{d}}{\mathrm{d}z}\right)p^\dagger + \frac{k_x\varrho^\dagger}{k_z} - \varrho^\dagger\hat{\boldsymbol{z}}, \end{aligned} \tag{6.36}$$

$$c\boldsymbol{b}^\dagger + u_z^\dagger\frac{\mathrm{d}\tilde{\boldsymbol{b}}}{\mathrm{d}z} = \frac{l\boldsymbol{b}^\dagger}{\mathrm{Rm}} + (i\alpha b_{0x} + i\beta b_{0y} + i\alpha\tilde{b}_x)\boldsymbol{u}^\dagger + b_{0z}\frac{\mathrm{d}\boldsymbol{u}^\dagger}{\mathrm{d}z} + b_z^\dagger\frac{\mathrm{d}\tilde{\boldsymbol{u}}}{\mathrm{d}z}, \tag{6.37}$$

$$c\varrho^\dagger + u_z^\dagger\frac{\mathrm{d}\tilde{\varrho}}{\mathrm{d}z} = \frac{l\varrho^\dagger}{\mathrm{Pe}} + k_z(k_z u_z^\dagger - k_x u_x^\dagger), \tag{6.38}$$

along with

$$i\alpha u_x^\dagger + i\beta u_y^\dagger + \frac{\mathrm{d}u_z^\dagger}{\mathrm{d}z} = 0, \quad i\alpha b_x^\dagger + i\beta b_y^\dagger + \frac{\mathrm{d}b_z^\dagger}{\mathrm{d}z} = 0. \tag{6.39}$$

Incorporating Floquet Theory

Since (6.36)-(6.39) constitutes a system of ODEs with periodic coefficients, we can again employ an aspect of Floquet theory to make progress towards forming an eigenvalue problem. See Chapter 4 for a full explanation of exactly how we use Floquet theory here.

In the same way as we did in Chapter 4, we may write $f^\dagger(z) = \exp(\mu z)\hat{f}(z)$, for some quantity μ. This investigation deals with finite-amplitude Alfvén-gravity waves, so in compliance with this restriction, we demand that μ is purely imaginary on a physical basis.

Equivalently, we may cast μ as $\mu := i\gamma$ for some $\gamma \in \mathbb{R}$, yielding the decomposition

$$f^\dagger(z) = \exp(i\gamma z)\hat{f}(z) \quad \text{for} \quad f \in \{\boldsymbol{u}, \boldsymbol{b}, p, \varrho\}. \tag{6.40}$$

Before going any further, we define two new operators to simplify the algebra. These are the convective derivative operator C and the Laplacian operator L:

$$C := \sigma + i\alpha\tilde{u}_x + \tilde{u}_z\left(i\gamma + \frac{\mathrm{d}}{\mathrm{d}z}\right), \quad L := -\alpha^2 - \beta^2 + \left(i\gamma + \frac{\mathrm{d}}{\mathrm{d}z}\right)^2. \tag{6.41}$$

We get the following system of equations when applying (6.40) to (6.36)-(6.39).

$$\begin{aligned} C\hat{\boldsymbol{u}} + \hat{u}_z\frac{\mathrm{d}\tilde{\boldsymbol{u}}}{\mathrm{d}z} &= \frac{L\hat{\boldsymbol{u}}}{\mathrm{Re}} + \left[i\alpha(b_{0x} + \tilde{b}_x) + i\beta b_{0y} + b_{0z}\left(i\gamma + \frac{\mathrm{d}}{\mathrm{d}z}\right)\right]\hat{\boldsymbol{b}} + \hat{b}_z\frac{\mathrm{d}\tilde{\boldsymbol{b}}}{\mathrm{d}z} \\ &\quad - \left[i\alpha\hat{\boldsymbol{x}} + i\beta\hat{\boldsymbol{y}} + \hat{\boldsymbol{z}}\left(i\gamma + \frac{\mathrm{d}}{\mathrm{d}z}\right)\right]\hat{p} + \frac{k_x\hat{\varrho}}{k_z}\hat{\boldsymbol{x}} - \hat{\varrho}\hat{\boldsymbol{z}}, \end{aligned} \tag{6.42}$$

$$C\hat{\boldsymbol{b}} + \hat{u}_z\frac{\mathrm{d}\tilde{\boldsymbol{b}}}{\mathrm{d}z} = \frac{L\hat{\boldsymbol{b}}}{\mathrm{Rm}} + \left[i\alpha(b_{0x} + \tilde{b}_x) + i\beta b_{0y} + +b_{0z}\left(i\gamma + \frac{\mathrm{d}}{\mathrm{d}z}\right)\right]\hat{\boldsymbol{u}} + \hat{b}_z\frac{\mathrm{d}\tilde{\boldsymbol{u}}}{\mathrm{d}z}, \tag{6.43}$$

$$C\hat{\varrho} + \hat{u}_z\frac{\mathrm{d}\tilde{\varrho}}{\mathrm{d}z} = \frac{L\hat{\varrho}}{\mathrm{Pe}} + \frac{k_z}{k^2}(k_z\hat{u}_z - k_x\hat{u}_x), \tag{6.44}$$

along with

$$i\alpha\hat{u}_x + i\beta\hat{u}_y + \left(i\gamma + \frac{\mathrm{d}}{\mathrm{d}z}\right)\hat{u}_z = 0, \quad i\alpha\hat{b}_x + i\beta\hat{b}_y + \left(i\gamma + \frac{\mathrm{d}}{\mathrm{d}z}\right)\hat{b}_z = 0. \tag{6.45}$$

Constructing a Matrix Equation

We now express each variable using its Fourier series representation.

This involves letting

$$\hat{f}(z) = \textstyle\sum_{n=-\infty}^{\infty} f_n \exp(inz) \quad \text{for} \quad f \in \{\boldsymbol{u}, \boldsymbol{b}, p, \varrho\}. \tag{6.46}$$

Overall, by combining decomposition (6.46) with decompositions (6.40) and (6.34), we arrive at the following expression for perturbation quantities f':

$$f'(x,y,z,t) = \sum_{n=-\infty}^{\infty} f_n \exp\left[i\alpha x + i\beta y + i(n+\gamma)z + \sigma t\right]. \tag{6.47}$$

The growth rate of the parametric instability is once again $\Re(\sigma)$. We proceed by constructing an eigenvalue problem for which σ is the eigenvalue from equations (6.42)-(6.43). We then need only take the real part of the eigenvalues σ found to obtain the growth rates we seek.

Upon substitution of (6.46) into (6.42)-(6.45), we find that the complete set of Fourier space equations of motion (6.49)-(6.56) contains all equations needed to produce the eigenvalue problem. Below, the algebraic Laplacian operator L_n is defined as

$$L_n \coloneqq -\alpha^2 - \beta^2 - (\gamma+n)^2. \tag{6.48}$$

To simplify the algebra, we define

$$\begin{aligned}
\Gamma_n^\nu &= L_n/\mathrm{Re} - i\tilde{u}_z(\gamma+n),\\
\Gamma_n^\eta &= L_n/\mathrm{Rm} - i\tilde{u}_z(\gamma+n),\\
\Gamma_n^\kappa &= L_n/\mathrm{Pe} - i\tilde{u}_z(\gamma+n).
\end{aligned}$$

We also define the disturbance wavevector as

$$\boldsymbol{k}' \coloneqq \alpha\hat{\boldsymbol{x}} + \beta\hat{\boldsymbol{y}} + (\gamma+n)\hat{\boldsymbol{z}}.$$

The Fourier space momentum equation components are

$$\begin{aligned}
(\sigma - \Gamma_n^\nu)u_n^x - i(\boldsymbol{k}'\cdot\boldsymbol{b}_0)b_n^x =& - i\alpha p_n + (k_x/k_z)\varrho_n - i\alpha u_w(u_{n-1}^x + u_{n+1}^x) + iu_w(u_{n+1}^z - u_{n-1}^z)\\
&+ i\alpha b_w(b_{n-1}^x + b_{n+1}^x) + ib_w(b_{n-1}^z - b_{n+1}^z), && (6.49)\\
(\sigma - \Gamma_n^\nu)u_n^y - i(\boldsymbol{k}'\cdot\boldsymbol{b}_0)b_n^y =& - i\beta p_n - i\alpha u_w(u_{n-1}^y + u_{n+1}^y) + i\alpha b_w(b_{n-1}^y + b_{n+1}^y), && (6.50)\\
(\sigma - \Gamma_n^\nu)u_n^z - i(\boldsymbol{k}'\cdot\boldsymbol{b}_0)b_n^z =& - i(\gamma+n)p_n - \varrho_n - i\alpha u_w(u_{n-1}^z + u_{n+1}^z) + i\alpha b_w(b_{n-1}^z + b_{n+1}^z). && (6.51)
\end{aligned}$$

The Fourier space induction equation components are

$$\begin{aligned}
(\sigma - \Gamma_n^\eta)b_n^x - i(\boldsymbol{k}'\cdot\boldsymbol{b}_0)u_n^x =& - i\alpha u_w(b_{n-1}^x + b_{n+1}^x) + ib_w(u_{n+1}^z - u_{n-1}^z)\\
&+ i\alpha b_w(u_{n-1}^x + u_{n+1}^x) + iu_w(b_{n-1}^z - b_{n+1}^z), && (6.52)\\
(\sigma - \Gamma_n^\eta)b_n^y - i(\boldsymbol{k}'\cdot\boldsymbol{b}_0)u_n^y =& - i\alpha u_w(b_{n-1}^y + b_{n+1}^y) + i\alpha b_w(u_{n-1}^y + u_{n+1}^y), && (6.53)\\
(\sigma - \Gamma_n^\eta)b_n^z - i(\boldsymbol{k}'\cdot\boldsymbol{b}_0)u_n^z =& - i\alpha u_w(b_{n-1}^z + b_{n+1}^z) + i\alpha b_w(u_{n-1}^z + u_{n+1}^z). && (6.54)
\end{aligned}$$

The Fourier space internal energy equation is

$$(\sigma - \Gamma_n^\kappa)\varrho_n = k_z(k_z u_n^z - k_x u_n^x) - i\alpha u_w(\varrho_{n-1} + \varrho_{n+1}) - \varrho_w(u_{n-1}^z + u_{n+1}^z). \tag{6.55}$$

The Fourier space solenoidal constraints are

$$i\alpha u_n^x + i\beta u_n^y + i(\gamma+n)u_n^z = 0, \quad i\alpha b_n^x + i\beta b_n^y + i(\gamma+n)b_n^z = 0. \tag{6.56}$$

As was done in Chapter 4, we eliminate p_n from the momentum equation. We form such an equation by taking $i\alpha\hat{\boldsymbol{x}}\cdot(6.42) + i\beta\hat{\boldsymbol{y}}\cdot(6.42) + (i\gamma + \mathrm{d}_z)\hat{\boldsymbol{z}}\cdot(6.42)$, which, in terms of Fourier modes, leaves

$$L_n p_n = i[\alpha k_x/k_z - (\gamma+n)]\varrho_n + 2\alpha u_w(u_{n-1}^z - u_{n+1}^z) + 2\alpha b_w(b_{n+1}^z - b_{n-1}^z). \tag{6.57}$$

We eliminate p_n from (6.49) and (6.51) through (6.57) and then construct an eigenvalue problem in terms of u_n^x, u_n^z, b_n^x, b_n^z and ϱ_n alone. From there, p_n can be calculated via (6.57). Variables u_n^y and b_n^y can then be calculated via (6.56).

Hence, we can arrive at a system of 5 equations for each value of n that we consider. To implement this system numerically we must truncate the infinite series into a finite series, still centred at $n = 0$. We use $2\mathcal{N} + 1$ modes in the calculation, such that

$$\hat{f}(z) = \sum_{n=-\mathcal{N}}^{\mathcal{N}} f_n \exp(inz) \quad \text{for} \quad f \in \{\boldsymbol{u}, \boldsymbol{b}, p, \varrho\}. \tag{6.58}$$

Substitution of (6.57) into (6.49) and (6.51) reveals that the eigenvalue problem is

$$M\boldsymbol{v} = \sigma\boldsymbol{v}, \tag{6.59}$$

where $\boldsymbol{v}$ is the vector defined as

$$\boldsymbol{v} = (u_{-\mathcal{N}}^x, u_{-\mathcal{N}}^z, b_{-\mathcal{N}}^x, b_{-\mathcal{N}}^z, \varrho_{-\mathcal{N}}, \ldots, u_0^x, u_0^z, b_0^x, b_0^z, \varrho_0, \ldots, u_{\mathcal{N}}^x, u_{\mathcal{N}}^z, b_{\mathcal{N}}^x, b_{\mathcal{N}}^z, \varrho_{\mathcal{N}}).$$

We define the matrix M as

$$M = \begin{pmatrix} M_{-\mathcal{N}}^2 & M_{-\mathcal{N}}^3 & & & & & & & & \mathbb{O} \\ M_{1-\mathcal{N}}^1 & M_{1-\mathcal{N}}^2 & M_{1-\mathcal{N}}^3 & & & & & & & \\ & M_{2-\mathcal{N}}^1 & M_{2-\mathcal{N}}^2 & M_{2-\mathcal{N}}^3 & & & & & & \\ & & \ddots & \ddots & \ddots & & & & & \\ & & & M_0^1 & M_0^2 & M_0^3 & & & & \\ & & & & \ddots & \ddots & \ddots & & & \\ & & & & & M_{\mathcal{N}-2}^1 & M_{\mathcal{N}-2}^2 & M_{\mathcal{N}-2}^3 & & \\ & & & & & & M_{\mathcal{N}-1}^1 & M_{\mathcal{N}-1}^2 & M_{\mathcal{N}-1}^3 & \\ \mathbb{O} & & & & & & & M_{\mathcal{N}}^1 & M_{\mathcal{N}}^2 & \end{pmatrix},$$

where M_n^1, M_n^2 and M_n^3 are 5×5 matrix-valued functions of n (i.e. 5×5 blocks) extracted from the coefficients in (6.49)-(6.57), and $\mathbb{O}$ represents an appropriately-sized block of zeroes. Explicit formule for M_n^1, M_n^2 and M_n^3 are included in Appendix A.2.1. The matrix M is a sparse tri-diagonal system of 5×5 blocks to be solved numerically.

6.2 Growth Rates

The numerical Floquet solver introduced in the previous section allows us to study instabilities of plane AGWs at any wave amplitude in a stably-stratified Boussinesq fluid permeated by a background magnetic field with any magnitude and orientation. Upon solving this numerical eigenvalue problem, the first task is to produce contour plots of the growth rate in (α, β)-space, revealing which modes of disturbance are subject to instability. We take an $n_\alpha \times n_\beta$ grid of α and β values and solve the eigenvalue problem individually for each of these pairs. We obtain a set of $10\mathcal{N} + 5$ eigenvalues for each pair. For each set of $10\mathcal{N} + 5$ values for σ, the recorded growth rate is the most positive value of $\Re(\sigma)$. In other words we record only the fastest-growing mode for each pair of (α, β) values. Any negative values of $\Re(\sigma)$ are set to zero in the growth rate contours that follow.

Resolution

We require a measure of how resolved the calculation is. For each use of the Floquet solver, we get $2\mathcal{N}+1$ values of the spectral energy density E_n, which is given by

$$E_n := |u_n^x|^2 + |u_n^y|^2 + |u_n^z|^2 + |b_n^x|^2 + |b_n^y|^2 + |b_n^z|^2 + |\varrho_n|^2 k^2/k_z^2. \tag{6.60}$$

E_n values are calculated for the fastest-growing eigenvalue σ. We then use

$$\Lambda := \frac{\max(E_n)}{\max(E_{-\mathcal{N}}, E_{\mathcal{N}})}$$

as our measure of how resolved the calculation is. We regard calculations for which $\Lambda > 10^6$ as being sufficiently resolved.

Influence of Introducing a Magnetic Field

In Figure 6.3 we present a visual demonstration of what changes regarding the proportion of (α, β)-space which is unstable upon adding a magnetic field to the model. The TRI tongues distributed along the α-axis which were present in the hydrodynamic setting are clearly not inhibited by introducing the magnetic field. However, the magnetic field produces new classes of instability which were not present in the hydrodynamic setting. In the next section we demonstrate how each class can be classified in terms of resonant interactions.

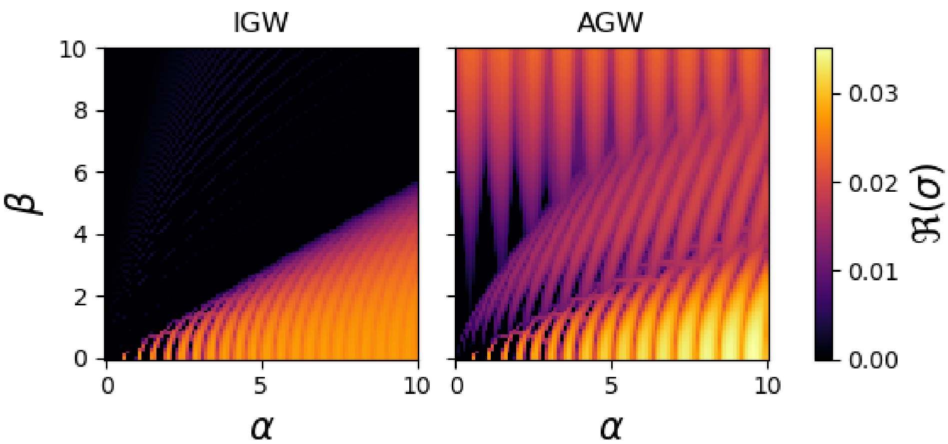

Figure 6.3: Growth rate contours in (α, β)-space for instabilities of an IGW in the absence of a magnetic field (left) and an AGW in the presence of a magnetic field for which $\zeta = 0$, $\xi = \pi/2$ and $b_0 = 0.05$ (right). Parameter values common to both plots: $a = 0.1$, $\theta = \pi/4$, $\gamma = 0$ and $\mathrm{Re} = \mathrm{Rm} = \mathrm{Pe} = 10^6$. Resolution: $\mathcal{N} = 40$, $n_\alpha = n_\beta = 100$.

6.2.1 Characterising the Instabilities

This section is dedicated to characterising the MHD instabilities on show in Figure 6.3 in terms of TRIs. With the addition of the magnetic field comes additional complexity regarding the types of resonant triads we can observe.

Resonance Curves

Recall that resonant triads are represented without loss of generality by equations with the following sign choices.

$$\boldsymbol{k} + \boldsymbol{k}_A - \boldsymbol{k}_B = 0, \tag{6.61}$$
$$\omega + \omega_A - \omega_B = 0. \tag{6.62}$$

where A and B are two Fourier components of the Floquet solution. The disturbance wavevector $\boldsymbol{k}_n$ is

$$\boldsymbol{k}_n := \alpha\hat{\boldsymbol{x}} + \beta\hat{\boldsymbol{y}} + (\gamma + n)\hat{\boldsymbol{z}}.$$

Recall that there are two ways in which (6.61) is naturally satisfied by two adjacent Fourier modes interacting with the primary wave.

$$\boldsymbol{k}_A = -\boldsymbol{k}_n \quad \text{and} \quad \boldsymbol{k}_B = -\boldsymbol{k}_{n-1}, \tag{6.63}$$
$$\boldsymbol{k}_A = +\boldsymbol{k}_n \quad \text{and} \quad \boldsymbol{k}_B = +\boldsymbol{k}_{n+1}. \tag{6.64}$$

We seek curves in (α, β)-space satisfying the resonance conditions (6.61) and (6.62). We again choose (6.64) in order to automatically satisfy (6.61). This gives us $\boldsymbol{k}_A$ and $\boldsymbol{k}_B$ in the transformed coordinates. To convert these to $\boldsymbol{K}_A$ and $\boldsymbol{K}_B$ in the original coordinates, we use

$$K_{AX} = (\gamma + n)K_X + \alpha K_Z, \tag{6.65}$$
$$K_{AY} = \beta K, \tag{6.66}$$
$$K_{AZ} = (\gamma + n)K_Z - \alpha K_X, \tag{6.67}$$
$$K_{BX} = (\gamma + n + 1)K_X + \alpha K_Z, \tag{6.68}$$
$$K_{BY} = \beta K, \tag{6.69}$$
$$K_{BZ} = (\gamma + n + 1)K_Z - \alpha K_X. \tag{6.70}$$

To find the regions of α, β space satisfying (6.62), we calculate

$$\Omega := |\omega + \omega_A - \omega_B|/N, \tag{6.71}$$

at each point on a grid of (α, β) values. We again plot only values of Ω smaller than some threshold value to illuminate the regions of (α, β)-space where resonance criterion (6.62) is approximately or exactly satisfied.

When considering magnetohydrodynamic resonances, there are more types of resonant interaction to consider. In the hydrodynamic setting, we just had one type of interaction: the interaction of two pure internal gravity daughter waves with one pure internal gravity primary wave. Now, since we are restricting ourselves to studying the stability of Alfvén-gravity primary waves, we must consider three different types of interaction, which are listed in Table 6.1.

The nature of the daughter wave frequencies ω_A and ω_B changes depending on which type of wave interaction we study. In Table 6.2 we provide expressions for ω_A and ω_B pertaining to each different combination of daughter waves. These are the sign choices which are necessary to produce triadic resonance when the wavenumber and frequency resonance conditions contain the signs featured in (6.61) and (6.62).

Primary Wave	Daughter Wave A	Daughter Wave B
Alfvén-gravity	Alfvén-gravity	Alfvén-gravity
Alfvén-gravity	Alfvén-gravity	Alfvén
Alfvén-gravity	Alfvén	Alfvén

Table 6.1: Possible resonant interactions in the MHD system.

A	B	ω_A	ω_B
AW	AW	$+\dfrac{\boldsymbol{K}_A \cdot \boldsymbol{B}_0}{\sqrt{\mu_0\rho_0}}$	$-\dfrac{\boldsymbol{K}_B \cdot \boldsymbol{B}_0}{\sqrt{\mu_0\rho_0}}$
AGW	AW	$\pm\sqrt{\dfrac{N^2K_{A\perp}^2}{K_A^2} + \dfrac{(\boldsymbol{K}_A \cdot \boldsymbol{B}_0)^2}{(\mu_0\rho_0)}}$	$\mp\dfrac{\boldsymbol{K}_B \cdot \boldsymbol{B}_0}{\sqrt{\mu_0\rho_0}}$
AGW	AGW	$-\sqrt{\dfrac{N^2K_{A\perp}^2}{K_A^2} + \dfrac{(\boldsymbol{K}_A \cdot \boldsymbol{B}_0)^2}{(\mu_0\rho_0)}}$	$+\sqrt{\dfrac{N^2K_{B\perp}^2}{K_B^2} + \dfrac{(\boldsymbol{K}_B \cdot \boldsymbol{B}_0)^2}{(\mu_0\rho_0)}}$

Table 6.2: Sign choices required for triadic resonance with different combinations of daughter waves A and B.

Classifying AGW Instabilities Using Resonance Classes

We can attribute the instability bands in contours such as the AGW panel of Figure 6.3 to three types of resonant interaction. In Figure 6.4, we fix an Alfvén-gravity wave as the primary wave and plot the resonance curves for the case where both daughter waves A and B are both hybrid Alfvén-gravity waves (AGWs), the case where both A and B are pure Alfvén waves and for the case where the daughter waves are of different types. Figure 6.4 features the same parameter values used in the AGW panel of 6.3. The purpose of Figure 6.4 is to attribute each instability band computed by the eigenvalue solver (6.59) to one of the three types of resonant triad interaction listed in Table 6.1. The labels on the panels where Ω is plotted indicate the type of daughter waves involved in the resonant interaction in each case, i.e. 'AGW-AGW' refers to the case where both daughter waves A and B are AGWs, 'AW-AW' refers to the case where both daughter waves are AWs and 'AGW-AW' refers to the case where we have one daughter wave of each type.

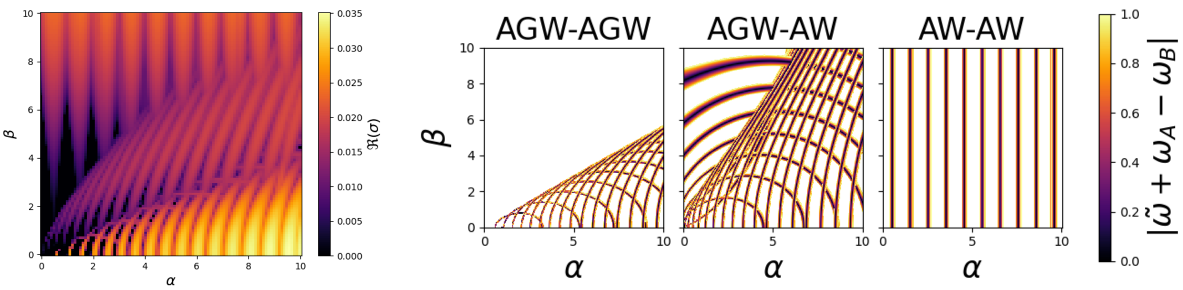

Figure 6.4: (Left) Contours of the growth rate in wavenumber space computed by solving (6.59). Parameter values: $a = 0.1$, $\theta = \pi/4$, $\zeta = 0$, $\xi = \pi/2$, $b_0 = 0.05$, $\gamma = 0$, $\mathcal{N} = 40$. (Right) Distance Ω from exact resonance for all three types of resonant triad, computed using (6.71).

The fact that instability bands are aligned with the β-coordinate axis in the scenario where both daughter waves A and B are AWs is explained by the lack of any β-dependence in the resonance conditions (6.61) and (6.62). In the same way it explains the fact that resonance bands for AW-AW interactions show up as vertical lines in Figure 6.4. Along AW-AW instability bands, $\Re(\sigma) = 0$ when $\beta = 0$, which is consistent with asymptotic formula (5.92) for AGW-AW-AW resonances.

6.2.2 Influence of Magnetic Field Strength

For this section, we fix the uniform background magnetic field at an angle of $\zeta = 0$ with respect to the original X-axis and observe how the strength of this uniform background magnetic field affects the growth rate of the instabilities at play. In this section, the field is oriented perpendicular to the direction of gravity. We started to explore this case in Figures 6.3 and 6.4, but now we vary b_0.

Growth Rates at Small Amplitudes

We want to see whether the field strength affects the tongues of parametric instability visible for small-amplitude ($a = 0.1$) AGWs. Does it enhance them? Does it inhibit them? Does it have no discernable effect on them at all? We plot growth rates in (α, β)-space for an IGW with $a = 0.1$, $\theta = \pi/4$, $\zeta = 0$ and $\xi = \pi/2$ for a variety of different field strengths b_0 in Figures 6.5, 6.6 and 6.7.

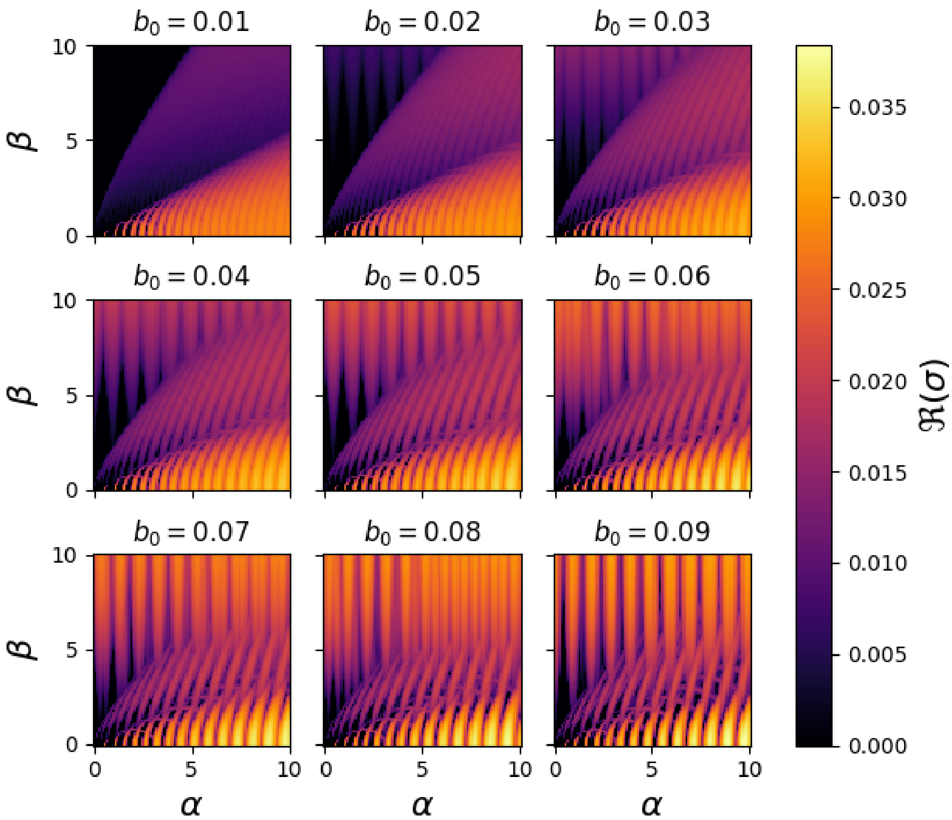

Figure 6.5: Growth rate contours in (α, β)-space for different values of the background magnetic field strength. Parameter values: $a = 0.1$, $\theta = \pi/4$, $\zeta = 0$, $\xi = \pi/2$, $\gamma = 0$ and $\mathrm{Re} = \mathrm{Rm} = \mathrm{Pe} = 10^6$. Resolution: $\mathcal{N} = 40$, $n_\alpha = n_\beta = 100$.

There is a noticeable increase in the maximum growth rate observed in this region of (α, β)-space as we increase b_0 in Figure 6.5. The location and density of the resonance bands change with increasing field strength. This effect is particularly visible in Figure 6.6. Overall, the instabilities induced by AGW-AGW-AW interactions and AGW-AW-AW interactions exhibit lower growth rates (~ 0.010) than the AGW-AGW-AGW interactions (~ 0.025). At the lowest field strengths observed, the proportion of parameter space which is unstable increases with field strength (Figures 6.5 and 6.6). We can therefore conclude that an AGW is more unstable than an IGW in the limit $b_0 \ll 1$ for the parameter values used in these figures. At the highest field strengths observed, the instability bands get narrower with increasing b_0 (Figure 6.7).

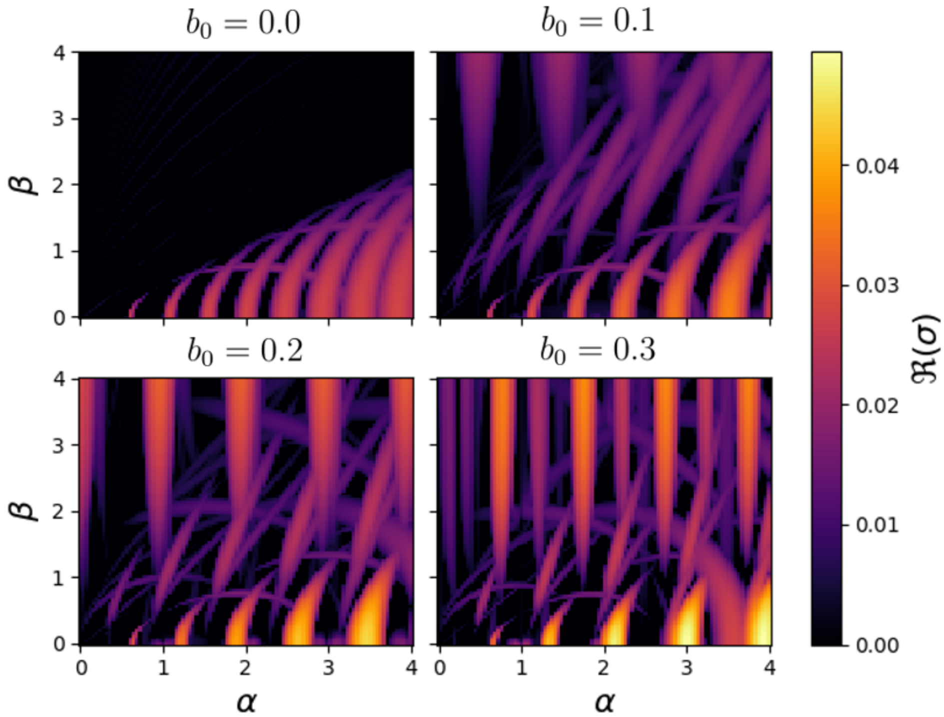

Figure 6.6: Growth rate contours for different magnetic field strengths b_0. Parameter values: $a = 0.1$, $\theta = \pi/4$, $\zeta = 0$, $\xi = \pi/2$, $\gamma = 0$, $\mathrm{Re} = \mathrm{Rm} = \mathrm{Pe} = 10^6$. Resolution: $\mathcal{N} = 15$ and $n_\alpha = n_\beta = 100$.

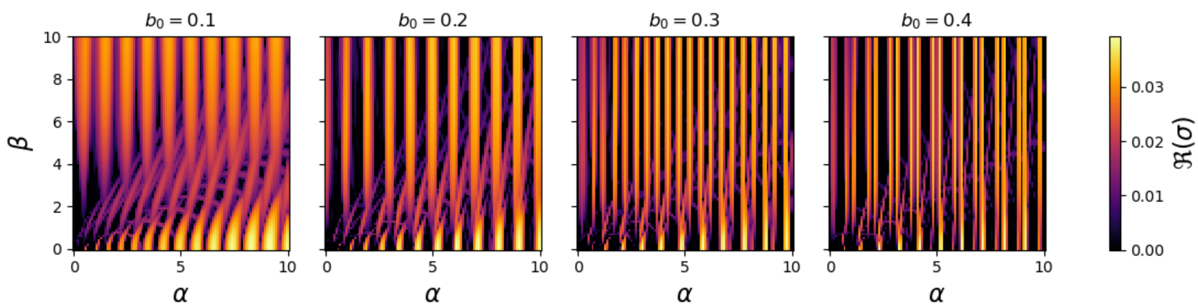

Figure 6.7: Growth rate contours for different magnetic field strengths b_0. Parameter values: $a = 0.1, \theta = \pi/4, \zeta = 0, \xi = \pi/2, \gamma = 0, \mathrm{Re} = \mathrm{Rm} = \mathrm{Pe} = 10^6$. Resolution: $\mathcal{N} = 40$ and $n_\alpha = n_\beta = 100$.

Growth Rates at Large Amplitudes

So we have studied the effects of magnetic fields on instabilities of small-amplitude primary waves ($a = 0.1$). We now increase the amplitude of the primary wave to the marginally overturning threshold ($a = 1$) to see what the effects of magnetic fields are on instabilities of breaking AGWs, i.e. AGWs which are statically unstable.

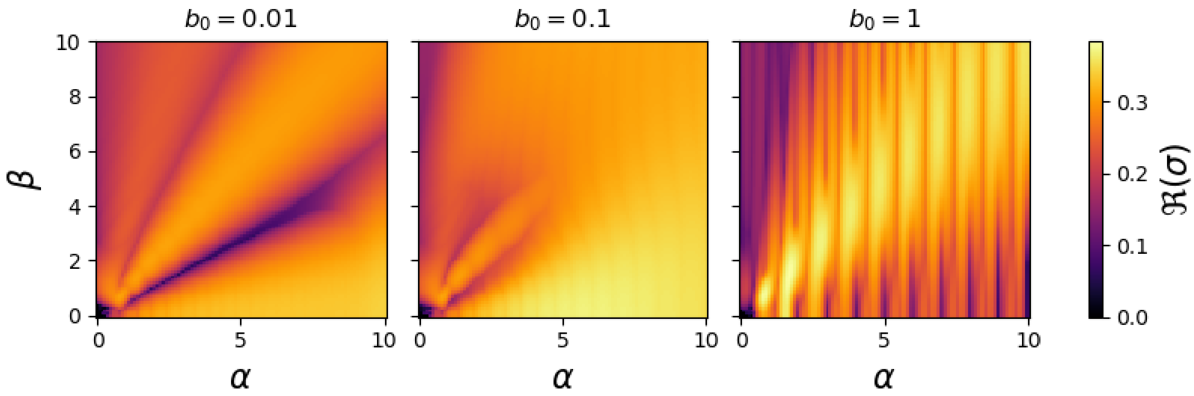

Figure 6.8: Growth rate contours in (α, β)-space for different values of the background magnetic field strength. Parameter values: $a = 1$, $\theta = \pi/4$, $\zeta = 0$, $\xi = \pi/2$, $\gamma = 0$ and $\mathrm{Re} = \mathrm{Rm} = \mathrm{Pe} = 10^6$. Resolution: $\mathcal{N} = 40$, $n_\alpha = n_\beta = 100$.

In Figure 6.8 we view instabilities of unit amplitude primary waves with different orders of magnitude for the background magnetic field strength. At $b_0 = 0.01$, (α, β)-space arranges itself into three distinct regions (Regions I, II and III) in the same way that it did for $a = 1$ in the absence of a magnetic field (Figure 4.25). Increasing the field strength to $b_0 = 0.1$ makes Regions I, II and III become less distinct. We find that a field strength $b_0 = 1$ changes the behaviour significantly. At each order of magnitude for the magnetic field strength, we see that the primary wave is unstable at this amplitude across almost the entirety of the portion of parameter space considered. The fastest-growing unstable modes at $b_0 = 1$ roughly occupy the line $\alpha = \beta$. Modes with low α are stabilised at $b_0 = 1$. Overall, growth rates are similar for different field strengths when $a = 1$. The field strength influences which particular modes of instability are the fastest-growing, but it does not change the overall conclusion that AGWs are generally unstable.

6.2.3 Influence of Magnetic Field Orientation

We now seek to identify the influence of the magnetic field orientation on AGW instabilities. Such research is important because in principle a magnetic field in the radiative zone could have any orientation with respect to the primary AGW. The orientation of the field can have consequences regarding the fate of propagating IGWs. In magnetic stars, propagating IGWs can either be reflected or trapped once they reach surfaces of magnetic flux. Whether they get reflected or trapped is dependent on the orientation of the background magnetic field with respect to the stratification (Loi and Papaloizou, 2018).

Influence of Angle ζ

We start by focusing on ζ, the angle $\boldsymbol{B}_0$ makes with the X-axis when $\xi = \pi/2$. When determining the influence of ζ, we fix the other background magnetic field angle ξ at a value of $\xi = \pi/2$, which corresponds to a background magnetic field confined to the (X, Z)-plane (i.e. coplanar with the primary wave). We contour the growth rate in (α, β)-space for an AGW with $a = 0.1$ and $\theta = \pi/4$ in Figures 6.9 and 6.10.

When varying the angle of the uniform background magnetic field with respect to the transformed x-axis, we fix the magnetic field strength at $b_0 = 0.02$ (Figure 6.9) and $b_0 = 0.05$ (Figure 6.10). The overall conclusion we can draw from these figures is that the value of the field angle ζ does not change the fact that AGWs are generally unstable. The maximum growth rates observed in this (α, β) domain are not massively influenced by ζ. What ζ does change is which modes of disturbance are the fastest-growing. Overall, when comparing Figures 6.9 and 6.10, we find that ζ has a much larger influence on growth rates when b_0 is larger.

The introduction of the magnetic field has an insignificant effect on the growth rates observed in the hydrodynamic setting when the magnetic field is oriented at $\zeta = 3\pi/4$ for the range of wavenumbers used in Figure 6.9. This matches expectations because at this angle, $\boldsymbol{b}_0$ is perpendicular to the direction of $\boldsymbol{k}$ ($\theta = \pi/4$). We hence get no contribution from the $\boldsymbol{k} \cdot \boldsymbol{b}_0$ term in the AGW dispersion relation, removing any influence of the magnetic field on the primary wave. This explains why the contours at $\zeta = 3\pi/4$ in Figure 6.9 look almost identical to the hydrodynamic contours for the same set of parameter values. The primary wave is effectively an IGW when $|\zeta - \theta| = \pi/2$. The magnetic field can still influence the disturbance however, through the $\boldsymbol{k}' \cdot \boldsymbol{b}_0$ term. There is a significant difference between the corresponding hydrodynamic contours and the results for $\zeta = 3\pi/4$ with $b_0 = 0.05$ (Figure 6.10).

At $\zeta = \pi/4$, the background magnetic field $\boldsymbol{b}_0$ is aligned with the wavevector $\boldsymbol{k}$, maximising the value of the $\boldsymbol{k} \cdot \boldsymbol{b}_0$ term in the AGW dispersion relation and thereby maximising the influence of the magnetic field on the primary wave. We can see this in both Figure 6.9 and Figure 6.10.

Results have only been shown for field angles in the interval $\zeta \in [0, \pi)$. Results for field angles in the interval $\zeta \in [\pi, 2\pi)$ do not reveal any additional information because the MHD equations are invariant under the transformation $\boldsymbol{b}_0 \to -\boldsymbol{b}_0$.

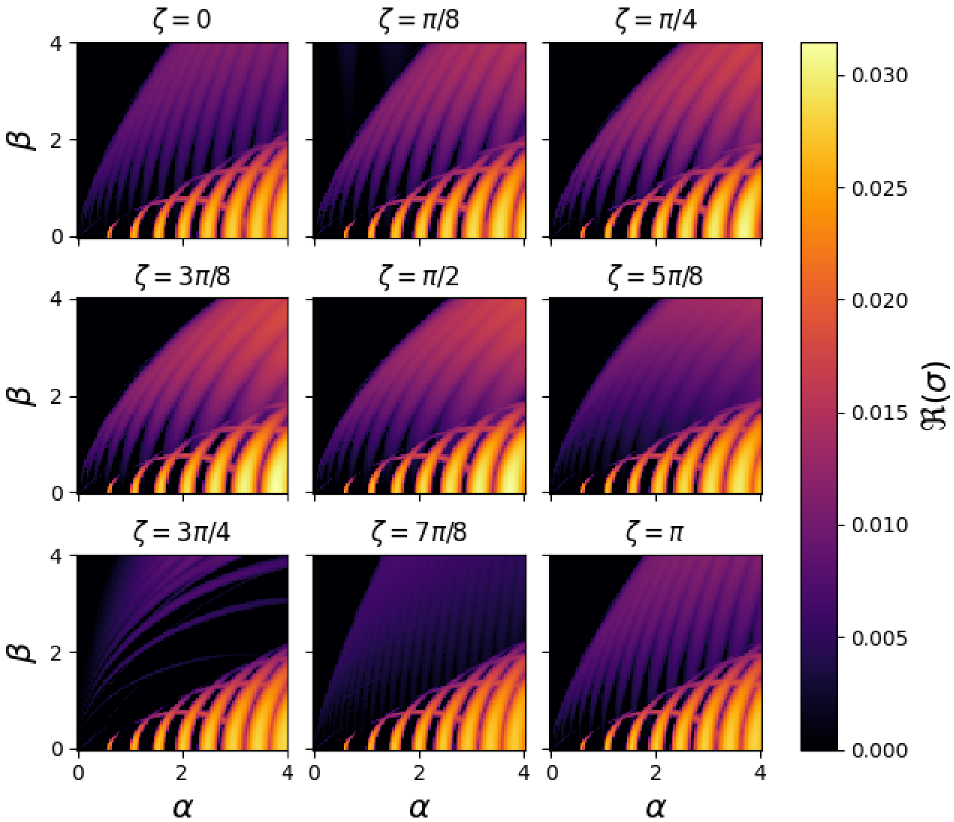

Figure 6.9: Growth rate contours in wavenumber space for different values of the magnetic field angle ζ. Parameter values: $a = 0.1, \theta = \pi/4, \xi = \pi/2, b_0 = 0.02, \gamma = 0, \mathcal{N} = 12, \mathrm{Re} = \mathrm{Rm} = \mathrm{Pe} = 10^6$.

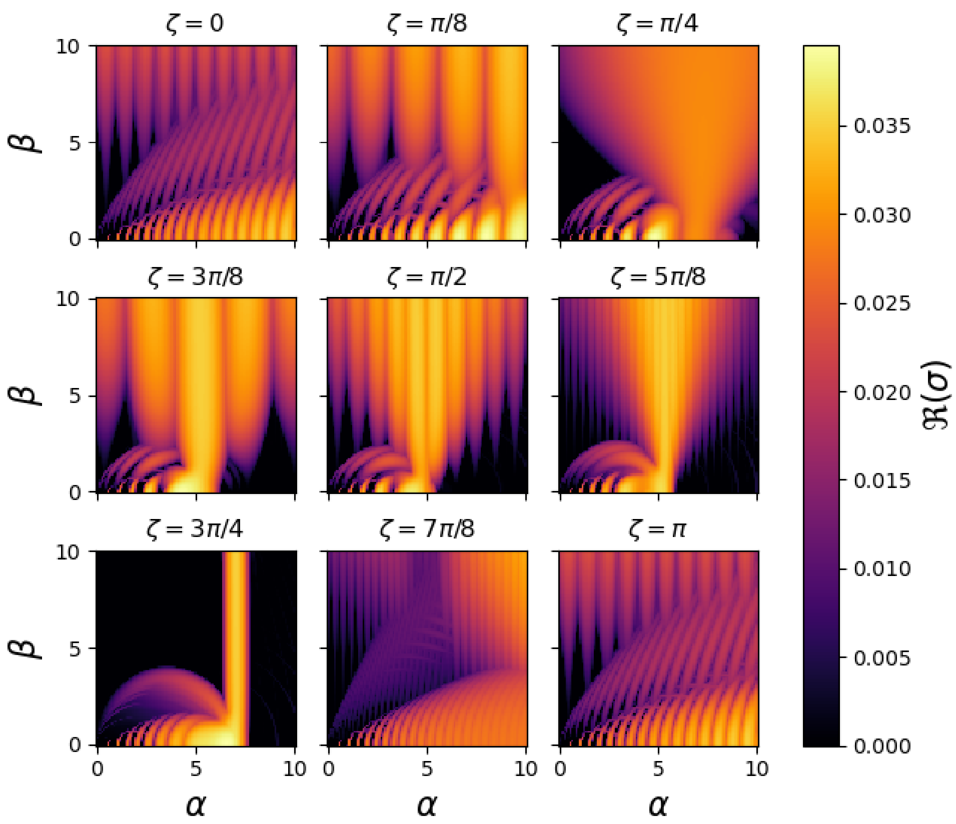

Figure 6.10: Growth rate contours in wavenumber space for different values of the magnetic field angle ζ. Parameter values: $a = 0.1, \theta = \pi/4, \xi = \pi/2, b_0 = 0.05, \gamma = 0, \mathcal{N} = 40, \mathrm{Re} = \mathrm{Rm} = \mathrm{Pe} = 10^6$.

Physical Significance of Magnetic Field Orientations

θ	ζ	**Aligned axis**	**Significance**	**Implication**
$\pi/4$	0	X	Perpendicular to stratification	
$\pi/4$	$\pi/4$	z	Parallel with primary wave	$\boldsymbol{k} \cdot \boldsymbol{b}_0$ maximised
$\pi/4$	$\pi/2$	Z	Aligned with stratification	
$\pi/4$	$3\pi/4$	x	Perpendicular to primary wave	$\boldsymbol{k} \cdot \boldsymbol{b}_0 = 0$ (IGW)
$\pi/4$	π	X	Perpendicular to stratification	

Table 6.3: Physical significance of different magnetic field angles ζ for a primary wave with $\theta = \pi/4$.

Table 6.3 summarises how best to interpret each of the important magnetic field orientations we consider. Figure 6.9 is consistent with a crucial result of the above table associated with the field angle $\zeta = 3\pi/4$. The $\zeta = 3\pi/4$ panel of Figure 6.9 is almost identical to the growth rate contours for the same set of parameter values in the absence of a magnetic field. This is because, as stated in the table, $\boldsymbol{k} \cdot \boldsymbol{b}_0 = 0$ in the case where $\zeta = 3\pi/4$, meaning that the dispersion relation for the primary wave is reduced to the dispersion relation for pure internal gravity waves. In other words, we are effectively studying the stability of a pure internal gravity wave in the $\zeta = 3\pi/4$ panel of Figure 6.9. When $\boldsymbol{k} \cdot \boldsymbol{b}_0$ is maximised at $\zeta = \pi/4$, we observe the broadest AGW-AW-AW resonance bands of any ζ value. It is expected that the background magnetic field will have the greatest influence on the primary wave at $\zeta = \pi/4$. This case, in which $\boldsymbol{k}$ and $\boldsymbol{b}_0$ are parallel, is discussed in more detail in Section 6.2.5.

The $\zeta = 3\pi/4$ panel of Figure 6.10 is significant because for a primary wave with

$\theta = \pi/4$, it depicts the case in which the magnetic field vector is perpendicular to the primary wavevector. We observe behaviour in which the AGW-AW-AW interactions are confined to a single band of resonance located at a single value of α. Moreover, this α value acts as a critical value beyond which AGW-AGW-AGW resonances and AGW-AGW-AW resonances do not occur for this set of parameter values. To improve our understanding of this behaviour, we plot the associated resonance curves of Ω in (α, β)-space in Figure 6.11. This reinforces the conclusion that there is just one resonance band visible for AGW-AW-AW interactions. Figure 6.11 also reinforces the conclusion that this α value serves as a threshold above which AGW-AGW-AGW resonances and AGW-AGW-AW resonances do not occur. In Section 6.2.4 we demonstrate how this idea can be understood analytically, along with providing a formula for predicting the value of α at which this AGW-AW-AW resonance band appears.

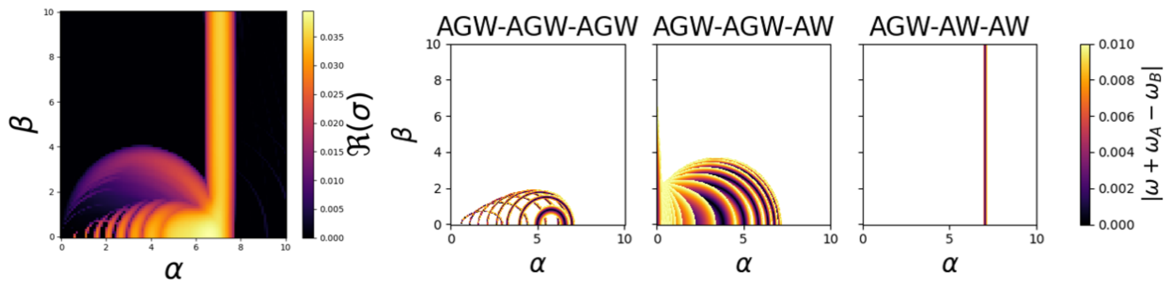

Figure 6.11: Growth rate contours in wavenumber space, along with associated resonance curves Ω for each class of resonant triad interaction computed using (6.71). Parameter values: $a = 0.1$, $\theta = \pi/4$, $\zeta = 3\pi/4$, $\xi = \pi/2$, $b_0 = 0.05$, $\gamma = 0$, $\mathcal{N} = 40$, $\mathrm{Re} = \mathrm{Rm} = \mathrm{Pe} = 10^6$.

Growth Rates at Overturning Amplitude

What effect does magnetic field orientation ζ have at higher amplitudes? In Figure 6.12 we repeat the results of Figure 6.10 for an $a = 1$ primary AGW. We find that varying the field orientation at this amplitude has less influence on the instabilities than varying it at $a = 0.1$. The orientation of the field does not change the overall picture, which is that plane AGWs are generally unstable at $a = 1$. In other words, most of parameter space is unstable for all ζ values. The maximum growth rates observed in this (α, β) domain are largely unaffected by ζ.

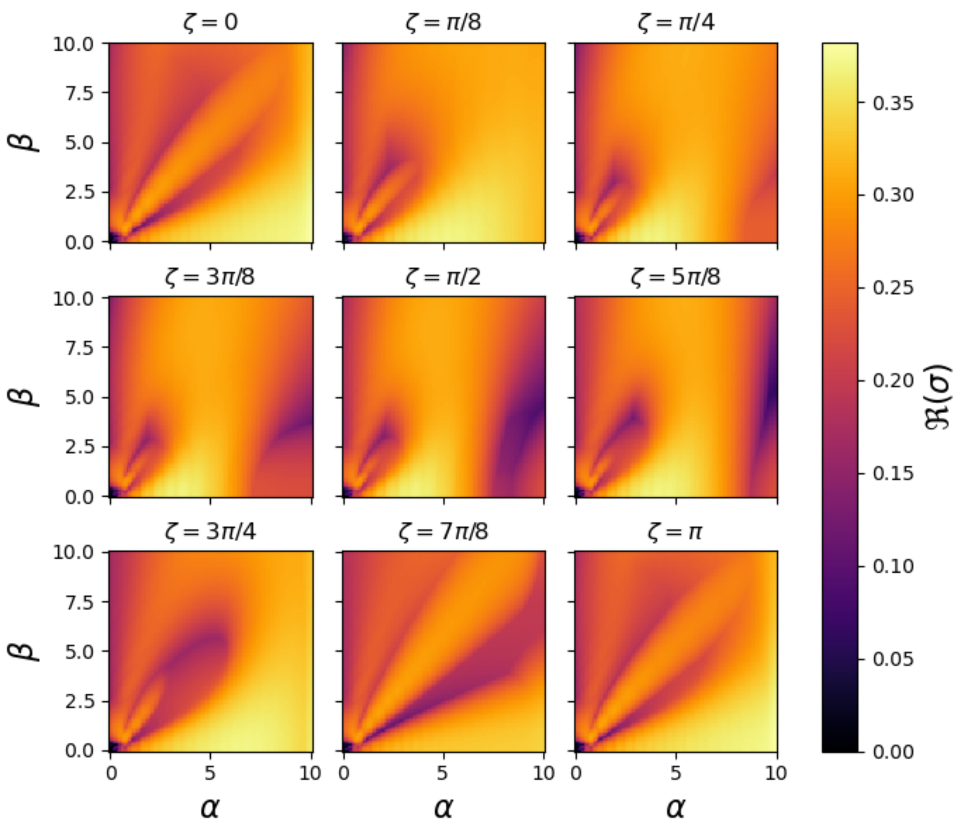

Figure 6.12: Growth rate contours in wavenumber space for different values of the magnetic field angle ζ. Parameter values: $a = 1, \theta = \pi/4, \xi = \pi/2, b_0 = 0.05, \gamma = 0, \mathcal{N} = 40, \mathrm{Re} = \mathrm{Rm} = \mathrm{Pe} = 10^6$.

Influence of Angle ξ

So far we have only considered background magnetic fields confined to the (X, Z)-plane (i.e. with a fixed angle of $\xi = \pi/2$). In this section we remove this restriction on the value of ξ and allow $\boldsymbol{B}_0$ to deviate from the (X, Z)-plane. We instead fix ζ at a value of $\zeta = 0$, such that $\boldsymbol{B}_0$ is confined to the (X, Y)-plane.

In Figure 6.13 we contour the growth rate in (α, β)-space for different values of ξ. Overall, introducing a non-zero Y-component in $\boldsymbol{B}_0$ does not significantly affect the maximum growth rates observed in this (α, β) domain. For most angles ξ considered, the value of ξ does not affect the proportion of parameter space which is unstable (except for the case $\xi = 0$). The value of ξ does affect the distribution of unstable modes in (α, β)-space, however.

The orientation of the instability bands induced by AGW-AW-AW interactions changes as ξ changes. Panel $\xi = 0$ corresponds with a magnetic field purely in the Y-direction, so naturally the possibility of AGW-AW-AW resonance occuring is dependent only on the value of β. Similarly, panel $\xi = \pi/2$ corresponds with a magnetic field perpendicular to the Y-direction, so the value of β has no bearing on whether AGW-AW-AW resonance occurs. Within each individual instability band induced by AGW-AW-AW interactions, the resonance conditions are uniformly satisfied in the direction perpendicular to the orientation of the field. The orientation of the instability bands associated with AGW-AGW-AW resonances also changes as ξ changes, but to a lesser extent than those associated with AGW-AW-AW interactions.

The $\xi = 0$ panel of Figure 6.13 is significant because it depicts the situation in which $\boldsymbol{B}_0$ is oriented perpendicular to the (X, Z)-plane, to which the primary wavevector is confined. This makes the $\xi = 0$ panel of Figure 6.13 physically equivalent to the $\zeta = 3\pi/4$ panel of Figure

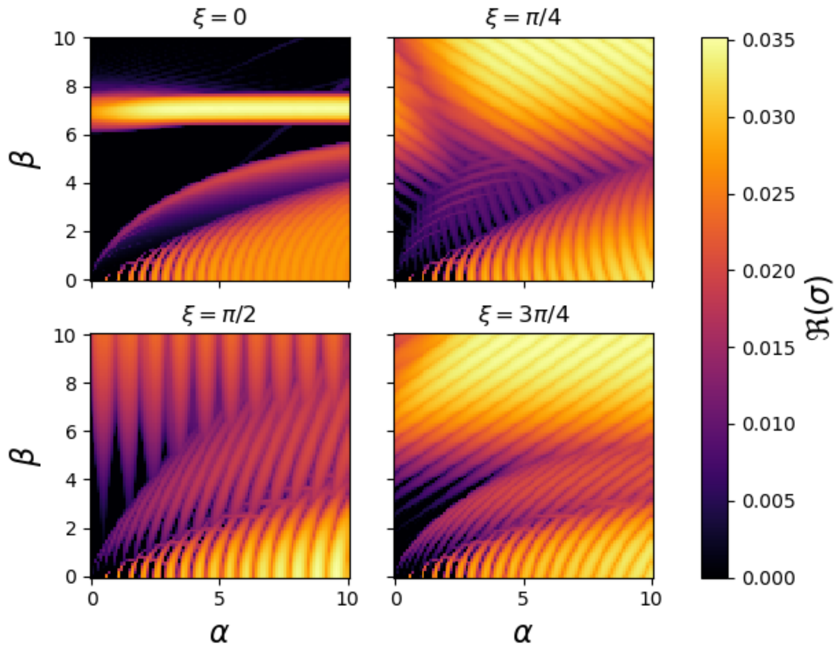

Figure 6.13: Growth rate contours (left) in wavenumber space for instabilities of an AGW for a selection of different magnetic field orientations ξ. Parameter values: $a = 0.1$, $\theta = \pi/4$, $\zeta = 0$, $b_0 = 0.05$, $\gamma = 0$, $\mathrm{Re} = \mathrm{Rm} = \mathrm{Pe} = 10^6$. Resolution: $\mathcal{N} = 40$, $n_\alpha = n_\beta = 100$.

6.10. In Section 6.2.4 we demonstrate how the value of β at which AGW-AW-AW resonance occurs can be calculated exactly in the case $\xi = 0$. Importantly, $\xi = 0$ is the value for which $\boldsymbol{B}_0$ is perpendicular to the phase velocity of the primary wave. This is why the $\xi = 0$ panel from Figure 6.13 exhibits similar behaviour to the $\zeta = 3\pi/4$ panel from Figure 6.10.

6.2.4 Magnetic Field Vector Perpendicular to Primary Wavevector

In this section we consider magnetic field vectors $\boldsymbol{B}_0$ which lie perpendicular to the primary wavevector $\boldsymbol{K}$. This particular relationship between $\boldsymbol{B}_0$ and $\boldsymbol{K}$ is interesting because the quantity $\boldsymbol{K} \cdot \boldsymbol{B}_0$ is crucial to the dynamics of AGWs and AWs. When $\boldsymbol{K} \cdot \boldsymbol{B}_0 = 0$, the AGW dispersion relation (2.79) reduces to the IGW dispersion relation (2.65). In this scenario, the primary wave is effectively an IGW, but the daughter waves it resonantly interacts with are still either AGWs or AWs. This is because $\boldsymbol{K}_A \cdot \boldsymbol{B}_0$ and $\boldsymbol{K}_B \cdot \boldsymbol{B}_0$ are still non-zero in general. The situation in which $\boldsymbol{B}_0$ and $\boldsymbol{K}$ are perpendicular is the only situation in which a pure IGW can exist in the magnetised Boussinesq fluids which we study.

It turns out that we can derive analytical formulae for predicting the locations of AGW-AW-AW resonances in the case where $\boldsymbol{B}_0$ and $\boldsymbol{K}$ are perpendicular. For resonance bands independent of α, we can predict the resonant β value and for resonance bands independent of β, we can predict the resonant α value.

Exact Formula for Location of AGW-AW-AW Resonances with $\theta = \pi/4$ and $\zeta = 3\pi/4$

We can derive a formula to compute the exact value of β at which the AGW-AW-AW resonance occurs in Figure 6.11. In Figure 6.11, $\zeta = 3\pi/4$ and $\theta = \pi/4$ which means the direction of the background magnetic field is perpendicular to the phase velocity of the primary wave. This

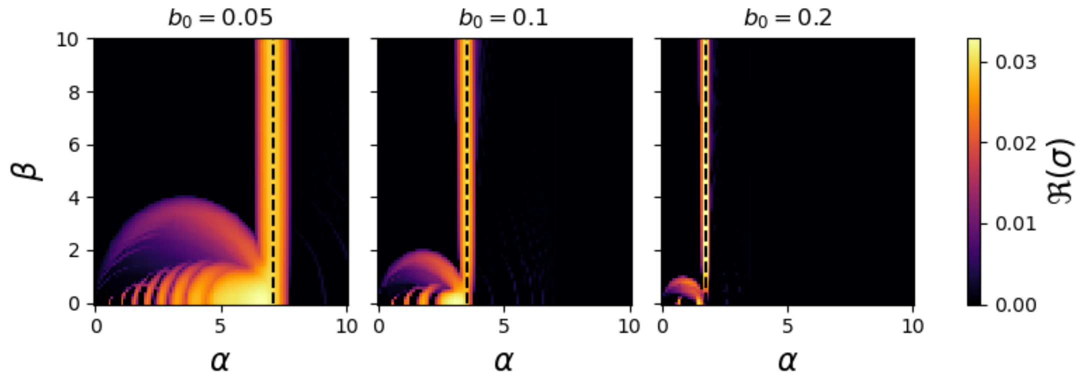

Figure 6.14: Growth rate contours in wavenumber space for instabilities of an AGW in the presence of a background magnetic field lying perpendicular to the phase velocity of the primary wave. Dashed lines: exact values of α at which AGW-AW-AW resonance occurs computed using formula (6.75). Parameter values: $a = 0.1$, $\theta = \pi/4$, $\zeta = 3\pi/4$, $\xi = \pi/2$, $\gamma = 0$, $\mathrm{Re} = \mathrm{Rm} = \mathrm{Pe} = 10^6$. Resolution: $\mathcal{N} = 40$, $n_\alpha = n_\beta = 100$.

gives $\boldsymbol{k} \cdot \boldsymbol{b}_0 = 0$ and therefore the AGW dispersion relation becomes simply

$$\omega/N = \cos\theta, \tag{6.72}$$

i.e. the primary wave is effectively an IGW. The daughter waves have the following frequencies in this case:

$$\omega_A/N = \boldsymbol{k}_A \cdot \boldsymbol{b}_0 = \alpha b_0, \tag{6.73}$$
$$\omega_B/N = -\boldsymbol{k}_A \cdot \boldsymbol{b}_0 = -\alpha b_0. \tag{6.74}$$

Substitution of (6.72), (6.73) and (6.74) into resonance condition (6.62) yields

$$|\alpha| = \frac{\cos\theta}{2b_0}. \tag{6.75}$$

We can use formula (6.75) to compute the exact value of α at which AGW-AW-AW resonance occurs for a primary wave with $|\zeta - \theta| = \pi/2$. In Figure 6.14 we show excellent agreement in resonant α values between numerical Floquet calculations and calculations using formula (6.75) for a selection of different field strengths. In Section 6.2.3, we discussed how this resonant α value is a critical value above which AGW-AGW-AGW and AGW-AGW-AW resonances do not occur for this set of parameter values. As we increase the value of b_0, the critical value of α decreases. This means that as we increase b_0, the AGW-AW-AW instabilities occur on larger spatial scales. Equation (6.75) implies that for $b_0 \gg 1$, modes of disturbance which are unstable to AGW-AW-AW interactions have spatial scales which are far larger than that of the primary wave.

Exact Formula for Location of AGW-AW-AW Resonances with $\xi = 0$

In the case where $\xi = 0$, the background magnetic field satisfies $\boldsymbol{b}_0 = b_0\hat{\boldsymbol{y}}$, which means $\boldsymbol{k} \cdot \boldsymbol{b}_0 = 0$ and therefore the AGW dispersion relation becomes simply

$$\omega/N = \cos\theta, \tag{6.76}$$

i.e. the primary wave is effectively an IGW. The daughter waves have the following frequencies in this case:

$$\omega_A/N = \boldsymbol{k}_A \cdot \boldsymbol{b}_0 = k_{Ay}\boldsymbol{b}_0 = \beta\boldsymbol{b}_0, \tag{6.77}$$
$$\omega_B/N = -\boldsymbol{k}_A \cdot \boldsymbol{b}_0 = -k_{Ay}\boldsymbol{b}_0 = -\beta\boldsymbol{b}_0. \tag{6.78}$$

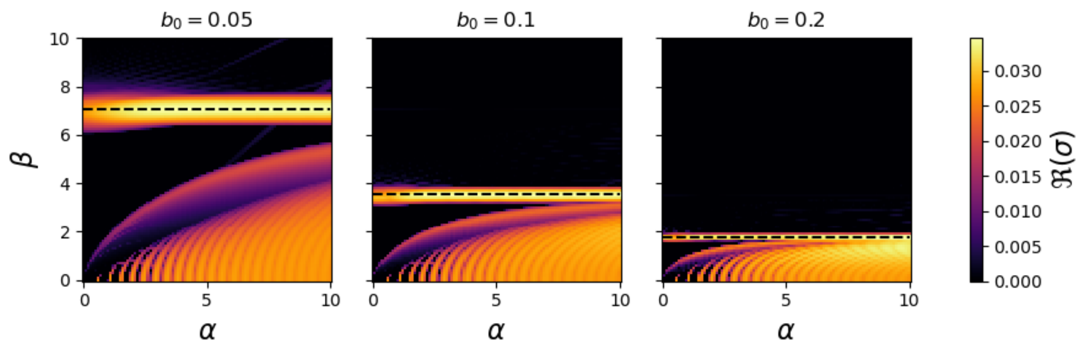

Figure 6.15: Growth rate contours in wavenumber space for instabilities of an AGW in the presence of a background magnetic field lying perpendicular to the phase velocity of the primary wave. Dashed lines: exact values of β at which AGW-AW-AW resonance occurs computed using formula (6.79). Parameter values: $a = 0.1$, $\theta = \pi/4$, $\xi = 0$, $\gamma = 0$, $\mathrm{Re} = \mathrm{Rm} = \mathrm{Pe} = 10^6$. Resolution: $\mathcal{N} = 40$, $n_\alpha = n_\beta = 100$.

Substitution of (6.76), (6.77) and (6.78) into resonance condition (6.62) yields

$$|\beta| = \frac{\cos\theta}{2b_0}. \tag{6.79}$$

We can use formula (6.79) to compute the exact value of β at which AGW-AW-AW resonance occurs for a background magnetic field purely in the $\hat{\boldsymbol{y}}$ direction. Note that formula (6.79) for resonant β values is identical to formula (6.75) for resonant α values. In Figure 6.15 we show excellent agreement in resonant β values between numerical Floquet calculations and calculations using formula (6.75) for a selection of different field strengths. Figure 6.15 and Figure 6.14 are analogous. They both depict the scenario in which $\boldsymbol{b}_0$ lies at right-angles to $\boldsymbol{k}$.

Increasing b_0 reduces the resonant value of β, increasing the spatial scales of AGW-AW-AW disturbances in the y-direction. In Section 6.2.3, we discussed how this resonant β value is a critical value above which AGW-AGW-AGW and AGW-AGW-AW resonances do not occur for this set of parameter values. This critical β is analagous to the critical α which arose in Figure 6.14. Formula (6.79) similarly tells us that in the limit $b_0 \gg 1$, unstable modes of disturbance have much larger spatial scales than that of the primary wave.

6.2.5 Magnetic Field Vector Aligned with Primary Wavevector

Here we focus on the case in which the magnetic field vector $\boldsymbol{b}_0$ is aligned with the primary wavevector $\boldsymbol{k}$. This relationship between the directions of $\boldsymbol{b}_0$ and $\boldsymbol{k}$ gives us the maximum possible value of $\boldsymbol{k} \cdot \boldsymbol{b}_0$ for any given magnitudes k and b_0.

In Figure 6.10, we can see from the $\zeta = \pi/4$ panel that at a field strength of $b_0 = 0.05$, the fact that $\boldsymbol{b}_0$ and $\boldsymbol{k}$ are aligned maximises the proportion of parameter space which is unstable to AGW-AW-AW TRIs. We also find that a significant amount of parameter space is unstable to AGW-AGW-AGW TRIs. However, the instability behaviour becomes very different when we increase the field strength to $b_0 = 0.2$ and beyond.

In Figure 6.16 we contour the growth rate in wavenumber space for a situation in which $\boldsymbol{b}_0$ and $\boldsymbol{k}$ are aligned at background magnetic field strengths in the range $b_0 \in [0.1, 0.4]$. To produce this plot, we define the scale factor $\psi(b_0)$ as

$$\psi(b_0) := \max_{(\alpha,\beta)}[\Re(\sigma)]|_{b_0}. \tag{6.80}$$

To clarify this definition, for any field strength b_0, the scale factor $\psi(b_0)$ is the maximum value of $\Re(\sigma)$ observed in the chosen (α, β) domain at that value of b_0. In each panel of Figure 6.16 we scale the growth rate by ψ calculated at the value of b_0 corresponding to that panel. Rescaling the growth rate improves the visibility of the results when using the same colorbar for each panel. The behaviour at $b_0 = 0.1$ is similar to the behaviour shown in the $b_0 = 0.05$ panel of Figure 6.10. This is not the case for $b_0 \geq 0.2$ in Figure 6.16, though. We observe an unfamiliar class of instability appearing between $\alpha = 0$ and $\alpha = 5$ when the field strength is $b_0 = 0.3$. We also find that instability bands induced by AGW-AGW-AGW TRIs at field strengths of $b_0 = 0.2$ and above are very sparse in this (α, β) domain. This suggests that magnetic fields have a stabilising effect for this combination of parameters. Stronger fields stabilise a number of modes which were unstable for smaller values of b_0. In Section 6.4.1, we compare the numerical growth rates of Figure 6.16 with asymptotic predictions made using the AGW-AGW-AGW growth rate formula 5.82 derived in Chapter 5. Overall, b_0 has a significant influence on growth rates observed when the background magnetic field is aligned with the primary wavevector.

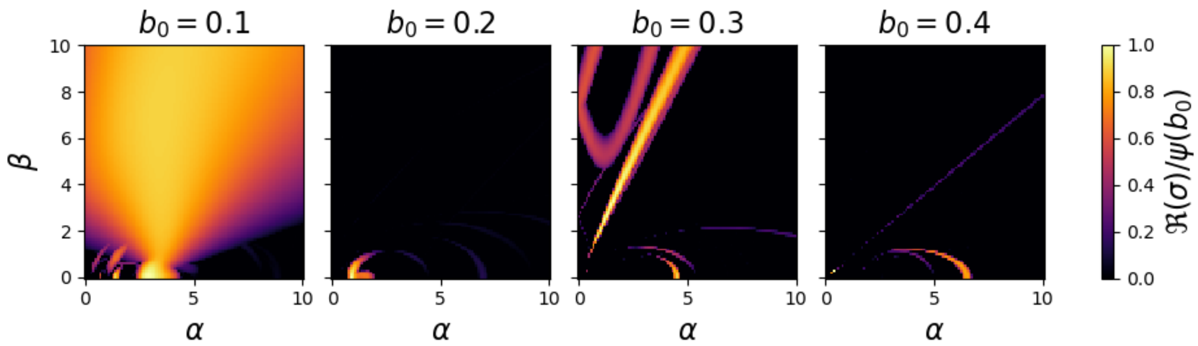

Figure 6.16: Growth rate contours in wavenumber space. The scale factor $\psi(b_0)$ is computed using formula (6.80). Parameter values: $a = 0.1$, $\theta = \pi/4$, $\zeta = \pi/4$, $\xi = \pi/2$, $b_0 = 0.3$, $\gamma = 0$, $\mathrm{Re} = \mathrm{Rm} = \mathrm{Pe} = 10^6$. Resolution: $\mathcal{N} = 20$.

6.3 Energetics

What physical processes drive the instabilities of the finite-amplitude AGWs we observe in this chapter? That is the question we wish to answer in this section.

In Chapter 4 we only had to form evolution equations for two types of energy density: kinetic energy density E_K and potential energy E_P. The kinetic energy evolution equation was derived from the momentum equation and the potential energy evolution equation was derived from the internal energy equation. The introduction of a magnetic induction equation in this chapter gives rise to an additional evolution equation, this time pertaining to magnetic energy density E_M. It also modifies the evolution equation for E_K. The evolution equation for E_M is derived from the induction equation.

6.3.1 Deriving a Formula for the Total Energy Density

Kinetic Energetics

We define the *kinetic energy density* E_K of the disturbance as

$$E_K := |\hat{u}_x|^2 + |\hat{u}_y|^2 + |\hat{u}_z|^2. \tag{6.81}$$

The momentum equation in component form is

$$\hat{u}_z \frac{\mathrm{d}\tilde{u}_x}{\mathrm{d}z} + C\hat{u}_x = \frac{L\hat{u}_x}{\mathrm{Re}} + \left[i\alpha(b_{0x} + \tilde{b}_x) + i\beta b_{0y} + b_{0z}\left(i\gamma + \frac{\mathrm{d}}{\mathrm{d}z}\right)\right]\hat{b}_x + \hat{b}_z \frac{\mathrm{d}\tilde{b}_x}{\mathrm{d}z} - i\alpha\hat{p} + \frac{k_x\hat{\varrho}}{k_z}, \tag{6.82}$$

$$C\hat{u}_y = \frac{L\hat{u}_y}{\mathrm{Re}} + \left[i\alpha(b_{0x} + \tilde{b}_x) + i\beta b_{0y} + b_{0z}\left(i\gamma + \frac{\mathrm{d}}{\mathrm{d}z}\right)\right]\hat{b}_y - i\beta\hat{p}, \tag{6.83}$$

$$C\hat{u}_z = \frac{L\hat{u}_z}{\mathrm{Re}} + \left[i\alpha(b_{0x} + \tilde{b}_x) + i\beta b_{0y} + b_{0z}\left(i\gamma + \frac{\mathrm{d}}{\mathrm{d}z}\right)\right]\hat{b}_z - \left(i\gamma + \frac{\mathrm{d}}{\mathrm{d}z}\right)\hat{p} - \hat{\varrho}. \tag{6.84}$$

We use the identity $z^*z \equiv |z|^2$ and the identity $(z + z^*)/2 \equiv \Re(z)$ for any $z \in \mathbb{C}$ to get an equation for the kinetic energy density E_K. We take $[\hat{u}_x^*(6.82) + (6.82)^*\hat{u}_x]/2$ to get an equation for $|\hat{u}_x|^2$. We take $[\hat{u}_y^*(6.83) + (6.83)^*\hat{u}_y]/2$ to get an equation for $|\hat{u}_y|^2$. We take $[\hat{u}_z^*(6.84) + (6.84)^*\hat{u}_z]/2$ to get an equation for $|\hat{u}_z|^2$. Taking the sum of all three of these gives the kinetic energy density evolution equation we seek. By manipulating the pressure terms using mass continuity, this equation simplifies to

$$\begin{aligned}\left(\sigma_r + \frac{\tilde{u}_z}{2}\frac{\mathrm{d}}{\mathrm{d}z}\right)E_K = \Re\left[-(\hat{u}_x^*\hat{u}_z)\frac{\mathrm{d}\tilde{u}_x}{\mathrm{d}z} - \frac{\mathrm{d}}{\mathrm{d}z}(\hat{p}^*\hat{u}_z) + \frac{\hat{\boldsymbol{u}}^*\cdot L\hat{\boldsymbol{u}}^*}{\mathrm{Re}} + \left(\frac{k_x\hat{u}_x^*}{k_z} - \hat{u}_z^*\right)\hat{\varrho}\right] \\ + \Re\left[(i\alpha b_{0x} + i\beta b_{0y} + i\alpha\tilde{b}_x)(\hat{\boldsymbol{u}}^*\cdot\hat{\boldsymbol{b}}) + b_{0z}\hat{\boldsymbol{u}}^*\cdot\left(i\gamma + \frac{\mathrm{d}}{\mathrm{d}z}\right)\hat{\boldsymbol{b}} + (\hat{u}_x^*\hat{b}_z)\frac{\mathrm{d}\tilde{b}_x}{\mathrm{d}z}\right].\end{aligned} \tag{6.85}$$

The buoyancy flux term $(k_x\hat{u}_x^*/k_z - \hat{u}_z^*)\hat{\varrho}$ which was present in the hydrodynamic evolution equation (4.79) for E_K is also present in (6.85). This term gets eliminated when we form an equation for the total energy density shortly. The same also happens to the term $i\alpha\tilde{b}_x(\hat{\boldsymbol{u}}^*\cdot\hat{\boldsymbol{b}})$, which represents the work done by the magnetic field on the fluid flow. We call this the 'Lorentz force' term.

Magnetic Energetics

We define the *magnetic energy density* E_M of the disturbance as

$$E_M := |\hat{b}_x|^2 + |\hat{b}_y|^2 + |\hat{b}_z|^2. \tag{6.86}$$

To obtain an equation for its evolution, we start with the induction equation in component form:

$$\hat{u}_z \frac{\mathrm{d}\tilde{b}_x}{\mathrm{d}z} + C\hat{b}_x = \frac{L\hat{b}_x}{\mathrm{Rm}} + \left[i\alpha(b_{0x} + \tilde{b}_x) + i\beta b_{0y} + b_{0z}\left(i\gamma + \frac{\mathrm{d}}{\mathrm{d}z}\right)\right]\hat{u}_x + \hat{b}_z\frac{\mathrm{d}\tilde{u}_x}{\mathrm{d}z}, \tag{6.87}$$

$$C\hat{b}_y = \frac{L\hat{b}_y}{\mathrm{Rm}} + \left[i\alpha(b_{0x} + \tilde{b}_x) + i\beta b_{0y} + b_{0z}\left(i\gamma + \frac{\mathrm{d}}{\mathrm{d}z}\right)\right]\hat{u}_y, \tag{6.88}$$

$$C\hat{b}_z = \frac{L\hat{b}_z}{\mathrm{Rm}} + \left[i\alpha(b_{0x} + \tilde{b}_x) + i\beta b_{0y} + b_{0z}\left(i\gamma + \frac{\mathrm{d}}{\mathrm{d}z}\right)\right]\hat{u}_z. \tag{6.89}$$

Taking $[\hat{b}_x^*(6.87) + (6.87)^*\hat{b}_x]/2$ gives

$$\left(\sigma_r + \frac{\tilde{u}_z}{2}\frac{\mathrm{d}}{\mathrm{d}z}\right)|\hat{b}_x|^2 = +\Re\left[\frac{\hat{b}_x^* L\hat{b}_x}{\mathrm{Rm}} - (\hat{b}_x^*\hat{u}_z)\frac{\mathrm{d}\tilde{b}_x}{\mathrm{d}z} + (\hat{b}_x^*\hat{b}_z)\frac{\mathrm{d}\tilde{u}_x}{\mathrm{d}z}\right] + \Re\left[(i\alpha b_{0x} + i\beta b_{0y} + i\alpha\tilde{b}_x)(\hat{b}_x^*\hat{u}_x) + b_{0z}\hat{b}_x^*\left(i\gamma + \frac{\mathrm{d}}{\mathrm{d}z}\right)\hat{u}_x\right]. \quad (6.90)$$

Taking $[\hat{b}_y^*(6.88) + (6.88)^*\hat{b}_y]/2$ gives

$$\left(\sigma_r + \frac{\tilde{u}_z}{2}\frac{\mathrm{d}}{\mathrm{d}z}\right)|\hat{b}_y|^2 = \Re\left[\frac{\hat{b}_y^* L\hat{b}_y}{\mathrm{Rm}} + (i\alpha b_{0x} + i\beta b_{0y} + i\alpha\tilde{b}_x)(\hat{b}_y^*\hat{u}_y) + b_{0z}\hat{b}_y^*\left(i\gamma + \frac{\mathrm{d}}{\mathrm{d}z}\right)\hat{u}_y\right]. \quad (6.91)$$

Taking $[\hat{b}_z^*(6.89) + (6.89)^*\hat{b}_z]/2$ gives

$$\left(\sigma_r + \frac{\tilde{u}_z}{2}\frac{\mathrm{d}}{\mathrm{d}z}\right)|\hat{b}_z|^2 = \Re\left[\frac{\hat{b}_z^* L\hat{b}_z}{\mathrm{Rm}} + (i\alpha b_{0x} + i\beta b_{0y} + i\alpha\tilde{b}_x)(\hat{b}_z^*\hat{u}_z) + b_{0z}\hat{b}_z^*\left(i\gamma + \frac{\mathrm{d}}{\mathrm{d}z}\right)\hat{u}_z\right]. \quad (6.92)$$

Taking the sum of (6.90)-(6.92) produces the desired equation for the evolution of the magnetic energy density.

$$\left(\sigma_r + \frac{\tilde{u}_z}{2}\frac{\mathrm{d}}{\mathrm{d}z}\right)E_M = +\Re\left[\frac{\hat{\boldsymbol{b}}^* \cdot L\hat{\boldsymbol{b}}}{\mathrm{Rm}} - (\hat{b}_x^*\hat{u}_z)\frac{\mathrm{d}\tilde{b}_x}{\mathrm{d}z} + (\hat{b}_x^*\hat{b}_z)\frac{\mathrm{d}\tilde{u}_x}{\mathrm{d}z}\right] + \Re\left[(i\alpha b_{0x} + i\beta b_{0y} + i\alpha\tilde{b}_x)(\hat{\boldsymbol{b}}^* \cdot \hat{\boldsymbol{u}}) + b_{0z}\hat{\boldsymbol{b}}^* \cdot \left(i\gamma + \frac{\mathrm{d}}{\mathrm{d}z}\right)\hat{\boldsymbol{u}}\right]. \quad (6.93)$$

We observe that

$$\Re\left[(i\alpha\tilde{b}_x + i\alpha b_{0x} + i\beta b_{0y} + i\gamma b_{0z})(\hat{\boldsymbol{b}}^* \cdot \hat{\boldsymbol{u}})\right] = \Re\left[-(i\alpha\tilde{b}_x + i\alpha b_{0x} + i\beta b_{0y} + i\gamma b_{0z})(\hat{\boldsymbol{u}}^* \cdot \hat{\boldsymbol{b}})\right]. \quad (6.94)$$

The RHS of (6.94) appears in the evolution equation (6.85) for kinetic energy density and the LHS of (6.94) appears in the evolution equation (6.93) for magnetic energy density, so when adding the two equations together (along with the equation for the evolution of potential energy density) to get an evolution equation for the total energy density, we get a cancellation. We also observe that

$$\Re\left(b_{0z}\hat{\boldsymbol{b}}^* \cdot \frac{\mathrm{d}\hat{\boldsymbol{u}}}{\mathrm{d}z}\right) = \Re\left(b_{0z}\hat{\boldsymbol{b}} \cdot \frac{\mathrm{d}\hat{\boldsymbol{u}}^*}{\mathrm{d}z}\right),$$

where the LHS comes from (6.93). When combining this with a term from (6.85), we get

$$b_{0z}\Re\left(\hat{\boldsymbol{b}} \cdot \frac{\mathrm{d}\hat{\boldsymbol{u}}^*}{\mathrm{d}z} + \hat{\boldsymbol{u}}^* \cdot \frac{\mathrm{d}\hat{\boldsymbol{b}}}{\mathrm{d}z}\right) = b_{0z}\Re\left[\frac{\mathrm{d}}{\mathrm{d}z}(\hat{\boldsymbol{u}}^* \cdot \hat{\boldsymbol{b}})\right].$$

We have encountered another conservative term which was not present in the hydrodynamic setting.

Potential Energetics

We define the *potential energy density* E_P of the disturbance as

$$E_P \coloneqq (k^2/k_z^2)|\hat{\varrho}|^2. \tag{6.95}$$

Our evolution equation for E_P remains the same as it did in Chapter 4:

$$\left(\sigma_r + \frac{\tilde{u}_z}{2}\frac{\mathrm{d}}{\mathrm{d}z}\right) E_P = \Re\left[-(\hat{u}_z^*\hat{\varrho})\frac{\mathrm{d}\tilde{\varrho}}{\mathrm{d}z}\frac{k^2}{k_z^2} + \frac{\hat{\varrho}^* L\hat{\varrho}}{\mathrm{Pe}}\frac{k^2}{k_z^2} + \left(\hat{u}_z^* - \frac{k\hat{u}_x^*}{k_z}\right)\hat{\varrho}\right]. \tag{6.96}$$

Combined Energetics

Now that we have a magnetic field in the system, we define the *total energy density* as

$$E \coloneqq E_K + E_M + E_P. \tag{6.97}$$

We can combine the evolution equations (6.85), (6.93) and (6.96) for the kinetic, magnetic and potential energy densities E_K, E_M and E_P to get an evolution equation for the total energy density E.

$$\begin{aligned}\left(\sigma_r + \frac{\tilde{u}_z}{2}\frac{\mathrm{d}}{\mathrm{d}z}\right) E = \Re&\left[\frac{\hat{\boldsymbol{u}}^* \cdot L\hat{\boldsymbol{u}}^*}{\mathrm{Re}} + \frac{\hat{\boldsymbol{b}}_x^* \cdot L\hat{\boldsymbol{b}}_x}{\mathrm{Rm}} + \frac{\hat{\varrho}^* L\hat{\varrho}}{\mathrm{Pe}}\frac{k^2}{k_z^2} - \frac{\mathrm{d}}{\mathrm{d}z}\left(\hat{p}^*\hat{u}_z\right) + b_{0z}\frac{\mathrm{d}}{\mathrm{d}z}(\hat{\boldsymbol{u}}^* \cdot \hat{\boldsymbol{b}})\right] \\ &+ \Re\left[\left(\hat{b}_x^*\hat{b}_z - \hat{u}_x^*\hat{u}_z\right)\frac{\mathrm{d}\tilde{u}_x}{\mathrm{d}z} + \left(\hat{u}_x^*\hat{b}_z - \hat{b}_x^*\hat{u}_z\right)\frac{\mathrm{d}\tilde{b}_x}{\mathrm{d}z} - (\hat{u}_z^*\hat{\varrho})\frac{\mathrm{d}\tilde{\varrho}}{\mathrm{d}z}\frac{k^2}{k_z^2}\right].\end{aligned} \tag{6.98}$$

When adding the kinetic, magnetic and potential energy density equations together, the buoyancy flux terms and the ‘Lorentz force’ terms from each cancel each other out. This is consistent with the idea that the buoyancy flux term represents conversion between kinetic and potential energy in either direction, and that the Lorentz force term represents conversion between kinetic and magnetic energy in either direction. Upon integration over one period of the primary wave, three of these terms vanish due to the 2π-periodicity of $\hat{f}$ variables. These are conservative terms. We are left with

$$\begin{aligned}\sigma_r \int_0^{2\pi} E\mathrm{d}z = &\int_0^{2\pi} \Re\left[\frac{\hat{\boldsymbol{u}}^* \cdot L\hat{\boldsymbol{u}}^*}{\mathrm{Re}} + \frac{\hat{\boldsymbol{b}}_x^* \cdot L\hat{\boldsymbol{b}}_x}{\mathrm{Rm}} + \frac{\hat{\varrho}^* L\hat{\varrho}}{\mathrm{Pe}}\frac{k^2}{k_z^2}\right]\mathrm{d}z \\ &+ \int_0^{2\pi} \Re\left[\left(\hat{b}_x^*\hat{b}_z - \hat{u}^*\hat{u}_z\right)\frac{\mathrm{d}\tilde{u}_x}{\mathrm{d}z} + \left(\hat{u}^*\hat{b}_z - \hat{b}_x^*\hat{u}_z\right)\frac{\mathrm{d}\tilde{b}_x}{\mathrm{d}z} - (\hat{u}_z^*\hat{\varrho})\frac{\mathrm{d}\tilde{\varrho}}{\mathrm{d}z}\frac{k^2}{k_z^2}\right]\mathrm{d}z.\end{aligned}$$

We arrive at a formula for σ_r:

$$\sigma_r = \mathcal{E}_K + \mathcal{E}_M + \mathcal{E}_P + \mathcal{D}_\nu + \mathcal{D}_\eta + \mathcal{D}_\kappa, \tag{6.99}$$

Equation (6.99) is the MHD equivalent of equation (4.83) for σ_r in the absence of a magnetic field. By introducing the magnetic field, we have introduced two new quantities which can contribute to σ_r: $\mathcal{E}_M$ and $\mathcal{D}_\eta$.

We can compare the value for σ_r that (6.99) produces with the value of σ_r found by the numerical Floquet solver. This formula for σ_r contains six terms, three of which can potentially drive the instabilities we study.

We define the contribution of *shear production* to the growth rate ($\mathcal{E}_K$) as:

$$\mathcal{E}_K := -\frac{1}{I_E}\int_0^{2\pi} \Re\left[\left(\hat{b}_x^*\hat{b}_z - \hat{u}_x^*\hat{u}_z\right)\frac{\mathrm{d}\tilde{u}_x}{\mathrm{d}z}\right]\mathrm{d}z.$$

We define the contribution of *buoyancy production* to the growth rate ($\mathcal{E}_P$) as:

$$\mathcal{E}_P := -\frac{k^2}{k_z^2 I_E}\int_0^{2\pi} \Re\left[\left(\hat{u}_z^*\hat{\varrho}\right)\frac{\mathrm{d}\tilde{\varrho}}{\mathrm{d}z}\right]\mathrm{d}z.$$

We define the contribution of *primary wave electric current* to the growth rate ($\mathcal{E}_M$) as:

$$\mathcal{E}_M := \frac{1}{I_E}\int_0^{2\pi} \Re\left[\left(\hat{u}_x^*\hat{b}_z - \hat{b}_x^*\hat{u}_z\right)\frac{\mathrm{d}\tilde{b}_x}{\mathrm{d}z}\right]\mathrm{d}z.$$

where I_E is the integral of the total energy density:

$$I_E := \int_0^{2\pi} E\mathrm{d}z = 2\pi\sum_{n=-\infty}^{\infty}\left(|u_n^x|^2 + |u_n^y|^2 + |u_n^z|^2 + |b_n^x|^2 + |b_n^y|^2 + |b_n^z|^2 + (k^2/k_z^2)|\varrho_n|^2\right).$$

In this configuration, the shear production comprises the product of the *Reynolds stress* $\mathcal{S}_R$ with the shear $\partial_z\tilde{u}_x$ and the product of the *Maxwell stress* $\mathcal{S}_M$ with the shear $\partial_z\tilde{u}_x$, where

$$\mathcal{S}_R := \hat{u}_x^*\hat{u}_z, \quad \mathcal{S}_M := \hat{b}_x^*\hat{b}_z.$$

Importantly, the growth rate σ_r is predominantly the combination of the shear production term $\mathcal{E}_K$, the buoyancy production term $\mathcal{E}_P$ and $\mathcal{E}_M$. The terms $\mathcal{E}_K$, $\mathcal{E}_M$ and $\mathcal{E}_P$ can only drive instability if they each have a positive non-zero value, and if their sum is positive.

The terms $\mathcal{D}_\nu$, $\mathcal{D}_\eta$ and $\mathcal{D}_\kappa$ represent any energy losses due to viscous, Ohmic and thermal dissipation. Such energy losses reduce the growth rate. At the value of Re, Rm and Pe we consider throughout most of this (10^6), the magnitudes of $\mathcal{D}_\nu$, $\mathcal{D}_\eta$ and $\mathcal{D}_\kappa$ are typically expected to be negligible in comparison to that of $\mathcal{E}_K$, $\mathcal{E}_M$ and $\mathcal{E}_P$. The dissipation terms are defined as

$$\mathcal{D}_\nu := \frac{1}{I_E}\int_0^{2\pi}\frac{\hat{\boldsymbol{u}}_x^*\cdot L\hat{\boldsymbol{u}}_x}{\mathrm{Re}}\mathrm{d}z,$$
$$\mathcal{D}_\eta := \frac{1}{I_E}\int_0^{2\pi}\frac{\hat{\boldsymbol{b}}_x^*\cdot L\hat{\boldsymbol{b}}_x}{\mathrm{Rm}}\mathrm{d}z,$$
$$\mathcal{D}_\kappa := \frac{1}{I_E}\int_0^{2\pi}\frac{k^2}{k_z^2}\frac{\hat{\varrho}^* L\hat{\varrho}}{\mathrm{Pe}}\mathrm{d}z.$$

These can be computed exactly from the numerical eigenfunctions f_n via the formulae

$$\mathcal{D}_\nu = \frac{2\pi}{I_E} \sum_{n=-\infty}^{\infty} L_n \left(\frac{|u_n^x|^2 + |u_n^y|^2 + |u_n^z|^2}{\mathrm{Re}} \right), \tag{6.100}$$

$$\mathcal{D}_\eta = \frac{2\pi}{I_E} \sum_{n=-\infty}^{\infty} L_n \left(\frac{|b_n^x|^2 + |b_n^y|^2 + |b_n^z|^2}{\mathrm{Rm}} \right), \tag{6.101}$$

$$\mathcal{D}_\kappa = \frac{2\pi}{I_E} \sum_{n=-\infty}^{\infty} \frac{k^2}{k_z^2} L_n \left(\frac{|\varrho_n|^2}{\mathrm{Pe}} \right). \tag{6.102}$$

Types of Energy Transfer

We can further separate the different contributions to the growth rate into:

$$\mathcal{E}_1 := \frac{1}{I_E} \int_0^{2\pi} \Re \left[-\left(\hat{u}_x^* \hat{u}_z \right) \frac{\mathrm{d}\tilde{u}_x}{\mathrm{d}z} \right] \mathrm{d}z, \tag{6.103}$$

$$\mathcal{E}_2 := \frac{1}{I_E} \int_0^{2\pi} \Re \left[\left(\hat{b}_x^* \hat{b}_z \right) \frac{\mathrm{d}\tilde{u}_x}{\mathrm{d}z} \right] \mathrm{d}z, \tag{6.104}$$

$$\mathcal{E}_3 := -\frac{k^2}{k_z^2 I_E} \int_0^{2\pi} \Re \left[\left(\hat{u}_z^* \hat{\varrho} \right) \frac{\mathrm{d}\tilde{\varrho}}{\mathrm{d}z} \right] \mathrm{d}z, \tag{6.105}$$

$$\mathcal{E}_4 := \frac{1}{I_E} \int_0^{2\pi} \Re \left[\left(\hat{u}_x^* \hat{b}_z \right) \frac{\mathrm{d}\tilde{b}_x}{\mathrm{d}z} \right] \mathrm{d}z, \tag{6.106}$$

$$\mathcal{E}_5 := \frac{1}{I_E} \int_0^{2\pi} \Re \left[-\left(\hat{b}_x^* \hat{u}_z \right) \frac{\mathrm{d}\tilde{b}_x}{\mathrm{d}z} \right] \mathrm{d}z. \tag{6.107}$$

We summarise the types of energy transfer associated with each production term in Table 6.4. Each of the five terms represents the transfer of energy between the primary wave and the disturbance in both directions. All that differs between the transfers is whether conversion of the energy type takes place, or whether the energy type remains the same. For instance, $\mathcal{E}_2$ is associated with conversion of primary wave kinetic energy into disturbance magnetic energy and vice versa. However $\mathcal{E}_5$ is associated with the transfer of magnetic energy between the primary wave and the disturbance. The various energy transfer directions and accompanying physical processes are illustrated in Figure 6.17. Here, the 'Lorentz force' label represents the work done by the magnetic field on the fluid flow.

Term	Identity	Source equation	Primary wave energy type	Disturbance energy type
(1)	$\hat{u}_x^* \hat{u}_z \partial_z \tilde{u}_x$	Momentum	Kinetic	Kinetic
(2)	$\hat{b}_x^* \hat{b}_z \partial_z \tilde{u}_x$	Induction	Kinetic	Magnetic
(3)	$\hat{u}_z^* \hat{\varrho} \partial_z \tilde{\varrho}$	Thermodynamic	Potential	Potential
(4)	$\hat{u}_x^* \hat{b}_z \partial_z \tilde{b}_x$	Momentum	Magnetic	Kinetic
(5)	$\hat{b}_x^* \hat{u}_z \partial_z \tilde{b}_x$	Induction	Magnetic	Magnetic

Table 6.4: Energy transfer routes associated with each production term.

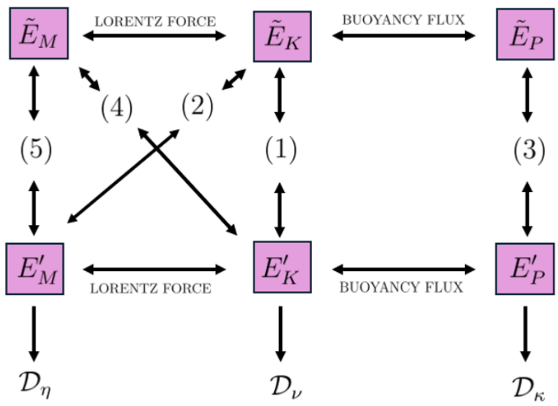

Figure 6.17: Schematic depicting processes of energy transfer in the MHD system. $\tilde{E}_M$, $\tilde{E}_K$ and $\tilde{E}_P$ denote the primary wave energy densities of the magnetic, kinetic and potential varieties respectively. E'_M, E'_K and E'_P represent the corresponding energy densities associated with the disturbance.

Implementation

We wish to calculate the values of $\mathcal{E}_1 - \mathcal{E}_5$ given by (6.103)-(6.107) corresponding to the fastest growing mode at each point on the (α, β) grid. At each grid point, we have a complex eigenvalue σ with maximal real part σ_r. Associated with this eigenvalue σ are 7 eigenvectors of length $2\mathcal{N} + 1$:

$$\begin{aligned}
\boldsymbol{v}_1 &= (u^x_{-\mathcal{N}}, \dots, u^x_0, \dots, u^x_{\mathcal{N}}),\\
\boldsymbol{v}_2 &= (u^y_{-\mathcal{N}}, \dots, u^y_0, \dots, u^y_{\mathcal{N}}),\\
\boldsymbol{v}_3 &= (u^z_{-\mathcal{N}}, \dots, u^z_0, \dots, u^z_{\mathcal{N}}),\\
\boldsymbol{v}_4 &= (b^x_{-\mathcal{N}}, \dots, b^x_0, \dots, b^x_{\mathcal{N}}),\\
\boldsymbol{v}_5 &= (b^y_{-\mathcal{N}}, \dots, b^y_0, \dots, b^y_{\mathcal{N}}),\\
\boldsymbol{v}_6 &= (b^z_{-\mathcal{N}}, \dots, u^z_0, \dots, b^z_{\mathcal{N}}),\\
\boldsymbol{v}_7 &= (\varrho^z_{-\mathcal{N}}, \dots, \varrho^z_0, \dots, \varrho^z_{\mathcal{N}}).
\end{aligned} \tag{6.108}$$

We calculate the integrals from each of $\mathcal{E}_K$, $\mathcal{E}_M$ and $\mathcal{E}_P$ using the trapezoidal rule. To do so, we define functions representing the integrand in each case:

$$\begin{aligned}
F_K(z) &= \Re[\hat{b}^*_x(z)\hat{b}_z(z) - \hat{u}^*_x(z)\hat{u}_z(z)]\partial_z\tilde{u}_x(z),\\
F_M(z) &= \Re[\hat{u}^*_x(z)\hat{b}_z(z) - \hat{b}^*_x(z)\hat{u}_z(z)]\partial_z\tilde{b}_x(z),\\
F_P(z) &= \Re[\hat{u}^*_z(z)\hat{\varrho}(z)]\partial_z\tilde{\varrho}(z).
\end{aligned}$$

We can calculate the individual functions $\hat{f}(z)$ within via (6.58). Fourier coefficients f_n are extracted from eigenvector components within $\boldsymbol{v}_1$-$\boldsymbol{v}_7$ from (6.108). We can thus calculate $\mathcal{E}_K$, $\mathcal{E}_M$ and $\mathcal{E}_P$ numerically on a discretised domain $z \in [0, 2\pi)$ via

$$\begin{aligned}
\mathcal{E}_K &= 1/I_E \textstyle\int_0^{2\pi} F_K(z)\mathrm{d}z,\\
\mathcal{E}_M &= 1/I_E \textstyle\int_0^{2\pi} F_M(z)\mathrm{d}z,\\
\mathcal{E}_P &= -k^2/(k_z^2 I_E) \textstyle\int_0^{2\pi} F_P(z)\mathrm{d}z,
\end{aligned}$$

where I_E is computed via

$$I_E = 2\pi \textstyle\sum_{n=-\mathcal{N}}^{\mathcal{N}}(|u^x_n|^2 + |u^y_n|^2 + |u^z_n|^2 + |b^x_n|^2 + |b^y_n|^2 + |b^z_n|^2 + k^2/k_z^2|\varrho_n|^2).$$

α	$\mathcal{E}_K$	$\mathcal{E}_M$	$\mathcal{E}_P$	σ_r	$\Re(\sigma)$
0.60854561	0.01215413	1.37174195e-06	0.01371742	0.02586957	0.02586957
1.08768148	0.01286912	1.43026246e-06	0.01430262	0.02716500	0.02716501
1.55082784	0.01303596	1.44847819e-06	0.01448478	0.02750682	0.02750683
2.00873507	0.01311273	1.45536759e-06	0.01455368	0.02764288	0.02764290
2.46427470	0.01315998	1.45820411e-06	0.01458204	0.02770649	0.02770650
2.91854292	0.01319521	1.45908425e-06	0.01459084	0.02773610	0.02773620
3.37204945	0.0132248	1.45877644e-06	0.01458776	0.02774580	0.02774587
3.82506357	0.01325112	1.45757193e-06	0.01457572	0.02774085	0.02774089

Table 6.5: Values of energetic quantities calculated at values of α satisfying exact triadic resonance. σ_r values are computed via (6.99). $\Re(\sigma)$ values are computed via the numerical Floquet solver (6.59). Parameter values: $a = 0.1$, $\theta = \pi/4$, $\zeta = 0$, $\xi = \pi/2$, $b_0 = 0.01$, $\beta = 0$, $\gamma = 0$, $\mathrm{Re} = \mathrm{Rm} = \mathrm{Pe} = 10^6$. Resolution: $\mathcal{N} = 20$, $n_\alpha = n_\beta = 100$.

Energy Balance

Here, we check that the numerical growth rates computed by solving (6.59) match up to those computed using formula (6.99) for σ_r. On top of approximating $\mathcal{E}_K$, $\mathcal{E}_M$ and $\mathcal{E}_P$ via the trapezoidal rule, such a check requires the computation of values for $\mathcal{D}_\nu$, $\mathcal{D}_\eta$ and $\mathcal{D}_\kappa$. This is achieved through formulae (6.100), (6.101) and (6.102). At each point in parameter space we check, we compute the values of $\mathcal{E}_K$, $\mathcal{E}_M$, $\mathcal{E}_P$, $\mathcal{D}_\nu$, $\mathcal{D}_\eta$ and $\mathcal{D}_\kappa$ using the functions $\hat{f}(z)$ corresponding to the eigenvalue σ with maximum real part found by solving (6.59) at that point.

In particular, we check that the following is satisfied to a suitable degree of accuracy:

$$\sigma_r = \Re(\sigma), \tag{6.109}$$

where σ_r is given by formula (6.99) and σ is the eigenvalue with the maximum real part of the eigenvalue problem (6.59) constituting the numerical Floquet solver. In Tables 6.5 and 6.6 we present values detailing the degree of accuracy to which the relationship (6.109) is preserved by the implementation for field strengths of $b_0 = 0.01$ and $b_0 = 1$ respectively. We do this by fixing $\beta = 0$ and calculating the relevant quantities at each α value which exactly satisfies the triadic resonance criterion (6.61). Tables 6.5 and 6.6 confirm that energetic balance is sufficiently satisfied by the implementation.

It is surprising that for each value of α considered, the values of $\mathcal{E}_M$ and $\mathcal{E}_P$ are identical in Table 6.6. This implies that at a field strength of $b_0 = 1$, the disturbances associated with instabilities of AGWs have magnetic and potential energies which are exactly equipartitioned. It is also surprising that for each value of α considered, the values of $\mathcal{E}_M$ and $\mathcal{E}_P$ always differ by a factor of 10^4.

α	$\mathcal{E}_K$	$\mathcal{E}_M$	$\mathcal{E}_P$	σ_r	$\Re(\sigma)$
0.86659311	0.02461027	0.00599704	0.00599704	0.03659997	0.03659999
1.82220387	0.03090588	0.00443727	0.00443727	0.03976876	0.03976879
2.80804249	0.03297327	0.00338087	0.00338087	0.03971201	0.03971219
3.80204804	0.03386448	0.00269954	0.00269954	0.03922518	0.03922527
4.79899905	0.03431633	0.00223744	0.00223744	0.03873339	0.03873859
5.79724780	0.03457611	0.00190705	0.00190705	0.03830892	0.03831747
6.79615239	0.03474158	0.00166035	0.00166035	0.03795347	0.03796100
7.79542278	0.03484934	0.00146933	0.00146933	0.03764762	0.03765721

Table 6.6: Values of energetic quantities calculated at values of α satisfying exact triadic resonance. σ_r values are computed via (6.99). $\Re(\sigma)$ values are computed via the numerical Floquet solver (6.59). Parameter values: $a = 0.1$, $\theta = \pi/4$, $\zeta = 0$, $\xi = \pi/2$, $b_0 = 1$, $\beta = 0$, $\gamma = 0$, $\mathrm{Re} = \mathrm{Rm} = \mathrm{Pe} = 10^6$. Resolution: $\mathcal{N} = 20$, $n_\alpha = n_\beta = 100$.

6.3.2 Influence of Parameters

In Section 6.3.2, we plot energetic quantities on the (α, β)-plane to determine how b_0 and ζ influence what physical processes are driving the instabilities of AGWs energetically. In each case, we wish to determine which of the source terms $\mathcal{E}_1$-$\mathcal{E}_5$ are dominant (if any).

Influence of Magnetic Field Strength

What changes about the way the instabilities are driven physically as we vary the magnetic field strength b_0? In Figures 6.18- 6.25, we compare the values of each of the production terms $\mathcal{E}_1$-$\mathcal{E}_5$ at different background magnetic field strengths b_0.

In Figure 6.18 we plot energetic quantities at $b_0 = 0.01$. Here, we expect the dominant source terms to be $\mathcal{E}_1$ and $\mathcal{E}_3$ because these terms are not influenced by the magnetic field, which is weak. Indeed, we find that the energetics are effectively hydrodynamic. The source terms $\mathcal{E}_2$, $\mathcal{E}_4$ and $\mathcal{E}_5$ make no visible contribution to the growth rate at a low field strength of $b_0 = 0.01$. For the instability bands induced by AGW-AGW-AW interactions, neither of $\mathcal{E}_1$ nor $\mathcal{E}_3$ is obviously the dominant source term. For the instability bands induced by AGW-AGW-AGW interactions, the energetics follow the same trends that they did for IGW-IGW-IGW interactions in Figure 4.23, computed in the absence of a magnetic field.

Figure 6.20 emphasises just how little of a contribution the electric current terms $\mathcal{E}_4$ and $\mathcal{E}_5$ make to the growth rate, even at a slightly higher magnetic field strength of $b_0 = 0.1$. Here, the dominant source terms are still $\mathcal{E}_1$ and $\mathcal{E}_3$. At $b_0 = 1$, however, in Figure 6.23, the electric current terms start to make a significant contribution. From Table 6.6 we know that $\mathcal{E}_M$ and $\mathcal{E}_P$ become of equal size at a field strength of $b_0 = 1$ for this set of parameter values.

Figure 6.24 highlights a case in which the magnetic current contributions $\mathcal{E}_4$ and $\mathcal{E}_5$ are similar in magnitude but opposite in sign, resulting in a slow-growing instability. In this figure, the magnetic field strength chosen is $b_0 = 10$, which is much larger than values of b_0 chosen for all other figures in this chapter. The growth rates in Figure 6.24 are substantially smaller than those observed at lower field strengths in this chapter. This could imply that strong background magnetic fields have a stabilising effect on instabilities of AGWs in Boussinesq fluids. We saw an example of another situation in which strong magnetic fields have a stabilising effect on AGW instabilities in Figure 6.16. This was the case in which $\boldsymbol{B}_0$ and $\boldsymbol{K}$ are parallel. We have found two separate sources of evidence for the idea that strong background magnetic fields have a stabilising effect on instabilities of AGWs in Boussinesq fluids.

In Figure 6.25 we demonstrate how the energetics vary when increasing b_0 incrementally from $b_0 = 0.1$ to $b_0 = 0.4$. The bands induced by AGW-AW-AW interactions which point vertically downwards in the β-direction are entirely driven by shear production, in equal parts by the Reynolds stress and Maxwell stress. In keeping with this idea, we also find that the Reynolds stress $\mathcal{E}_1$ and the Maxwell stress $\mathcal{E}_2$ make approximately equal contributions to the growth rate for the instabilities corresponding to AGW-AW-AW interactions in Figure 6.25. $\mathcal{E}_4$ and $\mathcal{E}_5$ have been excluded from Figure 6.25 because they make no contribution to the growth rate for any of the magnetic field strengths in this range.

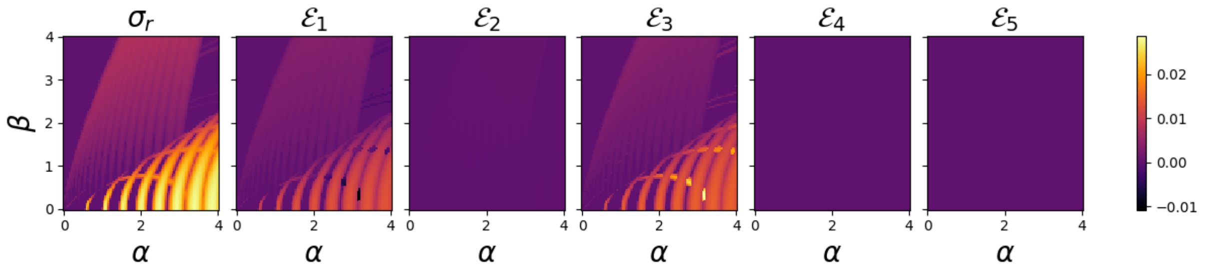

Figure 6.18: Production values alongside growth rate σ_r for a range of α and β values. Parameter values: $a = 0.1$, $\theta = \pi/4$, $\zeta = 0$, $\xi = \pi/2$, $b_0 = 0.01$, $\gamma = 0$, $\mathrm{Re} = \mathrm{Rm} = \mathrm{Pe} = 10^6$. Resolution: $\mathcal{N} = 20$, $n_\alpha = n_\beta = 100$.

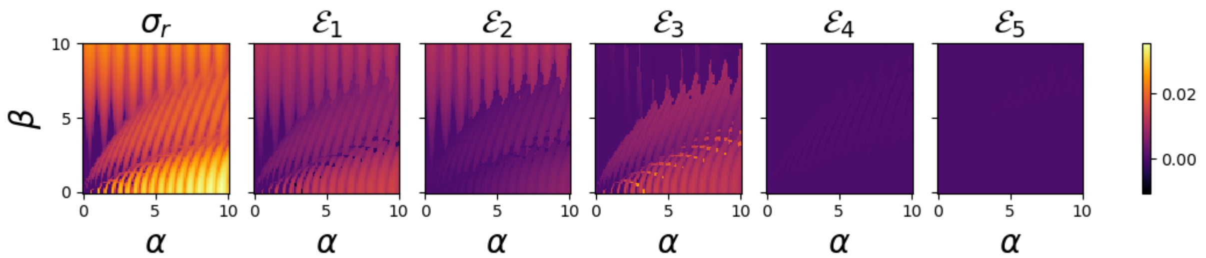

Figure 6.19: Production values alongside growth rate σ_r for a range of α and β values. Parameter values: $a = 0.1$, $\theta = \pi/4$, $\zeta = 0$, $\xi = \pi/2$, $b_0 = 0.05$, $\gamma = 0$, $\mathrm{Re} = \mathrm{Rm} = \mathrm{Pe} = 10^6$. Resolution: $\mathcal{N} = 40$, $n_\alpha = n_\beta = 100$.

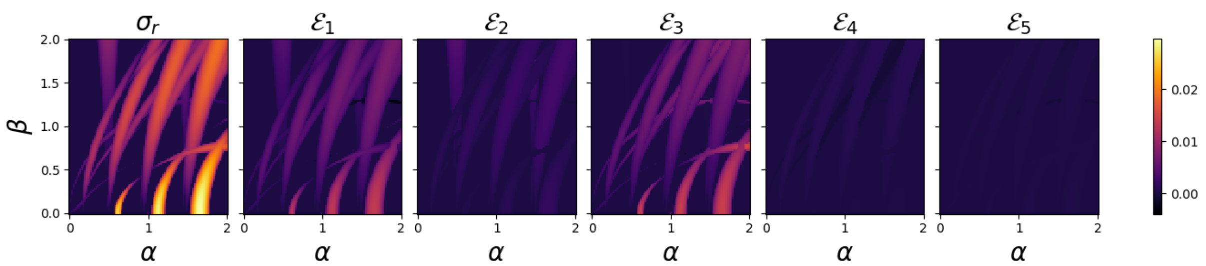

Figure 6.20: Production values alongside growth rate σ_r for a range of α and β values. Parameter values: $a = 0.1$, $\theta = \pi/4$, $\zeta = 0$, $\xi = \pi/2$, $b_0 = 0.1$, $\gamma = 0$, $\mathrm{Re} = \mathrm{Rm} = \mathrm{Pe} = 10^6$. Resolution: $\mathcal{N} = 10$, $n_\alpha = n_\beta = 100$.

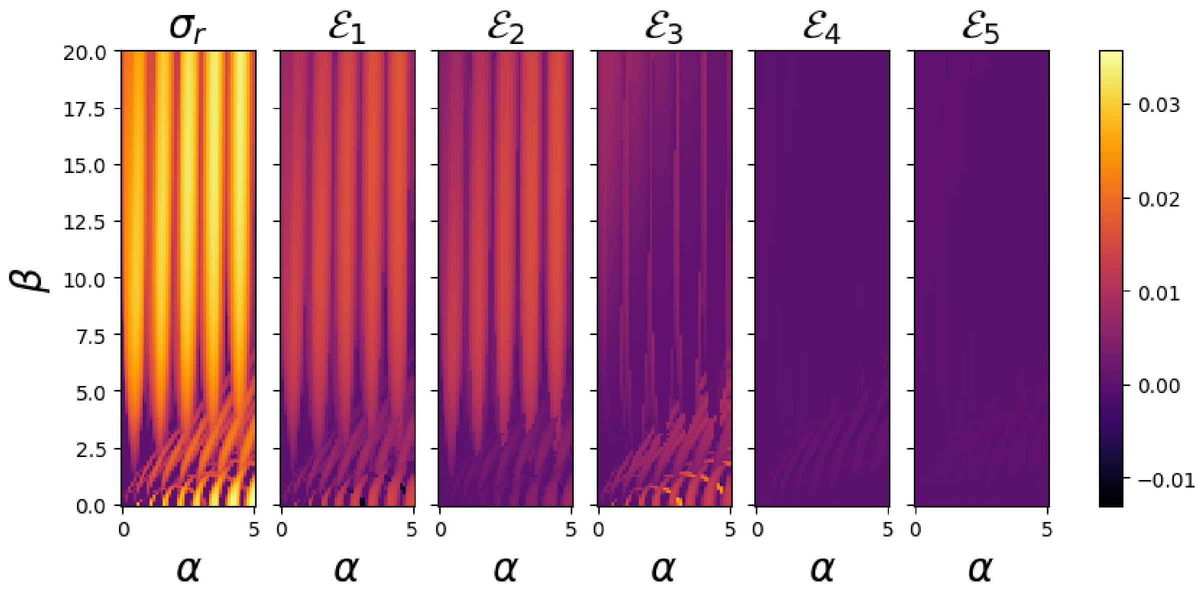

Figure 6.21: Production values alongside growth rate σ_r for a range of α and β values. Parameter values: $a = 0.1$, $\theta = \pi/4$, $\zeta = 0$, $\xi = \pi/2$, $b_0 = 0.1$, $\gamma = 0$, $\mathrm{Re} = \mathrm{Rm} = \mathrm{Pe} = 10^6$. Resolution: $\mathcal{N} = 30$, $n_\alpha = 50, n_\beta = 200$.

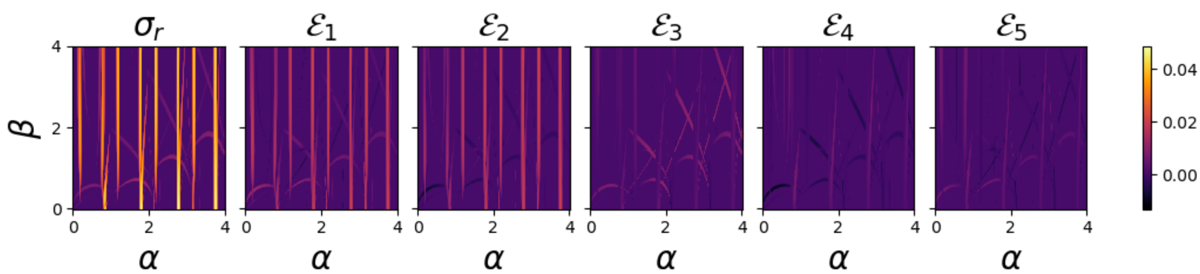

Figure 6.22: Production values alongside growth rate σ_r for a range of α and β values. Parameter values: $a = 0.1$, $\theta = \pi/4$, $\zeta = 0$, $\xi = \pi/2$, $b_0 = 1$, $\gamma = 0$, $\mathrm{Re} = \mathrm{Rm} = \mathrm{Pe} = 10^6$. Resolution: $\mathcal{N} = 20$, $n_\alpha = n_\beta = 500$.

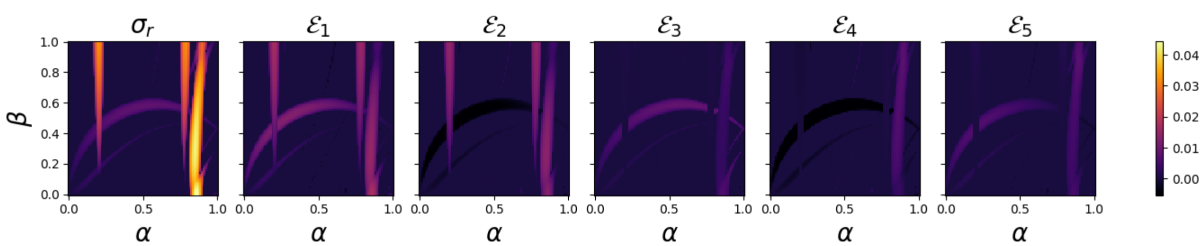

Figure 6.23: Production values alongside growth rate σ_r for a range of α and β values. Parameter values: $a = 0.1$, $\theta = \pi/4$, $\zeta = 0$, $\xi = \pi/2$, $b_0 = 1$, $\gamma = 0$, $\mathrm{Re} = \mathrm{Rm} = \mathrm{Pe} = 10^6$. Resolution: $\mathcal{N} = 20$, $n_\alpha = n_\beta = 100$.

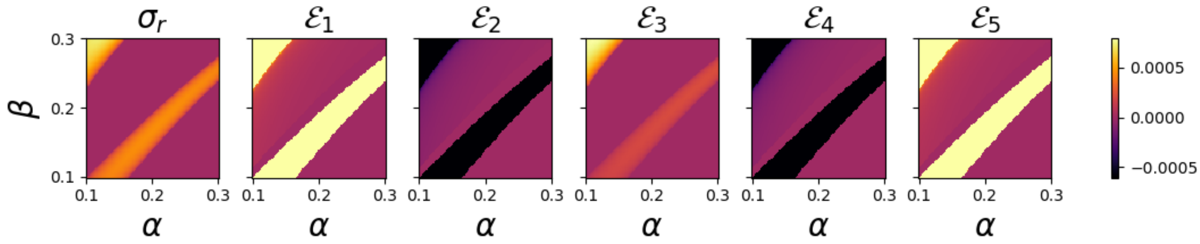

Figure 6.24: Production values alongside growth rate σ_r for a range of α and β values. Parameter values: $a = 0.1$, $\theta = \pi/4$, $\zeta = 0$, $\xi = \pi/2$, $b_0 = 10$, $\gamma = 0$, $\mathrm{Re} = \mathrm{Rm} = \mathrm{Pe} = 10^6$. Resolution: $\mathcal{N} = 10$, $n_\alpha = 100, n_\beta = 100$.

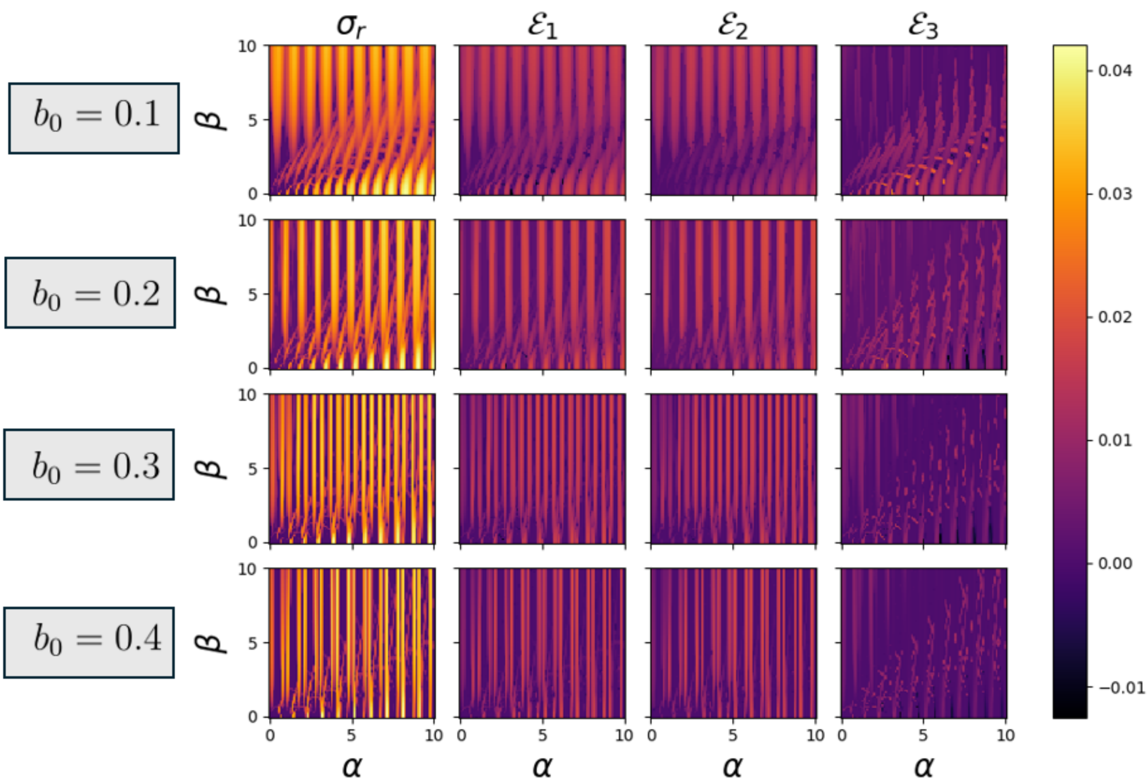

Figure 6.25: Production values alongside growth rate σ_r as a function of disturbance wavenumbers α and β for a range of magnetic field strengths b_0. Parameter values: $a = 0.1$, $\theta = \pi/4$, $\zeta = 0$, $\xi = \pi/2$, $\gamma = 0$, $\mathrm{Re} = \mathrm{Rm} = \mathrm{Pe} = 10^6$. Resolution: $\mathcal{N} = 40$, $n_\alpha = n_\beta = 100$.

Influence of Magnetic Field Orientation

So far we have only viewed instabilities at a magnetic field orientation of $\zeta = 0$. Here, we view what changes about the instabilities when varying ζ. In Figures 6.26 and 6.27 we plot energetic quantities for AGW instabilities at a selection of different ζ values. We omit the $\mathcal{E}_4$ and $\mathcal{E}_5$ panels because $\mathcal{E}_4$ and $\mathcal{E}_5$ make no visible contribution to the growth rate σ_r for this set of parameters. Like in previous figures within this section, we continue to observe an equal contribution of the Reynolds stress $\mathcal{E}_1$ and the Maxwell stress $\mathcal{E}_2$ to the AGW-AW-AW TRIs at all values of ζ we consider.

At $\zeta = 0$, $\mathcal{E}_3$ makes only a small contribution to σ_r for AGW-AW-AW interactions. For AGW-AGW-AW interactions, $\mathcal{E}_1$ and $\mathcal{E}_3$ are the dominant source terms. For AGW-AGW-AGW interactions, $\mathcal{E}_2$ makes a small contribution to σ_r, albeit much smaller than that of $\mathcal{E}_1$ or $\mathcal{E}_3$. The angle $\zeta = 0$ corresponds to a magnetic field vector which lies perpendicular to the direction of gravity. This might explain why $\mathcal{E}_2$ has such a minimal contribution to the AGW-AGW-AGW growth rates.

At $\zeta = \pi/8$, $\zeta = \pi/4$ and $\zeta = 5\pi/8$, the source term $\mathcal{E}_3$ makes a very small contribution to σ_r in the case of AGW-AW-AW interactions. At $\zeta = 3\pi/8$, $\zeta = \pi/2$ and $\zeta = 3\pi/4$, the contribution of $\mathcal{E}_3$ is negligibly small. At $\zeta = 7\pi/8$, the source term $\mathcal{E}_2$ is by far the weakest contributor to σ_r for AGW-AGW-AGW instabilities. The source term $\mathcal{E}_3$ makes the smallest contribution to the growth rates of AGW-AGW-AW instabilities.

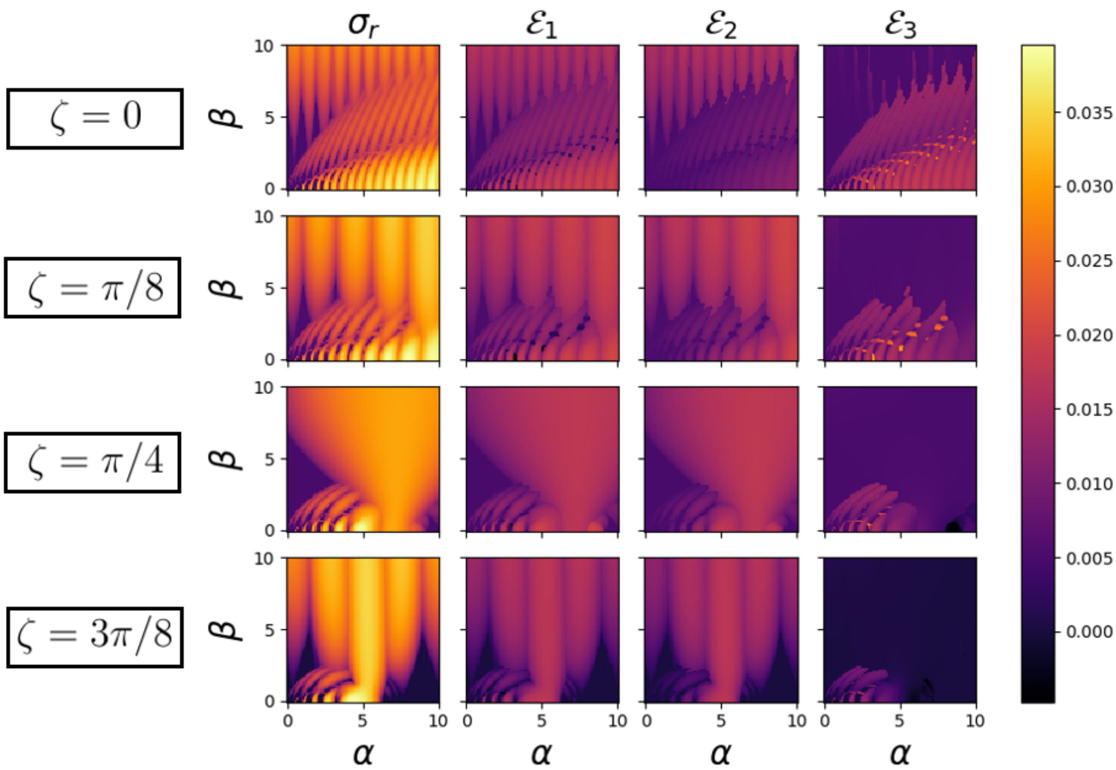

Figure 6.26: Production values alongside growth rate σ_r for a range of α and β values. Parameter values: $a = 0.1$, $\theta = \pi/4$, $\xi = \pi/2$, $b_0 = 0.05$, $\gamma = 0$, $\mathrm{Re} = \mathrm{Rm} = \mathrm{Pe} = 10^6$. Resolution: $\mathcal{N} = 40$, $n_\alpha = n_\beta = 100$.

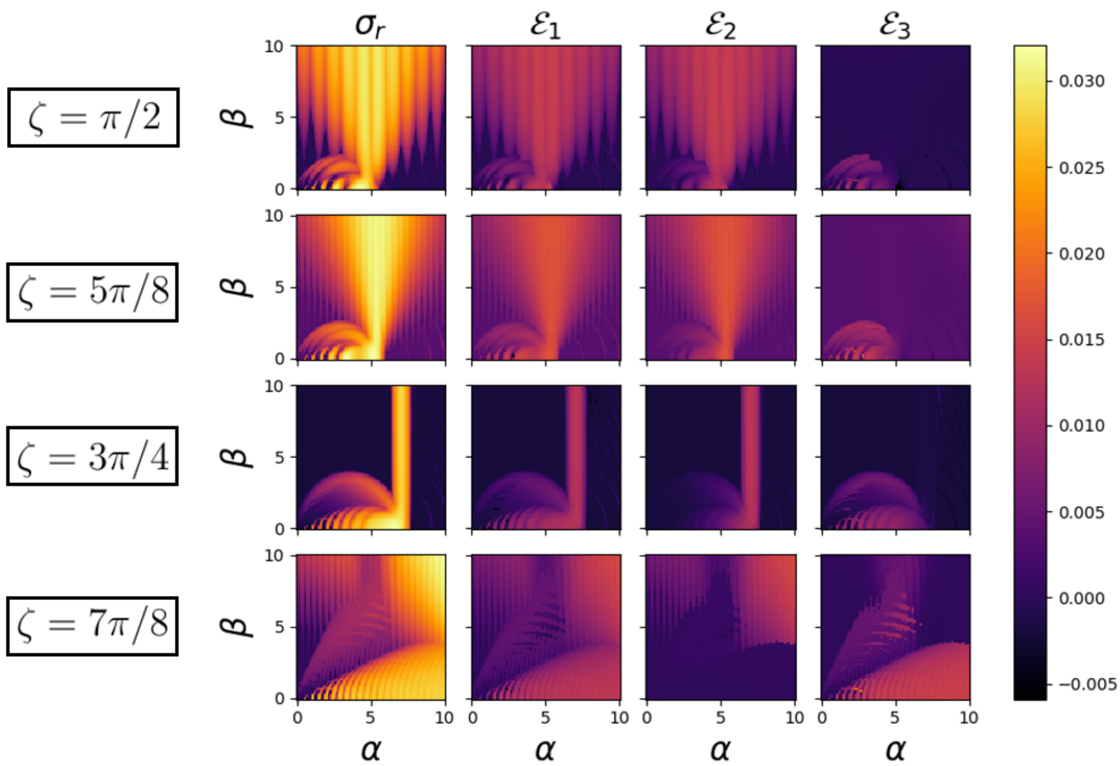

Figure 6.27: Production values alongside growth rate σ_r for a range of α and β values. Parameter values: $a = 0.1$, $\theta = \pi/4$, $\xi = \pi/2$, $b_0 = 0.05$, $\gamma = 0$, $\mathrm{Re} = \mathrm{Rm} = \mathrm{Pe} = 10^6$. Resolution: $\mathcal{N} = 40$, $n_\alpha = n_\beta = 100$.

6.4 Comparing Numerical and Theoretical Growth Rates

MHD Exact Resonances

Section 6.2.1 told us which type of resonant interaction we should expect in each of three distinct regions of (α, β)-space. It told us whether we should expect AGW-AGW-AGW interactions, AGW-AGW-AW interactions, or AGW-AW-AW interactions.

The next step is to use the asymptotic theory from Chapter 5 to predict the growth rates at points of exact triadic resonance. We perform this for both AGW-AGW-AGW interactions and AGW-AW-AW interactions. In particular, we seek to identify α values at which exact triadic resonance occurs by finding resonant α as a function of n at a fixed value of β axis at $\gamma = 0$. The value we fix β at will depend on whether we are considering AGW-AGW-AGW resonances, AGW-AGW-AW resonances or AGW-AW-AW resonances, since each type of resonance occurs in a different region of parameter space. For each Fourier mode n that we consider, we fix $\boldsymbol{K}$ and compute $\boldsymbol{K}_A$ and $\boldsymbol{K}_B$ at resonant values of α using formulae (6.65)-(6.70) to ensure that wavevector resonance condition (6.61) is satisfied.

> The resonance condition (6.62) for frequencies amounts to $\Omega(\alpha) = 0$, where
>
> $$\Omega(\alpha) := [\omega + \omega_A(\alpha) - \omega_B(\alpha)]/N.$$

Finding the root α of this function $\Omega(\alpha)$ gives us the α value satisfying exact parametric resonance for each Fourier mode n. The nature of the daughter wave functions $\omega_A(\alpha)$ and $\omega_B(\alpha)$ changes depending on which type of wave interaction we study. Formulae for these functions can be found in Table 6.2 from earlier in this chapter.

Primary Wave	Daughter Wave A	Daughter Wave B
Alfvén-gravity	Alfvén-gravity	Alfvén-gravity
Alfvén-gravity	Alfvén-gravity	Alfvén
Alfvén-gravity	Alfvén	Alfvén

Table 6.7: Possible resonant interactions in the MHD system between two daughter waves and a primary wave of hybrid Alfvén-gravity character.

At resonant α values we compute theoretical growth rates $\Re(s)$ using the framework of Chapter 5. We check for consistency between these theoretical growth rates $\Re(s)$ with the numerical growth rates $\Re(\sigma)$ found using the Floquet solver earlier in this chapter. We do this for two of the different types of interaction mentioned in Table 6.7.

6.4.1 Growth Rates as a Function of Wavenumber

AGW-AGW-AGW Interactions

So far we have computed growth rates $\Re(\sigma)$ using the numerical Floquet solver (6.59). We compare these with growth rates $\Re(s)$ predicted asymptotically for AGW-AGW-AGW interactions using the following formula derived in Chapter 5.

$$s = \pm a\sqrt{\frac{c_2 c_4}{c_1 c_3}}. \tag{6.110}$$

Expressions for the coefficients c_i in the case of AGW-AGW-AGW interactions are provided in Section 5.2.2. We compare the two methods of computing the growth rate along the line $\beta = 0$. We have demonstrated that this line typically contains the fastest-growing modes of disturbance in the case of AGW-AGW-AGW interactions for our choice of parameter values. We first plot $\Re(\sigma)$ by solving (6.59). On the same set of axes, we then plot $\Re(s)$ using (6.110) at points where the resonance conditions (6.61) and (6.62) are exactly satisfied for AGW-AGW-AGW interactions. We do this for a range of different magnetic field strengths b_0 in Figures 6.28, 6.29, 6.30 and 6.31.

The agreement between $\Re(\sigma)$ and $\Re(s)$ is strong for $b_0 < 1$ (Figures 6.28 and 6.29). The agreement for $b_0 > 1$ is visibly weaker (Figure 6.30). As we increase b_0, we observe a reduction in the width of the resonance bands for AGW-AGW-AGW interactions. We require an extremely high α resolution to capture such narrow resonance bands. After repeating the calculation for smaller a values, we conclude that the amplitude value used in Figure 6.30 is insufficiently small. To remedy this, in Figure 6.31 the amplitude is reduced to $a = 10^{-4}$. Using this value of a results in much stronger agreement.

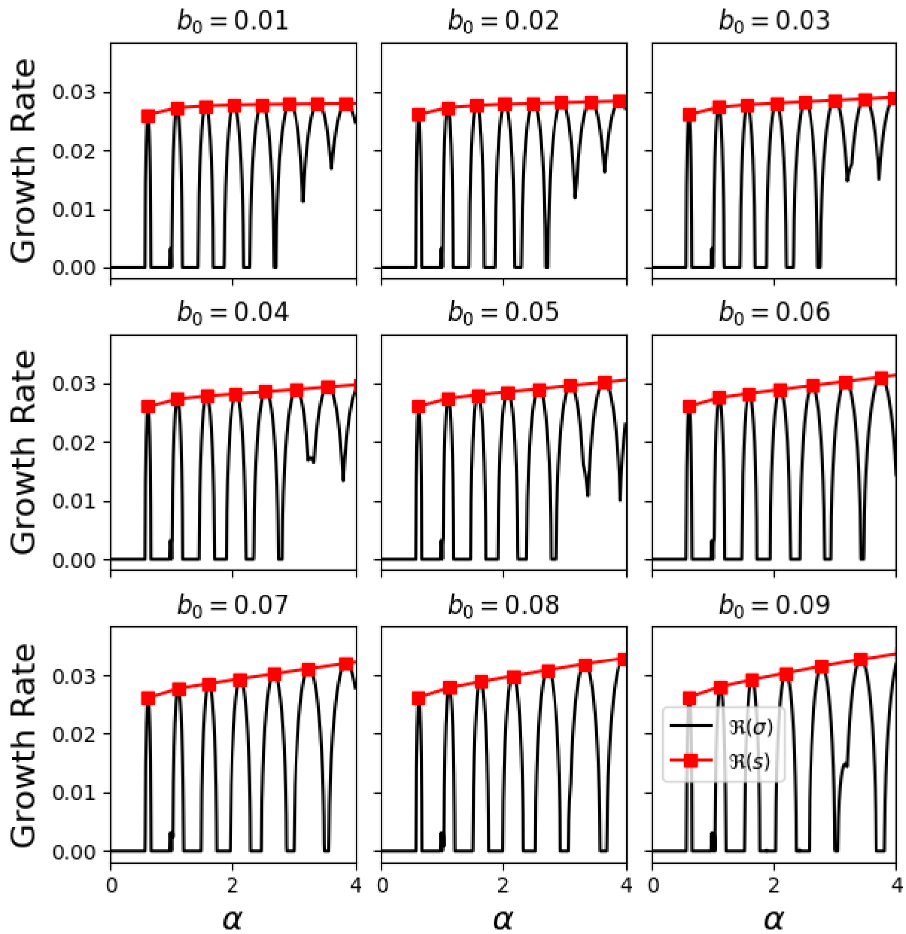

Figure 6.28: Ideal Floquet growth rates $\Re(\sigma)$ alongside theoretical predictions $\Re(s)$ as a function of α for different values of the magnetic field strength b_0. Each value of $\Re(s)$ represents the AGW-AGW-AGW TRI corresponding to one Fourier mode n, computed using (6.110). Parameter values: $a = 0.1$, $\theta = \pi/4$, $\zeta = 0$, $\xi = \pi/2$, $\beta = 0$, $\gamma = 0$. Resolution: $\mathcal{N} = 20$.

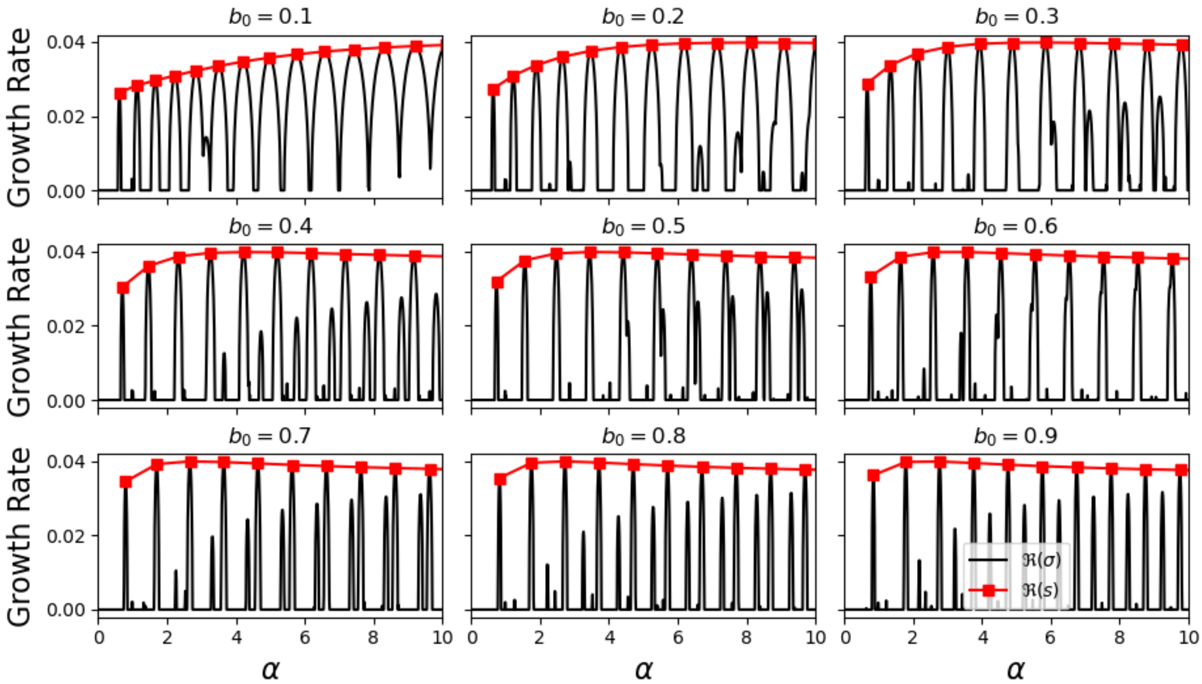

Figure 6.29: Ideal Floquet growth rates $\Re(\sigma)$ alongside theoretical predictions $\Re(s)$ as a function of α for different values of the magnetic field strength b_0. Each value of $\Re(s)$ represents the AGW-AGW-AGW TRI corresponding to one Fourier mode n. Parameter values: $a = 0.1$, $\theta = \pi/4$, $\zeta = 0$, $\xi = \pi/2$, $\beta = 0$, $\gamma = 0$. Resolution: $\mathcal{N} = 20$.

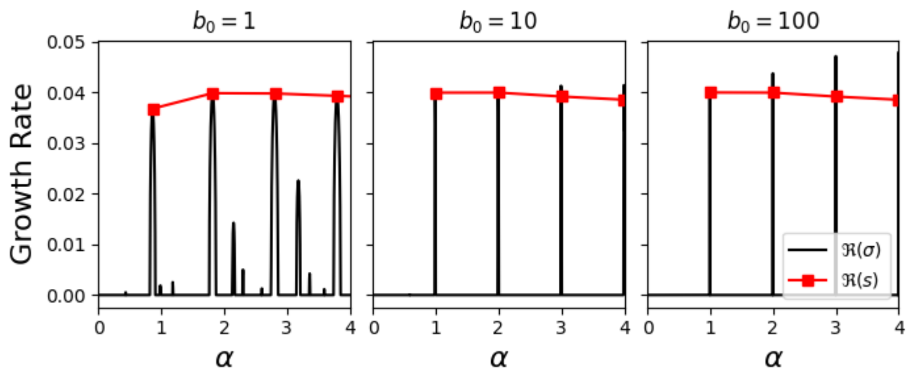

Figure 6.30: Ideal Floquet growth rates $\Re(\sigma)$ alongside theoretical predictions $\Re(s)$ as a function of α for different values of the magnetic field strength b_0. Each value of $\Re(s)$ represents the AGW-AGW-AGW TRI corresponding to one Fourier mode n, computed using (6.110). Parameter values: $a = 0.1$, $\theta = \pi/4$, $\zeta = 0$, $\xi = \pi/2$, $\beta = 0$, $\gamma = 0$. Resolution: $\mathcal{N} = 20$.

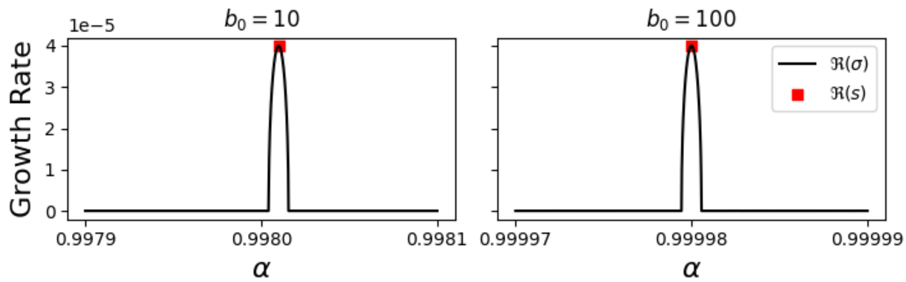

Figure 6.31: Ideal Floquet growth rates $\Re(\sigma)$ as a function of α alongside theoretical prediction $\Re(s)$ for the AGW-AGW-AGW TRI corresponding to Fourier mode $n = -2$, computed using (6.110). Parameter values: $a = 10^{-4}$, $\theta = \pi/4$, $\zeta = 0$, $\xi = \pi/2$, $\beta = 0$, $\gamma = 0$, $\mathcal{N} = 20$.

Magnetic Field Vector Aligned with Primary Wavevector

This section continues the investigation introduced in Section 6.2.5 in which $\theta = \zeta$ with $\xi = \pi/2$. In that section, we plotted growth rates in (α, β)-space for four different values of $\boldsymbol{b}_0$ in Figure 6.16. Here, we found that at higher field strengths, a much smaller proportion of parameter space is unstable to AGW-AGW-AGW resonance compared with lower field strengths at the same equal values of θ and ζ with $\xi = \pi/2$.

In Figure 6.32, we plot asymptotic and numerical growth rates as a function of α for the same parameter values used in Figure 6.16. We find that asymptotics break down when $\zeta = \theta$ and $\xi = \pi/2$ at field strengths of $b_0 = 0.3$ and $b_0 = 0.4$. The Floquet solver reveals very few AGW-AGW-AGW instability bands for this set of parameter values. On the other hand, the asymptotics predict much higher growth rates for the bands which the Floquet solver does produce and also predict similar growth rates for bands not found by the Floquet solver. It is unclear why the two methods for calculating the growth rate do not agree in this case.

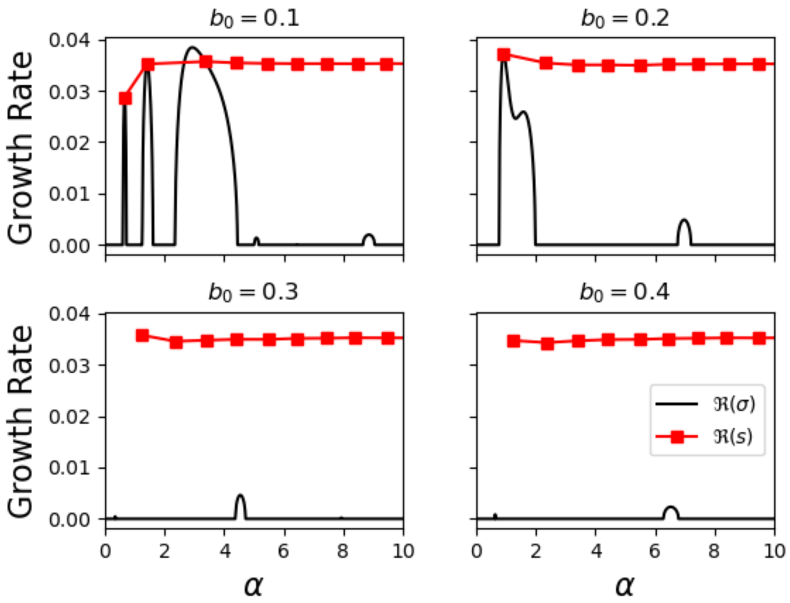

Figure 6.32: Ideal Floquet growth rates $\Re(\sigma)$ alongside theoretical predictions $\Re(s)$ as a function of α for different values of the magnetic field strength b_0. Each value of $\Re(s)$ represents the AGW-AGW-AGW TRI corresponding to one Fourier mode n, computed using (6.110). Parameter values: $a = 0.1$, $\theta = \pi/4$, $\zeta = \pi/4$, $\xi = \pi/2$, $\beta = 0$, $\gamma = 0$. Resolution: $\mathcal{N} = 40$.

AGW-AW-AW Interactions

We now compare Floquet growth rates $\Re(\sigma)$ with growth rates $\Re(s)$ predicted asymptotically by the following formula derived in Chapter 5, which pertains to AGW-AW-AW interactions.

$$s = \pm \frac{a\beta^2 \cos\theta}{2K_{A\perp}K_{B\perp}}. \tag{6.111}$$

We do so along the line $\beta = 10$, a region of (α, β)-space which we have shown to be unstable to AGW-AW-AW interactions for our choice of parameter values through the plotting of resonance curves Ω. We first plot $\Re(\sigma)$ by solving (6.59). On the same set of axes, we then plot $\Re(s)$ using

(6.111) at points where the resonance conditions (6.61) and (6.62) are exactly satisfied for AGW-AW-AW interactions. We do this for a range of different magnetic field strengths b_0 in Figures 6.33-6.34 and for a range of different magnetic field angles ζ in Figures 6.35-6.37.

In Figures 6.33-6.34, the agreement between $\Re(\sigma)$ and $\Re(s)$ is very good. The Floquet solver produces some instability bands at values of α which lie in between the α values at which AGW-AW-AW resonance occurs, suggesting that these instability bands can not be attributed to AGW-AW-AW interactions.

In Figures 6.35, the agreement between $\Re(\sigma)$ and $\Re(s)$ is very good for most of the ζ values considered, but at $\zeta = 7/8$ we observe an approximate interval $\alpha \in [4, 6]$ in which $\Re(\sigma)$ and $\Re(s)$ do not agree. We attempt to reconcile this in two ways. First, we plot $\Re(\sigma)$ and $\Re(s)$ for the same set of parameter values at a smaller amplitude $a = 0.02$ than the original amplitude $a = 0.1$. We show this in Figure 6.36. We do this because the formula for $\Re(s)$ was derived using a small-amplitude approximation and is only expected to be valid when $a \ll 1$. We find that reducing the value of a does not improve the agreement between $\Re(\sigma)$ and $\Re(s)$. The second attempt to reconcile the disagreement is shown in Figure 6.37, where we increase the number of terms $\mathcal{N}$ in the truncated Fourier series representation of the disturbance from $\mathcal{N} = 20$ to $\mathcal{N} = 50$. We also restrict our domain to the problematic region $\alpha \in [4, 6]$. We find that this also does not improve the agreement between $\Re(\sigma)$ and $\Re(s)$. We conclude that the reason for the disagreement between $\Re(\sigma)$ and $\Re(s)$ is not related to the validity of the small-amplitude approximation or whether the numerical calculation is sufficiently resolved in terms of Fourier modes.

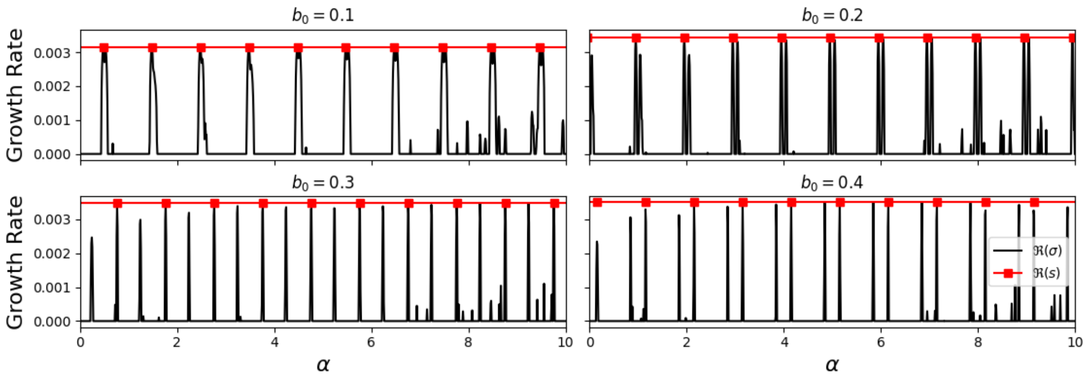

Figure 6.33: Ideal Floquet growth rates $\Re(\sigma)$ as a function of α alongside theoretical prediction $\Re(s)$ for AGW-AW-AW TRIs, computed using (6.111). Parameter values: $a = 0.01$, $\theta = \pi/4$, $\zeta = 0$, $\xi = \pi/2$, $\beta = 10$, $\gamma = 0$, $\mathcal{N} = 20$.

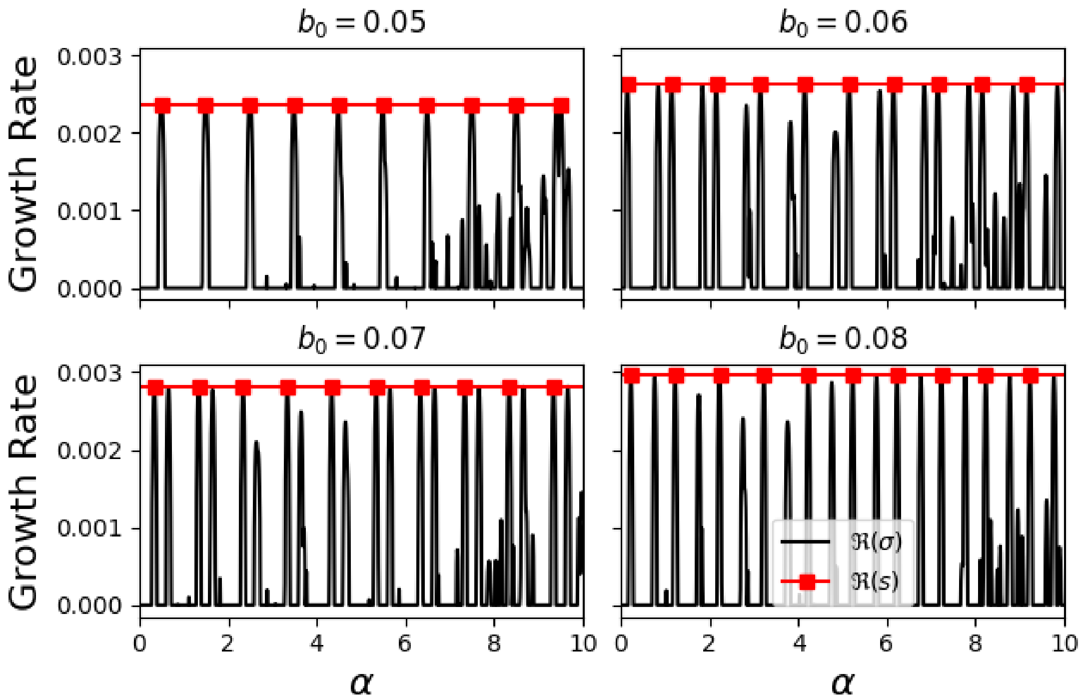

Figure 6.34: Ideal Floquet growth rates $\Re(\sigma)$ as a function of α alongside theoretical prediction $\Re(s)$ corresponding to an AGW-AW-AW TRI, computed using (6.111). Parameter values: $a = 0.01$, $\theta = \pi/4$, $\zeta = 0$, $\xi = \pi/2$, $\beta = 10$, $\gamma = 0$, $\mathcal{N} = 20$.

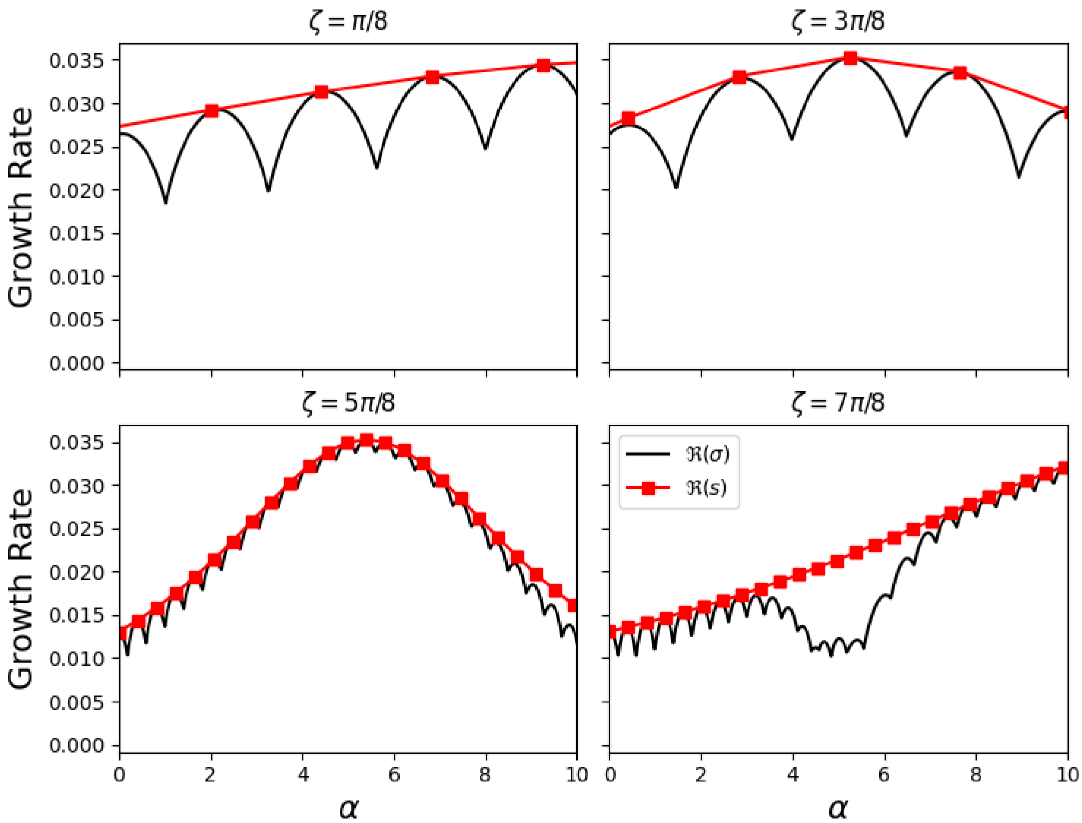

Figure 6.35: Ideal Floquet growth rates $\Re(\sigma)$ as a function of α alongside theoretical prediction $\Re(s)$ corresponding to an AGW-AW-AW TRI computed using (6.111) for different ζ values. Parameter values: $a = 0.1$, $\theta = \pi/4$, $\xi = \pi/2$, $b_0 = 0.05$, $\beta = 10$, $\gamma = 0$, $\mathcal{N} = 20$.

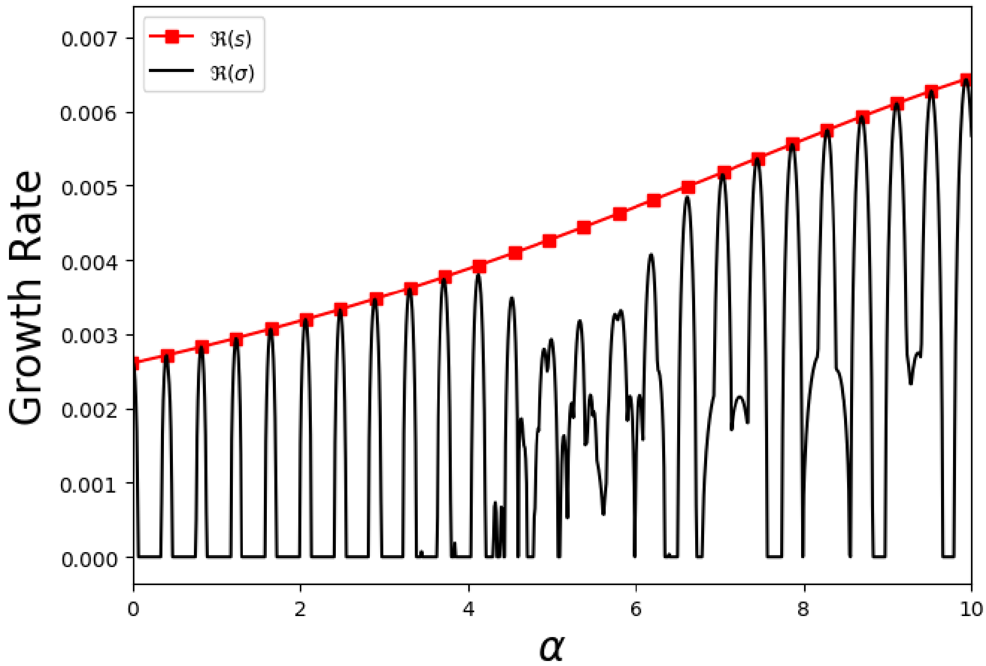

Figure 6.36: Ideal Floquet growth rates $\Re(\sigma)$ as a function of α alongside theoretical prediction $\Re(s)$ corresponding to an AGW-AW-AW TRI, computed using (6.111). Parameter values: $a = 0.02$, $\theta = \pi/4$, $\zeta = 7\pi/8$, $\xi = \pi/2$, $b_0 = 0.05$, $\beta = 10$, $\gamma = 0$, $\mathcal{N} = 20$.

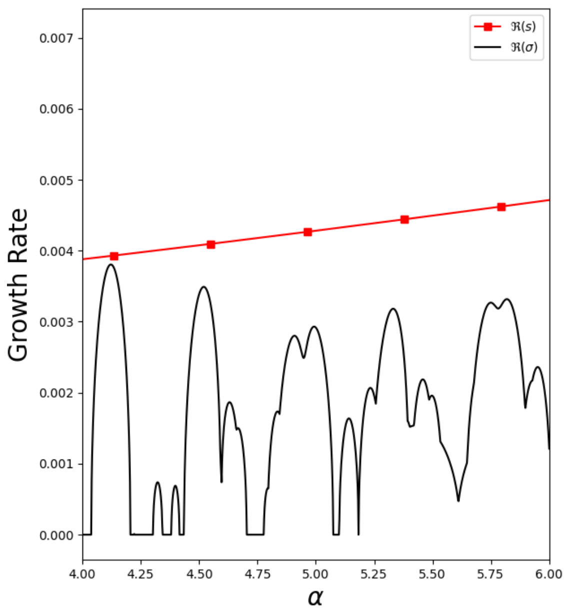

Figure 6.37: Ideal Floquet growth rates $\Re(\sigma)$ as a function of α alongside theoretical prediction $\Re(s)$ corresponding to an AGW-AW-AW TRI, computed using (6.111). Parameter values: $a = 0.02$, $\theta = \pi/4$, $\zeta = 7\pi/8$, $\xi = \pi/2$, $b_0 = 0.05$, $\beta = 10$, $\gamma = 0$, $\mathcal{N} = 50$.

6.4.2 Absolute Error and Relative Error

This section verifies that the agreement between the two methods of computing the growth rate does in fact improve as we reduce the size of the small parameter a. To test this numerically, we calculate

$$\delta(a) := |\sigma(a) - \sigma_0(a)|\,, \quad \Delta(a) := \left|\frac{\sigma(a) - \sigma_0(a)}{\sigma_0(a)}\right|,$$

for a series of descending values of a. σ is the value computed by the numerical eigenvalue problem and $\sigma_0 = \Re(s)$ is calculated from (6.110), the asymptotic growth rate formula we derived in Chapter 5. We plot absolute errors δ and relative errors Δ for a set of amplitude values a corresponding to AGW-AGW-AGW interactions in Figure 6.38. We find results which are comparable with the absolute and relative errors observed for IGW-IGW-IGW interactions in Chapter 4. The relative and absolute errors decrease with decreasing a until we reach $a = 10^{-4}$.

We compute absolute and relative errors for AGW-AW-AW interactions in Figure 6.39. The trends are comparable with those observed for AGW-AW-AW interactions, though this time the relative and absolute errors stop decreasing at $a = 10^{-5}$ as we reduce the size of a.

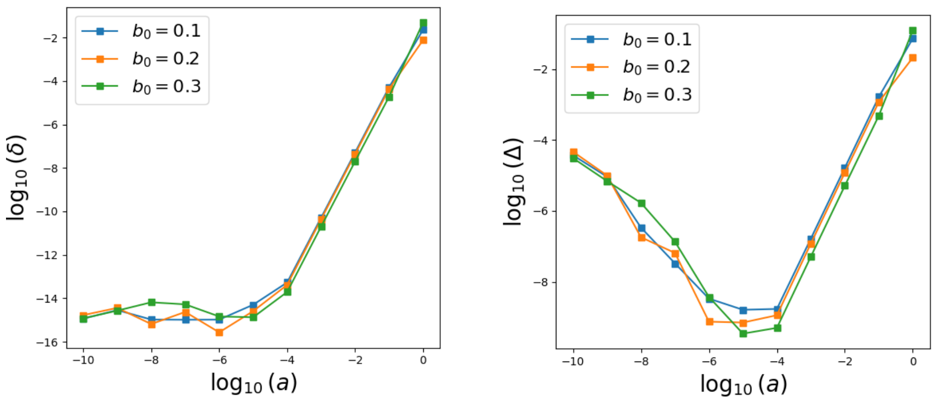

Figure 6.38: Absolute error δ and relative error Δ in the growth rate as a function of amplitude a calculated at a resonant value of α corresponding to Fourier mode $n = -5$ for an AGW-AGW-AGW TRI. Parameter values: $a \in (10^{-10}, 1)$, $\theta = \pi/4$, $\zeta = 0$, $\xi = \pi/2$, $\alpha = 0.20087$, $\beta = 0$, $\gamma = 0$. Resolution: $n_a = 10$, $\mathcal{N} = 50$.

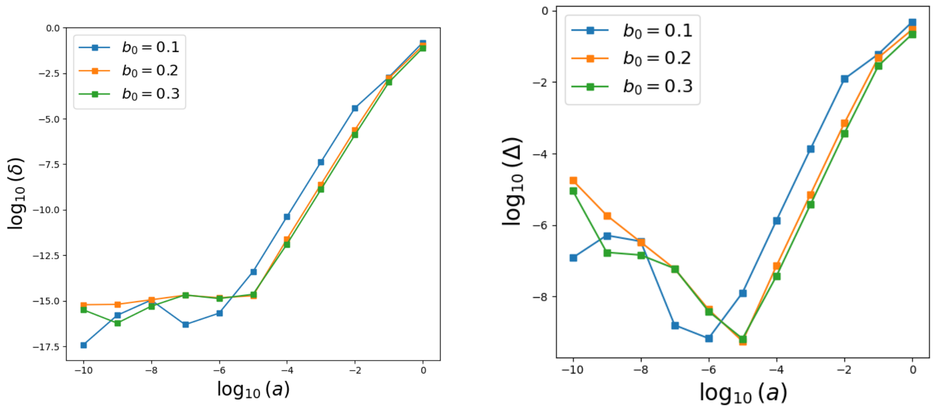

Figure 6.39: Absolute error δ and relative error Δ in the growth rate as a function of amplitude a calculated at a resonant value of α corresponding to Fourier mode $n = -5$ for an AGW-AW-AW TRI. Parameter values: $a \in (10^{-10}, 1)$, $\theta = \pi/4$, $\zeta = 0$, $\xi = \pi/2$, $\alpha = 0.20087$, $\beta = 10$, $\gamma = 0$. Resolution: $n_a = 10$, $\mathcal{N} = 50$.

6.4.3 Growth Rates Maximised over Wavenumber Space

Growth Rates Maximised over α and β

In the absence of a magnetic field, we know that the the dependence of the instability growth rate maximised over α and β on the amplitude parameter is approximately linear. McEwan and Robinson (1975) were the first to discover this relationship for a plane IGW. We wish to see if this trend extends to the MHD setting (i.e. to see if it remains true for AGWs). In future work, we could derive an expression for the growth rate in the short wavelength limit for AGW-AGW-AGW interactions. It would be useful to try and demonstrate agreement between these growth rates and the Floquet growth rate maximised over α and β as a function of a, θ, ζ and b_0. This would be important for astrophysical applications.

In Figures 6.40 and 6.41, we plot the 'maximum Floquet growth rate' at ten different values of a in the range $a \in [0, 2]$. At each value of a, we maximise the growth rate over the wavenumber range $\alpha \in [0, 4]$ and $\beta \in [0, 4]$. We also take 100 values of a in the range $a \in [0, 2]$ and plot the accompanying theoretical prediction for 'maximum growth rate' calculated using the AGW-AGW-AGW resonance formula (5.82) from Chapter 5. At each value of a, we fix $\beta = 0$ and find 10 resonant values of α. The maximum of these 10 values is recorded. We find that the approximately linear relationship between a and $\max[\Re(\sigma)]$ is preserved upon inclusion of the magnetic field. At larger values of a, we observe weaker agreement between the Floquet solver and the asymptotic prediction. This is expected given that the asymptotic prediction is a small-amplitude approximation.

Figure 6.41 emphasises just how incremental the overall increase in maximum growth rates is as we vary the order of magnitude of the background magnetic field strength. Even though the character of the wave changes with b_0 (i.e. transitions from pure IGW character to hybrid AGW character), the maximum growth rate observed is only marginally affected by varying b_0. The instability behaves similarly with strong fields compared to the hydrodynamic case. The gradient of the linear relationship between a and the growth rate does not change significantly with increasing b_0.

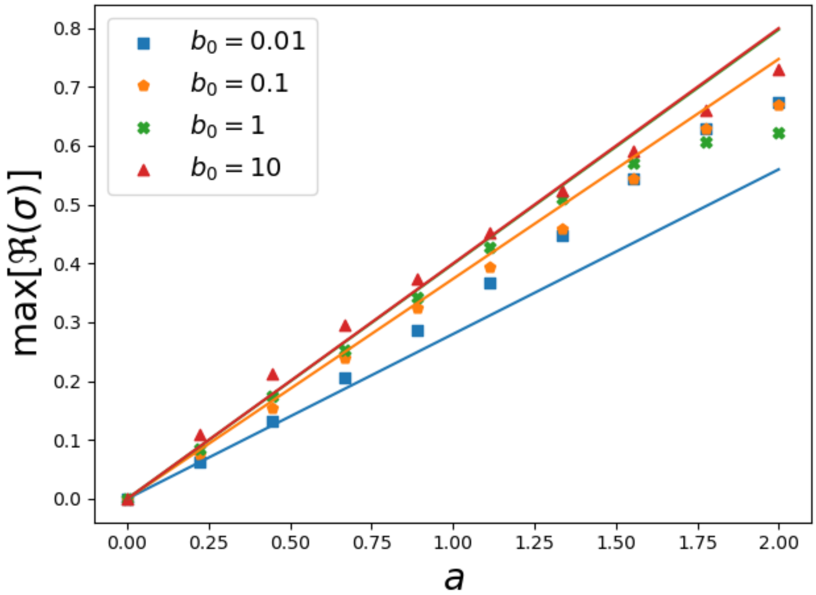

Figure 6.40: Dependence of growth rate maximised over our chosen range of α and β on primary wave amplitude for different magnetic field strengths. Points: Growth rates computed using the Floquet solver. Parameter values for points: $\theta = \pi/4$, $\zeta = 0$, $\xi = \pi/2$, $\alpha \in [0, 4]$, $\beta \in [0, 4]$, $\gamma = 0$, $\mathrm{Re} = \mathrm{Rm} = \mathrm{Pe} = 10^6$. Resolution: $\mathcal{N} = 40$, $n_\alpha = n_\beta = 10$. Lines: Theoretical predictions for growth rate calculated using formula (5.82) from Chapter 5. Parameter values for lines: $\theta = \pi/4$, $\zeta = 0$, $\xi = \pi/2$, $\alpha \in [0, 4]$, $\beta = 0$, $\gamma = 0$.

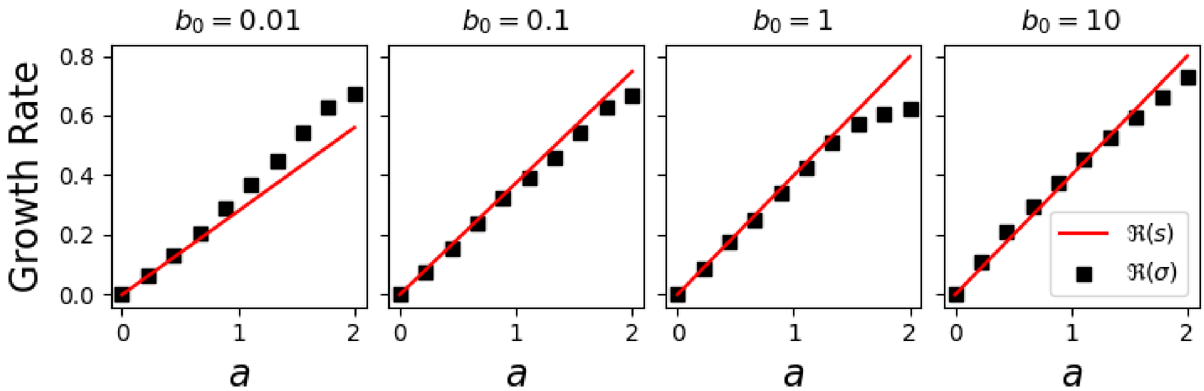

Figure 6.41: Dependence of growth rate maximised over our chosen range of α and β on primary wave amplitude for different magnetic field strengths. Points: Growth rates computed using the Floquet solver. Parameter values for points: $\theta = \pi/4$, $\zeta = 0$, $\xi = \pi/2$, $\alpha \in [0, 4]$, $\beta \in [0, 4]$, $\gamma = 0$, $\mathrm{Re} = \mathrm{Rm} = \mathrm{Pe} = 10^6$. Resolution: $\mathcal{N} = 40$, $n_\alpha = n_\beta = 10$. Lines: Theoretical predictions for growth rate calculated using formula (5.82) from Chapter 5. Parameter values for lines: $\theta = \pi/4$, $\zeta = 0$, $\xi = \pi/2$, $\alpha \in [0, 4]$, $\beta = 0$, $\gamma = 0$.

Growth Rates Maximised over α at Fixed β

In Figures 6.42 and 6.43, we plot the 'maximum Floquet growth rate' at ten different values of a in the range $a \in [0, 2]$. At each value of a, we maximise the growth rate over the wavenumber range $\alpha \in [0, 10]$ and fix $\beta = 0$. We also take 100 values of a in the range $a \in [0, 2]$ and plot the accompanying theoretical prediction for 'maximum growth rate' calculated using the AGW-AGW-AGW resonance formula from Chapter 5. At each value of a, we fix $\beta = 0$ and find 10 resonant values of α. The maximum of these 10 values is recorded. We again find that the approximately linear relationship between a and $\max[\Re(\sigma)]$ is preserved upon inclusion of the magnetic field, which is consistent with the findings of the previous subsection. Figure 6.43

provides more evidence that the overall increase in maximum growth rates is incremental as we vary the order of magnitude of the background magnetic field strength.

In Figure 6.44 we plot the ideal maximised growth rate $\Re(\sigma)$ as a function of b_0 at a field orientation of $\zeta = 0$. Each growth rate is maximised over $\alpha \in [0, 10]$ at fixed $\beta = 0$. We also overlay the theoretical prediction for the growth rate $\Re(s)$ at points of exact resonance in the case of AGW-AGW-AGW interactions. We find that AGW-AGW-AGW interactions are responsible for the fastest-growing instabilities at low values of b_0, but at larger b_0 these interactions are not the source of the fastest-growing instability. We find disagreement between $\Re(\sigma)$ and $\Re(s)$ at larger b_0.

In Figure 6.45 we plot the ideal maximised growth rate as a function of b_0 at a selection of different field orientations. For field angles $\zeta = \pi/4$ and $\zeta = 3\pi/8$, we find disagreement between $\Re(\sigma)$ and $\Re(s)$. In Figure 6.46 we try to reconcile this disagreement by reducing the wave amplitude from $a = 0.1$ to $a = 0.01$. We find that reducing a does not improve the agreement between $\Re(\sigma)$ and $\Re(s)$.

A possible conclusion we could draw is that above a certain field strength, we expect waves to be more stable than waves below that field strength. This is a recurring idea that has appeared throughout this chapter - that strong magnetic fields can have a stabilising effect on AGW disturbances.

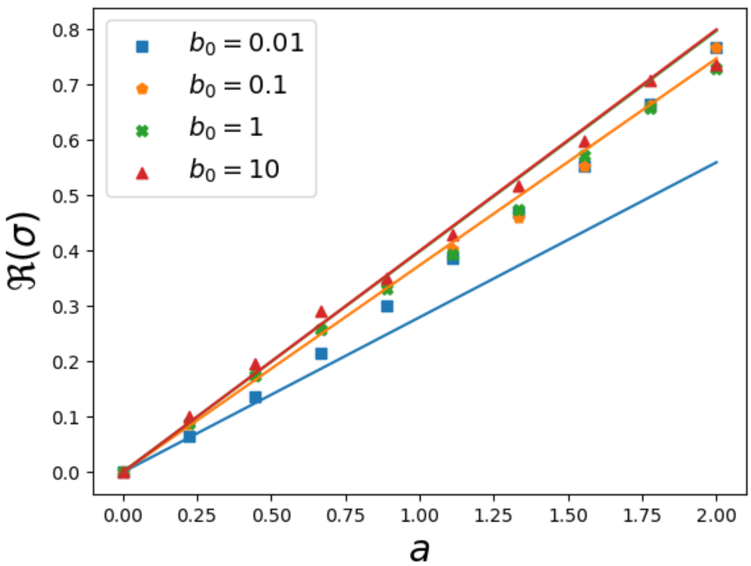

Figure 6.42: Dependence of growth rate maximised over our chosen range of α on primary wave amplitude for different magnetic field strengths. Points: Growth rates computed using the ideal form of the Floquet solver. Lines: Theoretical predictions for growth rate calculated using formula (5.82) from Chapter 5. Parameter values: $\theta = \pi/4$, $\zeta = 0$, $\xi = \pi/2$, $\alpha \in [0, 10]$, $\beta = 0$, $\gamma = 0$. Resolution: $\mathcal{N} = 40$, $n_\alpha = 100$.

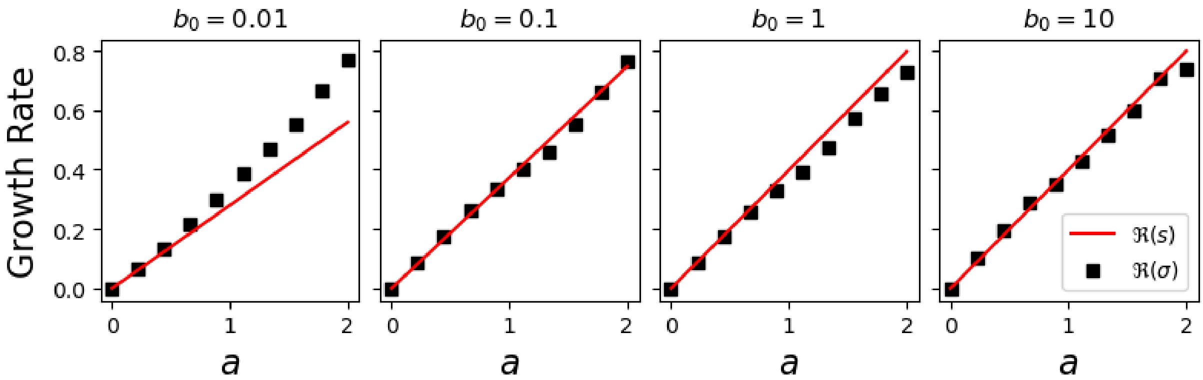

Figure 6.43: Dependence of growth rate maximised over our chosen range of α on primary wave amplitude for different magnetic field strengths. Points: Growth rates computed using the ideal form of the Floquet solver. Lines: Theoretical predictions for growth rate calculated using formula 5.82 from Chapter 5. Parameter values: $\theta = \pi/4$, $\zeta = 0$, $\xi = \pi/2$ $\alpha \in [0, 10]$, $\beta = 0$, $\gamma = 0$. Resolution: $\mathcal{N} = 40$, $n_\alpha = 100$.

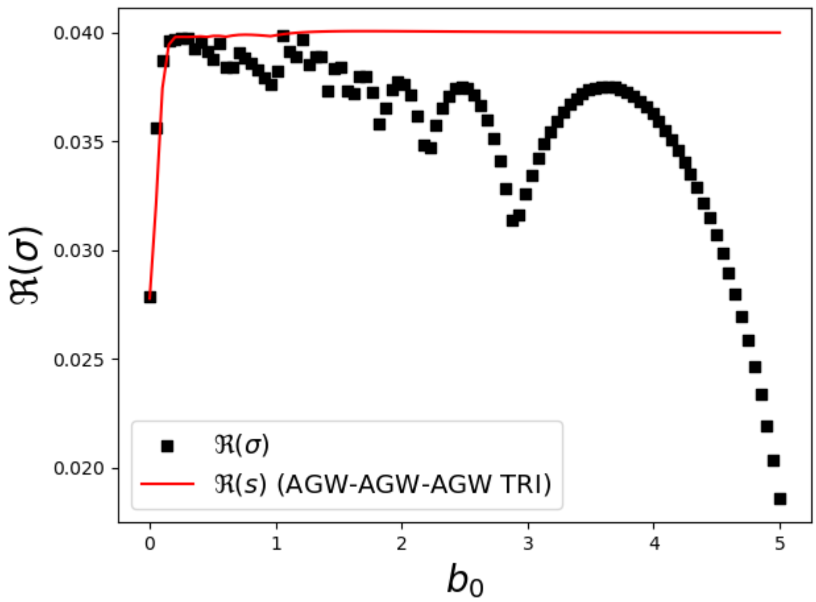

Figure 6.44: Dependence of ideal growth rate maximised over our chosen range of α on background magnetic field strength. Points: Growth rates computed by Floquet solver. Curve: theoretical maximum growth rate for an AGW-AGW-AGW TRI plotted using formula (5.82) from Chapter 5. Parameter values: $a = 0.1$, $\theta = \pi/4$, $\zeta = 0$, $\xi = \pi/2$, $\alpha \in [0, 10]$, $\beta = 0$, $\gamma = 0$. Resolution: $\mathcal{N} = 20$, $n_{b0} = 100$, $n_\alpha = 50$.

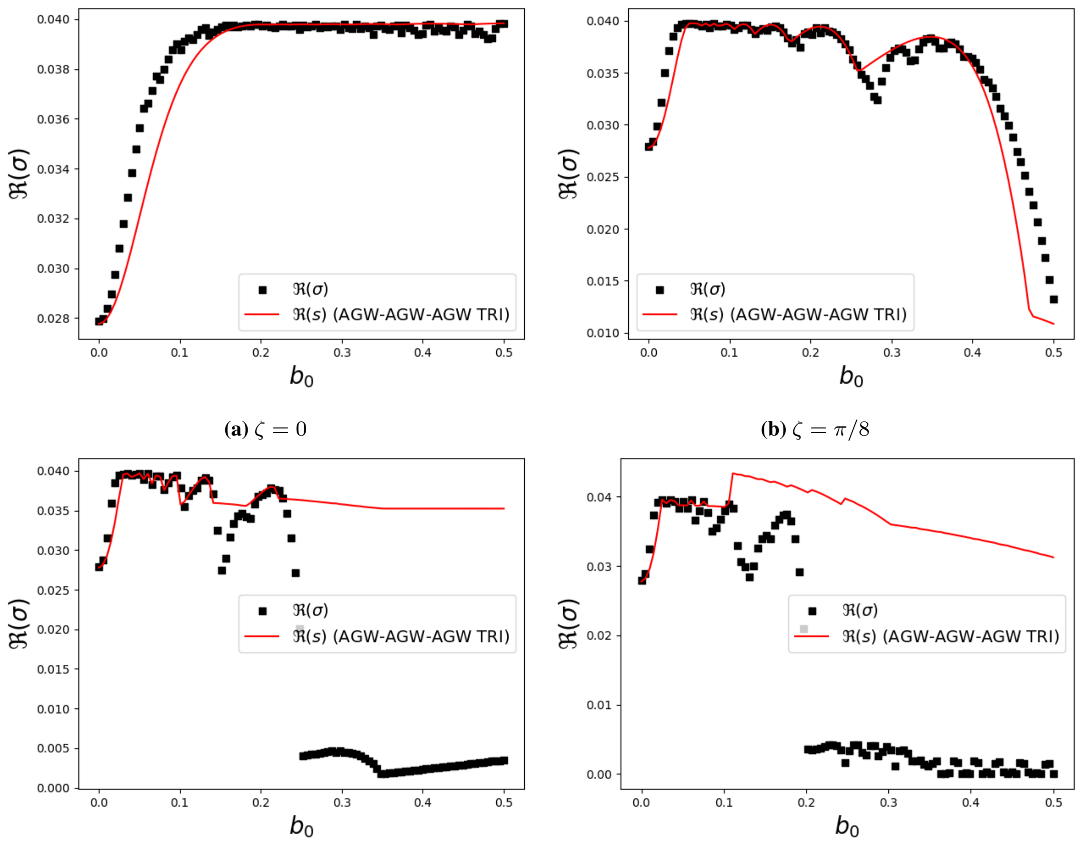

(a) $\zeta = 0$

(b) $\zeta = \pi/8$

(c) $\zeta = \pi/4$

(d) $\zeta = 3\pi/8$

Figure 6.45: Dependence of ideal growth rate maximised over our chosen range of α on background magnetic field strength. Points: Growth rates computed by Floquet solver. Curve: theoretical maximum growth rate for an AGW-AGW-AGW TRI plotted using formula (5.82). Parameter values: $a = 0.1$, $\theta = \pi/4$, $\xi = \pi/2$, $\alpha \in [0, 10]$, $\beta = 0$, $\gamma = 0$. Resolution: $\mathcal{N} = 20$, $n_{b0} = 100$, $n_\alpha = 100$.

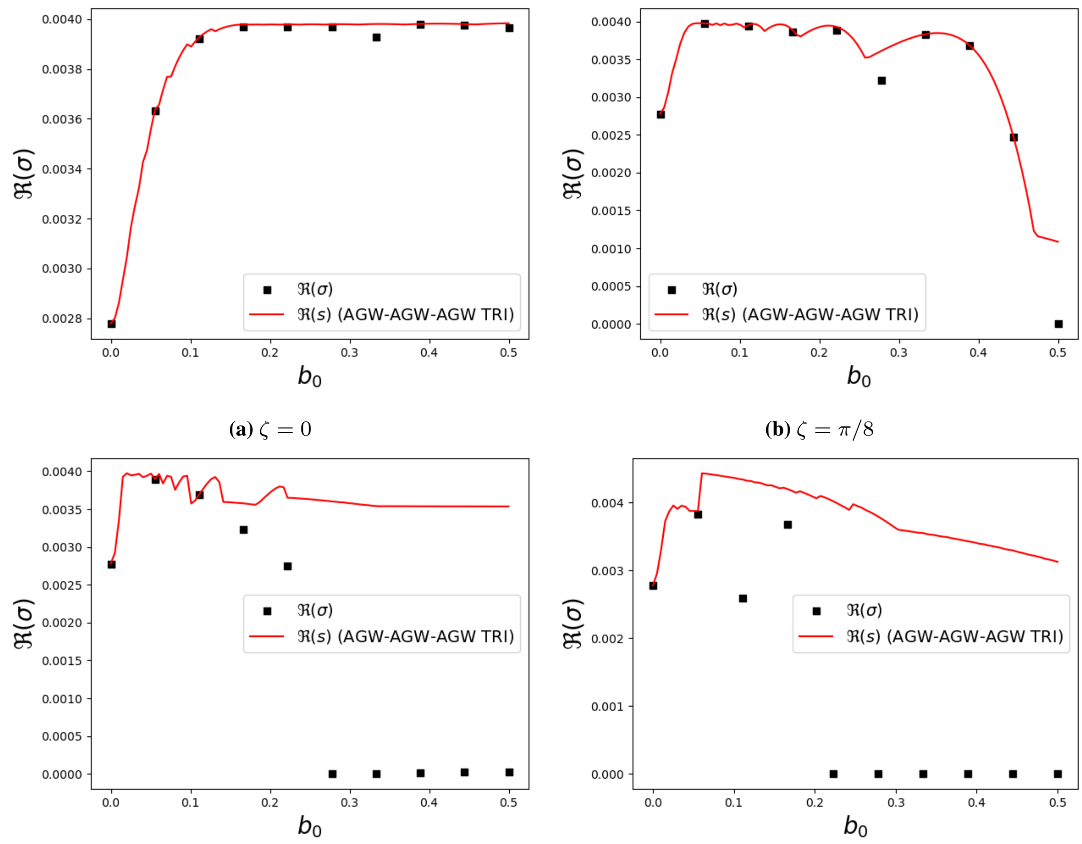

(a) $\zeta = 0$

(b) $\zeta = \pi/8$

(c) $\zeta = \pi/4$

(d) $\zeta = 3\pi/8$

Figure 6.46: Dependence of ideal growth rate maximised over our chosen range of α on background magnetic field strength. Points: Growth rates computed by Floquet solver. Curve: theoretical maximum growth rate for an AGW-AGW-AGW TRI plotted using formula (5.82) from Chapter 5. Parameter values: $a = 0.01$, $\theta = \pi/4$, $\xi = \pi/2$, $\alpha \in [0, 10]$, $\beta = 0$, $\gamma = 0$. Resolution: $\mathcal{N} = 20$, $n_{b0} = 10$, $n_\alpha = 100$.

6.5 Astrophysical Significance of Field Strength Values

Here we use solar data for N^2, ρ_0, ν, η and κ (each as a function of fractional radius $r/R_\odot$) to compute the dimensional magnetic field strength B_0 as a function of fractional radius for different values of the dimensionless field strength b_0. We first observe how each of these five quantities vary with fractional radius. To determine B_0 as a function of fractional radius $r/R_\odot$,

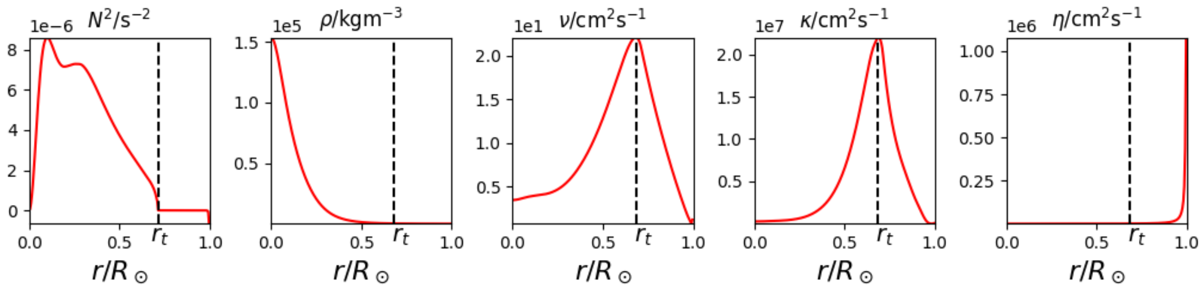

Figure 6.47: Solar quantities as a function of fractional radius. Squared buoyancy frequency N^2 and density ρ are taken from a solar model by Christensen-Dalsgaard et al. (1996). r_t marks the approximate fractional radial location occupied by the solar tachocline.

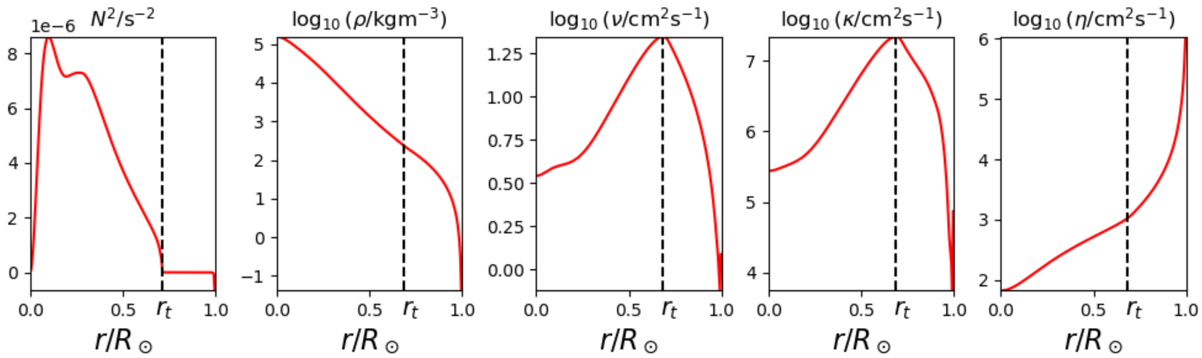

Figure 6.48: Base-10 logarithms of solar quantities as a function of fractional radius. Squared buoyancy frequency N^2 and density ρ are taken from a solar model by Christensen-Dalsgaard et al. (1996). r_t marks the approximate fractional radial location occupied by the solar tachocline.

we use the formula:

$$B_0 = \frac{N(r)\sqrt{\mu_0 \rho(r)} b_0}{K(r)}.$$

The permeability of free space is $\mu_0 = 4\pi \times 10^7 \mathrm{kg\ ms^{-2}A^{-2}}$. Values of N and ρ for different fractional radii are provided by Christensen-Dalsgaard et al. (1996). K is the wavenumber associated with the primary wave, which we take to be a tidally-forced Alfvén-gravity wave excited at the solar tachocline by an orbiting body. We find the primary wavevector norm $K(r)$ using the formula

$$K(r) = \frac{\sqrt{l(l+1)}}{\omega} \frac{N}{r}.$$

The primary wave frequency ω is given by $\omega = 2\pi/\mathcal{P}$, where $\mathcal{P}$ is the forcing period of the tidally-forced wave in units of days. l is the relevant spherical harmonic degree. According to

Fuller et al. (2014), this radial wavenumber is given by

$$K_r^2 = \frac{l(l+1)N^2}{r^2\omega^2}.$$

This formula is derived from WKB theory using scaling relations. We can rearrange this to get

$$\omega^2 = \frac{l(l+1)N^2}{r^2 K_r^2}.$$

This is the analogue of the Cartesian IGW dispersion relation in spherical polar coordinates.

Below we plot B_0 as a function of fractional radius for several different values of b_0 using the approach described above. According to Mestel and Weiss (1987), the magnetic field strength B_0 for a poloidal magnetic field in the solar tachocline is likely to be in the range $B_0 \in (B_{\min}, B_{\max})$, where $B_{\min} := 5 \times 10^{-1}$G and $B_{\max} := 5 \times 10^{3}$G. We overlay these bounds as dashed lines in Figure 6.49.

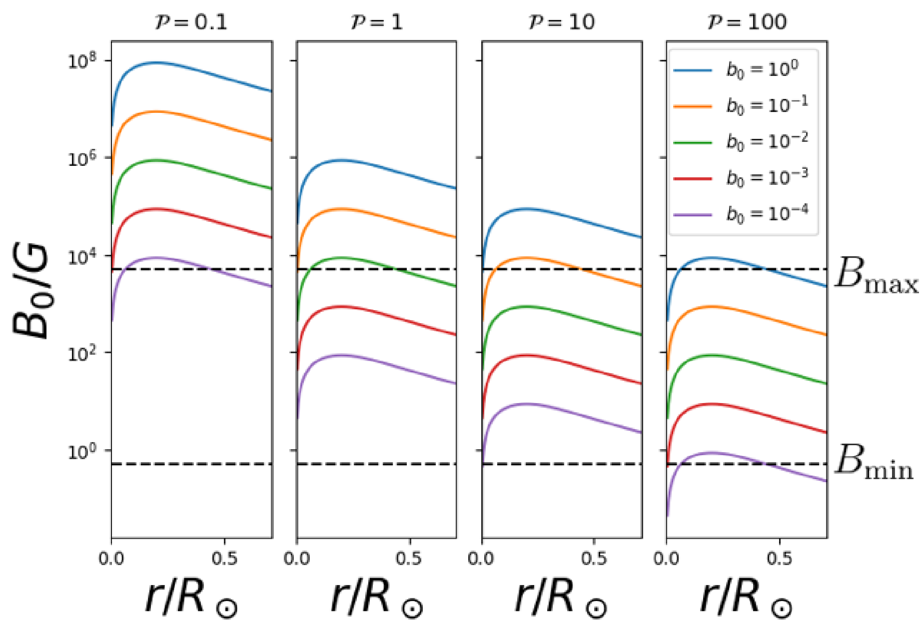

Figure 6.49: Dimensional background magnetic field strengths as a function of fractional solar radius for different dimensionless field strengths b_0, computed using data from Christensen-Dalsgaard et al. (1996) with spherical harmonic degree $l = 2$. The period $\mathcal{P}$ is in units of days. Black dashed lines: approximate bounds for the field strength of a poloidal magnetic field in the solar tachocline according to Mestel and Weiss (1987).

Summary

We took the Floquet method for constructing an eigenvalue problem with which to study wave instabilities presented in Chapter 4 and adapted it to solve the MHD equations for a stably-stratified Boussinesq fluid with constant buoyancy frequency N permeated by a uniform background magnetic field. We contoured the growth rate in wavenumber space and studied the influence of the magnetic field strength b_0 and the magnetic field angles ζ and ξ on the growth rates. The general picture that IGWs and AGWs are unstable for any wave amplitude does not change upon the introduction of a magnetic field. At small wave amplitudes, many of the instabilities observed can be attributed to three classes of TRI: AGW-AGW-AGW interactions, AGW-AGW-AW interactions and AGW-AW-AW interactions. This was confirmed by plotting resonance curves of the quantity Ω to reveal the expected location of each type of interaction in parameter space.

To determine what drives the instabilities physically, we derived equations for the MHD energetics based on the hydrodynamic energetic equations presented in Chapter 4. These were used to decompose growth rates of AGW instabilities into five constituent parts: Reynolds stress $\mathcal{E}_1$, Maxwell stress $\mathcal{E}_2$, buoyancy production $\mathcal{E}_3$ and two separate terms $\mathcal{E}_4$ and $\mathcal{E}_5$ which are related to the electric current. In most cases, Reynolds stress, Maxwell stress and buoyancy production make a far larger contribution to the growth rate than the two electric current terms for all types of TRI considered. We observed many parameter combinations at which the two electric current terms make no contribution to the growth rate. It is only when the magnetic field strength is sufficiently large that the electric current terms start to play a significant role. The Reynolds stress is most frequently the dominant source term out of all five, though buoyancy production makes a contribution comparable with Reynolds stress in the case where the magnetic field vector is perpendicular (or nearly perpendicular) to the direction of gravity. We also found that AGW-AGW-AGW instabilities are very similar energetically to IGW-IGW-IGW instabilities, which we studied in Chapter 4. In our energetic analysis, we focused entirely on instabilities of small-amplitude AGWs. It would be interesting to perform a similar energetic analysis for large-amplitude AGWs in future work.

Finally, we demonstrated agreement between the numerical growth rates found using the Floquet solver and the growth rates predicted asymptotically using the framework derived in Chapter 5. The agreement is strong in most cases, but the asymptotics break down for large field strengths in the case where the background magnetic field vector is aligned with the primary wavevector. It would be useful to understand why this occurs in future work.

Chapter 7

Discussion

The central theme of this thesis has been the conditions under which waves are unstable in stably-stratified Boussinesq fluids. In particular, we sought to establish what is different about such instabilities in the presence of a magnetic field when compared with the analogous instabilities in the absence of a magnetic field. Though the instabilities observed can be driven by a number of physical processes, we focused on those which are induced by TRIs. In the absence of a magnetic field, instabilities of small amplitude IGWs are predominantly induced by TRIs between three IGWs. With a non-zero magnetic field, the Boussinesq MHD equations permit two types of wave: AGWs and AWs. Instabilities of small-amplitude AGWs are predominantly induced by TRIs between AGWs and AWs in various combinations.

The three-wave interactions we considered consisted of one parent wave (which formed the basic state) and two daughter waves (which served as disturbances to the basic state). When a magnetic field was included, we chose to only consider parent waves of AGW character, which enabled three different classes of TRI: AGW-AGW-AGW interactions, AGW-AGW-AW interactions and AGW-AW-AW interactions. This problem has a more diverse range of interaction types than the analogous hydrodynamic problem, in which only IGW-IGW-IGW interactions are permitted.

Using multiple-scale asymptotics, Davis and Acrivos (1967) derived an analytical formula for the growth rate at points in parameter space at which IGW-IGW-IGW resonance is exactly satisfied. We reformulated this asymptotic framework and extended it to derive analogous formulae for the growth rate pertaining to AGW-AGW-AGW interactions and AGW-AW-AW interactions. In future work, it would be useful to derive a similar asymptotic formula for AGW-AGW-AW interactions, too. This is because we were able to demonstrate that instabilities of small-amplitude AGWs in Boussinesq fluids can be attributed to any of these three classes of TRI. We confirmed that this was true by plotting curves in wavenumber space along which both the triadic resonance criteria are satisfied, which reveals locations at which we should expect to see bands of non-zero instability growth rates.

The asymptotic formulae derived in this thesis predict growth rates at locations in parameter space at which resonance is exactly satisfied, but it is possible to derive asymptotic bounds defining regions of parameter space in which resonance is approximately satisfied. Mied (1976) derived such bounds for TRIs between IGWs. Similar bounds for TRIs between AGWs and AWs could be derived in future. One could also perform a perturbation expansion for the growth rate with b_0 as a small parameter to study the incremental effects of moving from IGW territory to AGW territory (i.e. of moving from $b_0 = 0$ to $0 < b_0 \ll 1$).

These asymptotic methods we used invoke expansions of the dependent variables in powers of the wave amplitude. The analytical formulae derived using these asymptotic methods are extracted at leading order in wave amplitude. It is for this reason that the asymptotic growth rate formulae are valid for small-amplitude waves only. To compute growth rates for any wave amplitude, we used a Floquet technique to construct an algebraic eigenvalue problem from the governing equations. This required us to linearise the governing equations with respect to disturbances from the plane wave solution which formed our basic state. We used an eigenvalue problem derived by Lombard and Riley (1996) to study instabilities of finite-amplitude IGWs in Boussinesq fluids. The eigenvalue problem was solved numerically to compute instability growth rates. We also extended this eigenvalue problem to study instabilities of finite-amplitude AGWs in Boussinesq fluids permeated by magnetic fields.

We contoured the growth rate in wavenumber space to reveal bands of instability, i.e. locations at which the growth rate is non-zero. Increasing the resolution $\mathcal{N}$ of the truncated Fourier series representation of the disturbance increases the number of instability bands which appear in these plots. For the ranges of disturbance wavevector components α and β considered, the growth rate contour plots can be divided into three distinct regions at small values of a. The first region corresponds to AGW-AGW-AGW interactions, the second to AGW-AGW-AW interactions and the third to AGW-AW-AW interactions. Instabilities of AGWs induced by AGW-AGW-AGW interactions were found to behave similarly to the instabilities induced by IGW-IGW-IGW instabilities in the corresponding hydrodynamic setting. The instability bands are of the same shape in both the hydrodynamic regime and the magnetohydrodynamic regime, though the position and density of the bands is modified by adding a magnetic field and varies with magnetic field strength. AGW-AW-AW bands take the form of straight lines, with orientations that depend on the orientation ξ of the background magnetic field. As a general rule, increasing the magnetic field strength increases the proportion of parameter space which is unstable.

At parameter values for which the criteria for TRI are exactly satisfied, we were able to demonstrate agreement between the numerical Floquet growth rates and the growth rates predicted using asymptotic methods. For each band of instability, there is a curve traversing the centre of the band along which triadic resonance is exactly satisfied. In particular, we found agreement for IGW-IGW-IGW interactions, AGW-AGW-AGW interactions and AGW-AW-AW interactions. It would be natural to seek agreement for AGW-AGW-AW interactions too if the relevant asymptotic formula is derived in future work. Though the asymptotics predicted instability successfully in almost all cases considered, we observed one situation in which the asymptotics broke down. This was the case with $\boldsymbol{b}_0$ aligned with $\boldsymbol{k}$. Here, we encountered parameter choices at which the asymptotics predicted instabilities for which the numerical Floquet solver did not provide evidence. It would be useful to determine why this is the case in future work.

In the absence of a magnetic field, a plane IGW propagating through a Boussinesq fluid is specified by two parameters: the dimensionless amplitude a and the wavevector orientation θ. In the presence of a magnetic field, the wave is specified by two other parameters in addition to a and θ: the background magnetic field strength b_0 and the background magnetic field orientation ζ. Though the orientation of a 3D background magnetic field must be specified by two angles in spherical polar coordinates (ζ and ξ), the value of ξ has no effect on the primary wave. This is because in the dispersion relation describing the primary wave, the magnetic field appears only through the $\boldsymbol{K} \cdot \boldsymbol{B}_0$ term. Since $\boldsymbol{K}$ does not possess a Y-component, only the X and Z components of $\boldsymbol{B}_0$ are needed to specify the primary wave. The field orientation in the (X, Z)-plane is entirely specified by ζ.

McEwan and Robinson (1975) found that there is a linear relationship between the maximum growth rate of IGW instabilities and the wave amplitude a. There is no such linear relationship between the growth rate and θ, though a curve of the growth rate against θ can be produced. The linear relationship between the growth rate and a is preserved when a non-zero magnetic field is introduced. The gradient of this linear relationship is almost unchanged by increasing the magnetic field strength b_0. The maximum growth rate observed increases with the transition from $b_0 = 0$ to $b_0 \neq 0$, but not significantly, which is not obvious given that the dispersion relation of an IGW changes significantly when a magnetic field is introduced.

The background magnetic field $\boldsymbol{B}_0$ we used in this thesis was uniform. We made this assumption on the basis that we used a local Cartesian box model, small enough such that any variation in $\boldsymbol{B}_0$ was treated as negligible. We might expect $\boldsymbol{B}_0$ to vary significantly throughout the radial extent of a star, so a sensible extension to this work would be to consider vertical variation in $\boldsymbol{B}_0$ (i.e. a $\boldsymbol{B}_0(Z)$ profile). Based on the solar model of Christensen-Dalsgaard et al. (1996), the buoyancy frequency certainly varies across the radial extent of a stellar interior, so an $N(Z)$ profile could similarly be adopted in future work. TRIs of IGWs in a stably-stratified Boussinesq fluid with vertical variation in the buoyancy frequency profile have been studied by Kav et al. (2025). A similar model with an added magnetic field could be used to study TRIs of AGWs in the case where N has vertical variation.

We took the background state in this thesis to be one of magnetohydrostatic equilibrium. The unperturbed fluid was considered to be in a state of rest. Since the fluid in stars rotates, it makes sense to have a background flow. It is well established that many stars are differentially rotating at the radiative-convective interface, which naturally lends itself to a background shear profile. Future study could adopt a background shear profile like that of Salhi and Nasraoui (2013). We could use the Floquet method of this thesis to describe instabilities of AGWs propagating through the background shear flow.

An obvious extension to the work completed in this thesis is to peform nonlinear simulations of instabilities of AGWs propagating through Boussinesq fluids permeated by magnetic fields. This would make it possible to directly observe how instabilities affect mixing and the transfer of energy and momentum in such fluids. For boundary conditions, a 3D periodic Cartesian box would be used. The full nonlinear Boussinesq MHD equations could be solved via a spectral solver such as Dedalus (Burns et al., 2020). It would be useful to compare the results of these simulations with the linear stability analysis of Chapter 6. Nonlinear simulations of breaking IGWs have been performed by Liu et al. (2010), amongst many others. A sensible place to start regarding nonlinear simulations of AGWs could be to include a magnetic field in the model of Liu et al. (2010), for example.

We sought an understanding of what impact adding a magnetic field has on IGW instabilities. There is no reason to stop at adding a magnetic field, however. At the outset of this thesis we eliminated the dynamics of inertial waves by neglecting rotation. The effects of rotation can justifiably be removed from the governing equations in a number of astrophysical contexts. For instance, in the Sun, $N^2 \gg \Omega^2$ can be locally satisfied, where Ω is the local angular speed of the solar plasma. The influence of rotation is hence negligible compared to that of stratification at these locations. We can neglect rotation in the study of tidally-excited IGWs for similar reasons. In future work, a more complex problem would involve including rotation in the Boussinesq MHD equations. It would be interesting to derive analogous asymptotic formulae and an analogous Floquet eigenvalue problem to study gravito-inertial-Alfvén waves - waves restored by buoyancy, the Lorentz force and the Coriolis force. This would give us a system governed by the dispersion relation of Kumar et al. (1999), who attempted to quantify the transport of angular momentum induced by gravito-inertial-Alfvén waves in the solar radiative zone. Their dispersion relation reduces to our dispersion relation when the Coriolis force is neglected. It would be interesting to study what impact rotation has on the results of this thesis.

Our work has many applications in astrophysical fluids. The results we have obtained provide us with a greater understanding of the instabilities which play a role in mixing and the transport of energy and angular momentum in astrophysical fluids. Understanding wave instabilities is crucial for understanding the dynamics of stably-stratified, magnetised fluids.

Appendix A

Derivations and Formulae

A.1 The Boussinesq MHD Equations

A.1.1 Decomposing the Lorentz force

Here we demonstrate how equation (2.24) is formed from (2.14) by decomposing the Lorentz force into a magnetic pressure term and a magnetic tension term. The momentum equation for a stably-stratified Boussinesq fluid is

$$\frac{\mathrm{D}\boldsymbol{U}}{\mathrm{D}T} = -\frac{1}{\rho_0}\nabla\mathcal{P} + \frac{\rho\boldsymbol{g}}{\rho_0} + \nu\nabla^2\boldsymbol{U} + \frac{1}{\mu_0\rho_0}(\nabla\times\boldsymbol{B})\times\boldsymbol{B}. \tag{A.1}$$

Using a vector identity, the Lorentz force can be written as

$$\frac{(\nabla\times\boldsymbol{B})\times\boldsymbol{B}}{\mu_0} = \underbrace{\frac{(\boldsymbol{B}\cdot\nabla\boldsymbol{B})}{\mu_0}}_{\text{TENSION}} - \underbrace{\frac{\nabla(B^2)}{2\mu_0}}_{\text{PRESSURE}}. \tag{A.2}$$

Placing (A.2) into (A.1) yields

$$\frac{\mathrm{D}\boldsymbol{U}}{\mathrm{D}T} = -\frac{1}{\rho_0}\nabla\left(\mathcal{P} + \frac{B^2}{2\mu_0}\right) + \frac{\rho\boldsymbol{g}}{\rho_0} + \nu\nabla^2\boldsymbol{U} + \frac{1}{\mu_0\rho_0}\boldsymbol{B}\cdot\nabla\boldsymbol{B}.$$

We define P as the sum of the fluid pressure and the magnetic pressure.

$$P := \mathcal{P} + \frac{B^2}{2\mu_0}.$$

This completes the derivation of equation (2.24).

A.1.2 Decomposing the Magnetic Induction Term

Here we demonstrate how equation (2.25) is formed from equation (2.15) by reformulating the magnetic induction term. The induction equation is

$$\frac{\partial\boldsymbol{B}}{\partial T} = \nabla\times(\boldsymbol{U}\times\boldsymbol{B}) + \eta\nabla^2\boldsymbol{B}. \tag{A.3}$$

We can rewrite the magnetic induction term from the induction equation using the following vector identity:

$$\nabla\times(\boldsymbol{U}\times\boldsymbol{B}) = \boldsymbol{U}(\nabla\cdot\boldsymbol{B}) - \boldsymbol{B}(\nabla\cdot\boldsymbol{U}) + (\boldsymbol{B}\cdot\nabla)\boldsymbol{U} - (\boldsymbol{U}\cdot\nabla)\boldsymbol{B}. \tag{A.4}$$

Due to the solenoidal constraints, (A.4) reduces to

$$\nabla \times (\boldsymbol{U} \times \boldsymbol{B}) = (\boldsymbol{B} \cdot \nabla)\boldsymbol{U} - (\boldsymbol{U} \cdot \nabla)\boldsymbol{B}. \tag{A.5}$$

Placing (A.5) into (A.3) completes the derivation of (2.25).

A.1.3 Vanishing Nonlinearities

In this section we show that when we substitute the plane wave solution (2.93) into the ideal Boussinesq MHD equations (2.32)-(2.36), all terms which are nonlinear in plane wave quantities $\tilde{F}$ vanish identically. Nonlinear terms in (2.32)-(2.36) take one of two forms:

$$\tilde{\boldsymbol{U}} \cdot \nabla \tilde{F} \quad \text{or} \quad \tilde{\boldsymbol{B}} \cdot \nabla \tilde{F} \quad \text{for} \quad F \in \{\boldsymbol{U}, \boldsymbol{B}, \rho\}.$$

When we substitute using the exponential form of the solution, these become

$$\tilde{\boldsymbol{U}} \cdot \nabla \tilde{F} = [2a \exp(i\boldsymbol{K} \cdot \boldsymbol{X} - i\omega T)\boldsymbol{U}_W \cdot \nabla]\, \tilde{F}$$
$$\tilde{\boldsymbol{B}} \cdot \nabla \tilde{F} = [2a \exp(i\boldsymbol{K} \cdot \boldsymbol{X} - i\omega T)\boldsymbol{B}_W \cdot \nabla]\, \tilde{F}.$$

We now replace $\boldsymbol{U}_W$ and $\boldsymbol{B}_W$ using (2.101), revealing that each form identically vanishes.

$$\tilde{\boldsymbol{U}} \cdot \nabla \tilde{F} = \left[a\omega \exp(i\boldsymbol{K} \cdot \boldsymbol{X} - i\omega T) \left(\frac{\hat{\boldsymbol{X}}}{K_X} - \frac{\hat{\boldsymbol{Z}}}{K_Z} \right) \cdot (iK_X \hat{\boldsymbol{X}} + iK_Z \hat{\boldsymbol{Z}}) \right] \tilde{F} = 0,$$
$$\tilde{\boldsymbol{B}} \cdot \nabla \tilde{F} = \left[a(\boldsymbol{K} \cdot \boldsymbol{B}_0) \exp(i\boldsymbol{K} \cdot \boldsymbol{X} - i\omega T) \left(\frac{\hat{\boldsymbol{Z}}}{K_Z} - \frac{\hat{\boldsymbol{X}}}{K_X} \right) \cdot (iK_X \hat{\boldsymbol{X}} + iK_Z \hat{\boldsymbol{Z}}) \right] \tilde{F} = 0.$$

A.2 Eigenvalue Problem

A.2.1 Matrix Coefficients

HD Submatrices

In the absence of a magnetic field, the eigenvalue problem we solve in Chapter 4 is

$$M\boldsymbol{v} = \sigma \boldsymbol{v}, \tag{A.6}$$

where $\boldsymbol{v}$ is the vector defined as

$$\boldsymbol{v} = (u^x_{-\mathcal{N}}, u^z_{-\mathcal{N}}, \varrho_{-\mathcal{N}}, \ldots, u^x_0, u^z_0, \varrho_0, \ldots, u^x_{\mathcal{N}}, u^z_{\mathcal{N}}, \varrho_{\mathcal{N}}).$$

We define the matrix M as

$$M = \begin{pmatrix}
M^2_{-\mathcal{N}} & M^3_{-\mathcal{N}} & & & & & & & & \mathbb{O} \\
M^1_{1-\mathcal{N}} & M^2_{1-\mathcal{N}} & M^3_{1-\mathcal{N}} & & & & & & & \\
& M^1_{2-\mathcal{N}} & M^2_{2-\mathcal{N}} & M^3_{2-\mathcal{N}} & & & & & & \\
& & \ddots & \ddots & \ddots & & & & & \\
& & & M^1_0 & M^2_0 & M^3_0 & & & & \\
& & & & \ddots & \ddots & \ddots & & & \\
& & & & & M^1_{\mathcal{N}-2} & M^2_{\mathcal{N}-2} & M^3_{\mathcal{N}-2} & & \\
& & & & & & M^1_{\mathcal{N}-1} & M^2_{\mathcal{N}-1} & M^3_{\mathcal{N}-1} & \\
\mathbb{O} & & & & & & & M^1_{\mathcal{N}} & M^2_{\mathcal{N}} &
\end{pmatrix}.$$

where M_n^1, M_n^2 and M_n^3 are 3×3 matrix-valued functions of n (i.e. 3×3 blocks) extracted from the coefficients in (4.38)-(4.43), and $\mathbb{O}$ represents an appropriately-sized block of zeroes. The lower diagonal submatrices are given by

$$M_n^1 := \begin{pmatrix} -i\alpha u_w & -iu_w\left(1+\frac{2\alpha^2}{L_n}\right) & 0 \\ 0 & -i\alpha u_w\left(1+\frac{2(\gamma+n)}{L_n}\right) & 0 \\ 0 & -i\varrho_w & -i\alpha u_w \end{pmatrix}.$$

The main diagonal submatrices are given by

$$M_n^2 := \begin{pmatrix} \Gamma_n^\nu & 0 & \left(1+\frac{\alpha^2}{L_n}\right)\frac{k_x}{k_z} - \frac{\alpha(\gamma+n)}{L_n} \\ 0 & \Gamma_n^\nu & \frac{\gamma+n}{L_n}\left[\alpha\frac{k_x}{k_z}-(\gamma+n)\right]-1 \\ -k_xk_z & k_z^2 & \Gamma_n^\kappa \end{pmatrix}.$$

The upper diagonal submatrices are given by

$$M_n^3 := \begin{pmatrix} -i\alpha u_w & iu_w\left(1+\frac{2\alpha^2}{L_n}\right) & 0 \\ 0 & i\alpha u_w\left(\frac{2(\gamma+n)}{L_n}-1\right) & 0 \\ 0 & -i\varrho_w & -i\alpha u_w \end{pmatrix}.$$

MHD Submatrices

In the MHD context of Chapter 6, the eigenvalue problem is the same as (A.6) used in Chapter 4, except for the following differences. The vector $\boldsymbol{v}$ is now defined as

$$\boldsymbol{v} = (u^x_{-\mathcal{N}}, u^z_{-\mathcal{N}}, b^x_{-\mathcal{N}}, b^z_{-\mathcal{N}}, \varrho_{-\mathcal{N}}, \dots, u^x_0, u^z_0, b^x_0, b^z_0, \varrho_0, \dots, u^x_{\mathcal{N}}, u^z_{\mathcal{N}}, b^x_{\mathcal{N}}, b^z_{\mathcal{N}}, \varrho_{\mathcal{N}}).$$

The lower diagonal submatrices are now given by

$$M_n^1 := \begin{pmatrix} -i\alpha u_w & -iu_w\left(1+\frac{2\alpha^2}{L_n}\right) & i\alpha b_w & ib_w\left(1+\frac{2\alpha^2}{L_n}\right) & 0 \\ 0 & -i\alpha u_w\left(1+\frac{2(\gamma+n)}{L_n}\right) & 0 & i\alpha b_w\left(1+\frac{2(\gamma+n)}{L_n}\right) & 0 \\ i\alpha b_w & -ib_w & -i\alpha u_w & iu_w & 0 \\ 0 & i\alpha b_w & 0 & -i\alpha u_w & 0 \\ 0 & -i\varrho_w & 0 & 0 & -i\alpha u_w \end{pmatrix}.$$

The main diagonal submatrices are now given by

$$M_n^2 := \begin{pmatrix} \Gamma_n^\nu & 0 & i\boldsymbol{k'}\cdot\boldsymbol{b}_0 & 0 & \left(1+\frac{\alpha^2}{L_n}\right)\frac{k_x}{k_z}-\frac{\alpha(\gamma+n)}{L_n} \\ 0 & \Gamma_n^\nu & 0 & i\boldsymbol{k'}\cdot\boldsymbol{b}_0 & \frac{\gamma+n}{L_n}\left[\alpha\frac{k_x}{k_z}-(\gamma+n)\right]-1 \\ i\boldsymbol{k'}\cdot\boldsymbol{b}_0 & 0 & \Gamma_n^\eta & 0 & 0 \\ 0 & i\boldsymbol{k'}\cdot\boldsymbol{b}_0 & 0 & \Gamma_n^\eta & 0 \\ -k_xk_z & k_z^2 & 0 & 0 & \Gamma_n^\kappa \end{pmatrix}.$$

The upper diagonal submatrices are now given by

$$M_n^3 := \begin{pmatrix} -i\alpha u_w & iu_w\left(1+\frac{2\alpha^2}{L_n}\right) & i\alpha b_w & -ib_w\left(1+\frac{2\alpha^2}{L_n}\right) & 0 \\ 0 & i\alpha u_w\left(\frac{2(\gamma+n)}{L_n}-1\right) & 0 & i\alpha b_w\left(1-\frac{2(\gamma+n)}{L_n}\right) & 0 \\ i\alpha b_w & ib_w & -i\alpha u_w & -iu_w & 0 \\ 0 & i\alpha b_w & 0 & -i\alpha u_w & 0 \\ 0 & -i\varrho_w & 0 & 0 & -i\alpha u_w \end{pmatrix}.$$

A.2.2 Symmetry Arguments

In this section we explain why can freely reduce the domains for (α, β, γ) to $\alpha \geq 0$, $\beta \geq 0$ and $\gamma \in [-1/2, 1/2)$ in numerical computations without any loss of important information. This relies on the following three symmetry arguments, which were made by Lombard and Riley (1996). If σ is an eigenvalue of M at (α, β, γ) with eigenvector $(\hat{u}_x, \hat{u}_y, \hat{u}_z, \hat{b}_x, \hat{b}_y, \hat{b}_z, \hat{p}, \hat{\varrho})$, then:

1. σ is an eigenvalue of M at $(\alpha, -\beta, \gamma)$ with eigenvector $(\hat{u}_x, \hat{u}_y, \hat{u}_z, \hat{b}_x, \hat{b}_y, \hat{b}_z, \hat{p}, \hat{\varrho})$,
2. σ^* is an eigenvalue of M at $-(\alpha, \beta, \gamma)$ with eigenvector $(\hat{u}_x^*, \hat{u}_y^*, \hat{u}_z^*, \hat{b}_x^*, \hat{b}_y^*, \hat{b}_z^*, \hat{p}^*, \hat{\varrho}^*)$,
3. σ is an eigenvalue of M at $(\alpha, \beta, \gamma + 1)$ with eigenvector $(\hat{u}_x, \hat{u}_y, \hat{u}_z, \hat{b}_x, \hat{b}_y, \hat{b}_z, \hat{p}, \hat{\varrho})$.

Because the Y-coordinate is unaffected by the rotation of the coordinate axes, the equations of motion are invariant under the transformation $\beta \to -\beta$. This justifies argument (1). For an eigenvalue σ^* at $-(\alpha, \beta, \gamma)$, the corresponding equations equivalent to (4.32)-(4.34) in Chapter 4 and the equations (6.42)-(6.45) in Chapter 6 are simply the complex conjugates of themselves. This justifies argument (2). The coefficient of z in the exponential representation (4.36) of the disturbance is $n + \gamma$. Since the summation in (4.36) is infinite, the exponential representation is invariant under the transformation $n + \gamma \to n + \gamma + m$, where m is an integer. Since n only takes integer values, (4.36) is invariant under the transformation $\gamma \to \gamma + m$ too. This justifies argument (3).

A.3 Asymptotics

A.3.1 Deriving the HD Amplitude Equations

Here we show how the coefficients c_1, c_2, c_3 and c_4 in amplitude equations (3.59) are derived by expanding the forcing terms contained within $\boldsymbol{G}$ in Chapter 3. Recall that the general solution to the leading order equation $\mathcal{L}\boldsymbol{U}_0' = 0$ is

$$\begin{aligned}\boldsymbol{U}_0' =& A(\tau)\boldsymbol{U}_A E_A + A^*(\tau)\boldsymbol{U}_A^* E_{-A} + \\ & B(\tau)\boldsymbol{U}_B E_B + B^*(\tau)\boldsymbol{U}_B^* E_{-B}.\end{aligned}$$

Recall from (2.101) that the primary wave can be expressed as

$$\tilde{\boldsymbol{U}} = a\check{\boldsymbol{U}} = a\boldsymbol{U}_W(E_W + E_{-W}), \tag{A.7}$$
$$\tilde{\rho} = a\check{\rho} = a\rho_W(E_W - E_{-W}). \tag{A.8}$$

Hence our forcing terms $\boldsymbol{F}_U$ and F_ρ (given by (3.43) and (3.44)) expand in the following way:

$$\begin{aligned}\boldsymbol{F}_U =& \left(\frac{\partial A}{\partial \tau}\boldsymbol{U}_A + iA\left[(\boldsymbol{K}_A \cdot \boldsymbol{U}_W)(E_W + E_{-W})\boldsymbol{U}_A + (\boldsymbol{K}_W \cdot \boldsymbol{U}_A)(E_W - E_{-W})\boldsymbol{U}_W\right]\right) E_A + \\ & \left(\frac{\partial B}{\partial \tau}\boldsymbol{U}_B + iB\left[(\boldsymbol{K}_B \cdot \boldsymbol{U}_W)(E_W + E_{-W})\boldsymbol{U}_B + (\boldsymbol{K}_W \cdot \boldsymbol{U}_B)(E_W - E_{-W})\boldsymbol{U}_W\right]\right) E_B + \text{c.c.} \\ F_\rho =& \left(\frac{\partial A}{\partial \tau}\rho_A + iA\left[(\boldsymbol{K}_A \cdot \boldsymbol{U}_W)(E_W + E_{-W})\rho_A + (\boldsymbol{K}_W \cdot \boldsymbol{U}_A)(E_W + E_{-W})\rho_W\right]\right) E_A + \\ & \left(\frac{\partial B}{\partial \tau}\rho_B + iB\left[(\boldsymbol{K}_B \cdot \boldsymbol{U}_W)(E_W + E_{-W})\rho_B + (\boldsymbol{K}_W \cdot \boldsymbol{U}_B)(E_W + E_{-W})\rho_W\right]\right) E_B + \text{c.c.}\end{aligned}$$

Above, c.c. is used to denote the complex conjugate of the terms that precede it. As a result of resonance conditions (3.12) and (3.13), some of the exponentials in the formulae for $\boldsymbol{F}_U$ and F_ρ simplify according to the following relations:

$$E_W E_A = E_B \quad \text{and} \quad E_{-W} E_B = E_A.$$

We put these into the formulae for $\boldsymbol{F}_U$ and F_ρ to reveal which are the only terms we need to retain in order to explicitly state the solvability conditions. In other words, we may rewrite $\boldsymbol{F}_U$ and F_ρ as

$$\begin{aligned}
\boldsymbol{F}_U &:= \left[\frac{\partial A}{\partial \tau}\boldsymbol{U}_A + iB(\boldsymbol{K}_B \cdot \boldsymbol{U}_w)\boldsymbol{U}_B - iB(\boldsymbol{K}_W \cdot \boldsymbol{U}_B)\boldsymbol{U}_W\right] E_A + \\
&\quad \left[\frac{\partial B}{\partial \tau}\boldsymbol{U}_B + iA(\boldsymbol{K}_A \cdot \boldsymbol{U}_W)\boldsymbol{U}_A + iA(\boldsymbol{K}_W \cdot \boldsymbol{U}_A)\boldsymbol{U}_W\right] E_B + \ldots \\
F_\rho &:= \left[\frac{\partial A}{\partial \tau}\rho_A + iB(\boldsymbol{K}_B \cdot \boldsymbol{U}_W)\rho_B + iB(\boldsymbol{K}_W \cdot \boldsymbol{U}_B)\rho_W\right] E_A + \\
&\quad \left[\frac{\partial B}{\partial \tau}\rho_B + iA(\boldsymbol{K}_A \cdot \boldsymbol{U}_W)\rho_A + iA(\boldsymbol{K}_W \cdot \boldsymbol{U}_A)\rho_W\right] E_B + \ldots
\end{aligned}$$

The ellipses contain terms proportional to exponential factors other than E_A or E_B, as well as the relevant complex conjugates. The next task is to use these expressions for $\boldsymbol{F}_U$ and F_ρ to expand the Z-component G_Z of $\boldsymbol{G}$. To do so, we define the following objects:

$$G_{UZ} := \partial_Z(\nabla_\perp \cdot \partial_\tau \boldsymbol{F}_U) - \nabla_\perp^2 \partial_T F_{UZ} \quad \text{and} \quad G_{\rho Z} := \nabla_\perp^2 F_\rho,$$

such that

$$G_Z = G_{UZ} + G_{\rho Z}.$$

We start by expanding G_{UZ}.

$$\begin{aligned}
G_{UZ} = &- i\omega_A K_A^2 \partial_\tau A U_{AZ} E_A - i\omega_A K_A^2 \partial_\tau A U_{AZ} E_A \\
&+ B\omega_A(\boldsymbol{K}_W \cdot \boldsymbol{U}_B)(K_{AX}K_{AZ}U_{WX} - K_{A\perp}^2 U_{WZ})E_A \\
&- A\omega_B(\boldsymbol{K}_w \cdot \boldsymbol{U}_A)(K_{BX}K_{BZ}U_{WX} - K_{B\perp}^2 U_{WZ})E_B \\
&- B\omega_A(\boldsymbol{K}_B \cdot \boldsymbol{U}_W)(K_{AX}K_{AZ}U_{BX} + K_{AY}K_{AZ}U_{BY} - K_{A\perp}^2 U_{BZ})E_A \\
&- A\omega_B(\boldsymbol{K}_A \cdot \boldsymbol{U}_W)(K_{BX}K_{BZ}U_{AX} + K_{BY}K_{BZ}U_{AY} - K_{B\perp}^2 U_{AZ})E_B + \ldots
\end{aligned}$$

Expanding $G_{\rho Z}$ gives

$$\begin{aligned}
G_{\rho Z} = &- K_{A\perp}^2[\partial_\tau A \rho_A + iB(\boldsymbol{K}_B \cdot \boldsymbol{U}_W)\rho_B + iB(\boldsymbol{K}_W \cdot \boldsymbol{U}_B)\rho_w]E_A \\
&- K_{B\perp}^2[\partial_\tau B \rho_B + iA(\boldsymbol{K}_A \cdot \boldsymbol{U}_W)\rho_A + iA(\boldsymbol{K}_W \cdot \boldsymbol{U}_A)\rho_W]E_B + \ldots
\end{aligned}$$

Extracting coefficients from the above expressions for G_{UZ} and $G_{\rho Z}$ yields the coefficients c_1, c_2, c_3 and c_4 appearing in the amplitude equations (3.59).

A.3.2 Deriving the MHD Amplitude Equations

Here we show how the coefficients c_1, c_2, c_3 and c_4 from the amplitude equations (5.80) are derived for both AGW-AGW-AGW interactions and AGW-AW-AW interactions. We give explicit expressions for the forcing terms mentioned in Chapter 5 in their most general form. Recall that the general solution to the leading order equation (5.48) is

$$\begin{aligned}\boldsymbol{U}_0' =& A(\tau)\boldsymbol{U}_A E_A + A^*(\tau)\boldsymbol{U}_A^* E_{-A} + \\ & B(\tau)\boldsymbol{U}_B E_B + B^*(\tau)\boldsymbol{U}_B^* E_{-B},\end{aligned}$$

and from (2.98)-(2.100) that the primary wave can be expressed as

$$\tilde{\boldsymbol{U}} = a\check{\boldsymbol{U}} = a\boldsymbol{U}_W(E_W + E_{-W}), \tag{A.9}$$

$$\tilde{\boldsymbol{B}} = a\check{\boldsymbol{B}} = a\boldsymbol{B}_W(E_W + E_{-W}), \tag{A.10}$$

$$\tilde{\rho} = a\check{\rho} = a\rho_W(E_W - E_{-W}). \tag{A.11}$$

Hence the forcing term $\boldsymbol{F}_U$ given by (5.68) can be expanded in the following way:

$$\begin{aligned}\boldsymbol{F}_U =& \frac{\partial A}{\partial \tau}\boldsymbol{U}_A E_A + \frac{\partial B}{\partial \tau}\boldsymbol{U}_B E_B + \\ & iA\left[(\boldsymbol{K}_A\cdot\boldsymbol{U}_W)(E_W+E_{-W})\boldsymbol{U}_A + (\boldsymbol{K}_W\cdot\boldsymbol{U}_A)(E_W-E_{-W})\boldsymbol{U}_W\right]E_A + \\ & iB\left[(\boldsymbol{K}_B\cdot\boldsymbol{U}_W)(E_W+E_{-W})\boldsymbol{U}_B + (\boldsymbol{K}_W\cdot\boldsymbol{U}_B)(E_W-E_{-W})\boldsymbol{U}_W\right]E_B - \\ & iA\left[(\boldsymbol{K}_A\cdot\boldsymbol{B}_W)(E_W+E_{-W})\boldsymbol{B}_A + (\boldsymbol{K}_W\cdot\boldsymbol{B}_A)(E_W-E_{-W})\boldsymbol{B}_W\right]E_A - \\ & iB\left[(\boldsymbol{K}_B\cdot\boldsymbol{B}_W)(E_W+E_{-W})\boldsymbol{B}_B + (\boldsymbol{K}_W\cdot\boldsymbol{B}_B)(E_W-E_{-W})\boldsymbol{B}_W\right]E_B + \text{c.c.}\end{aligned}$$

The forcing term $\boldsymbol{F}_B$ given by (5.69) is expanded as

$$\begin{aligned}\boldsymbol{F}_B =& \frac{\partial A}{\partial \tau}\boldsymbol{B}_A E_A + \frac{\partial B}{\partial \tau}\boldsymbol{B}_B E_B + \\ & iA\left[(\boldsymbol{K}_A\cdot\boldsymbol{U}_W)(E_W+E_{-W})\boldsymbol{B}_A + (\boldsymbol{K}_W\cdot\boldsymbol{U}_A)(E_W-E_{-W})\boldsymbol{B}_W\right]E_A + \\ & iB\left[(\boldsymbol{K}_B\cdot\boldsymbol{U}_W)(E_W+E_{-W})\boldsymbol{B}_B + (\boldsymbol{K}_w\cdot\boldsymbol{U}_B)(E_W-E_{-W})\boldsymbol{B}_W\right]E_B - \\ & iA\left[(\boldsymbol{K}_A\cdot\boldsymbol{B}_W)(E_W+E_{-W})\boldsymbol{U}_A + (\boldsymbol{K}_W\cdot\boldsymbol{B}_A)(E_W-E_{-W})\boldsymbol{U}_W\right]E_A - \\ & iB\left[(\boldsymbol{K}_B\cdot\boldsymbol{B}_W)(E_W+E_{-W})\boldsymbol{U}_B + (\boldsymbol{K}_W\cdot\boldsymbol{B}_B)(E_W-E_{-W})\boldsymbol{U}_W\right]E_B + \text{c.c.}\end{aligned}$$

The forcing term F_ρ given by (5.70) is expanded as

$$\begin{aligned}F_\rho =& \frac{\partial A}{\partial \tau}\rho_A E_A + \frac{\partial B}{\partial \tau}\rho_B E_B + \\ & iA\left[(\boldsymbol{K}_A\cdot\boldsymbol{U}_W)(E_W+E_{-W})\rho_A + (\boldsymbol{K}_W\cdot\boldsymbol{U}_A)(E_W+E_{-W})\rho_W\right]E_A + \\ & iB\left[(\boldsymbol{K}_B\cdot\boldsymbol{U}_W)(E_W+E_{-W})\rho_B + (\boldsymbol{K}_W\cdot\boldsymbol{U}_B)(E_W+E_{-W})\rho_W\right]E_B + \text{c.c.}\end{aligned}$$

Above, c.c. used to denote the complex conjugate of the terms that precede it. As a result of the resonance conditions (5.1) and (5.2), some of the exponentials in the formulae for $\boldsymbol{F}_U$, $\boldsymbol{F}_B$ and F_ρ simplify according to the following relations:

$$E_W E_A = E_B, \quad E_{-W}E_B = E_A. \tag{A.12}$$

We place (A.12) into the formulae for $\boldsymbol{F}_U$, $\boldsymbol{F}_B$ and F_ρ to reveal which are the only terms we need to retain in order to explicitly state the solvability conditions. In other words, we may rewrite $\boldsymbol{F}_U$ as

$$\begin{aligned}\boldsymbol{F}_U :=& \frac{\partial A}{\partial \tau}\boldsymbol{U}_A E_A + \frac{\partial B}{\partial \tau}\boldsymbol{U}_B E_B + \\ & iB\left[(\boldsymbol{K}_B\cdot\boldsymbol{U}_W)\boldsymbol{U}_B - (\boldsymbol{K}_B\cdot\boldsymbol{B}_W)\boldsymbol{B}_B - (\boldsymbol{K}_W\cdot\boldsymbol{U}_B)\boldsymbol{U}_W + (\boldsymbol{K}_W\cdot\boldsymbol{B}_B)\boldsymbol{B}_W\right]E_A + \\ & iA\left[(\boldsymbol{K}_A\cdot\boldsymbol{U}_W)\boldsymbol{U}_A - (\boldsymbol{K}_A\cdot\boldsymbol{B}_W)\boldsymbol{B}_A + (\boldsymbol{K}_W\cdot\boldsymbol{U}_A)\boldsymbol{U}_W - (\boldsymbol{K}_W\cdot\boldsymbol{B}_A)\boldsymbol{B}_W\right]E_B + \ldots\end{aligned}$$

We may rewrite $\boldsymbol{F}_B$ as

$$\begin{aligned}\boldsymbol{F}_B \coloneqq& \frac{\partial A}{\partial \tau}\boldsymbol{B}_A E_A + \frac{\partial B}{\partial \tau}\boldsymbol{B}_B E_B + \\ & iB\left[(\boldsymbol{K}_B \cdot \boldsymbol{U}_W)\boldsymbol{B}_B - (\boldsymbol{K}_B \cdot \boldsymbol{B}_W)\boldsymbol{U}_B - (\boldsymbol{K}_W \cdot \boldsymbol{U}_B)\boldsymbol{B}_W + (\boldsymbol{K}_W \cdot \boldsymbol{B}_B)\boldsymbol{U}_W\right] E_A + \\ & iA\left[(\boldsymbol{K}_A \cdot \boldsymbol{U}_W)\boldsymbol{B}_A - (\boldsymbol{K}_A \cdot \boldsymbol{B}_W)\boldsymbol{U}_A + (\boldsymbol{K}_W \cdot \boldsymbol{U}_A)\boldsymbol{B}_W - (\boldsymbol{K}_W \cdot \boldsymbol{B}_A)\boldsymbol{U}_W\right] E_B + \ldots\end{aligned}$$

We may rewrite F_ρ as

$$\begin{aligned}F_\rho \coloneqq& \frac{\partial A}{\partial \tau}\rho_A E_A + \frac{\partial B}{\partial \tau}\rho_B E_B \\ & iB\left[(\boldsymbol{K}_B \cdot \boldsymbol{U}_W)\rho_B + (\boldsymbol{K}_W \cdot \boldsymbol{U}_B)\rho_W\right] E_A + \\ & iA\left[(\boldsymbol{K}_A \cdot \boldsymbol{U}_W)\rho_A + (\boldsymbol{K}_W \cdot \boldsymbol{U}_A)\rho_W\right] E_B + \ldots\end{aligned}$$

The ellipses contain terms proportional to exponential factors other than E_A and E_B, as well as the relevant complex conjugates.

AGW Forcing Terms

In this section, we show how the MHD forcing terms provided above can be used to derive the coeffients c_i for AGWs in the amplitude equations (5.80). The explicit forms of G_{AZ} and G_{BZ} are

$$\begin{aligned}G_{AZ} &= i\omega_A K_{AZ}(\boldsymbol{K}_A \cdot \boldsymbol{F}_{uA}) - i\omega_A K_A^2 F_{uAZ} + iK_A^2(\boldsymbol{K}_A \cdot \boldsymbol{B}_0)F_{bAZ} - K_{A\perp}^2 F_{\rho A}, \\ G_{BZ} &= i\omega_B K_{BZ}(\boldsymbol{K}_B \cdot \boldsymbol{F}_{uB}) - i\omega_B K_B^2 F_{uBZ} + iK_B^2(\boldsymbol{K}_B \cdot \boldsymbol{B}_0)F_{bBZ} - K_{B\perp}^2 F_{\rho B}.\end{aligned}$$

The forcing terms are given by

$$\begin{aligned}\boldsymbol{F}_{uA} &\coloneqq \frac{\partial A}{\partial \tau}\boldsymbol{U}_A + iB\left[(\boldsymbol{K}_B \cdot \boldsymbol{U}_W)\boldsymbol{U}_B - (\boldsymbol{K}_B \cdot \boldsymbol{B}_W)\boldsymbol{B}_B - (\boldsymbol{K}_W \cdot \boldsymbol{U}_B)\boldsymbol{U}_W + (\boldsymbol{K}_W \cdot \boldsymbol{B}_B)\boldsymbol{B}_W\right], \\ \boldsymbol{F}_{uB} &\coloneqq \frac{\partial B}{\partial \tau}\boldsymbol{U}_B + iA\left[(\boldsymbol{K}_A \cdot \boldsymbol{U}_W)\boldsymbol{U}_A - (\boldsymbol{K}_A \cdot \boldsymbol{B}_W)\boldsymbol{B}_A + (\boldsymbol{K}_W \cdot \boldsymbol{U}_A)\boldsymbol{U}_W - (\boldsymbol{K}_W \cdot \boldsymbol{B}_A)\boldsymbol{B}_W\right], \\ \boldsymbol{F}_{bA} &\coloneqq \frac{\partial A}{\partial \tau}\boldsymbol{B}_A + iB\left[(\boldsymbol{K}_B \cdot \boldsymbol{U}_W)\boldsymbol{B}_B - (\boldsymbol{K}_B \cdot \boldsymbol{B}_W)\boldsymbol{U}_B - (\boldsymbol{K}_W \cdot \boldsymbol{U}_B)\boldsymbol{B}_W + (\boldsymbol{K}_W \cdot \boldsymbol{B}_B)\boldsymbol{U}_W\right], \\ \boldsymbol{F}_{bB} &\coloneqq \frac{\partial B}{\partial \tau}\boldsymbol{B}_B + iA\left[(\boldsymbol{K}_A \cdot \boldsymbol{U}_W)\boldsymbol{B}_A - (\boldsymbol{K}_A \cdot \boldsymbol{B}_W)\boldsymbol{U}_A + (\boldsymbol{K}_W \cdot \boldsymbol{U}_A)\boldsymbol{B}_W - (\boldsymbol{K}_W \cdot \boldsymbol{B}_A)\boldsymbol{U}_W\right], \\ F_{\rho A} &\coloneqq \frac{\partial A}{\partial \tau}\rho_A + iB\left[(\boldsymbol{K}_B \cdot \boldsymbol{U}_W)\rho_B + (\boldsymbol{K}_W \cdot \boldsymbol{U}_B)\rho_W\right], \\ F_{\rho B} &\coloneqq \frac{\partial B}{\partial \tau}\rho_B + iA\left[(\boldsymbol{K}_A \cdot \boldsymbol{U}_W)\rho_A + (\boldsymbol{K}_W \cdot \boldsymbol{U}_A)\rho_W\right].\end{aligned}$$

Extracting coefficients from the above expressions yields the expressions for c_i for the AGW amplitude equations.

AW Forcing Terms

In this section, we show how the MHD forcing terms in their most general from provided above can be used to derive the coeffients c_i for AWs in the amplitude equations (5.80). When daughter wave A is an AW, the explicit forms of G_{AX} and G_{AY} are

$$\begin{aligned}G_{AX} &= i\omega_A K_{AX}(\boldsymbol{K}_A \cdot \boldsymbol{F}_{uA}) + i\omega_A K_A^2(F_{bAX} - F_{uAX}) + K_{AX}K_{AZ}F_{\rho A}, \\ G_{AY} &= i\omega_A K_{AY}(\boldsymbol{K}_A \cdot \boldsymbol{F}_{uA}) + i\omega_A K_A^2(F_{bAY} - F_{uAY}) + K_{AY}K_{AZ}F_{\rho A},\end{aligned}$$

where the forcing terms for daughter wave A are given by

$$
\begin{aligned}
\boldsymbol{F}_{uA} &= \frac{\partial A}{\partial \tau}\boldsymbol{U}_A + iB\left[\boldsymbol{K}_B \cdot (\boldsymbol{U}_W - \boldsymbol{B}_W)\boldsymbol{U}_B + (\boldsymbol{K}_W \cdot \boldsymbol{U}_B)(\boldsymbol{B}_W - \boldsymbol{U}_W)\right], \\
\boldsymbol{F}_{bA} &= -\frac{\partial A}{\partial \tau}\boldsymbol{U}_A + iB\left[\boldsymbol{K}_B \cdot (\boldsymbol{U}_W - \boldsymbol{B}_W)\boldsymbol{U}_B + (\boldsymbol{K}_W \cdot \boldsymbol{U}_B)(\boldsymbol{U}_W - \boldsymbol{B}_W)\right], \\
F_{\rho A} &= \frac{\partial A}{\partial \tau}\rho_A + iB\left[(\boldsymbol{K}_B \cdot \boldsymbol{U}_W)\rho_B + (\boldsymbol{K}_W \cdot \boldsymbol{U}_B)\rho_W\right].
\end{aligned}
$$

When daughter wave B is an AW, the explicit forms of G_{BX} and G_{BY} are

$$
\begin{aligned}
G_{BX} &= i\omega_B K_{BX}(\boldsymbol{K}_B \cdot \boldsymbol{F}_{uB}) - i\omega_B K_B^2(F_{uBX} + F_{bBX}) + K_{BX}K_{BZ}F_{\rho B}, \\
G_{BY} &= i\omega_B K_{BY}(\boldsymbol{K}_B \cdot \boldsymbol{F}_{uB}) - i\omega_B K_B^2(F_{uBY} + F_{bBY}) + K_{BY}K_{BZ}F_{\rho B},
\end{aligned}
$$

where the forcing terms for daughter wave B are given by

$$
\begin{aligned}
\boldsymbol{F}_{uB} &= \frac{\partial B}{\partial \tau}\boldsymbol{U}_B + iA\left[(\boldsymbol{K}_A \cdot (\boldsymbol{U}_W + \boldsymbol{B}_W))\boldsymbol{U}_A + (\boldsymbol{K}_W \cdot \boldsymbol{U}_A)(\boldsymbol{U}_W + \boldsymbol{B}_W)\right], \\
\boldsymbol{F}_{bB} &= \frac{\partial B}{\partial \tau}\boldsymbol{U}_B + iA\left[-(\boldsymbol{K}_A \cdot (\boldsymbol{U}_W + \boldsymbol{B}_W))\boldsymbol{U}_A + (\boldsymbol{K}_W \cdot \boldsymbol{U}_A)(\boldsymbol{U}_W + \boldsymbol{B}_W)\right], \\
F_{\rho B} &= \frac{\partial B}{\partial \tau}\rho_B + iA\left[(\boldsymbol{K}_A \cdot \boldsymbol{U}_W)\rho_A + (\boldsymbol{K}_W \cdot \boldsymbol{U}_A)\rho_W\right].
\end{aligned}
$$

Extracting coefficients from the above expressions yields the expressions for c_i for the AW amplitude equations.

A.3.3 Short Wavelength Limit

In this section we show how formula (3.65) for the growth rate of an IGW TRI in the short wavelength limit is derived. When eliminating any appearances of daughter wave B using relations (3.18)-(3.19), the approximate expressions for the coefficients c_1, c_2, c_3 and c_4 become

$$
\begin{aligned}
c_1 \approx &- 2i\omega_A K_A^2 K_{A\perp}^2, \\
c_2 \approx &- \omega_A(\boldsymbol{K}_W \cdot \boldsymbol{U}_A)(\boldsymbol{U}_A \cdot \boldsymbol{U}_W) \\
&+ \omega_A(\boldsymbol{K}_A \cdot \boldsymbol{U}_W)(\boldsymbol{U}_A \cdot \boldsymbol{U}_A) \\
&+ i\rho_A(\boldsymbol{K}_A \cdot \boldsymbol{U}_W)(\boldsymbol{K}_{A\perp} \cdot \boldsymbol{K}_{A\perp}) \\
&- i\rho_W(\boldsymbol{K}_W \cdot \boldsymbol{U}_A)(\boldsymbol{K}_{A\perp} \cdot \boldsymbol{K}_{A\perp}),
\end{aligned}
$$

along with

$$
\begin{aligned}
c_3 \approx &+ 2i\omega_A K_A^2 K_{A\perp}^2, \\
c_4 \approx &- \omega_A(\boldsymbol{K}_W \cdot \boldsymbol{U}_A)(\boldsymbol{U}_A \cdot \boldsymbol{U}_W) \\
&- \omega_A(\boldsymbol{K}_A \cdot \boldsymbol{U}_W)(\boldsymbol{U}_A \cdot \boldsymbol{U}_A) \\
&- i\rho_A(\boldsymbol{K}_A \cdot \boldsymbol{U}_W)(\boldsymbol{K}_{A\perp} \cdot \boldsymbol{K}_{A\perp}) \\
&- i\rho_W(\boldsymbol{K}_W \cdot \boldsymbol{U}_A)(\boldsymbol{K}_{A\perp} \cdot \boldsymbol{K}_{A\perp}).
\end{aligned}
$$

We get

$$
\begin{aligned}
c_2 c_4 \approx &+ \omega_A^2\left[(\boldsymbol{K}_W \cdot \boldsymbol{U}_A)^2(\boldsymbol{U}_A \cdot \boldsymbol{U}_W)^2 - (\boldsymbol{K}_A \cdot \boldsymbol{U}_W)^2(\boldsymbol{U}_A \cdot \boldsymbol{U}_A)^2\right] \\
&+ 2i\omega_A K_{A\perp}^4\left[\rho_W(\boldsymbol{U}_A \cdot \boldsymbol{U}_W)(\boldsymbol{K}_W \cdot \boldsymbol{U}_A)^2 - \rho_A(\boldsymbol{U}_A \cdot \boldsymbol{U}_A)(\boldsymbol{K}_A \cdot \boldsymbol{U}_W)^2\right] \\
&+ K_{A\perp}^4\left[\rho_A^2(\boldsymbol{K}_A \cdot \boldsymbol{U}_W)^2 - \rho_W^2(\boldsymbol{K}_W \cdot \boldsymbol{U}_A)^2\right].
\end{aligned}
$$

Since we are conisidering a limit in which $K_A \gg K_W$, we can remove several of these terms by making order of magnitude estimates. We first make some deductions regarding the sizes of individual variables. For primary wave quantities, we can say that

$$\boldsymbol{K}_W \sim 1, \quad \boldsymbol{U}_W \sim 1, \quad \rho_W \sim 1.$$

For daughter wave quantities, we can say that

$$\omega_A \sim 1, \quad K_{A\perp} \sim K_A, \quad \boldsymbol{U}_A \sim K_A^2, \quad \rho_A \sim K_A^2.$$

We may then compare the relative sizes of each term from $c_2 c_4$:

$$\begin{aligned}
\omega_A^2 (\boldsymbol{K}_W \cdot \boldsymbol{U}_A)^2 (\boldsymbol{U}_A \cdot \boldsymbol{U}_W)^2 &\sim K_A^8,\\
\omega_A^2 (\boldsymbol{K}_A \cdot \boldsymbol{U}_W)^2 (\boldsymbol{U}_A \cdot \boldsymbol{U}_A)^2 &\sim K_A^{10},\\
K_{A\perp}^4 \rho_W^2 (\boldsymbol{K}_W \cdot \boldsymbol{U}_A)^2 &\sim K_A^8,\\
K_{A\perp}^4 \rho_A^2 (\boldsymbol{K}_A \cdot \boldsymbol{U}_W)^2 &\sim K_A^{10},\\
2i\omega_A K_{A\perp}^2 \rho_w (\boldsymbol{U}_A \cdot \boldsymbol{U}_W)(\boldsymbol{K}_W \cdot \boldsymbol{U}_A)^2 &\sim K_A^8,\\
2i\omega_A K_{A\perp}^2 \rho_A (\boldsymbol{U}_A \cdot \boldsymbol{U}_A)(\boldsymbol{K}_A \cdot \boldsymbol{U}_W)^2 &\sim K_A^{10}.
\end{aligned}$$

We find that terms can be grouped into just two orders of magnitude: those of size $O(K_A^8)$ and those of size $O(K_A^{10})$. Since we are considering the limit in which K_A is large, it is instructive to maintain only the terms of size $O(K_A^{10})$. This reduces $c_2 c_4$ to

$$c_2 c_4 \approx -(\boldsymbol{K}_A \cdot \boldsymbol{U}_W)^2 (\omega_A U_A^2 + i\rho_A K_{A\perp}^2)^2 + O(a^2 K_A^8).$$

But $\omega_A U_A^2 + i\rho_A K_{A\perp}^2 = 0$, so it turns out that only the $O(K_A^8)$ terms are non-zero.

$$c_2 c_4 \approx (\boldsymbol{K}_W \cdot \boldsymbol{U}_A)^2 \left[\omega_A (\boldsymbol{U}_A \cdot \boldsymbol{U}_W) + i\rho_W K_{A\perp}^2\right]^2.$$

This, when combined with our expressions for c_1 and c_3, gives formula 3.65.

$$s \approx \pm \frac{(\boldsymbol{K}_W \cdot \boldsymbol{U}_A)}{2\omega_A K_A^2 K_{A\perp}^2} \left[\omega_A (\boldsymbol{U}_A \cdot \boldsymbol{U}_W) + i\rho_W K_{A\perp}^2\right].$$

Bibliography

Aerts, C., Christensen-Dalsgaard, J., and Kurtz, D. W. (2010). *Asteroseismology*. Astronomy and Astrophysics Library. Springer Netherlands, Dordrecht.

Alfvén, H. and Lindblad, B. (1947). Granulation, Magneto-Hydrodynamic Waves, and the Heating of the Solar Corona. *Monthly Notices of the Royal Astronomical Society*, 107(2):211–219.

Aschwanden, M. J., Fletcher, L., Schrijver, C. J., and Alexander, D. (1999). Coronal Loop Oscillations Observed with the *Transition Region and Coronal Explorer*. *The Astrophysical Journal*, 520(2):880–894.

Aurière, M., Konstantinova-Antova, R., Petit, P., Charbonnel, C., Dintrans, B., Lignières, F., Roudier, T., Alecian, E., Donati, J. F., Landstreet, J. D., and Wade, G. A. (2008). EK Eridani: the tip of the iceberg of giants which have evolved from magnetic Ap stars. *Astronomy & Astrophysics*, 491(2):499–505.

Babcock, H. D. (1959). The Sun's Polar Magnetic Field. *The Astrophysical Journal*, 130:364.

Babcock, H. W. (1947). Zeeman Effect in Stellar Spectra. *The Astrophysical Journal*, 105:105.

Bailey, A. and Goodman, J. (2019). Understanding WASP-12b. *Monthly Notices of the Royal Astronomical Society*, 482(2):1872–1882.

Baldwin, M. P., Gray, L. J., Dunkerton, T. J., Hamilton, K., Haynes, P. H., Randel, W. J., Holton, J. R., Alexander, M. J., Hirota, I., Horinouchi, T., Jones, D. B. A., Kinnersley, J. S., Marquardt, C., Sato, K., and Takahashi, M. (2001). The quasi-biennial oscillation. *Reviews of Geophysics*, 39(2):179–229.

Barker, A. J. (2011). Three-dimensional simulations of internal wave breaking and the fate of planets around solar-type stars: Wave breaking in a solar-type star. *Monthly Notices of the Royal Astronomical Society*, 414(2):1365–1378.

Barker, A. J. and Ogilvie, G. I. (2010). On internal wave breaking and tidal dissipation near the centre of a solar-type star. *Monthly Notices of the Royal Astronomical Society*.

Barker, A. J. and Ogilvie, G. I. (2011). Stability analysis of a tidally excited internal gravity wave near the centre of a solar-type star: Gravity wave stability analysis. *Monthly Notices of the Royal Astronomical Society*, 417(1):745–761.

Bender, C. M. and Orszag, S. A. (1999). *Advanced Mathematical Methods for Scientists and Engineers I*. Springer New York, New York, NY.

Booth, J. A. T., McPhee-Shaw, E. E., Chua, P., Kingsley, E., Denny, M., Phillips, R., Bograd, S. J., Zeidberg, L. D., and Gilly, W. F. (2012). Natural intrusions of hypoxic, low pH water into nearshore marine environments on the California coast. *Continental Shelf Research*, 45:108–115.

Boussinesq, J. (1903). Theorie analytique de la chaleur vol 2 (paris: Gauthier-villars).

Brandenburg, A. (2005). The Case for a Distributed Solar Dynamo Shaped by Near-Surface Shear. *The Astrophysical Journal*, 625(1):539–547.

Brookes, J. R., Isaak, G. R., and Van Der Raay, H. B. (1976). Observation of free oscillations of the Sun. *Nature*, 259(5539):92–95.

Burgess, C. P., Dzhalilov, N. S., Rashba, T. I., Semikoz, V. B., and Valle, J. W. F. (2004). Resonant origin for density fluctuations deep within the Sun: helioseismology and magneto-gravity waves. *Monthly Notices of the Royal Astronomical Society*, 348(2):609–624.

Burns, K. J., Vasil, G. M., Oishi, J. S., Lecoanet, D., and Brown, B. P. (2020). Dedalus: A flexible framework for numerical simulations with spectral methods. *Physical Review Research*, 2(2):023068.

Cally, P. S. and Bogdan, T. J. (2024). MHD waves in homogeneous and continuously stratified atmospheres. In *Magnetohydrodynamic Processes in Solar Plasmas*, pages 99–153. Elsevier.

Christensen-Dalsgaard, J., Däppen, W., Ajukov, S. V., Anderson, E. R., Antia, H. M., Basu, S., Baturin, V. A., Berthomieu, G., Chaboyer, B., Chitre, S. M., Cox, A. N., Demarque, P., Donatowicz, J., Dziembowski, W. A., Gabriel, M., Gough, D. O., Guenther, D. B., Guzik, J. A., Harvey, J. W., Hill, F., Houdek, G., Iglesias, C. A., Kosovichev, A. G., Leibacher, J. W., Morel, P., Proffitt, C. R., Provost, J., Reiter, J., Rhodes, E. J., Rogers, F. J., Roxburgh, I. W., Thompson, M. J., and Ulrich, R. K. (1996). The Current State of Solar Modeling. *Science*, 272(5266):1286–1292.

Cui, C. and Latter, H. N. (2022). The saturation of the VSI in protoplanetary discs via parametric instability. *Monthly Notices of the Royal Astronomical Society*, 512(2):1639–1647.

Davidson, P. A. (2017). *Introduction to magnetohydrodynamics*. Cambridge texts in applied mathematics. Cambridge University Press, Cambridge, second edition edition.

Davis, R. E. and Acrivos, A. (1967). The stability of oscillatory internal waves. *Journal of Fluid Mechanics*, 30(4):723–736.

Degl'Innocenti, E. L. and Landolfi, M. (2004). *Polarization in Spectral Lines*. Springer Netherlands, Dordrecht.

Donati, J.-F. and Cameron, A. C. (1997). Differential rotation and magnetic polarity patterns on AB Doradus -. *Monthly Notices of the Royal Astronomical Society*, 291(1):1–19.

Donati, J.-F., Cameron, A. C., Hussain, G. A. J., and Semel, M. (1999). Magnetic topology and prominence patterns on AB Doradus. *Monthly Notices of the Royal Astronomical Society*, 302(3):437–456.

Donati, J.-F., Cameron, A. C., Semel, M., Hussain, G. A. J., Petit, P., Carter, B. D., Marsden, S. C., Mengel, M., Ariste, A. L., Jeffers, S. V., and Rees, D. E. (2003). Dynamo processes and activity cycles of the active stars AB Doradus, LQ Hydrae and HR 1099. *Monthly Notices of the Royal Astronomical Society*, 345(4):1145–1186.

Donati, J.-F. and Landstreet, J. (2009). Magnetic Fields of Nondegenerate Stars. *Annual Review of Astronomy and Astrophysics*, 47(1):333–370.

Donati, J.-F., Moutou, C., Farès, R., Bohlender, D., Catala, C., Deleuil, M., Shkolnik, E., Cameron, A. C., Jardine, M. M., and Walker, G. A. H. (2008). Magnetic cycles of the planet-hosting star tau Bootis. *Monthly Notices of the Royal Astronomical Society*, 385(3):1179–1185.

Drazin, P. G. (1977). On the instability of an internal gravity wave. *Proceedings of the Royal Society of London. A. Mathematical and Physical Sciences*, 356(1686):411–432.

Eddington, A. S. (1926). *The Internal Constitution of the Stars*. Cambridge University Press, 1 edition.

Finlay, C. (2007). Alfvén Waves. In Gubbins, D. and Herrero-Bervera, E., editors, *Encyclopedia of Geomagnetism and Paleomagnetism*, pages 3–6. Springer Netherlands, Dordrecht.

Fritts, D. C. and Alexander, M. J. (2003). Gravity wave dynamics and effects in the middle atmosphere. *Reviews of Geophysics*, 41(1):2001RG000106.

Fuller, J., Cantiello, M., Stello, D., Garcia, R. A., and Bildsten, L. (2015). Asteroseismology can reveal strong internal magnetic fields in red giant stars. *Science*, 350(6259):423–426.

Fuller, J., Lecoanet, D., Cantiello, M., and Brown, B. (2014). Angular momentum transport via internal gravity waves in evolving stars. *The Astrophysical Journal*, 796(1):17.

Garcia Lopez, R. J. and Spruit, H. C. (1991). Li depletion in F stars by internal gravity waves. *The Astrophysical Journal*, 377:268.

Garrett, C. and Munk, W. (1972). Space-Time scales of internal waves. *Geophysical Fluid Dynamics*, 3(3):225–264.

Garwood, J. C., Lucas, A. J., Naughton, P., Alford, M. H., Roberts, P. L. D., Jaffe, J. S., deGelleke, L., and Franks, P. J. S. (2020). A novel cross-shore transport mechanism revealed by subsurface, robotic larval mimics: Internal wave deformation of the background velocity field. *Limnology and Oceanography*, 65(7):1456–1470.

Gillet, N., Gerick, F., Jault, D., Schwaiger, T., Aubert, J., and Istas, M. (2022). Satellite magnetic data reveal interannual waves in Earth's core. *Proceedings of the National Academy of Sciences*, 119(13):e2115258119.

Gladkikh, V. and Tenzer, R. (2012). A Mathematical Model of the Global Ocean Saltwater Density Distribution. *Pure and Applied Geophysics*, 169(1-2):249–257.

Goldreich, P. and Sridhar, S. (1995). Toward a theory of interstellar turbulence. 2: Strong alfvenic turbulence. *The Astrophysical Journal*, 438:763.

Goodman, J. and Dickson, E. S. (1998). Dynamical Tide in Solar-Type Binaries. *The Astrophysical Journal*, 507(2):938–944.

Gough, D. O. and McIntyre, M. E. (1998). Inevitability of a magnetic field in the Sun's radiative interior. *Nature*, 394(6695):755–757.

Grayson, K. (2021). *Triadic Resonance Instability in finite-width internal gravity wave beams*. PhD thesis, Apollo - University of Cambridge Repository.

Green, S. F., Jones, M. H., and Clark, J. S., editors (2015). *An introduction to the sun and stars*. Cambridge University Press ; The Open University, Cambridge, United Kingdom : Milton Keynes, United Kingdom, second edition edition.

Guo, Z., Ogilvie, G. I., and Barker, A. J. (2023). Tidally excited gravity waves in the cores of solar-type stars: resonances and critical-layer formation. *Monthly Notices of the Royal Astronomical Society*, 521(1):1353–1373.

Hale, G. E. (1908). On the probable existence of a magnetic field in sun-spots. *Terrestrial Magnetism and Atmospheric Electricity*, 13(4):159–160.

Hathaway, D. H. (2011). A Standard Law for the Equatorward Drift of the Sunspot Zones. *Solar Physics*, 273(1):221–230.

Higgins, G. and Kennedy, G. C. (1971). The adiabatic gradient and the melting point gradient in the core of the earth. *Journal of Geophysical Research (1896-1977)*, 76(8):1870–1878.

Hillier, A., Barker, A., Arregui, I., and Latter, H. (2019). On Kelvin–Helmholtz and parametric instabilities driven by coronal waves. *Monthly Notices of the Royal Astronomical Society*, 482(1):1143–1153.

Hollweg, J. V. (1991). Alfvén Waves. In Ulmschneider, P., Priest, E. R., and Rosner, R., editors, *Mechanisms of Chromospheric and Coronal Heating*, pages 423–434. Springer Berlin Heidelberg, Berlin, Heidelberg.

Hughes, D. W. and Proctor, M. R. E. (1988). Magnetic Fields in the Solar Convection Zone: Magnetoconvection and Magnetic Buoyancy. *Annual Review of Fluid Mechanics*, 20(1):187–223.

Hughes, D. W., Rosner, R., and Weiss, N. O., editors (2007). *The Solar Tachocline*. Cambridge University Press, 1 edition.

Ionson, J. A. (1978). Resonant absorption of Alfvenic surface waves and the heating of solar coronal loops. *The Astrophysical Journal*, 226:650.

Jaschek, C. and Jaschek, M. (1987). *The Classification of Stars*. Cambridge University Press, 1 edition.

Kav, A., Sutherland, B. R., Varma, D., Pacary, C., and Joubaud, S. (2025). Triad near-resonant instability of vertically bounded internal waves in non-uniform stratification. *Journal of Fluid Mechanics*, 1018:A20.

Kimbley, A. (2024). *Axisymmetric Instabilities in Stellar and Planetary Magnetohydrodynamics*. PhD thesis, School of Mathematics, University of Leeds.

Kippenhahn, R., Weigert, A., and Weiss, A. (2012). *Stellar Structure and Evolution*. Astronomy and Astrophysics Library. Springer, Berlin Heidelberg, 2nd ed. 2012 edition.

Klimchuk, J. A. (2006). On Solving the Coronal Heating Problem. *Solar Physics*, 234(1):41–77.

Klostermeyer, J. (1982). On parametric instabilities of finite-amplitude internal gravity waves. *Journal of Fluid Mechanics*, 119:367–377.

Klostermeyer, J. (1983). Parametric instabilities of internal gravity waves in boussinesq fluids with large reynolds numbers. *Geophysical & Astrophysical Fluid Dynamics*, 26(1-2):85–105.

Klostermeyer, J. (1991). Two- and three-dimensional parametric instabilities in finite-amplitude internal gravity waves. *Geophysical & Astrophysical Fluid Dynamics*, 61(1-4):1–25.

Konstantinova-Antova, R., Aurière, M., Charbonnel, C., Drake, N., Wade, G., Tsvetkova, S., Petit, P., Schröder, K.-P., and Lèbre, A. (2013). Magnetic fields in single late-type giants in the Solar vicinity: How common is magnetic activity on the giant branches? *Proceedings of the International Astronomical Union*, 9(S302):373–376.

Kotov, V. A., Severnyi, A. B., and Tsap, T. T. (1978). Observations of oscillations of the Sun. *Monthly Notices of the Royal Astronomical Society*, 183:61–78.

Krtička, J., Mikulášek, Z., Henry, G. W., Kurfürst, P., and Karlický, M. (2017). Torsional oscillations and observed rotational period variations in early-type stars. *Monthly Notices of the Royal Astronomical Society*, 464(1):933–939.

Kumar, P. and Quataert, E. J. (1997). Angular Momentum Transport by Gravity Waves and Its Effect on the Rotation of the Solar Interior. *The Astrophysical Journal*, 475(2):L143–L146.

Kumar, P., Talon, S., and Zahn, J. (1999). Angular Momentum Redistribution by Waves in the Sun. *The Astrophysical Journal*, 520(2):859–870.

Kuperus, M., Ionson, J. A., and Spicer, D. S. (1981). On the Theory of Coronal Heating Mechanisms. *Annual Review of Astronomy and Astrophysics*, 19(1):7–40.

Käpylä, P. J., Browning, M. K., Brun, A. S., Guerrero, G., and Warnecke, J. (2023). Simulations of Solar and Stellar Dynamos and Their Theoretical Interpretation. *Space Science Reviews*, 219(7):58.

Landstreet, J. D. and Mathys, G. (2000). Magnetic models of slowly rotating magnetic Ap stars: aligned magnetic and rotation axes. *Astronomy and Astrophysics*, 359:213–226.

Lecoanet, D., Bowman, D. M., and Van Reeth, T. (2022). Asteroseismic inference of the near-core magnetic field strength in the main-sequence B star HD 43317. *Monthly Notices of the Royal Astronomical Society: Letters*, 512(1):L16–L20.

Lecoanet, D. and Quataert, E. (2013). Internal gravity wave excitation by turbulent convection. *Monthly Notices of the Royal Astronomical Society*, 430(3):2363–2376.

Lecoanet, D., Vasil, G. M., Fuller, J., Cantiello, M., and Burns, K. J. (2017). Conversion of internal gravity waves into magnetic waves. *Monthly Notices of the Royal Astronomical Society*, 466(2):2181–2193.

Li, G., Deheuvels, S., Li, T., Ballot, J., and Lignières, F. (2023). Internal magnetic fields in 13 red giants detected by asteroseismology. *Astronomy & Astrophysics*, 680:A26.

Li, T., Li, Y., Bi, S., Bedding, T. R., Davies, G., and Du, M. (2022). Asteroseismology of 3642 Kepler Red Giants: Correcting the Scaling Relations Based on Detailed Modeling. *The Astrophysical Journal*, 927(2):167.

Lighthill, M. J. (2001). *Waves in fluids*. Cambridge mathematical library. Cambridge University Press, Cambridge, UK ; New York.

Lin, H., Penn, M. J., and Tomczyk, S. (2000). A New Precise Measurement of the Coronal Magnetic Field Strength. *The Astrophysical Journal*, 541(2):L83–L86.

Lindzen, R. S. and Holton, J. R. (1968). A Theory of the Quasi-Biennial Oscillation. *Journal of the Atmospheric Sciences*, 25(6):1095–1107.

Liu, W., Bretherton, F. P., Liu, Z., Smith, L., Lu, H., and Rutland, C. J. (2010). Breaking of Progressive Internal Gravity Waves: Convective Instability and Shear Instability*. *Journal of Physical Oceanography*, 40(10):2243–2263.

Loi, S. T. (2020). Magneto-gravity wave packet dynamics in strongly magnetized cores of evolved stars. *Monthly Notices of the Royal Astronomical Society*, 493(4):5726–5742.

Loi, S. T. and Papaloizou, J. C. B. (2017). Torsional Alfvén resonances as an efficient damping mechanism for non-radial oscillations in red giant stars. *Monthly Notices of the Royal Astronomical Society*.

Loi, S. T. and Papaloizou, J. C. B. (2018). Effects of a strong magnetic field on internal gravity waves: trapping, phase mixing, reflection, and dynamical chaos. *Monthly Notices of the Royal Astronomical Society*, 477(4):5338–5357.

Lombard, P. N. and Riley, J. J. (1996). Instability and breakdown of internal gravity waves. I. Linear stability analysis. *Physics of Fluids*, 8(12):3271–3287.

Mathioudakis, M., Jess, D. B., and Erdélyi, R. (2013). Alfvén Waves in the Solar Atmosphere: From Theory to Observations. *Space Science Reviews*, 175(1-4):1–27.

Mathis, S. and De Brye, N. (2011). Low-frequency internal waves in magnetized rotating stellar radiation zones: I. Wave structure modification by a toroidal field. *Astronomy & Astrophysics*, 526:A65.

Mathis, S. and De Brye, N. (2012). Low-frequency internal waves in magnetized rotating stellar radiation zones: II. Angular momentum transport with a toroidal field. *Astronomy & Astrophysics*, 540:A37.

Matthaeus, W. H., Zank, G. P., Oughton, S., Mullan, D. J., and Dmitruk, P. (1999). Coronal Heating by Magnetohydrodynamic Turbulence Driven by Reflected Low-Frequency Waves. *The Astrophysical Journal*, 523(1):L93–L96.

Maunder, E. W. (1913). Distribution of Sun-spots in Heliographic Latitude, 1874-1913. (Plates 2-4.). *Monthly Notices of the Royal Astronomical Society*, 74(2):112–116.

McEwan, A. D. and Robinson, R. M. (1975). Parametric instability of internal gravity waves. *Journal of Fluid Mechanics*, 67(4):667–687.

McIntosh, S. W., De Pontieu, B., Carlsson, M., Hansteen, V., Boerner, P., and Goossens, M. (2011). Alfvénic waves with sufficient energy to power the quiet solar corona and fast solar wind. *Nature*, 475(7357):477–480.

McLellan, A. and Winterberg, F. (1968). Magneto-gravity waves and the heating of the solar corona. *Solar Physics*, 4(4):401–408.

Mestel, L. (2012). *Stellar magnetism*. Number 154 in International series of monographs on physics. Oxford University Press, Oxford ; New York, 2nd ed edition.

Mestel, L. and Weiss, N. O. (1987). Magnetic fields and non-uniform rotation in stellar radiative zones. *Monthly Notices of the Royal Astronomical Society*, 226(1):123–135.

Mied, R. P. (1976). The occurrence of parametric instabilities in finite-amplitude internal gravity waves. *Journal of Fluid Mechanics*, 78(4):763–784.

Moore, K. M., Barik, A., Stanley, S., Stevenson, D. J., Nettelmann, N., Helled, R., Guillot, T., Militzer, B., and Bolton, S. (2022). Dynamo simulations of jupiter's magnetic field: The role of stable stratification and a dilute core. *Journal of Geophysical Research: Planets*, 127(11):e2022JE007479. e2022JE007479 2022JE007479.

Mosser, B., Belkacem, K., Pinçon, C., Takata, M., Vrard, M., Barban, C., Goupil, M.-J., Kallinger, T., and Samadi, R. (2017). Dipole modes with depressed amplitudes in red giants are mixed modes. *Astronomy & Astrophysics*, 598:A62.

Mosser, B., Vrard, M., Belkacem, K., Deheuvels, S., and Goupil, M. J. (2015). Period spacings in red giants: I. Disentangling rotation and revealing core structure discontinuities. *Astronomy & Astrophysics*, 584:A50.

Mowbray, D. E. and Rarity, B. S. H. (1967a). The internal wave pattern produced by a sphere moving vertically in a density stratified liquid. *Journal of Fluid Mechanics*, 30(3):489–495.

Mowbray, D. E. and Rarity, B. S. H. (1967b). A theoretical and experimental investigation of the phase configuration of internal waves of small amplitude in a density stratified liquid. *Journal of Fluid Mechanics*, 28(1):1–16.

Munk, W. and Wunsch, C. (1998). Abyssal recipes II: energetics of tidal and wind mixing. *Deep Sea Research Part I: Oceanographic Research Papers*, 45(12):1977–2010.

Müller, P. and Willebrand, J. (1986). Compressibility effects in the thermohaline circulation: a manifestation of the temperature-salinity mode. *Deep Sea Research Part A. Oceanographic Research Papers*, 33(5):559–571.

Nakariakov, V. M., Ofman, L., and Arber, T. D. (2000). Nonlinear dissipative spherical Alfvén waves in solar coronal holes. *Astronomy and Astrophysics*, 353:741–748.

Ng, C. S. and Bhattacharjee, A. (1996). Interaction of Shear-Alfven Wave Packets: Implication for Weak Magnetohydrodynamic Turbulence in Astrophysical Plasmas. *The Astrophysical Journal*, 465:845.

Ofman, L. (2007). Coronal Heating and Acceleration of the Solar Wind. In *Coronal Heating and Acceleration of the Solar Wind*, volume 370, page 82.

Ofman, L., Davila, J. M., Nakariakov, V. M., and Viñas, A. (2005). High-frequency Alfvén waves in multi-ion coronal plasma: Observational implications. *Journal of Geophysical Research: Space Physics*, 110(A9):2004JA010969.

Ofman, L. and Wang, T. J. (2008). *Hinode* observations of transverse waves with flows in coronal loops. *Astronomy & Astrophysics*, 482(2):L9–L12.

Osterbrock, D. E. (1961). The Heating of the Solar Chromosphere, Plages, and Corona by Magnetohydrodynamic Waves. *The Astrophysical Journal*, 134:347.

Pinçon, C., Belkacem, K., and Goupil, M. J. (2016). Generation of internal gravity waves by penetrative convection. *Astronomy & Astrophysics*, 588:A122.

Plougonven, R. and Zhang, F. (2014). Internal gravity waves from atmospheric jets and fronts. *Reviews of Geophysics*, 52(1):33–76.

Prialnik, D. (2009). *An Introduction to the Theory of Stellar Structure and Evolution*. Cambridge University Press.

Priest, E. (2014). *Magnetohydrodynamics of the Sun*. Cambridge University Press, 1 edition.

Pringle, J. E. and King, A. (2007). *Astrophysical Flows*. Cambridge University Press.

Rayleigh, L. (1883). The Form of Standing Waves on the Surface of Running Water. *Proceedings of the London Mathematical Society*, s1-15(1):69–78.

Robinson, R. D., Worden, S. P., and Harvey, J. W. (1980). Observations of magnetic fields on two late-type dwarf stars. *The Astrophysical Journal*, 236:L155.

Robinson, Jr., R. D. (1980). Magnetic field measurements on stellar sources - A new method. *The Astrophysical Journal*, 239:961.

Rogers, T. M. and MacGregor, K. B. (2010). On the interaction of internal gravity waves with a magnetic field – I. Artificial wave forcing. *Monthly Notices of the Royal Astronomical Society*, 401(1):191–196.

Rogers, T. M. and MacGregor, K. B. (2011). On the interaction of internal gravity waves with a magnetic field - II. Convective forcing: Wave-field interaction. *Monthly Notices of the Royal Astronomical Society*, 410(2):946–962.

Russell, C., Jian, L., and Luhmann, J. (2019). The Solar Clock. *Reviews of Geophysics*, 57(4):1129–1145.

Saar, S. H. (1988). Improved methods for the measurement and analysis of stellar magnetic fields. *The Astrophysical Journal*, 324:441.

Salhi, A. and Nasraoui, S. (2013). Instability of subharmonic resonances in magnetogravity shear waves. *Physical Review E*, 88(6):063016.

Schatzman, E. (1993). Transport of angular momentum and diffusion by the action of internal waves. *Astronomy and Astrophysics*, 279:431–446.

Semel, M. (1989). Zeeman-Doppler imaging of active stars. I - Basic principles. *Astronomy and Astrophysics*, 225:456–466.

Severny, A. B., Kotov, V. A., and Tsap, T. T. (1976). Observations of solar pulsations. *Nature*, 259(5539):87–89.

Sonmor, L. J. and Klaassen, G. P. (1997). Toward a Unified Theory of Gravity Wave Stability. *Journal of the Atmospheric Sciences*, 54(22):2655–2680.

Spiegel, E. A. and Veronis, G. (1960). On the Boussinesq Approximation for a Compressible Fluid. *The Astrophysical Journal*, 131:442.

Sridhar, S. and Goldreich, P. (1994). Toward a theory of interstellar turbulence. 1: Weak Alfvenic turbulence. *The Astrophysical Journal*, 432:612.

Staquet, C. and Sommeria, J. (2002). Internal gravity waves: From instabilities to turbulence. *Annual Review of Fluid Mechanics*, 34(1):559–593.

Stello, D., Vanderburg, A., Casagrande, L., Gilliland, R., Aguirre, V. S., Sandquist, E., Leiner, E., Mathieu, R., and Soderblom, D. R. (2016). The k2 m67 study: revisiting old friends with k2 reveals oscillating red giants in the open cluster m67. *The Astrophysical Journal*, 832(2):133.

Sutherland, B. R. (2010). *Internal Gravity Waves*. Cambridge University Press, 1 edition.

Takahashi, K. and Langer, N. (2025). Standing torsional Alfvén waves as the source of the rotational period variation in magnetic early-type stars. *Astronomy & Astrophysics*, 696:A129.

Taroyan, Y. and Erdélyi, R. (2009). Heating Diagnostics with MHD Waves. *Space Science Reviews*, 149(1-4):229–254.

Turck-Chièze, S., Garcia, R. A., Couvidat, S., Ballot, J., Jiménez-Reyes, S. J., Fossat, E., Gelly, B., Mathur, S., Nghiem, P. A. P., Pallé, P., Robillot, J., and GOLF-Ng Technical Team (2004). Gravity Modes with a Resonant Scattering Spectrophotometer. In *Gravity Modes with a Resonant Scattering Spectrophotometer*, volume 559, page 85.

Varma, D., Mathur, M., and Dauxois, T. (2022). Instabilities in internal gravity waves. *Mathematics in Engineering*, 5(1):1–34.

Verhoogen, J. (1973). Thermal regime of the earth's core. *Physics of the Earth and Planetary Interiors*, 7(1):47–58.

Vigeesh, G., Jackiewicz, J., and Steiner, O. (2017). Internal Gravity Waves in the Magnetized Solar Atmosphere. I. Magnetic Field Effects. *The Astrophysical Journal*, 835(2):148.

Vosper, S. (1996). Gravity-wave drag on two mountains. *Quarterly Journal of the Royal Meteorological Society*, 122(532):993–999.

Weinberg, N. N., Davachi, N., Essick, R., Yu, H., Arras, P., and Belland, B. (2024). Orbital Decay of Hot Jupiters due to Weakly Nonlinear Tidal Dissipation. *The Astrophysical Journal*, 960(1):50.

Weinberg, N. N., Sun, M., Arras, P., and Essick, R. (2017). Tidal Dissipation in WASP-12. *The Astrophysical Journal Letters*, 849(1):L11.

Withbroe, G. L. and Noyes, R. W. (1977). Mass and Energy Flow in the Solar Chromosphere and Corona. *Annual Review of Astronomy and Astrophysics*, 15(1):363–387.

Yee, S. W., Winn, J. N., Knutson, H. A., Patra, K. C., Vissapragada, S., Zhang, M. M., Holman, M. J., Shporer, A., and Wright, J. T. (2020). The Orbit of WASP-12b Is Decaying. *The Astrophysical Journal Letters*, 888(1):L5.

Zahn, J. P. (1977). Tidal friction in close binary systems. *Astronomy and Astrophysics*, 57:383–394.

Zahn, J.-P., Talon, S., and Matias, J. (1996). Angular momentum transport by internal waves in the solar interior. Version Number: 1.

Zirker, J. B. (1993). Coronal Heating. *Solar Physics*, 148:43–60.